



University  
of Glasgow

Alganash, Blaid Sasi Abozeid (2015) *Numerical investigation of the combustion processes of various combustion regimes*. PhD thesis.

<http://theses.gla.ac.uk/7124/>

Copyright and moral rights for this thesis are retained by the author

A copy can be downloaded for personal non-commercial research or study

This thesis cannot be reproduced or quoted extensively from without first obtaining permission in writing from the Author

The content must not be changed in any way or sold commercially in any format or medium without the formal permission of the Author

When referring to this work, full bibliographic details including the author, title, awarding institution and date of the thesis must be given



# **Numerical investigation of the combustion processes of various combustion regimes**

A thesis submitted in fulfilment of the requirements  
for the degree of Doctor of Philosophy (PhD)

in the  
School of Engineering  
of the  
University of Glasgow

By

**Blaid Sasi Abozeid Alganash**  
B.Sc., M.Sc.

Systems, Power & Energy Research Division  
School of Engineering  
College of Science and Engineering  
University of Glasgow  
Glasgow UK

May 2015

Copyright © 2015 by Blaid Alganash  
All Rights Reserved

# Declaration

This dissertation is the result of my own work. Any published ideas or techniques from other works are fully acknowledged in accordance with the standard referencing practices.

.....

Blaid S. A. Alganash

May, 2015

# **Dedication**

This work is dedicated  
to my parents,  
my wife and my children

# Abstract

This thesis concerns numerical investigations of the combustion behaviour of various combustion regimes. The simulations are based on modelling the flow of the fuels in the combustion devices. Computational fluid dynamics (CFD) modelling and analysis were used in three different works. FLUENT software, which is based on the finite volume method, is used to carry out all the simulations. Firstly, numerical simulations were carried out to investigate the turbulent non-premixed combustion of a mixture of methane (CH<sub>4</sub>) 90% and nitrogen (N<sub>2</sub>) 10%, on volume basis, inside an axis-symmetric cylindrical chamber (base case). The objective is to investigate the turbulent flow, flame propagation, temperature and species concentration and evaluate the effects of different reduced reaction mechanisms of methane and the influence of various turbulence models on them. The turbulent combustion inside the chamber occurs under a condition for which the equivalence ratio ( $\phi$ ) of 1.04 is used. Instead of using fully detailed chemical kinetics schemes and to reduce the computational costs, four global reduced chemical kinetics mechanisms are employed in the combustion model and they are named as (M-I, M-II, M-III and M-IV). The simulations, in which M-I is used, are performed by Reynolds-Averaged Navier Stokes (RANS) approach with the three two-equation  $k$ - $\epsilon$  closures (standard, realizable and RNG) employed to model the turbulent flow. Concerning the chemistry-turbulence interaction, the finite-rate/eddy-dissipation model (FR/ED) is used. The first two of the above kinetics schemes are two-step reaction mechanisms and the other two are first-step and five-step reaction mechanisms, respectively. The latter one is used to assess the capability of FR/ED model for modeling such a mechanism. The influence of thermal radiation is also investigated by means of P-1 model. The standard  $k$ - $\epsilon$  model and realizable  $k$ - $\epsilon$  model are also modified and used in the course of simulations. Moreover, the reaction mechanism (M-II) is optimized to see its effects on the combustion process. The results are compared with the experimental data and gave good agreement. It is found that the best results are generally obtained using the modified standard  $k$ - $\epsilon$  model. Moreover, the simulation results using the realizable turbulence model are found to have large discrepancies compared to the experimental data. In comparison with the experimental data, the optimization of M-II ( $E_m = 1.6 \times 10^8$  J/kmol) is found to have good results in terms of temperature. Increasing the dilution of the fuel by N<sub>2</sub> is investigated. Four cases, CH<sub>4</sub> (85, 80, 75 and 100%) on volume basis, are performed. The latter one

concerns the combustion of pure methane. The results are compared with the base case and found that the base case is the best compromise to obtain the highest temperature inside the chamber.

Secondly, an axis-symmetric combustion model based on the Euler-Lagrange approach was formulated to model the combustion of pulverized bituminous coal. Three cases with three different char oxidation models are presented. In case 1 and case 2, the diffusion and kinetic/diffusion global char models are used, respectively. Whereas, to model char oxidation in case 3, the multi-surface reactions model is used. The volatiles released during the devolatilization stage, which is modelled using a single kinetic rate model, are treated as one species and its combustion is modelled using the FR/ED model. The predicted results have good agreement with the available experimental data and the best predictions are obtained from case 3. The results showed that the combustion inside the reactor was affected by the particulate size. It is found that the burnout of the particle with the diameter of 16  $\mu\text{m}$  at the exit of the furnace is 100%. Whereas, the burnout of the particles with diameters of 84, 154, 222, 291  $\mu\text{m}$  is approximately 86, 75, 35, 33, 29 %, respectively.

A number of simulations were carried out to find the best values of parameters suitable for predicting  $\text{NO}_x$  pollutants. The chemical formation and reduction rates of NO are calculated by post-processing data obtained from the previously reacting flow simulations. This method is computationally efficient. For volatile-N is assumed that the nitrogen is released via the intermediates HCN and  $\text{NH}_3$ . For char-N path way, it is assumed that all the nitrogen is released via the intermediate HCN. It is found that the assumption of the partition of volatile-N by 52% HCN, 10%  $\text{NH}_3$  and 38% NO has the best agreement with the experiment data. The influence of different operating parameters on the combustion process and  $\text{NO}_x$  formation was investigated as well.

For the same operating conditions and the same particles size distribution, the combustion of pulverised biomass alone, represented by straw, was investigated followed by the investigation of its firing with coal. The former one show a promising results under such operating conditions. It is found that the temperature distribution when burning straw particles is nearly the same as that obtained from burning coal because all the saw particles are completely burned out inside the furnace when compared with the coal particles. The  $\text{NO}_x$  model, in which the ratio of HCN to  $\text{NH}_3$  is suggested to be for the partitioning of volatile-N, shows that NO formation is reduced

by approximately 20% for case I and 26% for case II at the exit of the furnace when compared to coal. For the latter one the results of co-firing blends of coal with 10, 20, 30 and 40% share of biomass are presented and show the influence of co-firing on the combustion process. Co-firing of straw with coal enhances the combustion behaviour and increases the burnout of coal particles compared to that of coal firing only. It is seen that the burnout of the particles with sizes 84, 154 and 222  $\mu\text{m}$  is remarkably increased. On the other hand, the burnout of the other two particles (291  $\mu\text{m}$  and 360  $\mu\text{m}$ ) does not show a great change. The share of 10% of straw shows the highest temperature.

Thirdly, Two-phase computational modelling based on the Euler–Euler was developed to investigate the heterogeneous combustion processes of carbon particles inside a newly designed combustion chamber. A transient simulation was carried out for a small amount of carbon powder situated in a cup which was located at the centre of the combustion chamber. A heat source was provided to initiate the combustion with the air supplied by three injection nozzles. The combustion simulations are performed for particle sizes with different diameters (0.5mm, 1mm, 1.5mm, 2mm, 2.5mm and 3mm). The particle of 1mm diameter is assigned to the baseline case. The results show that the combustion is sustained in the chamber, as evidenced by the flame temperature. It is shown that, up to a time of 0.55 s, the higher temperature was gained from the case of carbon particles with the diameter of 3 mm and burning the carbon particles with a diameter of 0.5 mm produces lower temperature. This may be attributed to the residence time of the carbon particles and the design of the burner. The larger particles stay longer than the smaller ones inside the chamber. This may be due to the reason that the smaller particles follow the streamlines of the continuous phase and increasing the particle size leads to that the larger particles may deviate from the streamlines of the continuous phase and their slip velocity may increase resulting in enhancing convective transports of heat and species concentrations.

The influence of the chamber design was also investigated. The height of the chamber is doubled. With the same operating conditions, up to a time of approximately 0.55 s, it is found that burning carbon particles in the doubled height chamber produces higher temperature than the baseline case (particle diameter 1 mm) and after this time the opposite takes place. Most of the other cases do so.

# Acknowledgement

For their insight and encouragement, there are so many people who deserve a thank you during the course of this PhD, but firstly, I thank Allah for his many blessings and countless favours on me. I would like to thank Allah for giving me the health and the patience from the beginning to the end of this research study.

I owe a matchless and sincere gratitude to my supervisors, Dr Manosh C. Paul and Dr Ian Watson for their help and support. I would like to offer them my deepest thanks for their consistent support, warm encouragement, wise criticisms, insightful suggestions, scientific guidance and inspiring determination in preparing and improving of this thesis.

I must acknowledge the Ministry of Higher Education in Libya for providing the financial support for my PhD study and my stay in Glasgow.

I would like to thank all members of academic staff, IT staff, technical staff and administrative staff of school of engineering who have helped during the course of this work.

I am deeply indebted to my parents who dedicated their lives to ensure my success in my academic programme. I am very grateful to them for their moral support and encouragement during my stay abroad. I really owe them much that I cannot express. Most special thanks are to my wife and children for always being there for me. They have given up a lot in order to give me the opportunity to complete this work. They shared the joy and pain with me. I extend my thanks to my brothers, particularly Ahmad, sisters and relatives who stood by me.

Finally, I am delighted to acknowledge the support, the encouragement and the pleasant working environment I have received from all my colleagues. In particular, many thanks to my office mate Ahmad Alwaaly, Najeeb Yahya and Taiwo O. Oni.



# Contents

<b>Abstract.....</b>	<b>iii</b>
<b>Acknowledgement.....</b>	<b>v</b>
<b>List of figures.....</b>	<b>x</b>
<b>List of tables .....</b>	<b>xix</b>
<b>List of symbols.....</b>	<b>xix</b>
<b>List of abbreviations .....</b>	<b>1</b>
<b>1 Introduction.....</b>	<b>2</b>
1.1 Computational Fluid Dynamics (CFD).....	10
1.2 Purpose of the work.....	10
1.3 The importance of the research study .....	10
1.4 Thesis outline .....	10
<b>2 Literature review .....</b>	<b>11</b>
2.1 Solid fuels structure and properties .....	11
2.1.1 Non-renewable solid fuel (coal).....	14
2.1.2 Renewable solid fuel (biomass) .....	17
2.2 Coal versus biomass combustion .....	21
2.3 Combustion characteristics .....	23
2.4 Thermo-chemical conversion processes of solid fuels.....	24
2.5 Char oxidation (heterogeneous combustion).....	32
2.6 Combustion technologies .....	34
2.7 Modelling of solid fuel rates .....	37
2.7.1 Drying.....	38
2.7.2 Devolatilization models.....	38
2.7.3 Heterogeneous combustion models.....	41
<b>3 RANS simulations of methane combustion .....</b>	<b>44</b>
3.1 Introduction .....	44
3.2 Governing equations .....	47
3.2.1 The Navier-Stokes (N-S) equations .....	47
3.2.2 Species mass conservation equation .....	48
3.2.3 Energy conservation equation .....	49
3.2.4 The equation of state .....	51

3.3	Turbulence models .....	51
3.3.1	Transport equations for the standard $k$ - $\epsilon$ model .....	54
3.3.2	Transport equations for the RNG $k$ - $\epsilon$ model .....	54
3.3.3	Transport equations for the realizable $k$ - $\epsilon$ model .....	55
3.4	Thermal radiation .....	56
3.5	Chemistry modelling .....	58
3.5.1	Chemical kinetics .....	58
3.5.2	Reaction mechanism .....	59
3.5.3	Modelling turbulence/chemistry interactions .....	61
3.5.3.1	Eddy-dissipation model (EDM).....	62
3.5.3.2	Finite-rate/eddy-dissipation model (FR/ED) .....	63
3.5.3.3	Eddy dissipation concept model (EDC) .....	63
3.6	Numerical methods .....	64
3.7	Geometry and boundary conditions .....	64
3.8	Material properties .....	65
3.9	Computational domain and grid refinement.....	65
3.10	Results and discussion.....	71
3.10.1	Mechanism one (M-I).....	71
3.10.2	Mechanism (M-I) with modified turbulence model .....	90
3.10.3	Mechanism two (M-II) .....	98
3.10.4	Mechanisms M-III and M-IV .....	107
3.10.5	The effect of fuel concentration .....	115
3.11	Conclusion.....	118
<b>4</b>	<b>Pulverized combustion .....</b>	<b>120</b>
4.1	Introduction .....	120
4.2	Governing equations and used models.....	123
4.2.1	Gas phase.....	123
4.2.2	Modelling of the particulate phase .....	123
4.2.2.1	The particle equation of motion.....	124
4.2.2.2	Heat and mass transfer to and from particles calculations .....	125
4.2.2.3	Thermally-thin assumption.....	127
4.2.3	Combustion stages of fuel particle .....	127
4.2.4	Turbulent dispersion in gas-solid flow.....	128
4.2.5	Particle size distribution .....	130
4.2.6	Radiation .....	131

---

4.3	Pulverized coal combustion .....	131
4.3.1	Model geometry and operating conditions.....	131
4.4	Chemistry of coal .....	133
4.4.1.1	Devlatilization .....	133
4.4.1.2	Heterogeneous reactions.....	134
4.4.1.3	Gas phase reactions .....	136
4.4.2	Coal volatile elemental composition and enthalpy of formation .....	138
4.5	Mesh-independence study .....	140
4.6	Numerical methods .....	141
4.7	Modelling of NO <sub>x</sub> chemistry .....	142
4.7.1	Mechanisms of NO <sub>x</sub> formation .....	142
4.7.2	Kinetics of NO <sub>x</sub> reactions.....	144
4.7.3	Numerical procedure .....	149
4.8	Results and discussion of coal combustion model.....	151
4.8.1	Combustion model .....	151
4.8.1.1	Model validation.....	151
4.8.1.2	Temperature and mass fractions of combustion species .....	154
4.8.1.3	Particles depletion and burnout .....	162
4.8.2	NO <sub>x</sub> model.....	164
4.8.3	Effects of wall temperature .....	165
4.8.4	The influence of air inlet rate .....	170
4.9	Biomass pulverized combustion .....	179
4.9.1	Chemistry of straw and chemical reactions.....	179
4.9.2	Numerical solution .....	181
4.10	Results and discussion of straw combustion.....	181
4.10.1	Combustion results of pulverized straw .....	181
4.10.2	NO <sub>x</sub> formation from straw burning .....	187
Figure 4.59: The radial profiles of NO mass fraction at various axial locations. ....		189
4.10.3	Co-firing of coal and biomass particles.....	190
4.11	Conclusion.....	193
<b>5</b>	<b>Multiphase modelling (Euler-Euler approach).....</b>	<b>196</b>
5.1	Mathematical model.....	196
5.1.1	Conservation of mass and momentum .....	196
5.1.2	Conservation of energy .....	199
5.2	Turbulence modelling .....	200

---

5.3	Overview of numerical methods .....	201
5.4	Geometry and boundary conditions .....	201
5.5	Grid-independence study.....	203
5.6	Results and discussion.....	204
5.6.1	Base case .....	204
5.6.2	The influence of chamber height.....	213
5.7	Conclusion.....	224
<b>6</b>	<b>Final conclusions and recommendations for future research .....</b>	<b>225</b>
6.1	Conclusions .....	225
6.2	Recommendations for future research.....	228
	<b>References.....</b>	<b>230</b>
	<b>Appendix A.....</b>	<b>242</b>
	<b>Appendix B.....</b>	<b>243</b>
	<b>Appendix C.....</b>	<b>246</b>
	<b>Appendix D.....</b>	<b>248</b>
	<b>Appendix E.....</b>	<b>250</b>
	<b>Appendix F Publications and presentations .....</b>	<b>255</b>

# List of figures

Figure 1.1: Renewable energy sources till 2040. ....	11
Figure 1.2: The total global consumption of energy and the total renewable energy sources till 2040. ....	11
Figure 1.3: Renewable energy contribution (%) till 2040.....	12
Figure 1.4: The contribution of renewable energy sources to the world total primary energy consumption [9].....	12
Figure 1.5: Fuel shares in the world total primary energy supply 2011 [10].....	13
Figure 1.6: Product shares in the world renewable energy supply [10].....	13
Figure 1.7: Renewable share of power generation [3]. ....	14
Figure 2.1: Chemical composition of various solid fuels [26].....	13
Figure 2.2: Coal rank as a function of H/C and O/C atomic ratios [27]. ....	13
Figure 2.3: Coalification (adopted from [29]).....	14
Figure 2.4: Examples of biomass. ....	17
Figure 2.5: Thermo-chemical process for conversion of biomass into fuels, gases or chemicals.....	24
Figure 2.6: Various chemical and physical mechanisms during solid fuel combustion (adapted from [59]). ....	25
Figure 2.7: Combustion stages of a small biomass particle (adapted from [26]).....	26
Figure 2.8: Thermo-gravimetric weight loss curves of four wood samples: ○ spruce, □ birch, ● beech white and ■ acacia (adapted from [26]). ....	29
Figure 2.9: Char combustion (adapted from [110]). ....	33
Figure 2.10: Coal combustion systems outline (adapted from [117]).....	35
Figure 2.11: Two-stage semi-global reaction mechanisms for (a) cellulose; (b) wood. ....	40
Figure 3.1: Geometrical configuration of the burner. ....	64
Figure 3.2: Computational grid. ....	66
Figure 3.3: Velocity along the axial distance of the furnace for three different meshes. ....	67
Figure 3.4: Temperature along the axial distance of the furnace for three different meshes. ....	67
Figure 3.5: Radial profiles of velocity at $x = 0.312$ m for three different meshes.....	68
Figure 3.6: Radial profiles of velocity at $x = 0.612$ m for three different meshes.....	68
Figure 3.7: Radial profiles of velocity at $x = 0.912$ m for three different meshes.....	69

Figure 3.8: Radial profiles of temperature at $x = 0.612$ m for three different meshes...	69
Figure 3.9: Radial profiles of temperature at $x = 0.912$ m for three different meshes...	70
Figure 3.10: Velocity profile inside the chamber for $k-\epsilon$ standard case (M-I).....	71
Figure 3.11: Axial velocity profile inside the chamber for $k-\epsilon$ standard case (M-I).....	72
Figure 3.12: Velocity field vectors inside the chamber for $k-\epsilon$ standard case (M-I).....	72
Figure 3.13: The variation of axial velocity along the radial direction at different axial locations $k-\epsilon$ standard case (M-I).....	72
Figure 3.14: Velocity magnitude along the centreline of the chamber (M-I).....	73
Figure 3.15: Axial velocity along the centreline of the chamber (M-I).....	73
Figure 3.16: Temperature distributions for standard $k-\epsilon$ case (M-I).....	74
Figure 3.17: Temperature distributions for RNG $k-\epsilon$ case (M-I).....	74
Figure 3.18: Temperature distributions for Realizable $k-\epsilon$ case (M-I).....	75
Figure 3.19: Temperature distributions for standard $k-\epsilon$ case (without radiation) (M-I).....	75
Figure 3.20: CH <sub>4</sub> mass fraction for standard $k-\epsilon$ case (M-I).....	76
Figure 3.21: O <sub>2</sub> mass fraction for standard $k-\epsilon$ case (M-I).....	76
Figure 3.22: CO <sub>2</sub> mass fraction for standard $k-\epsilon$ case (M-I).....	76
Figure 3.23: CO mass fraction for standard $k-\epsilon$ case (M-I).....	76
Figure 3.24: Rate of methane destruction reaction (r-2) in (kmol/m <sup>3</sup> /s) for standard $k-\epsilon$ case (M-I).....	77
Figure 3.25: Rate of reaction (r-3) in (kmol/m <sup>3</sup> /s) for standard $k-\epsilon$ case (M-I).....	77
Figure 3.26: Rate of reaction (r-4) in (kmol/m <sup>3</sup> /s) for standard $k-\epsilon$ case (M-I).....	77
Figure 3.27: The profiles of reaction rate along the centreline of the chamber for standard $k-\epsilon$ case (M-I).....	78
Figure 3.28: Gas temperature along the centreline of the chamber (M-I).....	78
Figure 3.29: Comparison between the experimental and predicted data of gas temperature for all cases- (M-I). Ideal results lie on the line indicated by $y = z$ . ....	79
Figure 3.30: CH <sub>4</sub> mass fraction along the central line (M-I).....	80
Figure 3.31: O <sub>2</sub> mass fraction along the central line (M-I).....	81
Figure 3.32: CO mass fraction along the central line (M-I).....	82
Figure 3.33: CO <sub>2</sub> mass fraction along the central line (M-I).....	83
Figure 3.34: Radial temperature profile at axial location $x = 0.312$ m, (M-I).....	85
Figure 3.35: Radial temperature profile at axial location $x = 0.912$ m, (M-I).....	85
Figure 3.36: Radial temperature profile at axial location $x = 1.312$ m, (M-I).....	86
Figure 3.37: Radial profile of O <sub>2</sub> mass fraction at axial location $x = 0.312$ m, (M-I).....	86

---

Figure 3.38: Radial profile of O <sub>2</sub> mass fraction at axial location $x = 0.912$ m, (M-I). ..87	87
Figure 3.39: Radial profile of O <sub>2</sub> mass fraction at axial location $x = 1.312$ m, (M-I). ..87	87
Figure 3.40: Radial profile of CO <sub>2</sub> mass fraction at axial distance $x = 0.312$ m, (M-I).88	88
Figure 3.41: Radial profile of CO <sub>2</sub> mass fraction at axial distance $x = 0.912$ m, (M-I).88	88
Figure 3.42: Radial profile of CO <sub>2</sub> mass fraction at axial distance $x = 1.312$ m, (M-I).89	89
Figure 3.43: Radial profile of CO mass fraction at axial location $x = 1.312$ m, (M-I). ..89	89
Figure 3.44: Gas temperature along the centreline of the chamber (M-I with modified turbulence models). ....90	90
Figure 3.45: O <sub>2</sub> mass fraction along the centreline of the chamber (M-I with modified turbulence models). ....91	91
Figure 3.46: CO mass fraction along the centreline of the chamber (M-I with modified turbulence models). ....92	92
Figure 3.47: CO <sub>2</sub> mass fraction along the centreline of the chamber (M-I with modified turbulence models). ....92	92
Figure 3.48: Radial temperature profile at axial location $x = 0.312$ m, (M-I with modified turbulence models).....93	93
Figure 3.49: Radial temperature profile at axial location $x = 0.912$ m, (M-I with modified turbulence models).....94	94
Figure 3.50: Radial temperature profile at axial location $x = 1.312$ m, (M-I with modified turbulence models).....94	94
Figure 3.51: Radial profile of O <sub>2</sub> mass fraction at axial location $x = 0.312$ m, (M-I with modified turbulence models).....95	95
Figure 3.52: Radial profile of O <sub>2</sub> mass fraction at axial location $x = 0.912$ m, (M-I with modified turbulence models).....95	95
Figure 3.53: Radial profile of O <sub>2</sub> mass fraction at axial location $x = 1.312$ m, (M-I with modified turbulence models).....96	96
Figure 3.54: Radial profile of CO <sub>2</sub> mass fraction at axial location $x = 0.312$ m, (M-I with modified turbulence models).....96	96
Figure 3.55: Radial profile of CO <sub>2</sub> mass fraction at axial location $x = 0.912$ m, (M-I with modified turbulence models).....97	97
Figure 3.56: Radial profile of CO <sub>2</sub> mass fraction at axial location $x = 1.312$ m, (M-I with modified turbulence models).....97	97
Figure 3.57: Radial profile of CO mass fraction at axial location $x = 1.312$ m, (M-I with modified turbulence models).....98	98
Figure 3.58: Gas temperature along the centreline of the chamber, (M-II). ....100	100

---

Figure 3.59: O <sub>2</sub> mass fraction along the centreline of the chamber, (M-II).....	100
Figure 3.60: CO <sub>2</sub> mass fraction along the centreline of the chamber, (M-II). .....	101
Figure 3.61: CO mass fraction along the centreline of the chamber, (M-II).....	101
Figure 3.62: Radial temperature profile at axial location $x = 0.312$ m, (M-II). .....	102
Figure 3.63: Radial temperature profile at axial location $x = 0.912$ m, (M-II). .....	102
Figure 3.64: Radial temperature profile at axial location $x = 1.312$ m, (M-II). .....	103
Figure 3.65: Radial profile of O <sub>2</sub> mass fraction at axial location $x = 0.312$ m, (M-II). .....	103
Figure 3.66: Radial profile of O <sub>2</sub> mass fraction at axial location $x = 0.912$ m, (M-II). .....	104
Figure 3.67: Radial profile of O <sub>2</sub> mass fraction at axial location $x = 1.312$ m, (M-II). .....	104
Figure 3.68: Radial profile of CO <sub>2</sub> mass fraction at axial location $x = 0.312$ m, (M-II). .....	105
Figure 3.69: Radial profile of CO <sub>2</sub> mass fraction at axial location $x = 0.912$ m, (M-II). .....	105
Figure 3.70: Radial profile of CO <sub>2</sub> mass fraction at axial location $x = 1.312$ m, (M-II). .....	106
Figure 3.71: Radial profile of CO mass fraction at axial location $x = 1.312$ m, (M-II). .....	106
Figure 3.72: Gas temperature along centreline of the chamber for all cases. ....	108
Figure 3.73: O <sub>2</sub> mass fraction along the centreline of the chamber for all cases. ....	109
Figure 3.74: CO <sub>2</sub> mass fraction along the centreline of the chamber for all cases. ....	109
Figure 3.75: CO mass fraction along the centreline of the chamber for all cases.....	110
Figure 3.76: Radial temperature profiles at axial location $x = 0.312$ m for all cases...	110
Figure 3.77: Radial temperature profile at axial location $x = 0.912$ m for all cases. ...	111
Figure 3.78: Radial temperature profile at axial location $x = 1.312$ m for all cases. ...	111
Figure 3.79: Radial profile of O <sub>2</sub> mass fraction at axial location $x = 0.312$ m for all cases. ....	112
Figure 3.80: Radial profile of O <sub>2</sub> mass fraction at axial location $x = 0.912$ m for all cases. ....	112
Figure 3.81: Radial profile of O <sub>2</sub> mass fraction at axial location $x = 1.312$ m for all cases. ....	113
Figure 3.82: Radial profile of CO <sub>2</sub> mass fraction at axial location $x = 0.312$ m for all cases. ....	113

---



Figure 3.83: Radial profile of CO <sub>2</sub> mass fraction at axial location $x = 0.912$ m for all cases. ....	114
Figure 3.84: Radial profile of CO <sub>2</sub> mass fraction at axial location $x = 1.312$ m for cases. ....	114
Figure 3.85: Radial profile of CO mass fraction at axial location $x = 1.312$ m for all cases. ....	115
Figure 3.86: Gas temperature along centreline of the chamber for different cases with different percentages of CH <sub>4</sub> (volume basis). ....	116
Figure 3.87: CH <sub>4</sub> mass fraction along the centreline of the chamber for different cases with different percentages of CH <sub>4</sub> (volume basis). ....	116
Figure 3.88: O <sub>2</sub> mass fraction along the centreline of the chamber for different cases with different percentages of CH <sub>4</sub> (volume basis). ....	117
Figure 3.89: CO <sub>2</sub> mass fraction along the centreline of the chamber for different cases with different percentages of CH <sub>4</sub> (volume basis). ....	117
Figure 3.90: CO mass fraction along the centreline of the chamber for different cases with different percentages of CH <sub>4</sub> (volume basis). ....	118
Figure 4.1: The interaction between gas phase and particulate phase [158]. ....	124
Figure 4.2: Coupling regions for particle-fluid turbulence interaction [198]. ....	124
Figure 4.3: Trajectories of particles for a single cell [202]. ....	130
Figure 4.4: Geometry of the axisymmetric combustor. ....	132
Figure 4.5: The grid of the computational domain. ....	140
Figure 4.6: The variation of temperature predicted along the centreline of the reactor with different grids (coal 1). ....	141
Figure 4.7: The variation of temperature predicted along the line ( $y = 70$ cm) of the reactor with different grids (coal 1). ....	141
Figure 4.8: Fuel-NO pathways: (a), (b) [227], (c) and (d) [218]. ....	147
Figure 4.9: Mass fraction of O <sub>2</sub> for coal 1 along the axial distance of the reactor. ....	152
Figure 4.10: Mole fraction of CO <sub>2</sub> for coal 1 along the axial distance of the reactor. ....	152
Figure 4.11: Mass fraction of O <sub>2</sub> for coal 2 along the axial distance of the reactor. ....	153
Figure 4.12: Mole fraction of CO <sub>2</sub> for coal 2 along the axial distance of the reactor. ....	153
Figure 4.13: Comparison between the experimental and simulated data of O <sub>2</sub> mass fraction for coal 1. Ideal results lie on the line indicated by $y = z$ . ....	154
Figure 4.14: Comparison between the experimental and simulated data of CO <sub>2</sub> mole fraction for coal 1. Ideal results lie on the line indicated by $y = z$ . ....	155

Figure 4.15: The variation of volatile mass fraction for coal 1 in the axial direction of the reactor. ....	155
Figure 4.16: Volatile mass fraction distribution for coal 1: (a) case 1, (b) case 2 and (c) case 3. ....	156
Figure 4.17: Gas temperature variation for coal 1 along the axial distance of the reactor. ....	157
Figure 4.18: Predicted temperature distribution for coal 1: (a) Case 1, (b) Case 2 and (c) Case 3. ....	158
Figure 4.19: Particles burnout for coal 1. ....	158
Figure 4.20: Mass fraction of O <sub>2</sub> distribution for coal 1: (a) case 1, (b) case 2 and (c) case 3. ....	160
Figure 4.21: The distribution of CO <sub>2</sub> mass fraction for coal 1: (a) case 1, (b) case 2 and (c) case 3. ....	160
Figure 4.22: H <sub>2</sub> O mass fraction distribution for coal 1: (a) case 1, (b) case 2 and (c) case 3. ....	161
Figure 4.23: The distribution of N <sub>2</sub> mass fraction for coal 1: (a) case 1, (b) case 2 and (c) case 3. ....	161
Figure 4.24: The distribution of CO mass fraction for coal 1 (case 3). ....	162
Figure 4.25: The distribution of H <sub>2</sub> mass fraction for coal 1 (case 3). ....	162
Figure 4.26: Mass fraction of CO and H <sub>2</sub> for coal 1 along the axial distance of the reactor. ....	162
Figure 4.27: Mass depletion of particles with different sizes for case 3. ....	163
Figure 4.28: Burnout of particles with different sizes for Case 3. ....	164
Figure 4.29: NO weight fraction for various runs along the axial distance of the reactor. ....	165
Figure 4.30: The variation of gas temperature along the centreline for various wall temperatures. ....	165
Figure 4.31: The variation of volatile concentration along the centreline for various wall temperatures. ....	166
Figure 4.32: The variation of O <sub>2</sub> concentration along the centreline for various wall temperatures. ....	167
Figure 4.33: The variation of CO <sub>2</sub> mass fraction along the centreline for various wall temperatures. ....	168
Figure 4.34: The variation of H <sub>2</sub> O mass fraction along the centreline for various wall temperatures. ....	168

---

Figure 4.35: The variation of CO mass fraction along the centreline for various wall temperatures. ....	169
Figure 4.36: The variation of H <sub>2</sub> mass fraction along the centreline for various wall temperatures. ....	169
Figure 4.37: Variation of species mass fraction at the exit of the reactor for various wall temperatures. ....	170
Figure 4.38: NO weight fraction along the axial distance of the reactor for various wall temperatures. ....	170
Figure 4.39: The variation of gas temperature along the centreline at different secondary air inlet velocities. ....	171
Figure 4.40: The variation of volatile concentration along the centreline at different secondary air inlet velocities. ....	172
Figure 4.41: The variation of O <sub>2</sub> concentration along the centreline at different secondary air inlet velocities. ....	173
Figure 4.42: Stream lines: (a) 11.5 m/s, (b) 13.5 m/s, (c) 15.5 m/s and (d) 17.5 m/s. .	173
Figure 4.43: The variation of CO <sub>2</sub> mass fraction along the centreline at different secondary air inlet velocities. ....	174
Figure 4.44: The variation of H <sub>2</sub> O mass fraction along the centreline at different secondary air inlet velocities. ....	175
Figure 4.45: The variation of CO mass fraction along the centreline at different secondary air inlet velocities. ....	176
Figure 4.46: The variation of H <sub>2</sub> mass fraction along the centreline at different secondary air inlet velocities. ....	176
Figure 4.47: Mass depletion of particles: (a) 16 μm, (b) 84 μm, (c) 154 μm, (d) 222 μm, (e) 291 μm and (f) 360 μm at two secondary air inlet velocities. ....	178
Figure 4.48: NO weight fraction along the centreline at different secondary air inlet velocities.....	179
Figure 4.49: The variation of gas temperature along the centreline of the reactor. ....	182
Figure 4.50: Gas temperature distribution of (a) case I and (b) case II.....	183
Figure 4.51: Radial temperature profiles at different axial locations.....	184
Figure 4.52: The variation of volatiles mass fraction along the centreline of the furnace. ....	185
Figure 4.53: Volatiles mass fraction distribution: (a) case I and (b) case II. ....	185
Figure 4.54: The variation of species mass fraction along the centreline of the reactor. ....	186

---

---

Figure 4.55: Mass depletion of particles with different sizes for case I.....	186
Figure 4.56: Burnout of straw particles with different sizes. ....	187
Figure 4.57: Nitrogen concentration in char versus pyrolysis temperature for selected fuels and various experimental methods [217]. ....	188
Figure 4.58: The variation of NO concentration of straw along the centreline of the furnace.....	188
Figure 4.59: The radial profiles of NO mass fraction at various axial locations. ....	189
Figure 4.60: The variation of gas temperature along the centreline of the furnace for different co-firing cases.....	190
Figure 4.61: Distribution of gas temperature: 10% straw (a), 20% straw (b), 30% straw (c) and 40% straw.....	191
Figure 4.62: Mass weighted-average mass fraction of CO <sub>2</sub> at the exit of the furnace.	192
Figure 4.63: Particles burnout at the exit of the reactor. ....	192
Figure 5.1: (a) Combustion chamber (Model 1) with holder frame, (b) computational domain and (c) grid of the domain. ....	202
Figure 5.2: Maximum temperature inside the chamber for the particle size of 1 mm diameter for base case. ....	204
Figure 5.3: The variation of volume fraction of the solid phase at the middle plane for the base case (particle diameter of 1 mm) at different simulation times (s): (a) 0, (b) 0.05, (c) 0.1, (d) 0.15, (e) 0.2, (f) 0.25, (g) 0.30, (h) 0.35, (i) 0.40, (j) 0.45, (k) 0.50, (l) 0.55 and (m) 0.6. ....	205
Figure 5.4: The variation of temperature at the middle plane for the base case (1 mm particle diameter) showing at time (s): (a) 0.05, (b) 0.1, (c) 0.15, (d) 0.2, (e) 0.25, (f) 0.3, (g) 0.35, (h) 0.4, (i) 0.45, (j) 0.5, (k) 0.55 and (l) 0.6.....	207
Figure 5.5: Temperature contours at different horizontal locations in y direction and at different times (s) for the base case (1 mm particle size).....	208
Figure 5.6: The mass fraction of CO <sub>2</sub> at the middle plane at different time (s) for the base case (particle diameter of 1 mm): (a) 0.05, (b) 0.1, (c) 0.15, (d) 0.2, (e) 0.25, (f) 0.3, (g) 0.35, (h) 0.4, (i) 0.45, (j) 0.5 and (k) 0.55.....	209
Figure 5.7: Iso-surfaces at time 0.65 s for the base case for different particle sizes: (a) 1220 K, (b) 1250 K, (c) 1280 K, (d) 1400 K and (e) 1550 K. ....	210
Figure 5.8: The peak temperature variation with time (s) for different particle sizes for the base case. ....	212
Figure 5.9: The variation of volume fraction of the solid phase at the middle plane showing at different times (s) for the doubled-height case (particle diameter of 1 mm):	

(a) 0, (b) 0.05, (c) 0.1, (d) 0.15, (e) 0.2, (f) 0.25, (g) 0.30, (h) 0.35, (i) 0.40, (j) 0.45, (k) 0.50, (l) 0.55, (m) 0.6 and (n) 0.65. ....214

Figure 5.10: The distribution of temperature for the doubled-height case (1 mm particle diameter) showing at different times (s): (a) 0.05, (b) 0.1, (c) 0.15, (d) 0.2, (e) 0.25, (f) 0.3, (g) 0.35, (h) 0.4, (i) 0.45, (j) 0.5, (k) 0.55, (l) 0.6 and (m) 0.65. ....216

Figure 5.11: Temperature contours at different locations in y direction and different times (s) for the doubled-height case (particle diameter of 1 mm). ....218

Figure 5.12: The mass fraction of CO<sub>2</sub> at different time (s) for the doubled-height case (particle diameter of 1 mm): (a) 0.05, (b) 0.1, (c) 0.15, (d) 0.2, (e) 0.25, (f) 0.3, (g) 0.35, (h) 0.4, (i) 0.45, (j) 0.5, (k) 0.55 and (l) 0.6. ....219

Figure 5.13: The peak temperature variation with time for different particle sizes for the doubled-height case. ....220

Figure 5.14: Iso-surfaces at time 0.65 s for different doubled-height cases with different particle diameters: (a) 1220 K, (b) 1250 K, (c) 1280 K and (d) 1310 K. ....221

Figure 5.15: The peak temperature variation with time inside the chamber for both the base and doubled-height cases for different particle sizes: a) 0.5 mm, b) 1 mm, c) 1.5 mm, d) 2 mm and e) 2.5 mm. ....223

# List of tables

Table 2.1: Fuel properties for increasing coalification degree (wt. - %) [30].	15
Table 2.2: Coal properties for increasing rank (on % DAF basis) [31].	15
Table 2.3: Classification of anthracite and bituminous coals by rank (ASTM D 388-05) [34].	16
Table 2.4: Classification of bituminous, sub-bituminous and lignite coals by rank (ASTM D 388-05) [34].	17
Table 2.5: Analysis of various coals [37].	18
Table 2.6: Sources of biomass [16].	19
Table 2.7: Proximate analysis for several coal and biomass samples [39].	20
Table 2.8: Average of elemental analysis for many thousands of coal and biomass samples [46].	20
Table 3.1: Source terms.	56
Table 3.2: Reaction kinetics.	61
Table 3.3: Material properties.	65
Table 3.4: Number of mesh cells.	66
Table 3.5: Mesh independence temperature and flow rates at furnace outlet.	70
Table 3.6: Optimized values of activation energy for reaction (r-2).	98
Table 4.1: Operating conditions of pulverized coal combustion.	132
Table 4.2: Coal analysis data.	133
Table 4.3: Devolatilization and char oxidation models used in the simulation cases.	136
Table 4.4: Kinetic constants of reactions.	138
Table 4.5: Rate constants for thermal NO chemical reactions, $k = AT^{\beta} \exp - (E/R_u T)$ .	144
Table 4.6: Reaction kinetics.	148
Table 4.7: Oxygen reaction order.	149
Table 4.9: The chemical composition of straw.	180
Table 4.10: Constants of single rate devolatilization model.	180
Table 4.11: operating conditions of pulverized biomass combustion.	181
Table 5.1: Solver parameters.	201

# List of symbols

## Roman symbols

$A$	Pre-exponential factor [units vary]
$A_p$	Surface area of the particle [ $\text{m}^2$ ]
$A_g$	Specific internal surface area of char particle [ $\text{m}^2$ ]
$a$	Absorbing coefficient [ $\text{m}^{-1}$ ]
$a$	Oxygen reaction order
$a'_{im}$	Reaction order with respect to species $i$
$a_1, a_2, a_3$	Constants
$Bi$	Biot number
$C_1$	Diffusion rate coefficient [ $\text{m}^3/\text{K}^{0.75}\text{s}$ ]
$c_p$	Specific heat [ $\text{J}/\text{kg K}$ ]
$C_{1\epsilon}, C_{2\epsilon}, C_{3\epsilon}, C_\mu$	Model constants
$C_1, C_2$	Constants
$C_D$	Drag coefficient [ $\text{kg}/\text{m}^3\text{s}$ ]
$C_i$	Species concentration [ $\text{kmol}/\text{m}^3$ ]
$C_R$	Reactant concentration [ $\text{kmol}/\text{m}^3$ ]
$C_{ox}$	Oxidant concentration [ $\text{kmol}/\text{m}^3$ ]
$D_{i,m}$	Diffusion coefficient for oxidant [ $\text{m}^2/\text{s}$ ]
$D_o$	Diffusion rate [ $\text{m}^2/\text{s}$ ]
$D_e$	Effective diffusion coefficient [ $\text{m}^2/\text{s}$ ]
$D_i$	Diffusion coefficient of species $i$ [ $\text{m}^2/\text{s}$ ]
$Da$	Damköhler number
$d_p$	Particle diameter [ $\text{m}$ ]
$\bar{d}$	Mean diameter of the particles [ $\text{m}$ ]
$E$	Activation energy [ $\text{J}/\text{kmol}$ ]
$e$	Specific total energy [ $\text{J}/\text{kg}$ ]
$f_{v,o}$	Volatile fraction
$f_{comb}$	Combustible fraction
$f_h$	Fraction of heat absorbed by the particle
$F_d$	Drag force [ $\text{N}$ ]

---

$F_{vol}$	Mass fraction of volatiles in DAF coal
$F_{char}$	Mass fraction of char in DAF coal
$g$	Gravitational acceleration [ $m/s^2$ ]
$G_b$	Generation of turbulence kinetic energy due to buoyancy
$G_k$	Generation of turbulence kinetic energy due to mean velocity gradients
$G$	Incident radiation [ $W/m^2$ ]
$H$	Enthalpy [ $J/kg$ ]
$h_i^\circ$	Heat of formation of species $i$ [ $J/kmol$ ]
$h_{fg}$	Latent heat of devolatilization [ $J/kg$ ]
$\hat{h}$	Convective heat transfer coefficient [ $W/m^2 K$ ]
$h_{pf}^\circ$	Enthalpy of formation of particle [ $J/kmol$ ]
$h_{f,products}^\circ$	Enthalpy of formation of products [ $J/kmol$ ]
$h_{f,reactants}^\circ$	Enthalpy of formation of reactants [ $J/kmol$ ]
$H_{reac}$	Enthalpy of reaction [ $J/kg$ ]
$hv_{vol}$	Volatile matter
$h_{gs}$	Heat transfer coefficient [ $W/m^2 K$ ]
$\Delta h_{f,i}$	Heat of formation [ $J/Kmol$ ]
$H_s$	Source term
$I$	Radiative intensity [ $W/m^2 sr$ ]
$J_{i,j}$	Diffusion flux [ $kg/m^2 s$ ]
$k$	Turbulence kinetic energy [ $m^2/s^2$ ]
$k$	Chemical reaction rate
$Le$	Lewis number
$L_c$	Ratio of particle volume to particle surface area [ $m$ ]
$l_e$	Eddy length scale [ $m$ ]
$m_p$	Mass [ $kg$ ]
$m_{p.o}$	Initial particle mass [ $kg$ ]
$M_w$	Molecular weight [ $kg/kmol$ ]
$m_{vol}^N$	Mass fraction of nitrogen in volatiles
$m_{char}^N$	Mass fraction of nitrogen in char
$m_{tot}^N$	Total mass fraction of nitrogen in DAF coal
$N_g$	Number of species in gas phase
$n$	Refractive index
$n$	Spread parameter

---



---

$N$	Apparent order of reaction
$P$	Pressure [pa]
$P_n$	Bulk partial pressure [pa]
$Q_r$	Internal production rate of thermal energy [W]
$q_j$	Energy flux [ $\text{W}/\text{m}^2$ ]
$q_j^c$	Energy flux due to conduction [ $\text{W}/\text{m}^2$ ]
$q_j^d$	Energy flux due to species diffusion [ $\text{W}/\text{m}^2$ ]
$q_j^D$	Energy flux caused by concentration gradients [ $\text{W}/\text{m}^2$ ]
$Q_{gs}$	Heat exchange between gas phase and solid phase [W]
$R_{i,m}$	Chemical production rate for species $i$ [ $\text{kmol}/\text{m}^3 \cdot \text{s}$ ]
$R_u$	Universal gas constant [J/ kmol K]
$Re$	Reynolds number
$\mathcal{R}$	Reaction kinetic rate [units vary]
$R_{i,r}$	Rate of particle species depletion [ $\text{kg}/\text{m}^2 \cdot \text{s}$ ]
$R_i$	Total rate of production of a certain species $i$ [ $\text{kmol}/\text{m}^3 \cdot \text{s}$ ]
$R_i^{hom}$	Net rate of production of species $i$ due to homogeneous chemical reactions [ $\text{kg}/\text{m}^3 \cdot \text{s}$ ]
$\bar{r}_{het}$	Rate of particle surface species depletion (char combustion rate) [ $\text{kg}/\text{s}$ ]
$\vec{r}$	Position vector
$S_b$	Stoichiometry
$Sc$	Schmidt number
$s_b$	Stefan-Boltzmann constant [ $5.67 \times 10^{-8} \text{ W}/\text{m}^2 \text{ K}^4$ ]
$S_k, S_\epsilon, S_\phi, S_{gs}, S_{sg}$	Source terms
$S_i$	Source term of production and reduction of NO
$\vec{s}, \vec{s}'$	Incoming and outgoing radiation direction vectors
$T$	Temperature [K]
$T^\circ$	Reference temperature (298.15 K)
$T_L$	Fluid Lagrangian integral time [s]
$u$	Velocity [m/s]
$\vec{U}$	Phase-weighted velocity [m/s]
$v'_{im}, v''_{im}$	Stoichiometric coefficients of the reactants or products of species $i$ in reaction $m$
$V_p$	Volume of particle or volume of dispersed phase [ $\text{m}^3$ ]
$V$	Specific volume [ $\text{m}^3$ ]
$\vec{v}$	Phase velocity [m/s]

---

$v_{r,s}$	Terminal velocity correlation for the solid phase
$X$	Mole fraction
$Y$	Mass fraction
$Y_d$	Mass fraction of particles
$x_j, x, y, z$	Cartesian coordinate

**Greek symbols**

$\alpha_p$	Particle volume fraction
$\rho$	Density [kg/m <sup>3</sup> ]
$\eta$	Effectiveness factor
$\varphi$	Thiele modulus
$\tau_t$	Turbulent time scale [s]
$\tau_c$	Chemical time scale [s]
$\tau_{ij}$	Viscous stress tensor [N/m <sup>2</sup> ]
$\mu$	Dynamic viscosity [kg/m s]
$\alpha$	Distribution coefficient
$\delta_{i,j}$	Kronecker delta
$\lambda$	Thermal conductivity [W/m K]
$\lambda_s$	Thermal conductivity of the particle [W/m K]
$\emptyset$	Flow variable [variable units]
$\mu_t$	Turbulent viscosity [kg/m s]
$\mu_B$	Bulk viscosity [kg/m s]
$\epsilon$	Turbulence dissipation rate [m <sup>2</sup> /s <sup>3</sup> ]
$\sigma_k$	Turbulent Prandtl number for $k$
$\sigma_\epsilon$	Turbulent Prandtl number for $\epsilon$
$\Gamma_\emptyset$	diffusion coefficient of the flow property [variable units]
$\mu_e$	Effective viscosity [kg/m s]
$\sigma_s$	Scattering coefficient [m <sup>-1</sup> ]
$\Omega$	Solid angle [Sr]
$\Phi$	Scattering phase function
$\phi$	Equivalence ratio
$\beta$	Temperature exponent
$\gamma$	Distribution Parameter of nitrogen between volatiles and char
$\epsilon_p$	Particle emissivity
$\theta_R$	Radiation temperature [K]

$\tau_e$	Eddy lifetime [s]
$\tau_{cross}$	Time for particle to cross an eddy [s]
$\tau_p$	Particle relaxation time [s]
$\alpha_i$	Volume fraction of phase $i$
$\hat{\rho}_i$	Effective density of phase $i$ [kg/m <sup>3</sup> ]
$\xi_s$	Bulk viscosity of solid phase [kg/m s]
$\bar{\tau}$	Stress-strain tensor [N/m <sup>2</sup> ]
$\tau_{t,g}$	Characteristic time of the energetic turbulent eddies [s]
$\xi$	Normally distributed random number

**Subscripts**

$i$	Species or phase
$p$	Particle
$g$	Gas
$s$	Solid
$c$	Char
$r$	Reaction
$m$	Reaction
$cr$	Chemical reaction
$ox$	Oxidant
$vap$	Vaporization
$vol$	Volatiles
$surr$	Surroundings

# List of abbreviations

<i>BP</i>	British petroleum
<i>EREC</i>	European Renewable Energy Council
<i>IEA</i>	International Energy Agency
<i>Mtoe</i>	Million ton oil equivalent
<i>EU</i>	European Union
<i>OECD</i>	Organization for Economic Co-operation and Development
<i>CFD</i>	Computational Fluid Dynamics
<i>RANS</i>	Rynolds-Averaged Navier Stokes
<i>DNS</i>	Direct Numerical Simulation
<i>RNG</i>	Renormalization-group
<i>LES</i>	Large-eddy simulations
<i>ASTM</i>	American Society for Testing and Material
<i>BFB</i>	Bubbling Fluidized Bed
<i>CFB</i>	Circulating Fluidized Bed
<i>PF</i>	Pulverized Fuel
<i>EDM</i>	Eddy-Dissipation Model
<i>FR/ED</i>	Finite Rate/Eddy-Dissipation model
<i>EDC</i>	Eddy-Dissipation concept
<i>FLM</i>	Flamelet model
<i>FG-DVC</i>	Functional Group-Devolatilization Vaporization Cross-linking
<i>CPD</i>	Chemical Percolation Devolatilization
<i>M-I</i>	Mechanism one
<i>M-II</i>	Mechanism two
<i>M-III</i>	Mechanism three
<i>M-IV</i>	Mechanism four
<i>DAF</i>	Dry-Ash-Free
<i>DPM</i>	Discrete Phase Model
<i>DRW</i>	Discrete Random Walk
<i>WSGGM</i>	Weighted-Sum-of Gray-Gases Model
<i>SIMPLE</i>	Semi-Implicit Method for Pressure Linked Equations
<i>HHV</i>	High Heating Value
<i>LHV</i>	Low Heating Value
<i>BET</i>	Brunauer, Emmett and Teller
<i>UDF</i>	User-Defined Function

# 1 Introduction

There is a gradual transition globally to carbon-neutral fuels to potentially reduce global warming and at the same time, dependency on traditional carbon-based fuels such as coal, oil and natural gases which are facing the risk of depletion. The supply of energy has been dominated by fossil fuels for decades and this dominance will continue in the near future. Currently, almost 80% of the world's energy is produced from fossil based fuels [1, 2]. But there is a general agreement that oil and natural gas are expected to be depleted within this century. In the British Petroleum (BP) reports, it was estimated that the world has approximately 50 years' reserves of oil and 60 years of natural gas remaining at that consumption rates of the year 2009 [3]. However, these predictions could vary as there is still the possibility to discover new reserves over the next few decades. Coal is still important in power generation because of its low cost and, based on major deposits existing on every continent, is expected to last for around 115 years which is significantly longer than the conventional oil and gas reserves [4].

Unfortunately, the dependency of global population on the production of energy through the burning of these fossil fuels has become high and this leads to the global consumption rising rapidly than the production. Moreover, the growth of carbon dioxide emissions has also been accelerated [3]. Indeed, because of the rise of the world's population the demand for energy has increased and become more abrupt in the coming years. Covering this increasing demand of energy in accordance with adherence to current emissions' limits is crucial and needs from us to look for other alternatives to produce energy.

Since the fossil fuel sources are limited and its burning causes many environmental problems, the renewable fraction has been increasing in the last decades. The major pollutants from combustion are soot, sulphur oxides ( $\text{SO}_x$ ), nitrogen oxides ( $\text{NO}_x$ ), unburned hydrocarbons (UHC), carbon dioxide ( $\text{CO}_2$ ) and carbon monoxide (CO).

Combustion of fossil fuels influences the environment mainly through emissions of nitrogen oxides ( $\text{NO}_x$ ) to atmosphere. These emissions comprise various nitrogen compounds such as nitrogen dioxide ( $\text{NO}_2$ ) and nitric oxide (NO) which are associated with a variety of environmental concerns such as the formation of acid rain and photochemical smog in urban air [5]. In addition, they participate in a chain reaction which can result in the depletion of ozone [6].

Burning coal is the main source of  $\text{SO}_x$ . When combined with water in the atmosphere, the emitted  $\text{SO}_x$  lead to form sulphuric acid and precipitates as acid rain, with devastating effects on aquatic life and soil erosion. Another serious, and potentially catastrophic, environmental problem is the global warming caused by the increased amount of anthropogenic  $\text{CO}_2$  in the atmosphere. Therefore, looking for ways for removing  $\text{CO}_2$  from the atmosphere is of increasing interest [7].

In the coming decades, supplying a sustainable energy is one of the greatest challenges that mankind will face, particularly because of the need to address climate change by energy producers. Moreover, the energy consumers want this energy to be secure and affordable. Nowadays, decisions regarding power generations are not only about technology and finances, but also taking into consideration the above mentioned factors. Depleting supplies of fossil fuels and the environmental issues caused by the burning of these fuels (growing greenhouse gas emissions) are the driving forces behind the global interest in sustainable, environmentally friendly and clean energy systems.

Indeed, renewable alternatives of energy have been a solution as well as sustainable development concerns have become a common sense worldwide. Basically, renewable energy is a type of energy produced from sources other than fossil fuels. These sources come in many forms such as wind, solar, hydro, geothermal energy and biomass or bioenergy. However, these resources cannot completely replace fossil fuels in the near future, but they can make a substantial contribution to supplying future energy demand if carefully managed. Furthermore, implementing renewable energy systems is dependent on aspects such as the availability of fossil fuels and renewable energy carriers and the economic possibilities. Biomass, wind, and geothermal energy are making relatively fast progress and are commercially competitive [8].

A global renewable energy scenario for 2040, by the European Renewable Energy Council (EREC), is shown in Figure 1.1, Figure 1.2 and Figure 1.3. The information has been extracted from [9]. The consumption of energy is in Million ton oil equivalent (Mtoe). It was claimed that by then nearly half of the global energy supplies will be provided by renewable energy sources with the condition that the cumulative growth rates are reached as shown in Figure 1.4.

Referring to the International Energy Agency (IEA) statistics [10], the total world energy primary supply was 13107 Mtoe in 2011. Figure 1.5 shows that only 13% of

worldwide energy consumption is covered by renewable resources with biomass takes the share of 9.7% followed by 2.3% which is provided by hydro power and the rest comes from the other renewables such as wind, solar, geothermal and tide.

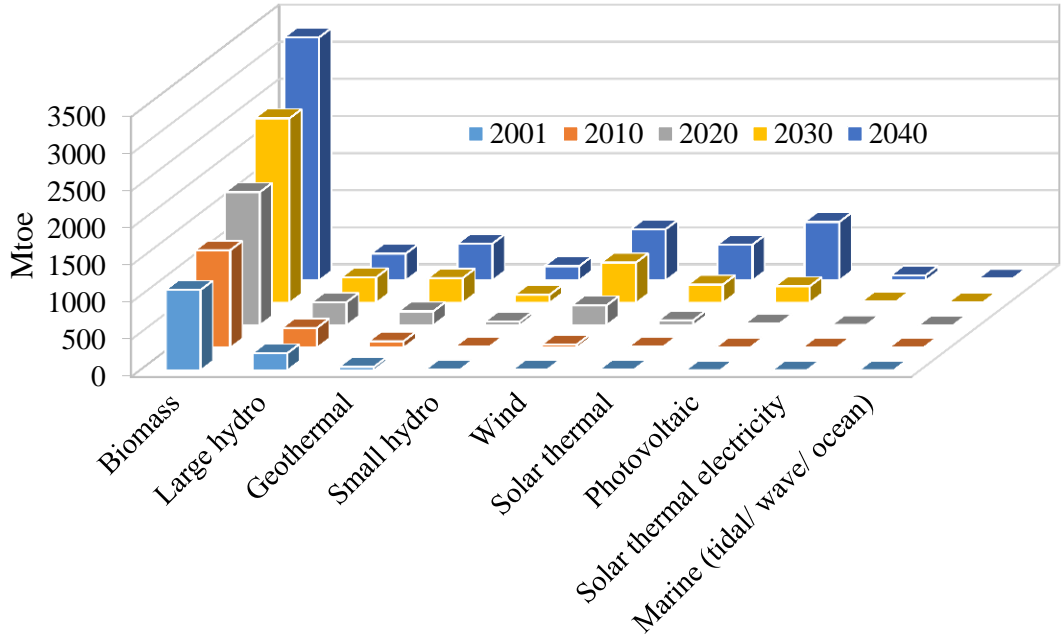


Figure 1.1: Renewable energy sources till 2040.

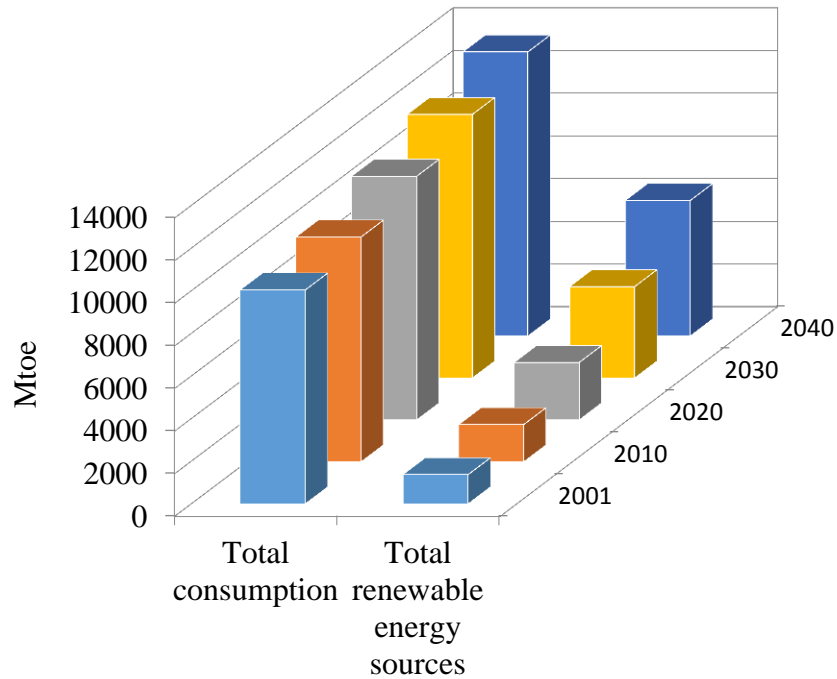


Figure 1.2: The total global consumption of energy and the total renewable energy sources till 2040.

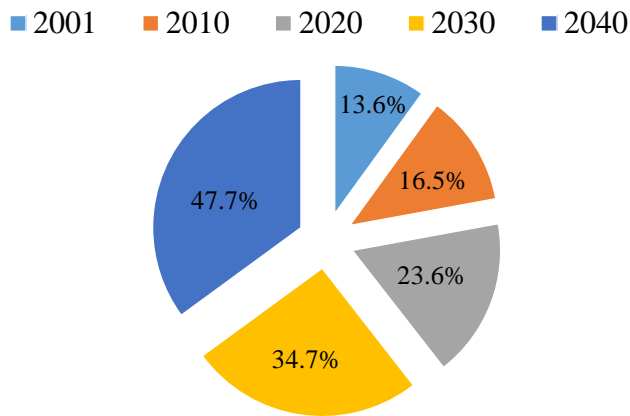


Figure 1.3: Renewable energy contribution (%) till 2040.

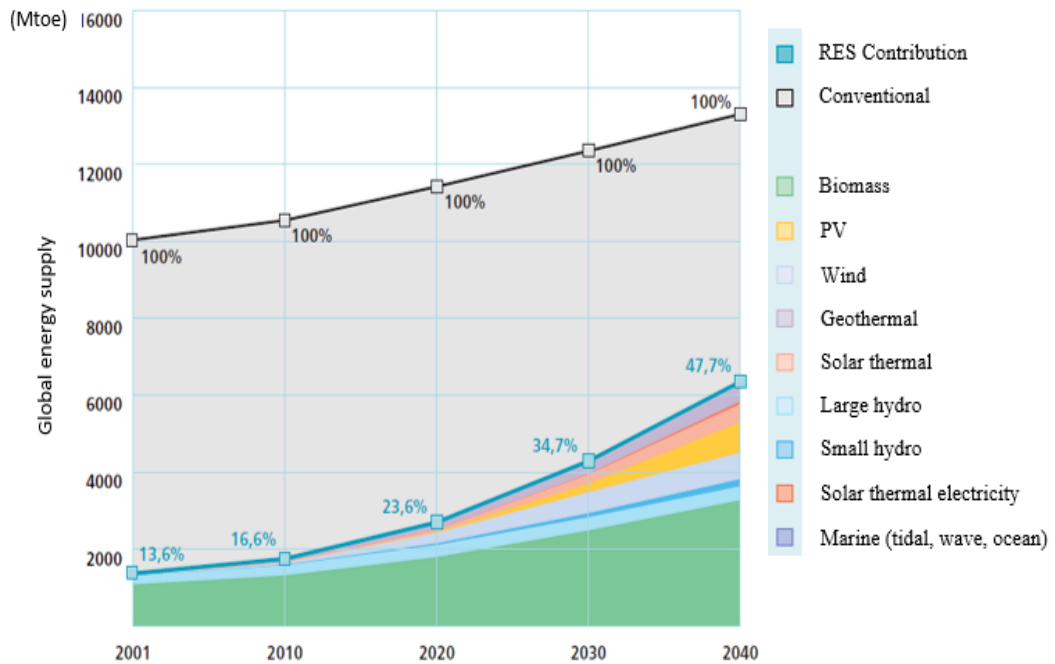


Figure 1.4: The contribution of renewable energy sources to the world total primary energy consumption [9].

Figure 1.6 also shows the global renewable energy supplies with biomass representing 74.9%, which is by far the largest source of renewable energy and this is because of its non-commercial use in developing countries.

With regards to BP energy outlook 2035 [3], renewable energy deployment for power has been led by Europe. The share of renewable sources in power generation in the European Union (EU) increases from 13% in 2012 to 32% in 2035 as shown in Figure 1.7. The increase of the renewable share in Europe is attributed to the implementation



of strong policies supporting renewable energy in the late 1990s and early 2000s. More recently, in 2007, the EU proposed a new renewable energy target by increasing the share of renewable energy to 20% by 2020 [10] and 45% by 2030 [11].

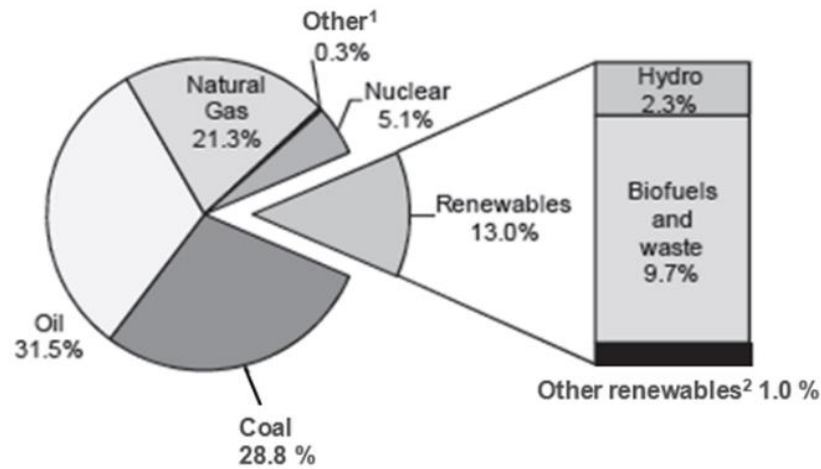


Figure 1.5: Fuel shares in the world total primary energy supply 2011 [10].

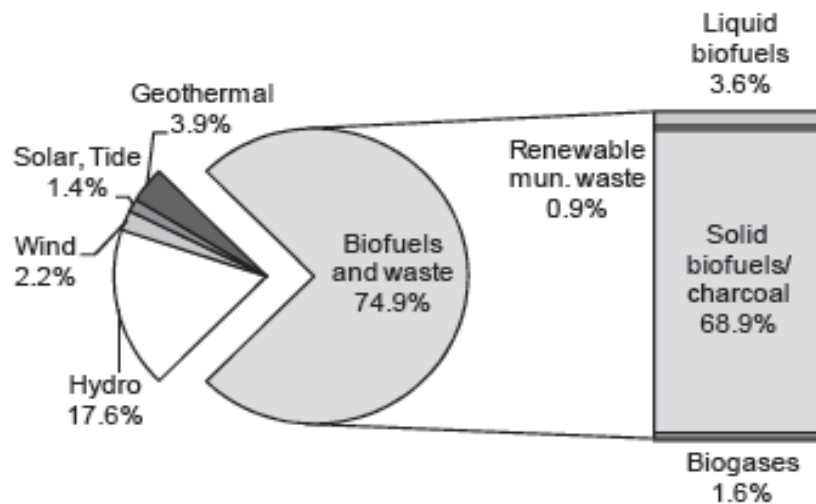


Figure 1.6: Product shares in the world renewable energy supply [10].

In spite of their environmental effects, coal and natural gas are still playing a paramount role in power sector as they accounts for 41.3% and 21.9 %, respectively, of the world total electricity production in 2011. Whereas, the contribution of renewables was 20% [10]. The coal share will decline to 37% by 2035 due to the increase of renewables share [3].

Among the renewable energy sources, biomass can be seen as a promising resource to producing energy and it is expected to have a strong growth within sectors such as heat and power generations and transportation biofuels in the coming decades. It is a worthwhile alternative, when compared with unpredictable wind energy and high cost

photovoltaic energy. Combustion of biomass was the oldest. It is the first on-demand source of energy that humans exploited and by which they started to make fire, cook and produce heat. It is still today the worldwide most spread out energy source used in a variety of applications for the production of heat and power. It can be said that the history of combustion is related to the availability and utilization of fuel. Furthermore, factors such as security supply, demand pressure, environmental concerns and political issues are the driving forces of energy production. In the mid-1800s, most of the world's energy needs had been supplied by biomass before the era of fossil fuel began when it started to be phased out in the industrialized countries. There was a transition towards energy production based on coal, then on oil and natural gas. But the first oil crisis in 1970s made biomass again to be a viable energy resource to potentially reduce oil consumption [12].

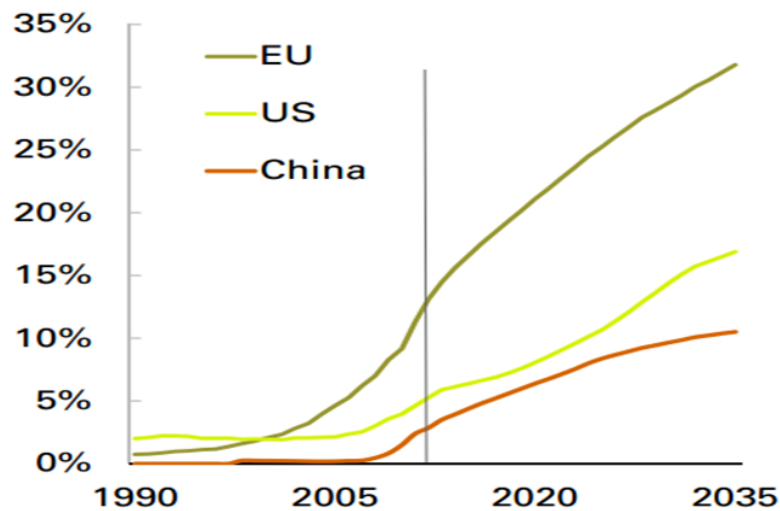


Figure 1.7: Renewable share of power generation [3].

In the developing part of the world, the use of biomass is mostly for domestic heating and cooking. On the other hand, because of its carbon-neutral its use for energy production is presently on the rise in the developed countries. In the Organisation for Economic Co-operation and Development (OECD) countries, the largest proportion of renewable energy was supplied by biofuels and waste in 2012 [10]. Recently, about 10% of the world's current energy consumption is met by biomass and over the last decades there has been a gradual increase of using biomass in energy systems [1]. The interest in using of biomass fuels for energy production purposes across the world has also been growing and most of energy scenarios indicate that they will be increasingly used worldwide. Biomass is considered to be one of the options to replace fossil fuels and its result will lead to decrease the emissions of greenhouse gases [13, 14].

Nussbaumer [15] gave an overview of the combustion technologies available in Europe with regulations on emissions and fundamentals of combustion of woody biomass. Possible direct combustion as well as an option of co-firing and gasification of biomass makes it a more attractive source of fuel for power production. However, a detailed study of complex and complicated combustion reactions of biomass requires a highly scientific focus, since the biomass, in general terms; include all materials derived from photosynthetic plants to animal wastes. The sources also include naturally grown forests, energy plantations, herbaceous plants or grasses, by-products from different industries such as agricultural, food, wood processing, manures, and paper industries or municipal solid waste [16].

The compositions and molecular structures found in any carbonaceous fuel, such as coal and biomass, are very complex. The main elements present in coal and biomass, determined by ultimate analyses, are usually carbon (C), hydrogen (H), oxygen (O) and nitrogen (N). Other elements found in nitrogen, sulphur, chloride and other impurities. The proximate analysis determines the percentages contents of moisture, volatiles, fixed carbon and ash.

Both, the volatiles which are released as a gas by heating and the content of fixed carbon provide a measure of the ease with which biomass can be ignited. Biomass is usually combustible because it has a high level of volatiles and therefore, forms a potential source of energy. However, it has lower energy content due to the higher O/C and H/C atomic ratios when compared to coal. In reality, biomass is regarded by many as CO<sub>2</sub>-neutral fuel as it does not contribute to any increase of CO<sub>2</sub> in atmosphere [17]. This means that the carbon dioxide generated from biomass combustion constitutes one of the elements of the carbon cycle between the atmosphere and the plant kingdom and, therefore, it does not affect the atmospheric carbon dioxide concentration. The renewability here comes from that the amount of biomass grown per unit time equals the amount of biomass used for producing energy in that unit and as a result it does not enhance the greenhouse effect. This leads to avoid the carbon dioxide emission and other pollutants associated with the combustion of coal and other fossil fuels when the energy produced from burning biomass substitutes the one that would otherwise be obtained by burning fossil fuels. Biomass is also characterized by less sulphur and nitrogen compared to coal.

Reaction methods of solid fuel combustion or gasification include fixed bed, fluidized bed and pulverized methods. The latter one is commonly used for power generation. The development in these technologies is required and due to the need to reduce the cost and time, numerical simulations emerges as powerful research tool that not only complement the experimental investigation but also due its ability to simulate more complex cases. In this thesis, FLUENT commercial code is used to simulate different combustion cases including the combustion of methane, coal and biomass.

## **1.1 Computational Fluid Dynamics (CFD)**

There are basically three approaches by which a problem in fluid mechanics and heat transfer can be solved. These approaches are experimental, theoretical and computational. The experimental approach is capable of being more realistic and the theoretical uses general information which is usually in a formula form and is usually restricted to simple geometries and linear problems. Computational fluid dynamics (CFD) is a methodology for solving complex problems in fluid dynamics and heat transfer. It is used to predict fluid flow by finding the numerical solution to a set of partial differential equations governing the continuity of mass, momentum and energy in the flow field. Problems with highly non-linear flows can be solved using CFD. In combustion, reactive flow processes are often characterized by a complex interaction of transport and chemical kinetics. Moreover, the chemistry may include either only gas phase or both gas and solid phases. In the latter case (combustion of solid fuels), multiple phases are present and the solid particles have a range of sizes and shapes. Chemical reactions are affected by adding sink or source terms in the equations for reactants and products as well as appropriate sources in the energy equation to account for exothermic and endothermic reactions. In terms of chemical kinetics, it is needed for prescribing the paths and rates through which chemical reactions take place because all combustion processes have some finite characteristic times defining the relevant phenomena. This set of equations is highly coupled and non-linear and as a result the problem domain must be discretized. In the discretization process, the governing equations are converted to a simple algebraic form that can be solved numerically. For discretization of these equations the finite volume method is used and a solution found through numerical methods. The ability of this method to cope with unstructured meshes allows the complicated geometries to be modelled. There are various methods for discretizing the equations such as first-order and second-order methods.

Turbulence is a significant complication to the problem of modelling of engineering flows and there are different techniques with different approaches have been developed to account for it that exist in literature. These approaches include direct numerical simulation (DNS), Reynolds Averaged (time-averaged) Navier-Stokes (RANS) and large-eddy simulation (LES). In DNS model, the governing equations are discretised and solved numerically and the attempt is even to resolve the smallest of structures, which requires fine meshes. Such approach removes the need for any turbulence model when using grids and time steps that are small enough to capture the real physics of turbulent flow. Thus, it is extremely computationally very expensive and viable only for turbulent flows in relatively simple geometries and flow cases at low Reynolds number as the number of cells increases with Reynolds number. Therefore, it is applied as a basic tool to fundamental research studies on turbulence. However, in engineering applications, the effects of turbulence can be calculated approximately using the other two approaches.

With regard to RANS approach, the attempt is to model the turbulence by artificially increasing the viscosity of the fluid, thereby increasing the rate of mixing and the resistance to flow and, for practical calculations, most of the industrial scale modelling of turbulent flows is being carried out by applying Reynolds Averaged Navier-Stokes (RANS) equations. This model ignores the turbulent fluctuations and calculates only the turbulent-averaged flow. Since there is no single RANS model can accurately predict all flow regimes, it is considerably cheaper than DNS simulations. Hence, it is a favored approach in engineering applications. However, turbulence models are required to close the stress terms that result from time averaging of Navier-Stokes equations. These terms are called Reynolds stresses. As a result of these extra terms, new unknowns are contributed to the RANS equations to close them and need to be related to the other variables. A wide range of turbulence models are available for this purpose in literature and the  $k-\epsilon$  model has become the most employed model in industrial CFD simulations.

LES is another approach that is considered somewhere between direct solution DNS and RANS approach. With this approach the governing equations are filtered to separate the large scale eddies, which depend on geometrical shape and boundary conditions of the flow field from the small scale ones, which do not depend upon the geometry and have a universal structure. The idea is to resolve only the large eddies, which carry the majority of the energy and dominate the physical behaviour of any

turbulent flow, accurately and to approximate the effects of the small scales. A sub-grid scale model is used to include the effects of the small eddies in the filtered equations. This approach is still costly as it is inherently three-dimensional and unsteady, but it is a feasible option for some real problems.

Generally, gas-solid flow (particle-laden) is the phenomena of the transport of particles, which are distinguishable from the carrier phase and can be dense or dilute. A simple way to differentiate between the dense and dilute particle-laden flows is based on the particle volume fraction  $\alpha_p$ . In industrial processes like fluidized beds, a particulate flow with  $\alpha_p < 0.15$  is considered to be dilute. Modelling of these systems is very complex because the flow field of the continuous phase as well as the motion of the particulate phase, need to be solved. This type of modelling is based on the type of reference frame. There are two basic approaches by which the solid particles are modelled, which are the Eulerian-Eulerian approach and the Eulerian-Lagrangian approach. In both cases the gas phase is treated by using an Eulerian reference frame. With regards to the particulate phase, it is treated as a continuous phase mixed with the fluid phase (these models are also known as continuum models or two-fluid models), whereas the solid particles are treated as discrete objects in the Lagrangian particle dispersion models. As these solid particles pass through the reactor their organic fraction is consumed, and their motion is tracked as they move through the flow field. However, the particles are tracked individually and as a result the computational time may be large. Therefore, it is assumed for this model that the dispersed phase occupies a volume fraction that is usually less than 10-12%. To reduce the computational time, only representative samples of the particles are tracked but the number of calculated trajectories should be sufficient to provide a complete picture of the particle behaviour in the turbulent flow. More details of CFD is given in [18]. In terms of biomass combustion and gasification field, there are significant challenges that one can face when modelling biomass combustion and gasification due to complexity of biomass composition. There are many CFD studies, regarding combustion and gasification of different biomass, but there is still needs to be studied especially the co-firing of biomass and coal, which is still developing. A review [19] that gives a summary of various CFD applications in the field of thermochemical conversion of biomass has been reported in literature.

## 1.2 Purpose of the work

The overall objective of this thesis is to understand what happens to solid fuels such as coal and biomass fuels during the combustion process. Particularly, the aim is to investigate the pulverized combustion of coal and biomass, including the temperature, species,  $\text{NO}_x$  formation and analyse the performance of combustion by applying computational fluid dynamics technique and this includes the followings:

1. Study the parameters that have important effects on the combustion of different types of solid fuel particles when subjected to different operating conditions.
2. Study the interactions between the gas phase and solid phase.
3. Develop a combustion model that includes solid the combustion stages of a solid fuel based on the available experimental data and computational modelling.
4. Compare the results predicted by the modelling with the available experimental data in order to validate the models.

## 1.3 The importance of the research study

The applications of solid fuel combustion and gasification are implemented in many different types of furnaces such as fixed beds reactors and moving bed ones, fluidized and circulating fluidized beds, and pulverized fuel burners. So this study will greatly help to develop better methods of combustion that can be implemented in such practical applications as well as help to reduce the emissions of greenhouse gases and decrease burning the fossil fuels as mentioned previously.

## 1.4 Thesis outline

This thesis is constructed as follows:

In chapter 2, an overview of the current status of combustion of coal and biomass is made. This includes the difference between the properties of the coal and biomass as well as the models which are used to their combustion rates.

In chapter 3, the combustion of one phase, which is the gas phase, is given. As it is well-known those gases (volatiles) are released when burning solid fuels and the most significant gases for solid fuels combustion due to their high activities are methane

(CH<sub>4</sub>), carbon monoxide (CO), and hydrogen (H<sub>2</sub>). Therefore, the oxidation of these gases is important when burning solid fuels. The combustion of methane (CH<sub>4</sub>), which is also important in practical combustion devices such as furnaces and gas turbines, is investigated in this chapter. The governing equations of turbulent reacting flow are described. Different global reaction mechanisms with different  $k-\epsilon$  turbulence models are used to model the combustion of methane. The effects of modified turbulence models on the combustion process are also investigated. The reaction mechanism by Westbrook and Dryer is optimized to see its effect as well. This chapter presents the modelling approach and numerical results of methane combustion in an axi-symmetric chamber. The predictions are presented and compared against the experiments conducted by Garreton and Simonin [20].

In chapter 4, the pulverized combustion of coal and biomass is investigated using the Euler-Lagrange approach. The particulate phase modelling is described. The formation of the nitric oxide (NO) during the combustion is also described and modelled. First, the volatiles released during the devolatilization stage of both fuels are treated as one species in all cases. The intention was to include many species in the combustion of volatiles in the next step, but, unfortunately, the time was not enough to do so. The particle size distribution for both coal and biomass particles is assumed to be the same and follow a Rosin-Rammler distribution curve. The results of the simulations, which are carried out in a 2-D axi-symmetric furnace, are presented and compared with the available experimental data. Moreover, the work is extended to investigate the influence of co-firing of coal and biomass on the burnout of coal particles.

In chapter 5, contrary to the cases presented in chapter 4, the Euler-Euler approach is used to investigate the heterogeneous combustion of carbon particles in a three-dimensional numerical model. The governing equations of both gas phase and solid phase are described. The carbon particles are burned inside a newly designed combustion chamber. Since the carbon particles are located in a small cap inside the chamber (static combustion); i.e. there is no continuous flow of the fuel, it is thought that this approach is more applicable for modelling such a case. The effects of the chamber design on the heterogeneous combustion of the particles are also investigated. The results are presented and discussed, and a conclusion is drawn.

In chapter 6, conclusions of the findings of the present study are summarized and some recommendations for improving the work in the future are given.



## 2 Literature review

In this chapter, a general review of the combustion of solid fuels has been given. First, a description of the properties of coal and biomass is to be presented. Then, an outline of the combustion processes and the effects of various factors such as temperature, particle size, heat rate on these processes are given. Finally, an overview on the combustion systems and the models used for modelling the combustion processes are discussed.

### 2.1 Solid fuels structure and properties

Combustion technologies such as fixed beds, fluidized beds, and pulverized combustion furnaces apply to a wide variety of practical carbonaceous solid fuels extending from low grade fuels to high grade fuels [21]. Solid fuels, used in combustion and gasification, are classified in the following two main categories:

1. Fossil solid fuels and are represented by coals (high grade fuels such as bituminous and anthracite and low grades like subbituminous coals, lignite and peat).
2. Renewable solid fuels and can be represented by biomass (low grade fuels).

The composition of fuel has a great influence on the characteristics and rates of solid fuel combustion and formation of emissions. Therefore, it should be known to enable valid modelling of the process. Modelling of solid fuel combustion or gasification requires data for physical and chemical properties. To evaluate coal or biomass properties that affect the design and operation of combustion systems, several types of analysis are performed which include the following:

- The proximate analysis, which involves a series of tests that heat and burn solid fuel and by which the percentages of moisture content, volatiles, fixed carbon (char) and ash are determined.
- The ultimate analysis, which gives the elemental analyses for carbon, hydrogen, nitrogen, sulphur, and oxygen. The latter is determined by difference in the balance between the sum of contents determined by the ultimate analysis and the total dry-ash-free (DAF) weight.
- The determination of the heating value by combustion of fuel sample in a calorimeter.

- The analysis of the grindability and the determination of the swelling index.
- The determination of the particle size distribution.

The composition of any fuel, in standard fuel analysis, is determined by proximate (technical) and ultimate (elemental) analyses. The methods employed for such analysis are thoroughly described in [22, 23]. On dry basis, renewable and fossil solid fuels consist of two fractions. They are the combustible organic substance and inert inorganic material (mineral matter). The former one is responsible for the energy content of the fuel. The latter one is not identical to the mineral content and presents significant challenges regarding the design and operation of furnaces. It is common, though, to give the ash content as a measure of the mineral matter in the fuel in combustion engineering due to the more complexity of the procedure for the determination of the mineral content than that for the determination of ash content. Performing the proximate analysis distinguishes the moisture, volatile matter, fixed carbon (char) and ash and serves as an indicator of combustion behaviour.

The main elements, which are determined by ultimate analysis in most solid fuels, include carbon (C), hydrogen (H), oxygen (O), sulfur (S) and nitrogen (N). Additional varying quantities constituents like chlorine (Cl), potassium (K) and sodium (Na) might be present in the fuel sample. The ultimate analysis gives a first estimation of emissions result from the combustion process. The combustion calculations of the stoichiometric oxygen demand, the flue gas quantity and the flue gas composition are based on the elemental composition of the fuel.

The variation of shares of the above mentioned elements in coal and in biomass has a great influence on the pyrolysis and combustion characteristics. The increase in hydrogen to carbon and, to lesser extent, the increase in oxygen to carbon ratio leads to increase the mass loss of the solid fuel particles during the pyrolysis stage. The mass evolved during pyrolysis can vary from a few percent and up to 70-80% of the total particle weight. Typically, anthracite coals lose less than 10% of their mass by pyrolysis and bituminous coals lose from 5 to 65% of their mass, whereas, the mass loss of lignite coals, peats and biomass can reach over 90%. This mass loss may last from a few seconds to several minutes, depending on the composition of fuel. The elemental composition and nature of the inorganic compound in solid fuels and trace metals also affect the fuel reactivity [24].

One of the differences between biomass and coals is the hydrogen-to-carbon H/C and oxygen-to-carbon O/C atomic ratios, with higher values for biomass. The change in atomic ratios H/C and O/C from biomass to peat, lignite, coal and anthracite is shown in Figure 2.1. The diagram was developed by Van Krevelen [25]. The increase in rank from biomass to bituminous coal involves de-oxygenation of solid fuel and an increase in carbon content and consequently a decrease in H/C ratio and a decrease in O/C ratio as illustrated in Figure 2.2.

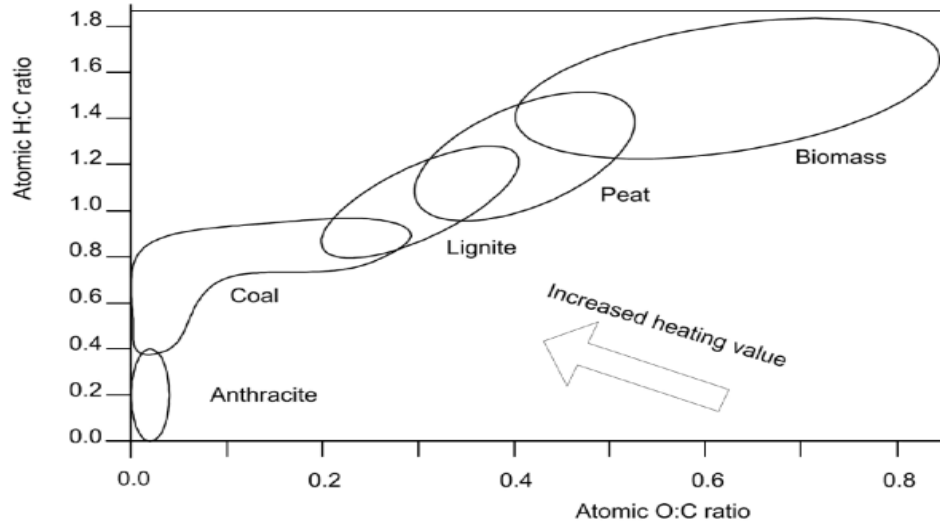


Figure 2.1: Chemical composition of various solid fuels [26].

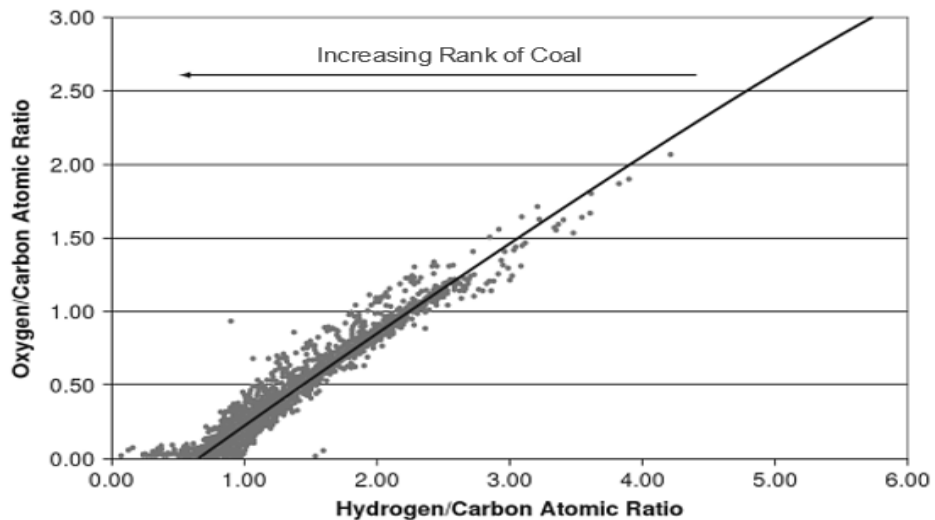


Figure 2.2: Coal rank as a function of H/C and O/C atomic ratios [27].

For simplicity, in many combustion models, the char is assumed to consist of carbon only and the elemental composition of volatiles is determined from the proximate and ultimate analysis data of the solid fuel. Other properties of fuel and process conditions such as air-fuel ratio and temperature are important in the combustion process. Moreover, the particle size of solid fuels varies greatly, depending upon grinding

technique and desired application. For example, the coal dust size in the case of a utility boiler application is much smaller than that in the case of fluidized bed gasifier. The particle sizes play a fundamental role in the combustion and gasification processes of solid fuels. Therefore, when the solid particles are injected into the combustor or the gasifier they cover a wide range of sizes and one can easily imagine that smaller particles carried by gas stream tend to be consumed faster and easier than the larger ones. Therefore, to specify a fuel system, it is necessary to define the relative numbers or masses of particles of different sizes, i.e. the particle size distribution.

### 2.1.1 Non-renewable solid fuel (coal)

Coals are mainly the results of slow deterioration of biomass and the degree of this deterioration determines the coal rank. Coal is a black, inhomogeneous fuel, formed from the partial decomposition of plant materials. It is used primarily as a fuel, so its heat of combustion is the most important property. The structure of coal varies based on time, the extent of temperature and therefore the amount of pressure applied to it over time. Typically, coal structure consists of numerous aromatic rings of five or six carbons bonded with principally hydrogen, nitrogen, sulphur, and oxygen atoms [28]. Coal is a mixture of organic material and mineral matter as mentioned before. The geological process of conversion of plant materials such as peat to coal, shown in Figure 2.3, is called coalification. It takes place in stages to produce different types of coals. The progress of this process in which plants are changed into coals is the base for coal classification. Elevated temperatures and pressures caused physical and chemical changes in the initial plant material and as a result it transformed first into peat, then into lignite (brown coal) and finally into hard coals.

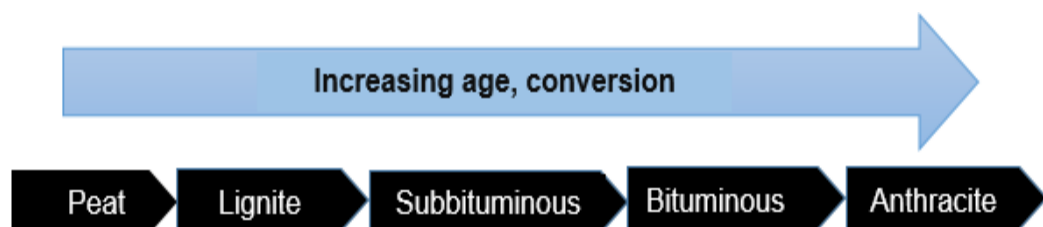


Figure 2.3: Coalification (adopted from [29]).

In the coalification process, the coal rank increases from lignite to anthracite. As shown in Table 2.1 and Table 2.2, increasing coalification degree means lower oxygen and hydrogen contents and accordingly higher carbon levels. In particular, coals are solid and unlike oil fuels, so it is impossible to easily adjust coal properties through refinery.

Therefore, it becomes very necessary to correctly identify the coal properties and logically classify coal types.

Table 2.1: Fuel properties for increasing coalification degree (wt. - %) [30].

Material	Moisture (air-dried)	C <sub>DAF</sub>	H <sub>DAF</sub>	O <sub>DAF</sub>
Wood	10-15	50	6.0	43
Peat	20-25	55-65	5.5	32
Lignite	15-25	65-73	4.5	21
Bituminous coal	1-13	78-92	5.3	8

Table 2.2: Coal properties for increasing rank (on % DAF basis) [31].

Coal type	Moisture	Volatiles	C	H	O	LHV
Lignite	31-70	42-65	62-73	4.3-5.9	20-30	23.7-29.5
Sub-bituminous	16-35	37-52	70-80	4.5-6.0	13-22	28.6-31.9
<b>Bituminous</b>						
High volatiles	1-21	32-49	76-88	4.9-6.0	4.5-16	30.9-37.2
Medium volatiles	1-4	20-32	84-91.5	4.5-5.4	2.0-8.5	34.2-37.2
Low volatiles	1-2	9-20	90.5-93.5	3.7-4.8	1.5-3.5	36.1-37.2
Anthracite	1.5-3	4-9	92.5-96	2.0-3.9	1-2.5	34.5-36.6

Regarding coal rank classification, several works, based on compositions, are dedicated. Among them is the work of Averit [32] and a more recent coal rank is presented by Hensel [33]. It increases from lignite to anthracite and is summarized below on weight fractions at dry and ash-free basis (wt. DAF):

- (1) Anthracite has volatile percentages between 1.8 and 10% and carbon between 91 and 94.4%. The carbon and hydrogen ratio (C/H) is between 23.4 and 46, and combustion enthalpy is between 34.4 and 35.7 MJ/kg.
- (2) For bituminous coal, the percentages are between 19 and 44.6% for volatile and between 77.7 and 89.9% for carbon. C/H is between 14.2 and 19.2, while combustion enthalpy is between 32 and 36.3 MJ/kg.
- (3) The volatile percentage of sub-bituminous coal is between 44.2 and 44.7% and that of carbon is between 73.9 and 76%. C/H is between 14.3 and 14.6, and combustion enthalpy is between 29 and 30.7 MJ/kg.

- (4) Lignite's volatile and carbon contents are approximately 47 and 71%, respectively. C/H and combustion enthalpy are around 14.5, 28.3 MJ/kg, respectively.

In the U.S., the American society for testing and material (ASTM) uses a method of classification that is based on a number of parameters obtained by various prescribed tests for the fixed carbon values as well as other physical properties. It distinguishes between four types of coal and each of each is subdivided into several groups as shown in Table 2.3 and Table 2.4. This method is based on approximate analysis. Coals containing less than 31% volatile matter on the mineral matter-free basis are classified on the basis of fixed carbon.

The fuel ratio which is the ratio of fixed carbon to volatile matter gives an indication of coal rank. In general, a coal with high rank has high fixed carbon content while the volatile matter reduces, which results in the increase of the fuel ratio. Proximate and ultimate analyses of various types of coals are listed in Table 2.5.

Table 2.3: Classification of anthracite and bituminous coals by rank (ASTM D 388-05) [34].

Rank	Fixed carbon limits (Dry mineral-matter-free basis), %		Volatile matter limits (Dry mineral-matter-free basis), %	
	Equal or greater than	Less than	Greater than	Equal or less than
Meta-Anthracite	98	n/a	n/a	2
Anthracite	92	98	2	8
Semi-anthracite	86	92	8	14
Low volatile bituminous coal	78	86	14	22
Medium volatile bituminous coal	69	78	22	31
High volatile A bituminous coal	n/a	69	31	n/a

Table 2.4: Classification of bituminous, sub-bituminous and lignite coals by rank (ASTM D 388-05) [34].

Rank	Gross calorific value limits (moisture, mineral-matter-free basis)			
	Btu/lb		MJ/kg	
	Equal or greater than	Less than	Equal or greater than	Less than
High volatile A bituminous coal	14000	n/a	32.557	n/a
High volatile B bituminous coal	13000	14000	30.232	32.557
High volatile C bituminous coal	11500	13000	26.743	30.232
Sub-bituminous A coal	10500	11500	24.418	26.743
Sub-bituminous B coal	9500	10500	22.09	24.418
Sub-bituminous C coal	8300	9500	19.30	22.09
Lignite A	6300	8300	14.65	19.30
Lignite B	n/a	6300	n/a	14.65

### 2.1.2 Renewable solid fuel (biomass)

Biomass is an umbrella that covers a great diversity of its sorts. It was defined as the biodegradable fraction of products, waste and residues from agriculture (including vegetal and animal substances), forestry and related industries, as well as the biodegradable fraction of industrial and municipal waste [35]. Figure 2.4 shows some examples of biomass.



Figure 2.4: Examples of biomass.

Biomass has been used for domestic purposes since a long time. It can be used to produce usable energy like heat, electricity or bio-energy. Therefore, it can be either converted into energy directly via combustion or into a secondary bio-fuel, which can be in the form of solid, liquid or gas. Bio-fuels can include charcoal which is a higher

energy density solid fuel, ethanol (liquid fuel) or producer gas. The latter is produced from the gasification of biomass. The conversion processes for the latter form include thermo-chemical, biochemical and physical chemical conversion [36].

Table 2.6 lists the two types of harvested biomass in food and non-food categories, and indicates the potential conversion products from them.

Table 2.5: Analysis of various coals [37].

Coal			Proximate analysis, % mass ar				Ultimate analysis, % mass on maf coal					LHV
Country	Region	Rank	Fixed carbon	Volatile matter	Water	Ash	C	H	O	N	S	maf coal MJ/kg
Germany	Rhein	Brown coal	17.3	20.0	60.0	2.7	67.5	5.0	26.5	0.5	0.5	26.2
USA	North Dakota	Lignite	27.8	24.9	36.9	10.4	71.0	4.3	23.2	1.1	0.4	26.7
USA	Montana	Sub-bituminous	43.6	34.7	10.5	11.2	76.4	5.6	14.9	1.7	1.4	31.8
USA	Illinois	Bituminous	39.3	37.0	13.0	10.7	78.4	5.4	9.9	1.4	4.9	33.7
Poland	Typical	Bituminous	54.9	35.6	5.3	4.2	82.8	5.1	10.1	1.4	0.6	36.1
S. Africa	Typical	Bituminous	51.3	32.7	2.2	13.8	83.8	4.8	8.4	2.0	1.0	34.0
China	Datung	Bituminous	50.9	28.1	11.9	9.1	84.4	4.4	9.5	0.9	0.8	33.4
India	Typical	Bituminous	30.0	23.0	7.0	40.0	75.5	6.4	15.2	1.5	1.4	32.1
Australia	Typical	Bituminous	44.9	41.1	4.5	9.5	81.3	5.8	10.0	2.0	0.9	33.8
Germany	Ruhr	Anthracite	81.8	7.7	4.5	6.0	91.8	3.6	2.5	1.4	0.7	36.2

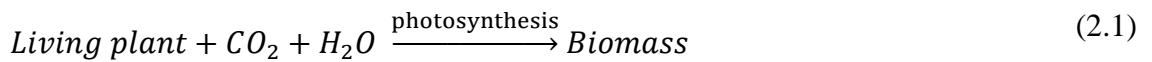
ar, as received; maf, moisture-and-ash-free.



Table 2.6: Sources of biomass [16].

Farm products	Corn, sugar cane, sugar beet, wheat, etc.	Produces ethanol
	Rape seed, soybean, palm sunflower seed, Jatropha, etc	Produces biodiesel
Ligno-cellulosic materials	Straw or cereal plants, husk, wood, scrap, slash, etc.	Can produce ethanol, bio-liquid, and gas

Biomass is considered renewable because of the process which is called photosynthesis takes place as biomass is grown. In this process,  $CO_2$  released from biomass combustion in the atmosphere is captured where, together with water ( $H_2O$ ), it is converted into organic matter under the influence of sunlight as represented by Equation (2.1).



Then, energy stored in biomass is again released into the atmosphere by its conversion into  $CO_2$  and  $H_2O$  by the following equation:



Moreover, the chemical energy stored in biomass is passed on to the animals and to the human that take the plants as food and as a result there will be waste that also contributes to biomass.

From the chemical point of view, virgin biomass such as wood, plants and leaves (Lingo-cellulose) consist of three main components of materials: cellulose, hemicellulose and lignin. In addition to the other ones which are “extractives” and minerals (inorganic compounds) [16, 38-40]. The detailed description of these components is found in the critical review paper [41]. Biomass can be classified based on the atomic ratios as shown in Figure 2.1, which shows that H/C and O/C than fossil fuels biomass has higher.

The proximate and ultimate analyses mentioned before, which are classification techniques developed for coal, are also applied to characterize biomass fuels. Various biomass fuels can be found in literature and for example large variations between biomass fuels were summarized by Vassilev et al [42] and Demirbas [43]. Biomass fuels are generally low in carbon and high in volatile matter and oxygen [39, 43, 44],

which lead to low calorific value. The typical weight percentages for C, H and O, respectively are 30 to 60 %, 5 to 6 % and 30 to 45 % [1, 24]. For coal, the typical compositions (mass percentages) include 65 to 95% C, 2 to 7% H, up to 25% O and 1 to 2% N [45]. Summary of the chemical compositions of several important fuels is provided in Table 2.7 and Table 2.8.

Table 2.7: Proximate analysis for several coal and biomass samples [39].

	Moisture* (%)	Volatile matter (%)	Fixed carbon (%)	Ash (%)	LHV (MJ/kg)
Wood	20	82	17	1	18.6
Wheat straw	16	59	21	4	17.3
Barley straw	30	46	18	6	16.1
Lignite	34	29	31	6	26.8
Bituminous coal	11	35	45	9	34

\*Intrinsic: the moisture content of material without the influence of weather effects.

Biomass, as carbon dioxide neutral fuel with good availability in most regions of the world, is still more attractive to energy producers. Many studies and investigations have been conducted on biomass gasification, combustion and co-firing. Properties similar to low-value coal allow comparison and access to detailed combustion data.

Table 2.8: Average of elemental analysis for many thousands of coal and biomass samples [46].

	Anthracite	Bituminous	Sub-bituminous	lignite	Grass	Straw	Wood chips	Waste wood
C	90.22	78.35	56.11	42.59	45.34	48.31	51.59	49.62
H	2.85	5.75	6.62	7.40	5.82	5.85	6.14	6.34
N	0.93	1.56	1.10	0.73	2.04	0.78	0.61	1.01
O	5.03	11.89	35.31	48.02	45.95	44.18	41.57	42.89
S	0.96	2.43	0.84	1.15	0.24	0.18	0.07	0.07
Cl	0.03	0.08	0.01	0.01	0.62	0.70	0.02	0.06

## 2.2 Coal versus biomass combustion

Selecting the combustion system (technology) is greatly based on the fuel properties such as the chemical composition, moisture and ash content, particle size, particle size distribution, temperature, pressure, etc. The important characteristic properties of biomass are: heating value, moisture content, volatile matter and ash etc. Biomass is a good candidate for replacing coal or for co-firing with it and one of the reasons behind this is that both biomass and coal are solid fuels and, from the view point of power generation, the equipment designed to burn coal are assumed to be able to use biomass as well. However, the chemical composition of biomass is different from that of coal. Furthermore, biomass properties vary significantly more than those of coal do.

Referring to Table 2.7, it can be seen that biomass has a higher fraction of oxygen and less carbon than coal as mentioned before. The hydrogen fraction is also somewhat higher than that of coal. Regarding nitrogen and chlorine contents, these components vary significantly among biomass fuels. For both biomass and coal, they are directly related to  $\text{NO}_x$  emissions and corrosion. Some biomass fuels like straw has contents of chlorine can exceed those of coal. When compared to coal, biomass has a higher moisture content and lower heating value as shown in Table 2.7. Moisture content affects the behaviour of pyrolysis. Product yields depend on the moisture content [47]. It can also cause many problems related to the ignition. It reduce the maximum possible temperature and increase the necessary residence time in the combustion chamber and this gives less room for preventing emissions as a result of incomplete combustion [43, 48].

In biomass combustion, fuel moisture is a limiting factor due its effect on heating value. The reaction of combustion is exothermic and the evaporation of water is strongly endothermic and, practically, a supplemental fuel such as natural gas is required for combustors that burn biomass in excess of 50 to 55% moisture wet basis [24] or it must be dried to a level where it becomes able to sustain combustion. Concerning the volatile matters, biomass has a very high volatile content in comparison with coal, (up to 80 % for biomass and less than 20% for coal), which causes it to have more flaming combustion and less char combustion (highly reactive fuel) [49]. Therefore, the higher volatile content in biomass can affect the optimum sizing and design of the combustion chamber, as well as the ideal flow rate and location of

combustion air. Furthermore, the higher amount of volatile matter leads to a dominating role of devolatilization in the overall conversion process of biomass particles. Ash is identified as the inorganic incombustible part of fuel which left after complete combustion [1]. Typically coal contains more ash than biomass and it reflects mineralogical composition, whereas the composition of biomass ash is based on the chemical components required for plant growth. Biomass ash contains inorganic elements in the form of salts while coal ash is bound mostly in silicates, which are more stable at high temperature. Thus, biomass ash is more disposed to form deposits in the combustor which is known as slagging and fouling [50]. Burning coal containing more carbon will increase carbon dioxide emissions deeply related to global warming.

With regard to the physical properties, An important variable in large scale biomass combustion applications especially where entrainment of fuel particles in the flue gas occurs, as in pulverized fuel combustion, is fuel particle size [26]. Biomass particles are typically much larger than pulverized coal particle. In comparison with traditional coal combustion, the large size of biomass particles has effects on biomass combustion [17, 51]. Solid fuels are burned at rates depend on two predominant factors, which are the rates of heat transfer and the kinetic rates of reactions. For the former one, particle size dominates the influence of heat transfer. Therefore, a rapid heating is found in small, thin particles (thermally thin) while heating is slower for coarser, thicker particles (thermally thick) [24]. Thermally thick particles are those where there is a significant temperature gradients inside them, whereas, for thermally thin particles it is assumed that the temperature distribution is uniform throughout the particles. To evaluate whether a particle can be considered as isothermal or not during heating the criterion based on Biot number is used. This number relates the internal heat transfer resistance to the external resistance. It is mentioned in the review paper [52] that when biomass is ground by milling, chipping or any other sizing process, the particles would still have a bigger size and great particle distribution. This is because of the higher moisture content and fibrous nature of many biomass fuels [53]. Regarding the pulverized biomass and coal there are significant differences between the particle sizes utilized for them. The average pulverized coal particle size is  $\sim 50 \mu\text{m}$  with top sizes of 100-120  $\mu\text{m}$ , whereas a biomass particle can be up to 200 times as large [46, 54]. However, it was reported that wood particles should be milled to a size less than 1000  $\mu\text{m}$  in order to reach a satisfactory burn-out with the residence times typical for pulverized fuel boilers [55]. Since the particle sizes of pulverised coal are small, they

allow complete combustion after around half a second in a furnace. The critical biomass particle size is 1000  $\mu\text{m}$  [56] and this is because the residence time is limited to few seconds which is similar to pulverized coal particles and the oxidation rate of non-micron range particles is limited by oxygen diffusion to the particles and not by reaction kinetics. However, particle specifications have not yet been defined for pulverized biomass in comparison with those of coal that are standardized [57]. Size reduction of biomass fuels is an intensive task that needs energy and is costly, but it could be an efficient way in terms of producing usable renewable energy. A study in which the pulverization of three different forest biomasses have been investigated [58].

The other parameter that affects the combustion process, the most aspect of operational control, is the temperature. The key parameter of heating rate, the residence time of solid and maximum temperature is the control of temperature. The residence time is directly influenced by the combustion temperature and to some extent by the mixing time [26].

## 2.3 Combustion characteristics

The heating value of a fuel, also called the calorific value, is defined as the heat released when combusting 1kg of it, with the assumption that the combustion products are cooled down to the initial temperature i.e. the flue gases have the same temperatures as the temperature of the fuel prior to combustion. This value, which is the so-called high heating value (HHV), is based on dry basis and it is measured directly in a calorific bomb. Whereas, the value that is calculated by subtracting the energy required for evaporating any moisture content of the fuel is called low heating value. This value, if the experimental methods are not possible, can be estimated using empirical correlations. There are many of these correlations in the literature that are used for estimating the heating value of solid fuels such as coal and biomass.

Parameters that are definitely related to the energy content of a solid fuel are the atomic ratio between oxygen and carbon O/C and the atomic ratio between hydrogen and carbon H/C. The diagram was previously shown in Figure 2.1 that relates together the LHV, the H/C and O/C ratio on a dry ash-free basis for all fuels, from carbon-rich anthracite to carbon-deficient woody biomass. The heating value of biomass fuels are lower than that of most coals and, on average, the heating value of biomass fuels usually ranges from 18 to 22 MJ/kg (on dry basis) [26]. However, according to [24] the

contents of C and H tend to increase the heating value. Every 1% increase of carbon mass fraction elevates the heating value of biomass by 0.39 MJ/kg while high content in oxygen results in low energy content. Therefore, the higher O/C ratio the lower energy content will be. For example, the higher heating value (HHV) of a biomass correlates well with the oxygen-to-carbon (O/C) ratio, reducing from 38 to about 15 MJ/kg while the O/C ratio increases from 0.1 to 0.7. The effective heating value of the fuel is reduced as a result of the increase of hydrogen-to-carbon (H/C) ratio. For example, fresh plant biomass like leaves has very low heating values due to its high H/C and O/C ratios. As it is also shown in Figure 2.1, the atomic ratios of a fuel decreases with increasing its geological age, which means that the older the fuel, the higher its energy content. For example, anthracite, which is a fossil fuel geologically formed over many thousands of years, has a very high heating value. On one hand, the lower H/C ratio of this solid fuel gives higher heat. On the other hand, the carbon intensity or the CO<sub>2</sub> emission from its combustion is high.

## 2.4 Thermo-chemical conversion processes of solid fuels

Reducing the pollutants does not depend only on the type of the fuel but also on the conversion processes and the technologies used to carry out them. The processes to thermo-chemically convert the chemically stored energy in solid fuels to usable forms of energy include pyrolysis, combustion and gasification as shown in Figure 2.5.

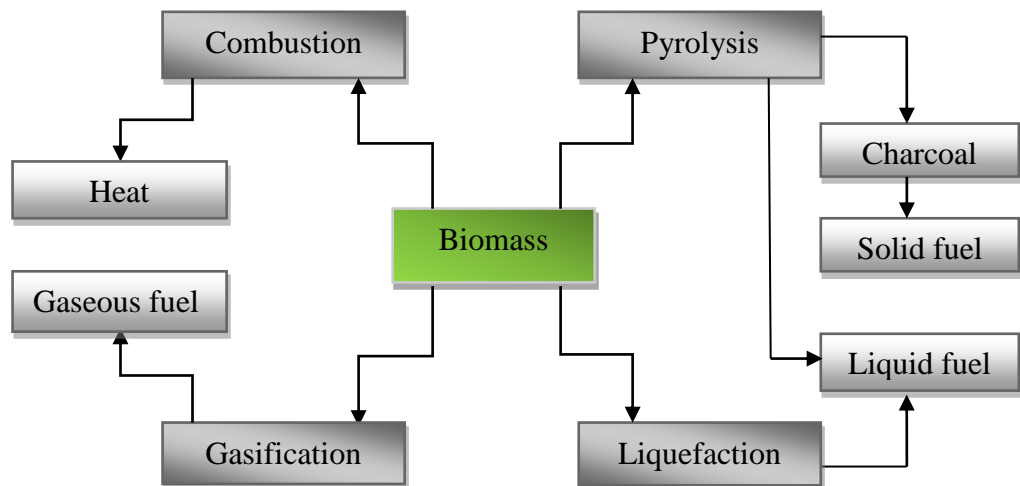


Figure 2.5: Thermo-chemical process for conversion of biomass into fuels, gases or chemicals.

Direct combustion of solid fuels is a conversion process by which heat is generated. When burning solid fuels to produce energy, chemically, the combustion process is an exothermic reaction between oxygen and the hydrocarbons that converts them into high

temperature gaseous emissions. Regarding the combustion of coal and biomass, it is the classic technology for household energy, especially for cooking. There are several major chemical and physical phenomena occurring during this process as illustrated in Figure 2.6. The ideal combustion is the complete oxidation of fuel molecules to  $\text{CO}_2$  and  $\text{H}_2\text{O}$ . In practice, combustion is always incomplete, and even in the idealised case of complete combustion. For example, the nitrogen in the air may react with the oxygen to produce nitrogen oxides and also many fuels contain elements other than carbon that may be transformed during combustion.

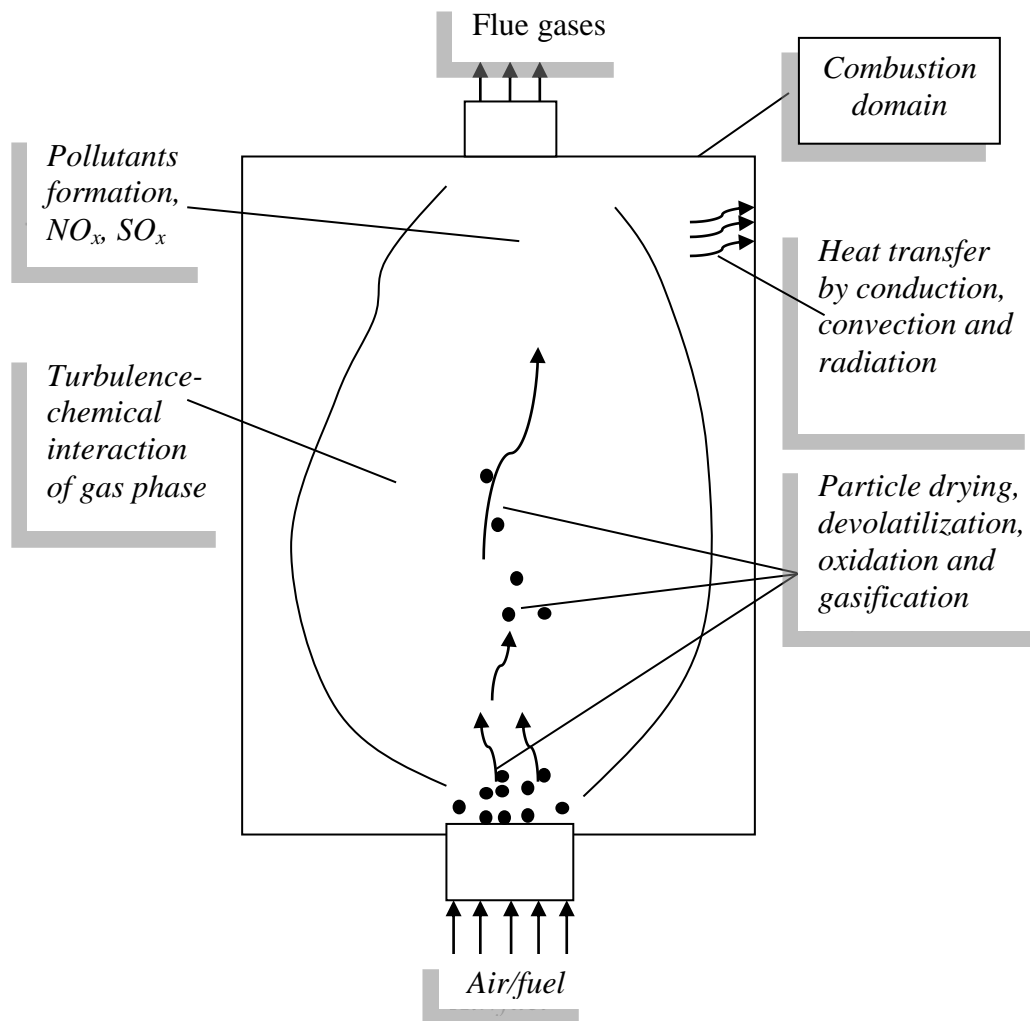


Figure 2.6: Various chemical and physical mechanisms during solid fuel combustion (adapted from [59]).

Figure 2.7 shows the volume loss and mechanisms involved in the combustion of a solid fuel. For the design and optimization of combustion systems, knowledge of these mechanisms is essential. The combustion process generally entails the combustion of the volatiles released during devolatilization stage (homogeneous combustion) followed by the char oxidation, which represents the reactions between the solid carbon and the

surrounded gases (heterogeneous combustion). It must be noted that the latter one may simultaneously proceed with devolatilization, depending on reaction conditions.

Devolatilization is the release of volatile matter by thermal decomposition. It is carried out in widely different environmental conditions and plays a paramount role in burning solid fuels. When it occurs in an inert atmosphere is termed pyrolysis, which, as a standalone technology, is a possible thermo-chemical conversion route of commercial importance in the production of a huge number chemical compounds.

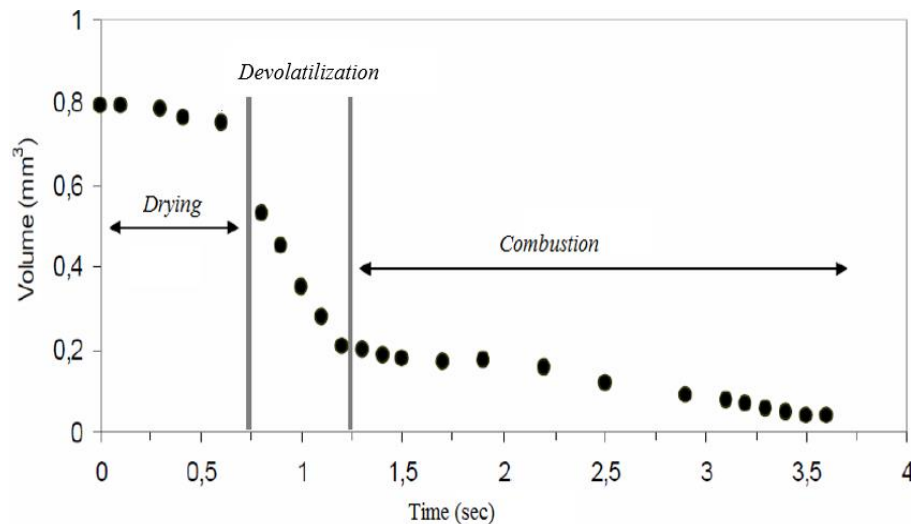


Figure 2.7: Combustion stages of a small biomass particle (adapted from [26]).

However, for engineering applications, in the absence of any reacting gas medium, it is defined as an endothermic reaction which converts solid fuel to a mixture of gas and solid residue at high temperature (950-1100 K). Based on biomass in a number of ways, pyrolysis as a thermo-chemical conversion route can be used as a part of renewable energy systems. For example, liquid and gas products produced from pyrolysis of biomass can be used directly for generating electricity. Moreover, high value products suitable for use as transport fuels are produced by upgrading the liquid product. Additionally, the char produced by pyrolysis can also be used as a renewable fuel and in its traditional form as charcoal is used for cooking in the developing regions. However, the traditional process of making charcoal is often seen as a major source of environmental degradation in the form of deforestation and pollution in rural areas [60].

Devolatilization is the term that typically used for the process occurring in an oxidising or combusting atmosphere such as the one present within a combustor and this context will be used in the present investigations. It is the process where combustible gases are



released from the solid fuel due to thermal decomposition [61]. As devolatilization proceeds, volatile gases are formed from the solid fuel matrix. These released gases diffuse towards the particle surface and may combust within or in the vicinity of the particle or in both of them. Despite its occurrence on a time scale that is much shorter than the subsequent char oxidation process, devolatilization has a profound effect on the whole combustion process [62, 63]. This process is the basic step in any combustion or gasification process of a solid fuel [61, 64].

During the devolatilisation, the degree of released volatiles and the composition of these volatiles and char depend on several parameters such as the fuel type and composition, particle size, pyrolysis temperature and heating rate and pressure. For more information about the effects of these parameter one can refer to the review papers by Yu et al. [65], Borah et al. [66] and Di Blasi [61]. The process of devolatilization accounts for up to 70% of weight loss experienced by coal and up to 95% for biomass and it takes place on a time scale shorter than char oxidation. Typically, the devolatilization products consist of CO, H<sub>2</sub>O, CO<sub>2</sub>, H<sub>2</sub> and light and heavy hydrocarbons (C<sub>x</sub>H<sub>y</sub>), which subsequently may react in an oxidising gas phase to produce CO<sub>2</sub> and H<sub>2</sub>O as well as the solid carbonaceous residue, char, which includes also the inorganic components (ash). The first five components are termed as light gas, and the last one as tar. Tar is a high molecular weight substance that is released in the gaseous phase and it condenses at room temperature. Normally, the assumptions made on the mechanisms of formation, the rate of biomass decomposition, and the final composition of the volatiles are differ from one researcher to another depends on the objectives of the modelling and the available experimental data for the particular situation. For example, in [67, 68] all these components are lumped together and treated as a single pseudo-product. It maintains the species balance and has an energy of information of that is consistent with the overall energy of the reaction. For the simplicity of combustion modelling, the same assumption has been made in the current investigations. The portions of the three products of pyrolysis process (gases tar and char) depend upon the type of pyrolysis that is determined by the residence time and temperature. High temperature and long residence time enhances the conversion of solid fuel into gaseous products, while for short residence time tends tar yields are favoured.

The most important parameter for the devolatilisation process among those mentioned above is the temperature. At increasing temperatures the mass loss due to thermal

decomposition of chemical bonds increase until only char and ash remain. In addition to that, higher temperatures lead to lower char yield in all pyrolysis reactions. The char composition is also affected by temperature, and therefore, at higher temperatures, the chars produced are rich in carbon [47].

The devolatilisation is also affected by the molecular structure of the solid fuel as it involves the breaking of chemical bonds. For example, coal devolatilization behaviour is different from that of biomass. Coal devolatilisation takes place at much higher temperatures. However, there is a broad range of coal types as outlined in § 2.1.1, each of which decomposes in slightly different manner. Generally, low rank coals generate high gas yields and low tar yields [69] like biomass. Bituminous coals generate a high yield of tar compared to other coals [69, 70], while high-rank coals exhibit low gas yields and also moderate or low tar yields [69]. On one hand, as it is heated, coal typically releases volatiles in three stages which are low temperature process, primary pyrolysis, and secondary pyrolysis [71].

The low temperature process (200-400°C) in which coal undergoes mild changes is related to removal of crystal-bound moisture and disruption of hydrogen bond. Then, during the primary pyrolysis at higher temperatures, the weakest covalent bonds break and produce fragments, which will be released as primary tar if they are small enough to vaporize and be transported out of the char particle. The secondary pyrolysis involves breaking the stronger covalent bonds. It initiates when the tar and certain light gases begin to undergo further reactions in the gas phase. On the other hand, biomass devolatilisation is mainly related to the content of lignocellulosic components which are cellulose, hemi-cellulose, and lignin. It results in a rapid weight loss as these components break down. It appears to be simple. However, the differences in chemical composition of these components and its breaking down at different temperature ranges make the devolatilization process complicated and the subsequent release of inherent volatiles lead to structural changes [72].

During pyrolysis, biomass typically starts to release volatiles at temperature of 160-300 °C [73, 74]. Cellulose and hemicellulose components contribute differently to the overall pyrolysis [75, 76] and they decompose in a somewhat narrow temperature interval. Whereas, lignin decomposes slowly through a wide temperature interval [77]. At a heating rate of 5°C/min, first, the decomposition of latter one takes place at lower temperatures around 250°C to 320°C. Then, the decomposition of the former one occurs at higher temperatures 310 to 380°C. The decomposition of the two

components, in some cases, may overlap and occur at similar rates. Finally, the thermal degradation of lignin takes place at 300 to 430°C [78]. It typically results in a continuous weight loss at slow rates in the regions of highest temperatures. Figure 2.8 depicts the thermal degradation of four 5mg wood samples at a rate of 10 °C/min. All the samples have the same trend for weight and derived weight as a function of temperature. The areas of weight loss for the three components of biomass are shown in the figure. It was reported in [61] that at low temperatures, the evolution of CO, CO<sub>2</sub> and H<sub>2</sub>O is mainly because of the degradation of extractives and hemicelluloses and as the temperature increases, the formation of tar vapours becomes predominant due to cellulose degradation. Lignin decomposition also attains fast rates and results in producing char and additional gases (CO<sub>2</sub>, CO, CH<sub>4</sub> and H<sub>2</sub>).

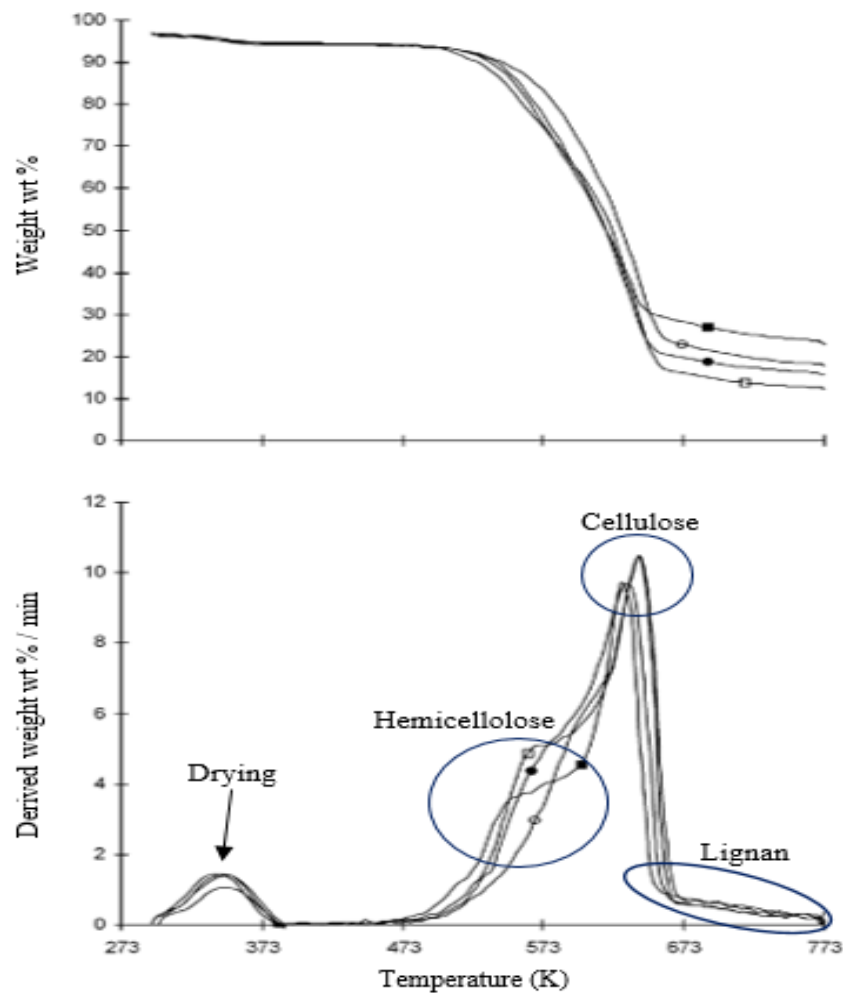


Figure 2.8: Thermo-gravimetric weight loss curves of four wood samples: ○ spruce, □ birch, ● beech white and ■ acacia (adapted from [26]).

The process of devolatilization, in the case of coal and depending on its type, occurs when the coal is first heated to temperature higher than 350°C [74] and both the chemical and pore structures change significantly. This is due to the release of the

volatile constituents of the coal in the form of gaseous compounds and tar in an inert environment. The yields of this process also include the char, which is the solid product that has higher carbon to hydrogen ratio than the original coal. The composition of these productions depends on the factors mentioned above. It was observed that amount of ultimate weight loss of coal during pyrolysis increases with increasing the peak temperature [79-81]. The yields of char are inversely impacted by temperature. Higher temperature decreases char yields, whereas, lower devolatilization temperature increases char yields.

The influence of particle size on the devolatilization process of solid fuels is related to the internal heat transfer and residence time of the reactive species in the particle. Therefore, the pyrolysis can be conventional (slow) or fast, based on the operating conditions that are used [16, 82]. Regarding the former one, the larger the particles the slower the heating rate and consequently, the slower the devolatilization rate. In the present study, the latter one has been considered due to its relevance to the pulverized combustion, where values reaching. For fast pyrolysis, the following conditions should be met: (a) high heating rate, (b) short vapour residence time. This, generally, entails that the solid fuel to be prepared as small particle sizes. Moreover, it needs a design that removes the vapours quickly from the presence of hot particles. Therefore, the understanding of the influence of particle sizes will be of importance in order to select appropriate size fraction for conversion efficiency and design of biomass combustion alone or co-combustion with coal [83].

It is easy to imagine that smaller particles carried by the gas stream tend to be consumed faster and more easily than the larger ones. Therefore, the particle size distribution influences not only the rate at which the fuel reacts with oxygen and other gases, but almost all other aspects of combustors and gasifiers as well.

In the case of biomass, grinding it into small particles is a challenging exercise because of the non-friable nature of biomass and its moisture content and requires energy. However, size reduction minimises the fibrous nature of biomass so that the burning rate is faster, enhances boundary layer diffusion and reduces heat transfer resistant [84, 85]. Di Blasi [86] studied the effects of parameters such as particle size, reactor heating, and temperature in a reactor. It was found that char yields increase as particle size increases and higher rates lead to higher volatile matter yields and lower char yields. A study of the combustion characteristics of a single biomass particle ranging in

size from 10  $\mu\text{m}$  to 20 mm was carried out [87]. It was concluded that the results were beneficial when used in assessing different combustion systems using biomass as a fuel such as pulverized fuel furnaces. Many other studies related to the influence of fuel particle size have been carried out [17, 87-90]. For coal devolatilization, the effect of particle size has also been observed [72].

In terms of the effect of heat rate, the volatile yield, the temperature range at which the volatiles are released and the rate of weight loss are influenced by heating rate [61]. Therefore, the range at which volatiles are released shifts towards higher temperatures for increasing heating rates. Therefore, it is almost impossible to avoid the influence of heating rate on pyrolysis. As mentioned before, pyrolysis can be slow or fast. Slow pyrolysis assumes that the heating rate of the sample is below 10 K/s, while the rates of the latter one can be above  $10^3$  K/s. The fast pyrolysis occurs. In almost all combustions of pulverized solid fuels, where the fast pyrolysis occurs, the heating rates of values reaching  $10^5$  or even  $10^6$  can be found. Whereas, fluidized bed imposes lower values, or around  $10^2$ – $10^4$  K/s and moderate to slow may happen in sections of moving or fixed bed combustion or gasification [91]. Pyrolysis has been studied in the case of biomass and extensively in the case of coal and numerous studies can be found in literature [51, 92-101].

Another process by which the thermal conversion of solid fuels is carried out is the gasification technology. It is defined as the thermal degradation of a solid fuel in the presence of an oxidizing agent such as oxygen, carbon dioxide or steam [26]. Its primary goals are to convert the non-ash fraction of the solid fuel to gas and produce gases that preserve, as much as possible, the heat of combustion value of the solid fuel. Combustion and gasification are two closely related processes, but there is a difference between them. The latter one packs energy into chemical bonds in the product gas, whereas in the former one these bonds are broken to release the energy. It should be noted that the term combustion is used for the gasification of char with the oxygen. It takes place at slightly lower temperatures than the combustion and aims to maximize the product gas which mainly consists of CO, CO<sub>2</sub>, H<sub>2</sub>O, H<sub>2</sub>, CH<sub>4</sub>, and other hydrocarbons. This technology, compared with the combustion, leads to reduce the emissions of CO<sub>2</sub> due to the limited amount of oxygen (an oxygen-deficient environment). It is an endothermic process and as a result leads to reduce the temperature. Comparison between these processes can be found in [102].

## 2.5 Char oxidation (heterogeneous combustion)

Despite the similarity of biomass and coal chars, there are large physical differences between them with regard to thermal conductivity, density, porosity, surface area and particle size and shape. In terms of biomass, several fundamental studies have been carried out focussing on the reactivity and conversion of either single biomass particles or biomass char [87, 100, 103, 104]. In addition, more information regarding char reactivity of coal and biomass can be found in many reviews e. g. [61, 105]. Char oxidation and gasification is the process to occur in solid fuel combustion systems proceeding simultaneously or after the devolatilization process. The latter is usually assumed because the blowing of volatile matter through the particle surface and the flame formed during the combustion of volatiles effectively inhibits the surrounding oxygen from reaching the char [106]. During this process the char is oxidized or gasified by means of heterogeneous reactions. The heterogeneous reactions take place between the solid phase (char) and surrounding gases in the gas phase. Since char conversion is the slowest reaction, the heterogeneous combustion rate is a crucial factor for industrial furnaces and gasifiers. It determines the time required for complete conversion of char. It accounts for the majority of time required for fuel particle burn out. Furthermore, it defines the necessary residence times in the furnace, which directly influences the necessary size of the unit and as a result the investment costs [107]. It is the rate-limiting step. The rate-limiting step can be chemical or diffusional as will be described next. The burn out of carbon is affected by several factors that include the amount of volatile matter quickly released from the fuel, porosity of the resulting char, char particle size, the reactant and its partial pressure, furnace temperature and the residence time. If residence time is long enough and particle size is fine, the burnout increases.

Heterogeneous reactions require a longer time than that of devolatilization. For complete combustion of char, the time required can be several of orders of magnitude larger than that for devolatilization. Since most of the char is carbon, CO and CO<sub>2</sub> are the dominating products of burning carbon. Therefore, the other elements may be neglected when considering the heat effect of char combustion, and the char is considered to be 100% carbon without making large errors. However, the elements that have a large effect on formation of environmental emissions such as nitrogen and sulphur needs to be known in order to determine the emissions formation correctly. For

the process of char combustion and gasification, an oxidizing agent (oxygen, steam, carbon dioxide, etc.) from the surrounding bulk flow must diffuse to the particle surface through a boundary layer [108]. Reactions of char with oxygen are called oxidation reactions and those with steam and carbon dioxide are called reduction reactions. However, char gasification rates for its reactions with  $\text{H}_2\text{O}$  and  $\text{CO}_2$  are negligible if the oxygen is present, and sufficiently we can only consider the char combustion with the oxygen [109].

In addition, in the case of gasification and especially for high hydrogen partial pressures, the reaction of char with hydrogen may also become important. There is a thin layer surrounds the char particle where the homogeneous reactions occur. Through this layer, the diffusion of gaseous reactants and products takes place. The former ones diffuse into the char surface, while the latter ones diffuse away to the gaseous phase as shown in Figure 2.9 .

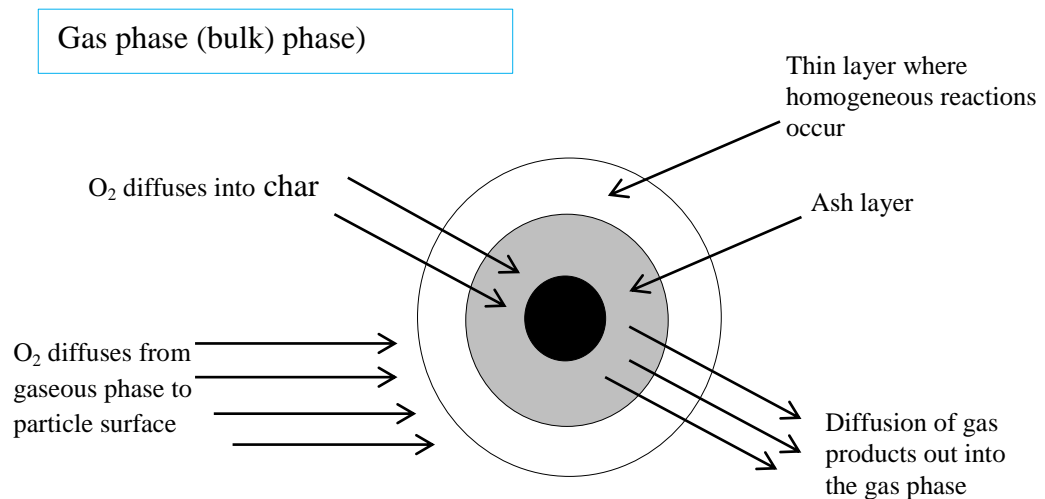


Figure 2.9: Char combustion (adapted from [110]).

Based on the process that controls the reaction rate of heterogeneous reaction rate, chemical kinetics, diffusion or a combination of them controls the combustion and gasification of char. One can refer to the comprehensive reviews [45, 105, 109, 111, 112] for more information regarding the combustion of char regimes. Based on the rate-controlling mechanism the oxidation of char may be divided into three combustion regimes [61]. The heterogeneous reaction rate is limited by chemical kinetics (regime I) if temperatures are low, a char particle is very small and the reaction rate is low. Therefore, the concentration of oxygen is uniform within both the entire particle and the bulk gas phase in this case.

On the other hand, large char particles at high temperature often burn under diffusion limitations (regime III). In such case, the chemical reactions are very fast so that oxygen is consumed at the outer surface of the particle which means that the penetration depth of oxygen and the external surface concentration of oxygen approaches zero. With increasing the temperature in comparison to that of regime I, the reaction rate is influenced by the combined effects of chemical kinetics and diffusion of oxygen (regime II) in the intermediate region.

In real combustion systems, various particles may burn under different regimes (the overall rate is influenced by a combination of adjoining zones and therefore, the analysis of oxidation regimes is more complicated. For example, pulverized fuel combustion has a significant distribution of particle sizes and therefore the oxidation of small particles of 1  $\mu\text{m}$  may follow regime I, while those of  $\geq 100 \mu\text{m}$  may burn under the conditions of regime II or III [105]. Under conditions of regime III, Biomass char particle are significantly more reactive than coal ones with respect to  $\text{O}_2$  and as a result a lower temperature is required for a biomass char particle to be oxidized than a coal char particle.

## 2.6 Combustion technologies

The application and knowledge of combustion of solid fuels are ancient. Solid fuels, in terms of wood from plant, have been used for cooking and generating heat since man discovered the fire. In modern times, they are burned in different ways. In principle, several combustion technologies exist for the combustion of solid fuels. The following ones can be distinguished:

- Fixed bed combustion
- Fluidized bed combustion
- Pulverized fuel combustion

Such solid fuel firing technologies are widespread and play a paramount role in generating heat and electricity. The choice of the proper firing system depends on many considerations. The basic principles of these systems are shown in Figure 2.10 and the distinction between them is based on the fuel feed techniques, the mode of heat-feedback and combustion. The advantages and disadvantages of these systems and the comparison between them can be found in [16, 113-115].



The fixed bed combustion systems have been used for burning solid fuels since a long time ago. In these systems, also known as grate firing systems, the primary combustion air is supplied through a bulk bed of fuel, where drying, devolatilization and char combustion take place. Typically, the primary air speed is 0.1 m/s in utility plants [116] which is insufficient to lift the fuel particles and they remain in the layer on the grate. In most of the combustion systems there are two or more locations through which the air is supplied. In these systems the combustible gases released from the fuel bed are burned with secondary air additions that are often located separately from the primary combustion zone [26].

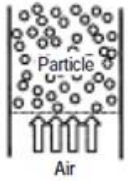

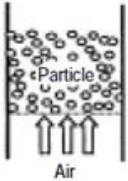
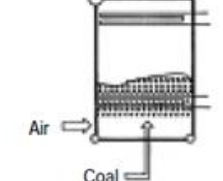
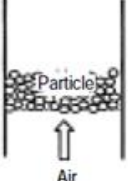
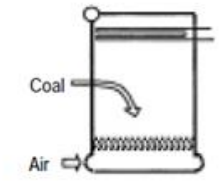
Principle		Outline of boiler			
Entrained Bed	↑ ↑ Fine Fast			Diameter Under 200 mesh ratio 70% Velocity 10~15m/s Temperature 1,400~1,500°C	Pulverized coal Boiler
Fluidized Bed	↑ ↑ Coal particle Air velocity			Diameter <10mm Velocity 1.4~10m/s Temperature 800~900°C	Fluidized bed boiler
Fixed Bed	↓ ↓ Coarse Slow			Diameter <30mm Velocity 0.8~1.5m/s	Stoker boiler

Figure 2.10: Coal combustion systems outline (adapted from [117]).

Fixed bed combustion systems are characterized by their flexibility regarding moisture content and fuel particle size [114, 118]. However, due to the poor mixing of air and solid particles longer reaction resident time is required to achieve full conversion of solid fuels. The poor mixing results in inhomogeneous combustion conditions at some parts of the grate. Moreover, ineffective mixing condition needs higher amount of excess air for complete combustion. The typical fixed bed combustion systems are grate furnaces and under-feed stokers. Based on the grate design, there are several different grate furnaces, including fixed grates, travelling grates, rotating grates and vibrating grates. All these types of furnaces have specific advantages and disadvantages depending on fuel properties [26]. Since no or minor fuel preparation is required, grate firing systems are preferred for fuels such as solid industrial wastes or biomass. The

grate furnaces can burn biomass fuels ranging in size from pellets (6-10 mm) to wood logs [26].

Increasing the air velocity leads to that the drag forces between the air and the particles become larger and the bed begins to expand in volume. Then, a limit, where the drag force is in balance with the gravitational force and the particles are suspended within the flow, is reached. At this point the particles start to exhibit fluid-like behaviour and the bed is considered to be at minimum fluidization state [119]. Fluidization technology gives very good heat and mass transfer characteristics. In this technology (fluidized bed combustion), solid fuels are burned in a suspension of gas and solid bed material (non-reactive material). Sand is usually used as the solid bed and located in the bottom part of the furnace. The primary air enters from below the bed through a nozzle distributor plate. Based on the air fluidization velocity and the particle size of the bed material, two different technologies, the bubbling fluidized bed combustion (BFB) and circulating fluidized bed combustion (CFB), are employed.

In BFB, the fluidization velocity is lower to keep the bed particles which are located in the bottom part of the furnace in suspension by the primary air. Whereas, in CFB, the fluidization velocity is high and the bed is continuously circulating and thus the bed particles are carried out of the bed and separated in a cyclone and circulated back into the combustion chamber [26]. The feed of solid fuel particles is located somewhere above the sand bed and these particles fall down and mix with sand and therefore they are being lifted. Fluidized bed reactors, compared to other combustion systems such as fixed beds reactors mentioned above, on one hand, are generally characterized by having a very wide operating range regarding fuel materials and moisture and because of the good mixing conditions the temperature profiles along them are uniform. Therefore, the formation of hot spots is avoided. On the other hand, they are inflexible with regard to fuel particle sizes [114]. Therefore, a suitable fuel pre-treatment system for particle size reduction is required. For CFB, a particle of biomass with size below 40 mm is recommended and regarding BFB units a size up to 80 mm can be used [26]. As outlined earlier, these types of furnaces provide better heat transfer within the fluidized bed and as a result the size of the boiler can be reduced. Furthermore, the lower temperatures in these furnaces make low level of NO<sub>x</sub> emissions.

In pulverised fuel (PF) combustion, also called dust or entrained combustion, fuel particles are pneumatically injected into a furnace. They are kept in suspension while

reacting with the ascending gas flow. The combustion of the released gas is achieved by supplying secondary air. Pulverized combustion technology requires both fuel particle sizes to be very fine and low moisture content [114]. Pulverised combustion of coal is the common technique that is used for generating electricity for industries and utilities in the world. It is only feasible in large scale applications. In comparison with the other two types of reactors, they are characterized by their ability to use various types of fuels with different composition (e.g. co-firing of coal and biomass) and their quick responses to changes in load. Being a rapid process disturbed over the entire furnace, the combustion process of the pulverized particles makes it possible to achieve higher capacities than the other two types of combustion systems. Fuel requirements for PF combustion are higher than those for grate or fluidised bed combustion. When burning coal in pulverized furnace, it must be ground to fine dust with 90–98% of particles smaller than 100  $\mu\text{m}$  to travel with the gas stream and they are characterized by short residence times no greater than a few seconds [37, 120, 121]. The higher moisture content and fibrous nature of many biomass fuels makes them harder to grind than coal and, according to van Loo and Koppejan [26], the maximum size for renewable fuels in PF boilers is 10-20 mm. However, as mentioned in § 2.2, it was reported that wood particles should be milled to less than 1 mm, which is the critical size, in order to reach a satisfactory burn-out within the residence times typical for PF boilers. This is due to two factors. First, the residence time in PF is limited to few seconds. Secondly, oxidation rate of non-micron range particles in PF furnaces is limited by the oxygen diffusion to the particle and not by reaction kinetics. Using biomass alone in pulverized combustion not yet at any advance stage because of the high cost of biomass pulverization (reduction to fine particles) and the challenge to reduce the moisture content [122].

## 2.7 Modelling of solid fuel rates

The field of combustion and gasification of solid fuels such as coal and biomass is one of the important sources for producing energy and power and it is always of great importance to understand the processes of burning such fuels. Combustion studies are required for the purpose of determining combustion characteristics under well-controlled conditions to aid in the design and operation of solid fuel combustion systems. This section presents the solid fuel combustion sub-models such as drying, devolatilization and char oxidation models.

### 2.7.1 Drying

One issue that is related to the combustion of solid fuels is the moisture content. The moisture content of coal is very little that it has not a great effect on the combustion process, while biomass contains large amounts of water that needs to be dried prior to combustion. The conversion process of solid fuels always starts with drying process. The water leaves the fuel particle as steam which cools down its outer surface. Proceedings of heat are needed for drying, and in return, this lowers the temperature in the combustion device. Therefore, as mentioned in § 2.2, for biomass combustion, it is not practically feasible to burn particles with high moisture content, since moisture content in excess of 55 wt % makes it very difficult to maintain the combustion process [24].

There are two forms of moisture in which a solid fuel particle can exist, which are free water and bound water. To categorize the moisture content in biomass, the criterion of fibre saturation point, which is approximately 30% wt db for wood, can be used. The moisture content is categorized as free water above this point and as bound water below it. There are various methods of modelling the moisture-drying process [123]. The thermal model is the simplest one in which the drying process begins when the fuel reaches a predefined temperature, which is typically 100 °C. Another model uses an algebraic expression for temperature as a function of moisture content. It is similar to the thermal model but the evaporation temperature is not constant. In some cases, moisture evaporation is assumed to be diffusion limited (diffusion expression method). The most common method is that in which the drying process is treated as an additional chemical reaction. It is so-called the first-order kinetic rate model. In this model, it is sufficient to add water and its vaporization heat to kinetic scheme. The reaction rate  $k_m$  can be expressed in first order Arrhenius form [124, 125]:



### 2.7.2 Devolatilization models

As it was mentioned before (see section 2.4) that the devolatilization process is complex owing to several influencing parameters, which include heating rate, temperature, moisture content, fuel chemical composition, pressure and particle size and shape. With regard to coal combustion, a number of models have been previously developed and implemented for the devolatilization of various coals. Several reviews of

these models have been published [69, 126]. These models include the simple ones such as constant model [127], single kinetic rate model [128] and the Kobayashi model (two competing rates model) [99]. The first one is the most basic devolatilization model that assumes the driving off of volatiles to take place at a constant rate. In the second model, it is assumed that the rate of volatiles release is first order dependent based on the amount of volatiles remaining in the fuel. The important shortcoming of this model is that it cannot account for the dependence of the volatile yield on the final temperature. To overcome this, the Kobayashi model is used to handle the devolatilization of coal and volatiles release through the implementation of two equations. One equation is for low temperatures and has a certain volatile yield and the other is for higher temperatures where it is assumed that the volatile yield could be much larger.

In addition to the above mentioned models, there are complex models, which are applicable over a wide range of coal types, including the functional group-devolatilization vaporization cross-linking model (FG-DVC) [129], the FLASHCHAIN structural model [130] and the chemical percolation devolatilization (CPD) [126]. These models are extremely complex and difficult to use for practical applications. Despite the important differences between coal and biomass, coal devolatilization models have been commonly adapted for the biomass devolatilization. In addition, many biomass pyrolysis/devolatilization models have been developed and comprehensive reviews on the various models and kinetics are presented by Di Blasi [97] and also given in [19, 131]. The kinetic mechanisms classification involves these three main global schemes:

1. One-step global mechanisms.
2. One-step multi-reaction mechanisms.
3. Multi-step semi-global mechanisms.

The way used by one-step global mechanism to define devolatilization rates is very simple. The products can be either (volatiles or char) or (gases, tar and char) as shown in equations (2.4) and (2.5).

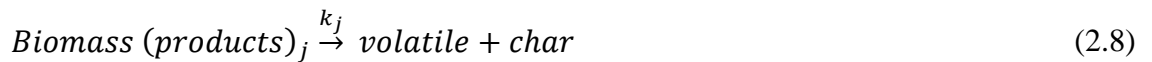




The rate of reaction ( $k_r$ ) is expressed in an Arrhenius fashion (equation (2.6)) and the necessary kinetic parameters are generally obtained experimentally using tube furnaces, thermo-gravimetric analysers, etc.

$$k_r = A_r \exp\left(\frac{-E_r}{R_u T}\right) \quad (2.6)$$

where  $A_r$  is pre-exponential factor,  $E_r$  is activation energy,  $R_u$  is universal gas constant and  $T$  is temperature ( $^{\circ}\text{K}$ ). The major drawback of this mechanism is its inability to predict the composition of volatiles and not accounting to various components of the virgin biomass. To overcome these limitations, One-step multi reaction mechanism has been developed as can be illustrated below:



where  $j$  is gases, tar or char. But this scheme neglects the secondary reactions (tarcracking to light molecular weight volatiles) which become significant when the temperatures become higher and there are sufficiently long residence times as well. To address this issue multi-step semi-global schemes have been considered. It is usually assumed that the fuel first decompose to so called active intermediates with lower degree of polymerization. Then, these intermediates decompose to other products. Two-stage semi-global reactions for both cellulose and wood are illustrated in Figure 2.11 [131]. It is assumed that all reactions are first order, irreversible and follow Arrhenius law (equation (2.6)). Kinetics of these two schemes are given in [132].

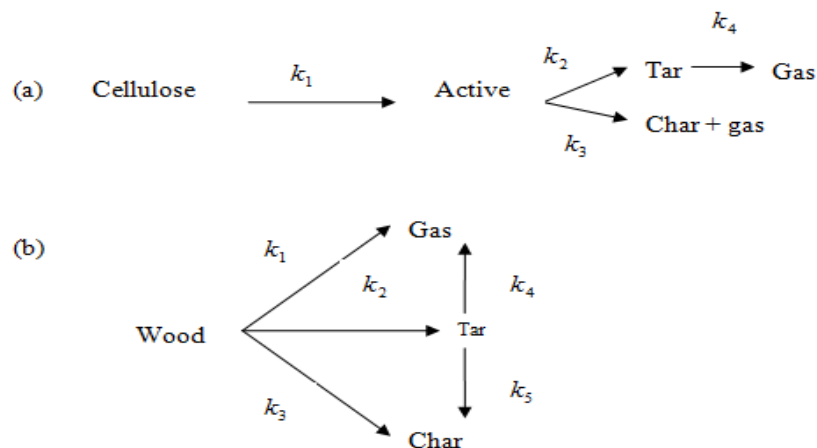


Figure 2.11: Two-stage semi-global reaction mechanisms for (a) cellulose; (b) wood.

### 2.7.3 Heterogeneous combustion models

The devolatilization process produces gaseous volatiles and solid char that both react further in homogeneous and heterogeneous reactions. The gaseous volatiles, at high temperature, react very fast towards their equilibrium composition (mixture of the main components  $\text{CO}_2$ ,  $\text{CO}$ ,  $\text{H}_2\text{O}$ ,  $\text{H}_2$  and  $\text{N}_2$ ). The heterogeneous reactions take place between char, which is assumed to be consisting of only carbon and these gases and determine the further solid fuel conversion.

A part from the reaction with oxygen which is simply termed char combustion that produces  $\text{CO}$  and  $\text{CO}_2$ , all reactions of char with any gaseous reactant other than oxygen refer to char gasification. The latter takes place at rate much slower than the former one and consequently the gasification reactions have a longer residence time within the furnace.

The heterogeneous reactions are considered to be influenced by many factors including the total active surface area, the local gas reactant concentration, local temperature, pressure, char structure and composition and the overall scheme can be described in these basic processes: diffusion of mass and heat through the boundary layer surrounding the solid fuel particle, diffusion of mass and heat within the porous structure of fuel and reaction of gases with solid surfaces [105]. The surface burnout reaction is represented by equation (2.9).



where  $S_b$  is the stoichiometry and defined in terms of mass of oxidant per mass of char  $C(s)$ . Its value depends on whether the gaseous product is  $\text{CO}$  or  $\text{CO}_2$ . There are several global char combustion models available in literature. One of these models is the diffusion-limited surface reaction rate. It assumes the conditions of regime III mentioned in §2.5, where the chemical reactions are assumed to be fast. In this regime, the oxidant (oxygen) is consumed as soon as reaches the particle surface. At high temperatures, surface reactions are so fast and this means that the partial pressure at the particle surface is assumed zero. This model is based on the work done by Baum and Street [127]. It is based on the assumption that the surface reaction proceeds at a rate determined by the diffusion of gaseous oxidant (oxygen) to particle surface i.e. the rate of combustion only depends on the mass transfer in the vicinity of the char particle and this rate is computed by the following equation:

$$\bar{r}_{het} = \frac{dm_p}{dt} = -4\pi d_p D_{i,m} \frac{Y_{ox} T_g \rho_g}{S_b (T_p + T_g)} \quad (2.10)$$

where  $S_b$ ,  $D_{i,m}$ ,  $d_p$ ,  $Y_{ox}$ ,  $T_p$ ,  $T_g$  and  $\rho_g$  are the stoichiometry of equation (2.9), the diffusion coefficient for oxidant in the bulk, the particle diameter, the local mass fraction of oxidant in the bulk the particle temperature, the gas temperature and the gas density, respectively. In this model, it is assumed that the diameter does not change and the kinetic contribution to the surface reaction rate is ignored. Range of the validity of the diffusion limited approach can be extended to the conditions of regime II. It was suggested by Baum and Street [127] and Field [133] to use a diffusion rate coefficient and a reaction rate coefficient. Thus, the effective surface reaction rate includes the effects of both bulk diffusion and chemical reaction rates. Therefore, the so-called kinetics/diffusion limited surface reaction model was developed. In this model, char reactivity is limited by the minimum of kinetic rate and the oxidant boundary layer diffusion.

In the kinetics/diffusion model, the diffusion rate is expressed by the following equation [127]:

$$D_o = C_1 \frac{[(T_p + T_g)/2]^{0.75}}{d_p} \quad (2.11)$$

and the kinetic rate is determined by:

$$\mathcal{R} = A e^{-(E/R_u T_p)} \quad (2.12)$$

then, char combustion rate is:

$$\bar{r}_{het} = \frac{dm_p}{dt} = -A_p P_{ox} \frac{D_o \mathcal{R}}{D_o + \mathcal{R}} = -A_p \frac{\rho R_u T_g Y_{ox}}{M_{w,ox}} \left( \frac{D_o \mathcal{R}}{D_o + \mathcal{R}} \right) \quad (2.13)$$

where  $A_p$  ( $A_p = \pi d_p^2$ ),  $P_{ox}$ ,  $C_1$  and  $M_{w,ox}$  are the surface area of the coal particle, the partial pressure of oxidant species in the gas phase, the diffusion rate coefficient and the molecular weight of oxidant, respectively. The above mentioned models only consider boundary layer diffusion and ignore some important phenomena like char porosity, changes in pore structure and external surface area during char combustion [134]. Contrary to this, the model that accounts for pore diffusion is the intrinsic reaction model, which is based on the model of Smith [135]. It is similar to kinetics/diffusion limited rate model. In this model, the diffusion rate is computed by equation (2.11), but the chemical rate is describes the combined effect of intrinsic reactivity and pore diffusion and expressed as following:



$$\mathcal{R} = \eta \frac{V_p}{A_p} \rho_p A_g k_i \quad (2.14)$$

where  $\eta$  is the effectiveness factor (the ratio of the actual combustion rate to the rate if no pore diffusion resistance existed),  $V_p$  is the volume of the particle,  $\rho_p$  is the apparent density of the char,  $A_g$  is the specific internal surface area of the char particle and  $k_i$  is the intrinsic chemical reaction rate, which is of Arrhenius form:

$$k_i = A e^{-(E/R_u T_p)} \quad (2.15)$$

where the pre-exponential factor  $A$  and the activation energy  $E$  can be measured for each char.  $\eta$  is solved as a function of Thiele modulus as

$$\eta = \frac{3}{\varphi} (\varphi \coth \varphi - 1) \quad (2.16)$$

where  $\varphi$  is the Thiele modulus:

$$\varphi = \frac{d_p}{2} \left[ \frac{S_p \rho_p A_g k_i P_{ox}}{D_e \rho_{ox}} \right] \quad (2.17)$$

and  $\rho_{ox}$  stands for the density of oxidant in the gas phase and  $D_e$  is the effective diffusion coefficient in the particle pores (for more details one can refer to [135])

The other model of char oxidation is the multiple surface reactions model, which describes that the particle surface species can be depleted or produced by the stoichiometry of the particle surface reaction.

# 3 RANS simulations of methane combustion

Methane is one of the main species resulted from the devolatilization process when burning solid fuels and modelling its oxidation is not only important in gas turbines but in oil, gas, pulverized coal-fired boilers and furnaces as well. Therefore, this chapter has been dedicated to the investigation of the turbulent diffusion combustion of both pure methane and its dilution with nitrogen based on Reynolds Averaged Navier-Stokes (RANS) approach. The investigation has focused on evaluating the effect of various turbulence models on the accuracy of CFD simulations. The Navier-Stokes equations are solved with  $k-\epsilon$  turbulence closures. Since several phenomena such as mixing, turbulence, radiative heat transfer, chemical kinetics take place during combustion process, and in order to obtain reasonable results, a rational approach with appropriate sub-models should be used. The standard and realizable  $k-\epsilon$  turbulence models are modified and their effects on the combustion process are also investigated. Different reduced global reaction mechanisms of methane combustion have been used. The reaction mechanism by Westbrook and Dryer is optimized to see its effect as well. The turbulence-chemistry interaction is modelled using a finite-rate/eddy dissipation model FR/ED. This chapter presents the modelling approach and numerical results of methane combustion in an axi-symmetric chamber. The results are compared with experimental data available in literature.

## 3.1 Introduction

In terms of fluid mechanics, modelling of turbulent combustion is one of the most important and complicated subjects due to the complicated nature of turbulence-chemistry interaction. Turbulent flames involve a wide range of coupled problems such as the mixing between the reactants and, more generally, all transport phenomena (heat transfer, molecular diffusion, turbulent transport, etc.). To carefully describe these problems, the fluid mechanical properties of the combustion system must be well-known. Combustion requires both the fuel and the oxidizer to be mixed at a molecular level. The other important things that are involved in turbulent flames include the chemical reaction schemes as well as the heat transfer due to radiation.

Detailed description chemistry is necessary to estimate the consumption rate of fuel, formation of combustion products and pollutant species and give a deeper insight into reactive flow processes. Therefore, a good knowledge of the chemistry schemes (chemical reaction schemes) is definitely required to predict the combustion processes. Such a detailed chemistry can contain hundreds of chemical species and thousands of elementary reactions.

In combustion systems at high temperatures, radiative heat transfer becomes significant and for accurate simulations, it needs to be taken into account. There are two main categories in which turbulent combustion can be classified which are premixed and non-premixed combustion. In the former one, the fuel and the oxidizer are first mixed homogeneously and then the mixture enters the combustion chamber. This type of combustion is found in the spark-ignition engine where the fuel and the oxidizer are mixed at the molecular level for a long time and then the energy of the spark initiates the combustion flame at first by laminar and then by turbulent propagation.

In turbulent non-premixed combustion, the fuel and the oxidizer enter the combustion chamber individually and the combustion takes place simultaneously with the turbulent mixing process. This type of combustion, which is of the primary interest in this chapter, is employed in a wide array of practical applications such as gas turbines and oil, gas, pulverized coal-fired boilers and furnaces. The widespread use of non-premixed combustion is the major motivation for the numerous model approaches to their numerical simulation [136]. The rate of the reaction is often controlled by the mixing rate and the molecular diffusion of the reactants towards the reaction zone and because the diffusion transport is essential in the effective mixing of the reactants at the molecular level, the non-premixed combustion is also known as diffusion combustion.

The developments of simplified models play a significant role in the understanding of solutions of complex systems of governing equations. Therefore, a lot of successful models include their validations against results from experiment have been worked out. Many computational studies regarding diffusion combustion have been carried out and numerous combustion models have been developed and used for different applications. There are many reviews dealt with non-premixed combustion such as Bilger et al. [137], Bilger [138], Peters [139], Veynante and Vervisch [140].

One of the important aspects in the numerical simulations of combustion of fuels such as methane is the modelling of kinetic mechanisms. In reality, this phenomenon can

involve a large number of species and reactions. In CFD simulations, for each species in the reaction mechanism, one species conservation equation needs to be solved. Therefore, to decrease the computational costs, the level of description of combustion chemistry has to be reduced down to a level that a few numbers of species and reactions are included. Moreover, the addition of chemical species makes the turbulent reaction modelling more complicated since the chemical reaction rates depend non-linearly on the concentration of species [141]. Then, the reduced mechanisms are favourable.

In this context, the present simulations were intended to apply different simplified reaction mechanisms accompanied with different turbulence models to model the turbulent diffusion combustion of both methane and its dilution with nitrogen. The major work includes the comparison between the selected reaction mechanisms and the investigation of the effects of different turbulence models and how they affect the simulation results when they are modified.

The other important aspects are the kinetics and mixing time scales. The interaction between combustion chemistry and turbulent mixing is important because the structure of non-premixed flames is mainly governed by the coupling between both mixing and chemical reactions. The chemistry could be considered infinitely fast when considering the chemical reaction characteristic time to be much smaller than the flow time scale, and correspondingly the Damköhler number is very high. The Damköhler number ( $Da$ ) is the ratio of chemical reaction and fluid dynamic mixing.

$$Da = \frac{\tau_t}{\tau_c} \quad (3.1)$$

where  $\tau_t$  is the turbulent time scale and  $\tau_c$  is the chemical time scale.

In this case, a simple finite rate model (FRM) is less unrealistic and otherwise to model the combustion, approaches such as eddy breakup model, also referred to as eddy-dissipation model (EDM) [142] in FLUENT, or flamelet models (FLM) could be used. However, the EDM model does not take into account the real gas effects, e.g. the exclusion of reactant concentration in the reaction rate calculation. The FLM assumes that the local chemical structure of a flame is independent of the physical complexity of the surrounding flow. Therefore, the flame structure resembles a laminar like structure. In this model, diffusion processes and chemistry are coupled. In the case of laminar flamelet model, all flame properties in the flame at any point in the flow are described

in terms of the mixture fraction and the strain rate (or scalar dissipation rate). This reduction of the complex chemistry to two variables allows the flamelet calculations to be pre-processed, and stored in look-up tables. Therefore, computational costs are reduced considerably. By using this model the calculation of a turbulent reactive flow with a detailed chemical kinetic can be achieved by solving only two additional transport equations for the mean mixture fraction and the mixture variance.

Accounting for chemistry on turbulent diffusion flames can be also described by more elaborate models such as finite rate/eddy dissipation model (FR/ED) and eddy dissipation concept model (EDC) [143] are used. In these two models, the chemical and mixing times are of the same order, thus, the mixing and chemical reactions are influenced by each other.

## 3.2 Governing equations

With regards to a homogeneous reacting flow, the change in pressure, temperature, density, velocity of the flow and concentration of species is as a result of fluid flow, molecular transport, radiation, and chemical reactions as mentioned in § 3.1.

### 3.2.1 The Navier-Stokes (N-S) equations

In reacting flows, properties such as mass, momentum and energy are conserved and as a result of this the mathematical modelling is basically based on a set of governing equations of the conservation of mass, momentum, energy, and chemical transport and reactions. These equations can be derived by considering a control volume as a system. Such an approach is known as control volume approach.

The law of mass conservation results in the mass continuity equation as shown below:

$$\frac{\partial \rho}{\partial t} + \frac{\partial}{\partial x_j}(\rho u_j) = 0 \quad (3.2)$$

where  $x_j$  ( $j = x, y, z$ ) are the Cartesian coordinates,  $u_j$  or  $(u_x, u_y, u_z)$  are the Cartesian components of the velocity vector  $\vec{u}$  [m/s],  $t$  [s] is the time coordinate and  $\rho$  [kg/m<sup>3</sup>] is the mixture density.

The law of momentum conservation leads to the following equation:

$$\frac{\partial(\rho u_i)}{\partial t} + \frac{\partial}{\partial x_j}(\rho u_i u_j) = -\frac{\partial}{\partial x_i} p + \frac{\partial}{\partial x_j}(\tau_{ij}) + \rho g_i \quad (3.3)$$

where  $p$  [Pa] is the static pressure,  $\tau_{ij}$  [N/m<sup>2</sup>] denotes the viscous stress tensor and  $\rho g_i$  [N/m<sup>3</sup>] is the gravitational body force. The body force can often be neglected when modelling chemical reactions. The viscous stress tensor can be expressed in terms of molecular viscosity,  $\mu$  [kg/m.s], and local velocity gradient as

$$\tau_{ij} = \mu \left( \frac{\partial}{\partial x_j} u_i + \frac{\partial}{\partial x_i} u_j - \frac{2}{3} \frac{\partial}{\partial x_k} u_k \delta_{i,j} \right) \quad (3.4)$$

where  $\delta_{i,j}$  is the kronecker delta i.e., ( $\delta_{i,j} = 1$  if  $i = j$  and  $\delta_{i,j} = 0$  otherwise).

### 3.2.2 Species mass conservation equation

In the case of fluid mixture and in addition to the Navier-Stokes equations, the species mass conservation equation is also needed to describe the chemically reacting flow.

$$\frac{\partial}{\partial t} (\rho Y_i) + \frac{\partial}{\partial x_j} (\rho u_j Y_i) = \frac{\partial}{\partial x_j} (J_{i,j}) + R_i^{hom} \quad i = 1, \dots, N_g \quad (3.5)$$

The two terms on left hand represent the rate of change of mass of species  $i$  and the net rate of decrease of mass of species  $i$  due to convection, respectively. The other two terms on right hand are the net rate of increase of mass of species  $i$  due to diffusion and the net rate of increase of mass of species  $i$  due to source.

In the above equation,  $Y_i$  is mass fraction of species  $i$  in the mixture,  $N_g$  is the number of species in the gas phase,  $R_i^{hom}$  [kg/m<sup>3</sup>.s] is the net rate of production of species  $i$  due to homogeneous chemical reactions and  $J_{i,j}$  [kg/m<sup>2</sup>.s] denotes the molecular mass flux of species  $i$ . Generally, it has three components which are known as mass diffusion, pressure diffusion and thermal diffusion [144]. For most combustion processes, the last two ones may be neglected [141]. Using the Fick's law the diffusion flux is given by

$$J_{i,j} = -\rho D_i \frac{\partial Y_i}{\partial x_j} \quad (3.6)$$

The description of mass flux is further simplified by introducing the non-dimensional Schmidt number.

$$Sc = -\frac{\mu}{\rho D_i} \quad (3.7)$$

then

$$J_{i,j} = -\frac{\mu}{Sc} \frac{\partial Y_i}{\partial x_j} \quad (3.8)$$

$D_i$  [m<sup>2</sup>/s] is the diffusion coefficient for species  $i$  and it will be different for different species. In this work, a simplification is made that all species have the same diffusion coefficient.

### 3.2.3 Energy conservation equation

The knowledge of temperature,  $T$ , is required for the evaluation of density and chemical reaction rate. It can be obtained by solving the energy equation which can take several forms having one of these, static temperature, static enthalpy and stagnation enthalpy or internal energy, as the principle variable. The governing equation can be written in the following form:

$$\frac{\partial}{\partial t}(\rho e) + \frac{\partial u_j}{\partial x_j}(\rho e + p) = -\frac{\partial}{\partial x_j}q_j + Q_r \quad (3.9)$$

where,  $q_j$  is the energy flux,  $Q_r$  is the internal production rate for thermal energy, for example due to radiation and  $e$  is the specific total energy and is given by

$$h = e + \frac{p}{\rho} \quad (3.10)$$

where  $h$  is the enthalpy of the mixture.

then equation (3.9) becomes as following:

$$\frac{\partial}{\partial t}(\rho h) + \frac{\partial u_j}{\partial x_j}(\rho h) = \frac{\partial p}{\partial t} - \frac{\partial}{\partial x_j}q_j + Q_r \quad (3.11)$$

The enthalpy in equation (3.10) is related to the temperature by its definition in terms of species enthalpy,

$$h = \sum_i^{N_g} Y_i h_i \quad (3.12)$$

where  $h_i$  is the absolute internal enthalpy for species  $i$  and for an ideal gas the enthalpy is an unique function of temperature. The enthalpy at given temperature is calculated from approximated by

$$h_i(T) = h_i^\circ + \int_{T^\circ}^T c_{p,i}(T) dT \quad (3.13)$$

where  $h_i^\circ$  is the heat of formation of species  $i$  at a reference temperature  $T^\circ$  (298.15 K) and  $c_{p,i}(T)$  is the specific heat at constant pressure of species  $i$ .

$$c_{p,i} = \left(\frac{\partial h}{\partial T}\right)_p \quad (3.14)$$

The specific heat for the mixture  $c_p$  at constant pressure is

$$c_p = \sum_i^{N_g} Y_i c_{p,i} \quad (3.15)$$

The energy flux  $q_j$  is divided into three different parts [141].

$$q_j = q_j^c + q_j^d + q_j^D \quad (3.16)$$

where  $q_j^c$  denotes energy flux due to conduction,  $q_j^d$  denotes energy flux due to species diffusion and  $q_j^D$  denotes energy flux caused by concentration gradients (Dofour effect). The latter is usually much smaller than the other two components [141], and has been neglected in this work.

The energy flux due to conduction is expressed by Fourier's law as following:

$$q_j^c = -\lambda \frac{\partial T}{\partial x_j} \quad (3.17)$$

with  $\lambda$  being the thermal conductivity of the mixture. As a function of enthalpy, by combining equations (3.12), (3.13) and (3.14) the energy flux due to conduction can be written as

$$q_j^c = \frac{\lambda}{c_p} \left( \sum_i^{N_g} h_i \frac{\partial Y_i}{\partial x_j} - \frac{\partial h}{\partial x_j} \right) \quad (3.18)$$

As indicated by the name, energy flux due to diffusion is caused by the diffusion of species with different enthalpy and is given by

$$q_j^d = \sum_i^{N_g} h_i J_{i,j} \quad (3.19)$$

$$q_j^d = -\frac{\mu}{sc} \sum_i^{N_g} h_i \frac{\partial Y_i}{\partial x_j} \quad (3.20)$$

then, the energy flux can be written as

$$q_j = -\lambda \frac{\partial T}{\partial x_j} - \frac{\mu}{sc} \sum_i^{N_g} h_i \frac{\partial Y_i}{\partial x_j} \quad (3.21)$$

Similar to the introduction of Schmidt number in mass flux, the non-dimensional Prandtl number  $Pr$  is introduced to simplify the description of energy flux

$$Pr = \frac{\mu c_p}{\lambda} \quad (3.22)$$

The Lewis number is the ratio of Schmidt and Prandtl numbers



$$Le = \frac{Sc}{Pr} \quad (3.23)$$

then, the total energy flux becomes,

$$q_j = \frac{\mu}{Pr} \left[ -\frac{\partial h}{\partial x_j} + \left(1 - \frac{1}{Le}\right) \sum_i^{N_g} h_i \frac{\partial Y_i}{\partial x_j} \right] \quad (3.24)$$

The Lewis number for most gases is close to unity [145], and by assuming  $Le = 1$ , equation (3.24) is further simplified. Equation (3.10) is further simplified by assuming that  $Le = 1$  to the following equation:

$$\frac{\partial}{\partial t} (\rho h) + \frac{\partial u_j}{\partial x_j} (\rho h) = \frac{\partial p}{\partial t} - \frac{\partial}{\partial x_j} \frac{\mu}{Pr} \left( -\frac{\partial h}{\partial x_j} \right) + Q_r \quad (3.25)$$

### 3.2.4 The equation of state

The mixture of reactants and products is treated as ideal gas and therefore the equation of state for density is needed to make the system of governing equations close. For the operating conditions of flames studied in this work the gas mixture can be assumed to behave as an ideal gas mixture and with the equation of state [146] the pressure  $P$  is given by

$$p = \rho R_u T \sum_i^{N_g} \frac{Y_i}{M_{w,i}} \quad (3.26)$$

Alternatively

$$p = \rho R_u \frac{T}{\sum_i^{N_g} X_i M_{w,i}} \quad (3.27)$$

where  $M_{w,i}$  and  $X_i$  are the molecular weight and mole fraction of species  $i$ , respectively,  $T$  is the mixture temperature in [K] and  $R_u$  is the universal gas constant ( $R_u = 8.1314$  KJ/kmol.K).

## 3.3 Turbulence models

In turbulent flows, all transport processes are enhanced by turbulent fluctuations but in laminar flows most of the transport processes take place on molecular level. The interaction of chemistry and turbulence leads to turbulent combustion. When the interaction of a flame and a turbulent flow occurs, the turbulence is modified by the combustion due to the strong flow accelerations through the flame front induced by the release of heat and due to the large kinematic viscosity changes associated with the

temperature changes. There are many practical devices in which turbulent combustion occurs like gas turbines, furnaces, boilers, internal combustion engines and rocket engines. In these devices, turbulence causes large fluctuations of mass fractions, temperature and density and moreover extinction can occur when turbulence effects are strong. Turbulent flows are characterized by the presence of a wide range of time and scales at which motion and fluctuations take place. The formation of turbulent eddies is present in a wide range of sizes, ranging from largest scales to small eddies (Kolmogorov scales), and transport most of the turbulent kinetic energy. The turbulence scale in comparison to laminar flame thickness characterizes turbulent flames and therefore the interaction of chemistry and turbulence plays an important role in turbulent combustion. The large scale eddies, which are responsible for the effective mixing, are exposed to the process of vortex stretching. They are significant as they carry most of the energy. In the process of vortex stretching, the motion in large scales is translated into the smaller eddies. In this way, the energy is passed on from large eddies to smaller and smaller eddies until reaching the smallest eddies, where the viscous effects are strong and energy is dissipated into heat through viscous dissipation. Such a process is known as energy cascade. In DNS simulations, as mentioned in §1.1, all of the motions contained in the flow are resolved. In order to account for the full nonlinear multi-scale effect of turbulence in a combustion process, the governing equations must be solved resolving the Kolmogorov scale eddies, which makes such simulations computationally expensive. Thus, DNS is restricted to low-Reynolds number turbulent flows and simple geometries. A review work on the current status of DNS applications to non-premixed combustion is done by Vervisch and Poinso [147].

Instead of directly solving the Navier-Stokes equations for turbulent flows, LES and time-averaging approaches are used. The former approach (see §1.1) is still expensive in terms of computational costs, but when compared to DNS, they are much more reasonable. Comprehensive reviews on LES of turbulent flows can be found in literature such as Moin [148] and Lesieur and Metais [149]. The latter one is solving the RANS equations (Reynolds-Averaged Navier-Stokes). These equations describe the behaviour of the time-averaged flow quantities instead of the exact instantaneous values. In this approach, RANS equations arise when the Reynolds decomposition (Equation (3.28)) is implemented into the Navier-Stokes equations. Reynolds decomposition refers to the separation of the flow variable  $\phi$  into two components: mean component,  $\bar{\phi}$ , and fluctuating component,  $\phi'$ .

$$\phi = \bar{\phi} + \phi' \quad (3.28)$$

For the velocity components:

$$u_i = \bar{u}_i + u'_i \quad (3.29)$$

The same is applied for pressure and other scalar quantities.

After applying the Favre-time-averaging procedure and neglecting the gravitational body force RANS equations are as follows:

$$\frac{\partial \rho}{\partial t} + \frac{\partial}{\partial x_j} (\rho u_j) + \frac{\partial}{\partial x_j} (\rho u_i) = 0 \quad (3.30)$$

$$\begin{aligned} \frac{\partial}{\partial t} (\rho u_i) + \frac{\partial}{\partial x_j} (\rho u_i u_j) \\ = -\frac{\partial p}{\partial x_i} + \frac{\partial}{\partial x_j} \left[ \mu \left( \frac{\partial}{\partial x_j} u_i + \frac{\partial}{\partial x_i} u_j - \frac{2}{3} \frac{\partial}{\partial x_k} u_k \delta_{i,j} \right) - \rho \overline{u'_i u'_j} \right] \end{aligned} \quad (3.31)$$

Additional unknown Reynolds stress term  $-\rho \overline{u'_i u'_j}$  [N/m<sup>2</sup>] is introduced and in order to close equation (3.31) this term should be modelled. A number of turbulent models have been proposed and among them are the two-equation turbulence models [150-152], but the most popular models presently are the  $k$ - $\epsilon$  model [153] and the  $k$ - $\omega$  model [154]. They have proven to give good results for different turbulent flow regimes. These turbulence models are commonly used with gas and coal combustion models for the simulation. In the present work, the  $k$ - $\epsilon$  models have been used. There are three  $k$ - $\epsilon$  models available in FLUENT, which are the standard, RNG (renormalization-group) [155], and realizable [156] models. They are based on solving two additional transport equations. A common method employs the Boussinesq hypothesis [157] is used in these turbulence models.

$$-\rho \overline{u'_i u'_j} = \mu_t \left( \frac{\partial}{\partial x_j} u_i + \frac{\partial}{\partial x_i} u_j \right) - \frac{2}{3} \delta_{i,j} \left( \mu_t \frac{\partial}{\partial x_k} u_k + \mu_B \right) \quad (3.32)$$

where  $\mu_t$  is the turbulent viscosity and  $\mu_B$  is called the bulk viscosity and also known as volume viscosity, which expresses the resistance of the fluid against the rapid changes in volume. It is identically zero for low density monotonic gases and it is not too important.

In the case of  $k$ - $\epsilon$ , two additional transport equations, for the turbulence kinetic energy  $k$  and the turbulence dissipation rate  $\epsilon$ , are solved, and  $\mu_t$  is computed as a function of  $k$  and  $\epsilon$ .

### 3.3.1 Transport equations for the standard $k$ - $\epsilon$ model

This model is a two-equation turbulence model proposed by Launder and Spalding [153]. It is a high-Reynolds number model. The model transport equations for  $k$  and  $\epsilon$  are given in equation (3.33) and (3.34) as given by FLUENT [158]. The turbulence kinetic energy is obtained from the following transport equation:

$$\frac{\partial}{\partial t}(\rho k) + \frac{\partial}{\partial x_i}(\rho k u_i) = \frac{\partial}{\partial x_j} \left[ \left( \mu + \frac{\mu_t}{\sigma_k} \right) \frac{\partial k}{\partial x_j} \right] + G_k + G_b - \rho \epsilon - Y_M + S_k \quad (3.33)$$

And the rate of dissipation is computed from the following equation:

$$\frac{\partial}{\partial t}(\rho \epsilon) + \frac{\partial}{\partial x_i}(\rho \epsilon u_i) = \frac{\partial}{\partial x_j} \left[ \left( \mu + \frac{\mu_t}{\sigma_\epsilon} \right) \frac{\partial \epsilon}{\partial x_j} \right] + C_{1\epsilon} \frac{\epsilon}{k} (G_k + C_{3\epsilon} G_b) - C_{2\epsilon} \frac{\epsilon^2}{k} + S_\epsilon \quad (3.34)$$

where  $\sigma_k$  and  $\sigma_\epsilon$  are the turbulent Prandtl numbers for  $k$  and  $\epsilon$  respectively,  $G_k$  is the generation of turbulent kinetic energy due to the mean velocity gradients (the production of turbulence kinetic energy),  $G_b$  is the generation of turbulence kinetic energy due to buoyancy, which is not considered in this study,  $Y_M$  is the dissipation rate due to fluctuating dilatation in compressible flow and  $C_{1\epsilon}$ ,  $C_{2\epsilon}$  and  $C_{3\epsilon}$  are model constants. The default values given by FLUENT [158] have been used for the model constants. To evaluate the turbulent viscosity  $\mu_t$ , equation (3.35) is used.

$$\mu_t = C_\mu \rho k^2 / \epsilon \quad (3.35)$$

where  $C_\mu$  is a constant. The default values of model constants are as following:

$$C_{1\epsilon} = 1.44, C_{2\epsilon} = 1.92, C_\mu = 0.09, \sigma_k = 1.0, \sigma_\epsilon = 1.3 \text{ and } Pr = 0.7$$

### 3.3.2 Transport equations for the RNG $k$ - $\epsilon$ model

This model has a similar form to the standard  $k$ - $\epsilon$  model. It was developed by Yaghoti and Orszag [155] in response to the empirical nature of the standard  $k$ - $\epsilon$  model. Rather than being based on observed fluid behaviour, this two-equation model was derived from the instantaneous Navier-Stokes equations using a statistical technique called renormalization group theory [159]. It takes into account low-Reynolds number effect.

$$\frac{\partial}{\partial t}(\rho k) + \frac{\partial}{\partial x_i}(\rho k u_i) = \frac{\partial}{\partial x_j} \left[ \alpha_k \left( \mu + \frac{\mu_t}{\sigma_k} \right) \frac{\partial k}{\partial x_j} \right] + G_k + G_b - \rho \epsilon - Y_M + S_k \quad (3.36)$$

$$\begin{aligned} \frac{\partial}{\partial t}(\rho\epsilon) + \frac{\partial}{\partial x_i}(\rho\epsilon u_i) \\ = \frac{\partial}{\partial x_j} \left[ \alpha_\epsilon \left( \mu + \frac{\mu_t}{\sigma_\epsilon} \right) \frac{\partial \epsilon}{\partial x_j} \right] + C_{1\epsilon} \frac{\epsilon}{k} (G_k + C_{3\epsilon} G_b) - C_{2\epsilon} \frac{\epsilon^2}{k} + S_\epsilon \end{aligned} \quad (3.37)$$

The quantities  $\alpha_k$  and  $\alpha_\epsilon$  are the inverse effective Prandtl numbers for  $k$  and  $\epsilon$ . The model constants in equation (3.37) have values analytically by the RNG theory, used by default in FLUENT [158], which are

$$C_{1\epsilon} = 1.42, \quad C_{2\epsilon} = 1.68$$

### 3.3.3 Transport equations for the realizable $k$ - $\epsilon$ model

The realizable  $k$ - $\epsilon$  model is an improvement on the standard  $k$ - $\epsilon$  model with respect to prediction of jet spreading rate according to FLUENT [158]. The transport equations for  $k$  and  $\epsilon$  in the realizable  $k$ - $\epsilon$  model are

$$\frac{\partial}{\partial t}(\rho k) + \frac{\partial}{\partial x_j}(\rho k u_j) = \frac{\partial}{\partial x_j} \left[ \left( \mu + \frac{\mu_t}{\sigma_k} \right) \frac{\partial k}{\partial x_j} \right] + G_k + G_b - \rho\epsilon - Y_M + S_k \quad (3.38)$$

and

$$\begin{aligned} \frac{\partial}{\partial t}(\rho\epsilon) + \frac{\partial}{\partial x_j}(\rho\epsilon u_j) = \frac{\partial}{\partial x_j} \left[ \left( \mu + \frac{\mu_t}{\sigma_\epsilon} \right) \frac{\partial \epsilon}{\partial x_j} \right] + \rho C_{1\epsilon} S_\epsilon - \rho C_{2\epsilon} \frac{\epsilon^2}{k + \sqrt{v\epsilon}} + \\ C_{1\epsilon} \frac{\epsilon}{k} C_{3\epsilon} G_b + S_\epsilon \end{aligned} \quad (3.39)$$

where

$$C_1 = \max \left[ 0.43, \frac{\eta}{\eta + 5} \right], \quad \eta = S \frac{k}{\epsilon}, \quad S = \sqrt{2S_{ij}S_{ij}}$$

In these equations,  $C_2$  and  $C_{1\epsilon}$  are constants and  $S_{ij}$  is the mean strain rate. The model constants are

$$C_{1\epsilon} = 1.44, \quad C_2 = 1.90, \quad \sigma_k = 1.0 \quad \text{and} \quad \sigma_\epsilon = 1.2$$

The governing equations as well as the equations of the turbulent kinetic energy and its rate of dissipation at steady state for incompressible flow in a 2d-axisymmetric coordinate system can be written in the following generalized form:

$$\frac{\partial}{\partial x} \left( \rho u \phi - \Gamma_\phi \frac{\partial \phi}{\partial x} \right) + \frac{1}{r} \frac{\partial}{\partial r} \left( r \rho v \phi - r \Gamma_\phi \frac{\partial \phi}{\partial r} \right) = S_\phi \quad (3.40)$$

where  $\rho$ ,  $u$ ,  $v$ ,  $\phi$ ,  $\Gamma_\phi$  and  $S_\phi$  are the density, velocity in  $x$  direction, velocity in  $r$  direction, flow property, diffusion coefficient of the flow property and source term of flow property on a volumetric basis, respectively.

Depending on  $\phi$ , equation (3.40) represents mass ( $m$ ), velocity components ( $u, v$ ), enthalpy ( $h$ ) and a range of species mass fraction ( $Y_i$ ). The variable  $\phi$  can also represent the turbulent scalars which are the turbulent kinetic energy ( $k$ ) and the rate of dissipation of this energy ( $\epsilon$ ) as summarized in Table 3.1. This table also shows the values for ( $\sigma_\phi$ ) and the source terms as well.

Table 3.1: Source terms.

Equation	$\phi$	$\Gamma_\phi$	$\sigma_\phi$	$S_\phi$
Continuity	1	0	1	0
Axial momentum	$u$	$\frac{\mu_e}{\sigma_\phi}$	1	$\frac{\partial}{\partial x} \left( \mu_e \frac{\partial u}{\partial x} \right) + \frac{1}{r} \frac{\partial}{\partial r} \left( r \mu_e \frac{\partial v}{\partial r} \right) - \frac{\partial P}{\partial r}$
Radial momentum	$v$	$\frac{\mu_e}{\sigma_\phi}$	1	$\frac{\partial}{\partial x} \left( \mu_e \frac{\partial u}{\partial x} \right) + \frac{1}{r} \frac{\partial}{\partial r} \left( r \mu_e \frac{\partial v}{\partial r} \right) - \frac{2\mu_e v}{r^2} - \frac{\partial P}{\partial r}$
Energy	$h$	$\frac{\lambda}{C_p} + \frac{\mu_t}{\sigma_\phi}$	0.9	$Q_r$
Species	$Y_i$	$\rho D_i + \frac{\mu_t}{\sigma_\phi}$	0.7	$R_i^{hom}$
Turbulent energy	$k$	$\mu + \frac{\mu_t}{\sigma_\phi}$	1	$G_k^1 - \rho\epsilon$
Turbulent dissipation rate	$\epsilon$	$\mu + \frac{\mu_t}{\sigma_\phi}$	1.3	$\frac{\epsilon}{k} (C_{\epsilon 1} G_k - C_{\epsilon 2} \rho\epsilon)$
Constants <sup>1</sup>	$C_\mu = 0.09, C_{\epsilon 1} = 1.44, C_{\epsilon 2} = 1.92$			
Other terms	$G_k^2 = \mu_t \left\{ 2 \left[ \left( \frac{\partial u}{\partial x} \right)^2 + \left( \frac{\partial v}{\partial r} \right)^2 \right] + \left( \frac{\partial u}{\partial r} + \frac{\partial v}{\partial x} \right)^2 \right\}$			
	$\mu_e = \mu + \mu_t$			
	$\mu_t = C_\mu \rho k^2 / \epsilon$			

where  $\mu$  and  $\mu_t$  are the laminar and turbulent viscosities, respectively.

<sup>1</sup> Constants for standard  $k$ - $\epsilon$  turbulence model, <sup>2</sup>  $G_k$  is the production term.

### 3.4 Thermal radiation

In most combustion systems, thermal radiation may have a large influence on the combustion process. By radiation energy will be transported from the high temperature gas mixture to its cooler surroundings and this transfer will result in lower combustion temperature. The thermal radiative heat flux  $Q_r$  from a blackbody to isothermal surroundings is given as

$$Q_r = s_b(T^4 - T_{surr}^4) \quad (3.41)$$

where  $s_b = 5.67 \times 10^{-8}$  [W/m<sup>2</sup>.K<sup>4</sup>] is the Stefan-Boltzmann constant and  $T_{surr}$  [K] is surroundings temperature. The radiative flux is proportional to  $T^4$  and therefore it becomes significant compared to the heat transfer due to convection or conduction. It depends on the hot combustion products, mainly carbon dioxide CO<sub>2</sub> and water vapour H<sub>2</sub>O, which absorb and emit a significant amount of radiation in the thermal spectrum. They show strong absorption/emissions in the infrared spectrum. In contrast, diatomic gases N<sub>2</sub> and O<sub>2</sub> have no significant absorption bands. Thermal radiation propagation is described by the radiative transport equation (RTE). The accuracy in describing radiative heat transfer is crucial in simulations of turbulent combustion systems and the exact solution of the RTE is extremely costly. Therefore, to obtain an approximation, there are various radiation models are used to simulate radiation heat transfer such as P-1 [160, 161], discrete transfer [162], discrete ordinates [163, 164] and rosseland [161] radiation models. In this study, P-1 radiation model (spherical harmonic method) was employed. This model is a first order approximation to the RTE. The radiation intensity is expressed by an orthogonal series of spherical harmonics. Therefore, it is mathematically simple and its implementation is easy. Additionally, it is computationally robust.

The equation of balance of radiative energy transfer in a specified direction  $\vec{s}$  through a small differential volume for an absorbing, emitting, and scattering medium can be written as

$$\frac{dI(\vec{r}, \vec{s})}{ds} + (a + \sigma_s)I(\vec{r}, \vec{s}) = an^2 \frac{s_b T^4}{\pi} + \frac{\sigma_s}{4\pi} \int_0^{4\pi} I(\vec{r}, \vec{s}') \Phi(\vec{s}, \vec{s}') d\Omega \quad (3.42)$$

where  $I$  [W/m<sup>2</sup>.sr] is the radiative intensity,  $a$  [m<sup>-1</sup>] and  $\sigma_s$  [m<sup>-1</sup>] are the absorbing and scattering coefficients respectively,  $n$  is the refractive index, which is important when considering radiation in semi-transport media,  $\Omega$  is the solid angle,  $\vec{s}$  and  $\vec{s}'$  are the incoming and outgoing radiation direction vectors,  $\vec{r}$  is the position vector and  $\Phi$  is the scattering phase function. In the above equation the term  $\frac{s_b T^4}{\pi}$  represents the blackbody radiative intensity at the temperature of the medium  $T$ .

P-1 model is based on the expansion of radiation intensity  $I$  into an orthogonal series of spherical harmonics. The radiation flux is calculated using the following equation:

$$Q_r = -\frac{1}{3(a+\sigma_s)-c\sigma_s} \nabla G \quad (3.43)$$

where  $C$  is the linear-anisotropic phase function coefficient and  $G$  is the incident radiation. By introducing the parameter  $\Gamma = 1/(3(a + \sigma_s) - C\sigma_s)$ , the above equation is simplified to

$$Q_r = -\Gamma \nabla G \quad (3.44)$$

The transport equation for  $G$  is given by

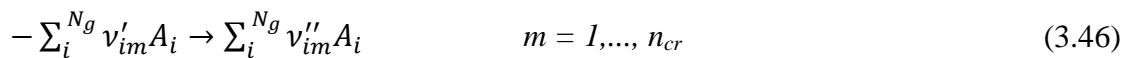
$$-\nabla \cdot Q = aG - 4as_b T^4 \quad (3.45)$$

## 3.5 Chemistry modelling

### 3.5.1 Chemical kinetics

In modelling gas phase, the source term  $R_i^{hom}$  [ $\text{kg}/\text{m}^3 \text{ s}$ ], which is the net rate of production of species  $i$  due to homogeneous chemical reactions, is found by appropriate reaction mechanism. Mostly, the chemical reactions occur on time scales comparable with that of the flow and the molecular transport processes. In this case, information about the rate of chemical reactions is needed. However, if one can assume that the chemical reactions are fast in comparison with the other processes like flow, diffusion and heat conduction, then, thermodynamics alone allow the description of the system locally.

In a general case, for the gas phase that consist of number of species  $N_g$  and number of chemical reactions  $n_{cr}$  the chemical reactions can be written in the following form



where  $A_i$  is the specification of species  $i$  and  $\nu'_{im}$  and  $\nu''_{im}$  are the stoichiometric coefficients of the reactants or products of species  $i$  in reaction  $m$ . The chemical production rate for species  $i$  can be expressed as

$$R_{i,m} = k_m (\nu''_{im} - \nu'_{im}) \prod_{i=1}^{N_g} C_i^{a'_{im}} \quad (3.47)$$

where  $C_i$  is species concentration [ $\text{kmol}/\text{m}^3$ ] and  $a'_{im}$  is the reaction order with respect to the species  $i$ . The reaction orders of elementary reactions are always integers and equal the molecularity of the reaction, but those of global reactions are not necessarily



integer because the global reactions can have complex rate laws. The rate coefficient of reaction  $m$  is  $k_m$  and is calculated from the following modified Arrhenius expression:

$$k_m = A_m T^{\beta_m} e^{-E_m/RT} \quad (3.48)$$

where  $A_m$  (units vary) is the pre-exponential factor,  $\beta_m$  is temperature exponent and  $E_m$  [J/kmol] is the activation energy.

In complex chemical schemes involving  $n_{cr}$  reactions the total rate of production of a certain species  $i$  is the sum of individual rates of each reaction producing the species  $i$ , which is given by

$$R_i = \sum_{m=1}^{n_{cr}} R_{i,m} \quad (3.49)$$

The rate is used as a source term in equation (3.5), which has the units [kg/m<sup>3</sup>.s]. To convert to required units, we multiply  $R_{i,m}$ , which is in [kmol/m<sup>3</sup>.s] by the molecular weight  $M_{w,i}$ . The net rate of production of species  $i$  due to homogeneous chemical reactions, is expressed by

$$R_i^{hom} = M_{w,i} R_i \quad (3.50)$$

### 3.5.2 Reaction mechanism

The oxidation of methane is widely dealt with in combustion modelling topic. Combustion occurs through a reaction mechanism which includes a number of elementary reactions that together lead to the overall reaction. Detailed mechanisms for the combustion of methane can include thousands of elementary reactions as discussed by Turns [90]. In general, detailed mechanisms are not applicable to CFD simulations because of the computation time involved to solve the large system of differential equations associated with such mechanisms when reaction kinetics are included. Therefore, to save time required for simulations, simplified combustion mechanisms are used.

Various chemical kinetic mechanisms reported in the literature are used to study methane–air diffusive flames. Simplified or reduced global mechanisms such as the two-step mechanism proposed by Westbrook and Dryer (WD) [165] and the 4-step mechanism by Jones and Lindstedt (JL) [166], which are multi-step reaction mechanisms, are often used in combustion modelling of hydrocarbons. Another reduced mechanism can be used in modelling methane is the 5-step mechanism

developed by Nicol et al. [167]. The other types of mechanisms include the detailed and the skeletal mechanisms. Many detailed mechanisms (full mechanisms) were developed such as Glarborg *et al.* [168], Miller and Bowman [169], C1/C2 mechanism of Warnatz and Maas [170] and the standard GRI-Mech. releases 1.2, 2.11 [171] and v.3.0 [172]. The skeletal mechanisms include Kazakov and Frenklach [173], Petersen and Hanson [174], Glarborg et al [175], Yungster and Rabinowitz [176], Li and Williams [177], Peter et al. [178] and Li and Williams[179]. There is a difference between all these mechanisms with respect to number of species and reactions with the full mechanisms have the large number.

Four reaction mechanisms are used in this study as shown in Table 3.2. They include a one-step reaction mechanism [180], the two-step reaction mechanism of Westbrook-Dryer [165] which is available as default in FLUENT. Another two-step mechanism [181] and the five-step mechanism developed by Nicol et al. [167] were selected. The rate expressions of these mechanisms are shown in Table 3.2. It is worth noting that the units for the pre-exponential parameter  $A_m$  vary depending on the reaction order and some of the values in Table 3.2 are given in the units (cm, cal, s and mol) and must be converted to SI units system, which is employed by FLUENT. The finite-rate/eddy-dissipation model (FR/ED) is employed to model turbulence/chemistry interaction. This model calculates both the Arrhenius and eddy-dissipation reaction rates. The later one is calculated according to the EDM, which is based on the work of Magnussen and Hjertager [142]. The reactions included in the mechanisms are:



Table 3.2: Reaction kinetics.

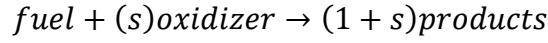
Reaction	$A_m$	$\beta_m$	$E_m$	Reaction order
Mechanism one (M-I): Two-step; units in (cm, cal, s and mol) [181].				
(r-2)	$2 \times 10^{15}$	0	$1.464 \times 10^8$	$[CH_4]^{0.9}[O_2]^{1.1}$
(r-3)	$2 \times 10^9$	0	$1.2 \times 10^4$	$[CO][O_2]^{0.5}$
(r-4)	$8.11 \times 10^{10}$	0	$7.72 \times 10^4$	$[CO_2]$
Mechanism two (M-II): Two-step (Westbrook-Dryer); units in (m, J, s, kmol) [165].				
(r-2)	$5.012 \times 10^{11}$	0	$2 \times 10^8$	$[CH_4]^{0.7}[O_2]^{0.8}$
(r-3)	$2.239 \times 10^{12}$	0	$1.7 \times 10^8$	$[CO]^{0.5}[O_2]^{0.25}[H_2O]^{0.5}$
Mechanism three (M-III): One-step; units in (cm, cal, s and mol) [180].				
(r-1)	$1.35 \times 10^{14}$	0	$1.26 \times 10^8$	$[CH_4][O_2]^2$
Mechanism four (M-IV): Five-step; units in (m, J, s, kmol) [167].				
(r-2)	$1.66 \times 10^{15}$		$1.7163 \times 10^8$	$[CH_4]^{1.46}[O_2]^{0.5217}$
(r-3)	$7.98 \times 10^{14}$		$9.655 \times 10^7$	$[CO]^{1.6904}[O_2]^{1.57}$
(r-4)	$2.233 \times 10^{14}$		$5.1805 \times 10^8$	$[CO_2]$
(r-5)	$8.831 \times 10^{23}$		$4.44 \times 10^8$	$[N_2]^{0.7211}[O_2]^{4.0111}$
(r-6)	$9.268 \times 10^{14}$	- 0.5	$5.73 \times 10^8$	$[N_2][O_2]^{0.5}$

### 3.5.3 Modelling turbulence/chemistry interactions

Gas phase reactions are homogeneous because the reactants are in the same phase. The gas flow is turbulent in most combustion applications and the characteristic features of the combustion process such as flame propagation, peak temperature and pollutant formation do not depend on these reactions and their corresponding rates alone. They are also affected by gas flow turbulence. It alters flame structure and may enhance these reactions increasing their rates. Furthermore, high levels of turbulent can inhibit the flame. On the other hand, the chemical reactions have an influence on the turbulence as outlined in §3.3. Combustion process involves chemical reactions take place in a wide range of time scales and turbulence also has its time scale. These time scales range from almost instantaneous to several seconds. Therefore, to capture and describe the phenomenon, all the characteristic time scales needs to be retained. All these effects are what so-called turbulence/chemistry interaction that needs to be modelled. To do so in finite volume simulations, there are different possibilities have been attempted in the literature. Several methods to model the gas phase reactions in finite volume simulations.

### 3.5.3.1 Eddy-dissipation model (EDM)

This model is based on the following single step reaction:



where  $s$  is the stoichiometric coefficient of the reaction. In this widely used model, the basic assumption is fast irreversible, one-step chemistry and because of this, the rate of combustion is determined by the turbulent mixing process. The simple idea of the eddy-dissipation model given in (3.51) and (3.52) is to consider that chemistry does not play any explicit role, while turbulent motions only control the reaction rate. It has been proposed for predicting the mean reaction rates for flows with high Damköhler number ( $Da \gg 1$ ) in turbulent diffusion flames. Therefore, infinitely fast chemical reactions can be assumed and the reaction rate is controlled by the characteristic turbulent time and by the limiting ingredient needed for reaction either fuel, or oxidizer or heat. In the case of rich mixture,  $O_2$  will be consumed completely and a proportional amount of fuel will be consumed, as determined by the stoichiometric coefficient ( $s$ ). In the case of lean mixture, fuel will be consumed completely together with a proportional fraction of  $O_2$ .

The chemical reaction rate is governed by the large eddy mixing time scale ( $k/\epsilon$ ).

The reactant mixing rate

$$R_{i,m} = v'_{im} M_{w,i} A \rho \frac{\epsilon}{k} \min_{\mathcal{R}} \left( \frac{Y_{\mathcal{R}}}{v'_{\mathcal{R}m} M_{w,\mathcal{R}}} \right) \quad (3.51)$$

The product mixing rate

$$R_{i,m} = v'_{im} M_{w,i} A B \frac{\epsilon}{k} \left( \frac{\sum_{\mathcal{P}} Y_{\mathcal{P}}}{\sum_j v'_{jm} M_{w,j}} \right) \quad (3.52)$$

where  $Y_{\mathcal{P}}$  is the mass fraction of any product species,  $\mathcal{P}$ ,  $Y_{\mathcal{R}}$  is the mass fraction of a particular reactant,  $\mathcal{R}$ , and  $A$  and  $B$  are empirical constants that take the values of 4.0 and 0.5, respectively.

In this model the reaction rate is proportional to the large eddy mixing time scale given by  $k/\epsilon$ . The reaction rate is taken as the smaller of the values determined with the above two equations. The advantages of this model include its simple implementations and reasonable results that can be achieved as will be shown next. Moreover, it is

computationally inexpensive. This model can be used for reactions with any number of reactants and products and even possible to use more than one global reaction. An example regarding the latter case is when considering CO as intermediate species in the combustion of methane. Because the oxidation of CO is a comparably slow reaction, CH<sub>4</sub> reaction is calculated first.

### 3.5.3.2 Finite-rate/eddy-dissipation model (FR/ED)

The EDM is based on the assumption that the chemical reactions are extremely fast and the reaction rate of species is totally controlled by turbulent mixing. Such assumption leads to that this model estimates a high combustion rate in the large dissipation zones. Therefore, the finite rate/eddy-dissipation model is considered. Regarding this model, the rate of reaction is determined by the Arrhenius and by eddy-dissipation equations. Reaction rates, equations (3.51) and (3.52) as well as the Arrhenius rate equation (3.47), are calculated. Local reaction rate is given as the minimum value of these two rates. In practice, the Arrhenius rate (equation (3.47)) acts as a kinetic switch, preventing reaction before the flame holder. When the flame is ignited, the eddy dissipation rate is generally smaller than that of Arrhenius, and the reaction is mixing limited. These models are used for reduced chemistry and it difficult to extend them to full chemistry mechanisms. Therefore, to include a detailed chemistry, the eddy-dissipation concept model (EDC) can be considered.

### 3.5.3.3 Eddy dissipation concept model (EDC)

It is based on the representation of turbulent flow by the energy cascade discussed in §3.3. The mechanical energy in the turbulent flow is primarily contained in the largest eddies and passed on to smaller and smaller eddies until reaching the smallest eddies, where the viscous effects are strong and energy is dissipated into heat through viscous dissipation. It assumes that the reactions take place in the regions where the dissipation of turbulence energy takes place. These regions (smallest eddies), where the dissipation takes place, are called fine structures. In regions where the turbulence levels are high, the mixing is fast and, as a result, the reaction rate is not limited by small-scale mixing. The kinetically controlled reaction rate has the smallest value. Whereas, in regions where turbulence levels are low small-scale mixing may be slow and limits the rate of reaction. With varying degree of complexity, the EDC is capable of handling chemical reactions ranging from the fast chemistry limit to a detailed description of the different elementary reactions involved in the combustion process. However, a detailed

chemistry calculation is computationally expensive. The calculation time for integrating the chemistry is high. The reactions, governed by Arrhenius rates, are solved numerically using ISAT algorithm. Therefore, a reduction in the calculation time can be reached.

### 3.6 Numerical methods

The simulations are carried out using the CFD package Fluent. Flow field equations are solved using simple pressure velocity coupling method [114] in which the mass conservation solution is used to obtain the pressure field at each flow iteration. The finite volume scheme is employed to discretize these equations. The discretization is done using the second-order scheme. The Standard scheme [115] is used for interpolation methods for pressure. The criterion of convergence is set to  $10^{-6}$  for energy and radiation and  $10^{-4}$  for the other terms of the transport equations. Regarding the radiative heat transfer, the (P1) radiation model and the weighted sum of gray gases model (WSGGM) proposed by Hottel and Sarofim [182] are employed into the simulations.

### 3.7 Geometry and boundary conditions

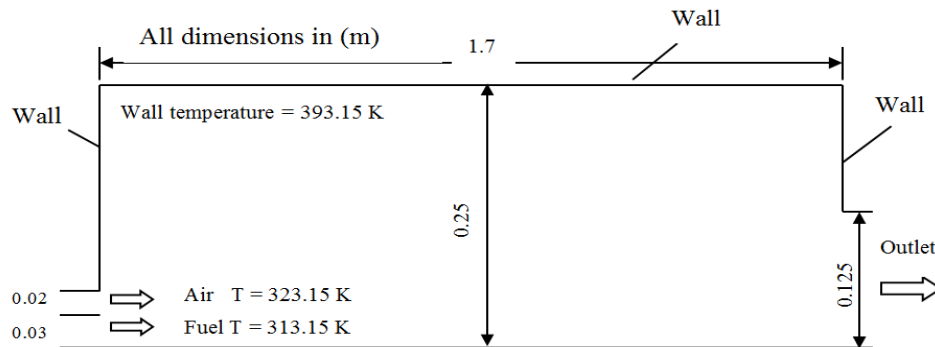


Figure 3.1: Geometrical configuration of the burner.

In this study the combustion chamber reported by Garretton and Simonin [20] is numerically simulated. The geometrical configuration of the burner is shown in Figure 3.1. The cylindrical chamber is 1.7 m in length with a diameter of 0.5 m. The fuel enters the chamber with a velocity of 7.67 m/s and temperature of 313.15 K. The velocity of air is 36.29 m/s and its temperature is 323.15 K with a corresponding Reynolds number is  $1.22 \times 10^6$ . The fuel is composed of 10% nitrogen ( $N_2$ ) and 90% methane ( $CH_4$ ) on volume basis. Full details of this chamber and its operating

conditions can be found in [20]. The computational domain of this chamber was also reported in [183-185]. The cases are simulated have an equivalence ratio of ( $\phi = 1.04$ ) which means that they are moderately fuel-rich. The equivalence ratio is given as the stoichiometric air to fuel ratio divided by the actual air to fuel ratio Equation (3.53).

$$\phi = \frac{(Air/Fuel)_{stoich}}{(Air/fuel)_{actual}} \quad (3.53)$$

### 3.8 Material properties

The material properties that have been used in the simulation are given in Table 3.3. The specific heat at constant pressure  $c_p$  for the gas mixture is obtained from equation (3.15). In this work,  $c_{pi}$  is determined from the piecewise-polynomial function of temperature and the default values provided by FLUENT were used (see appendix A).

Table 3.3: Material properties.

Property	Value
Thermal conductivity $\lambda$ [W/m.K]study	0.0454
Viscosity $\mu$ [kg/m.s]	$1.72 \times 10^{-5}$
Mass diffusion coefficient $D_i$ [ $m^2/s$ ]	$2.88 \times 10^{-5}$
Scattering coefficient $\sigma_s$ [ $m^{-1}$ ]	0
Refractive index $n$	1

### 3.9 Computational domain and grid refinement

For use in the CFD simulations, computational meshes of the interior volume of the furnace have been constructed. The dimensions used for meshes are shown in Figure 3.1. The mesh centreline is aligned with the x axis. All meshes have been constructed using GAMBIT. A two-dimensional axis-symmetric domain was utilized for which the common mesh elements are rectangles and triangles.

In the present study, the rectangular mesh elements were used. As shown in Figure 3.2 the cells are concentrated at the centreline where the flame is located and, as a result, large gradients in flow properties exist. Thus, more cells are concentrated here to more accurately resolve the gradients. The growth ratio of the distance between cell nodes has been used.

Generally, the accuracy of simulations increases as the number of cells increases. In order to determine a mesh that yields a mesh independent solution, a mesh independence study is required. The grid density was slightly varied by increasing number of cells. The meshes are designated A, B, C in order of increasing number of cells, which is given in Table 3.4 for each mesh.

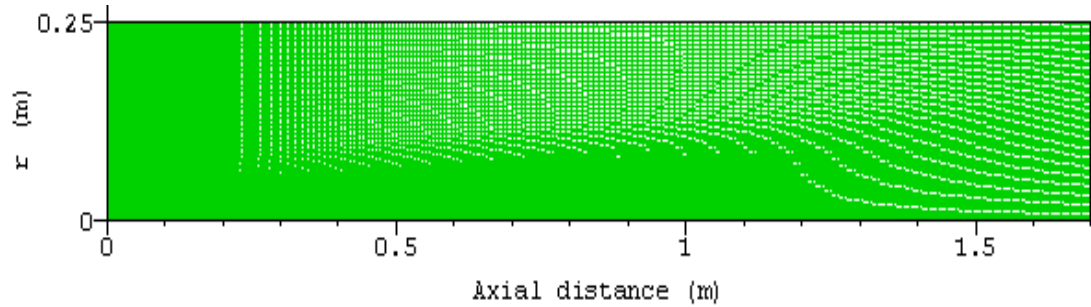


Figure 3.2: Computational grid.

Table 3.4: Number of mesh cells.

Mesh	Number of cells
A	23634
B	18395
C	13200

Converged solutions, in which the mechanism (M-I) shown in Table 3.2 was used for the simulations, were performed on the three computational meshes. The interaction between combustion chemistry and turbulent mixing was modelled using FR/ED model. To model the turbulence,  $k-\epsilon$  model was used. Ideally, all variables of interest should be monitored, but doing so leads to a large amount of data handling.

Figure 3.3 and Figure 3.4 show comparisons of velocity magnitude and temperature along the axial distance, respectively. The velocity and temperature in the radial direction at different axial locations are shown in Figure 3.5 to Figure 3.9. It can be seen from the figures that all the results obtained from the three meshes are very close except for the mesh C, which shows very small discrepancies in the radial variation of the chosen variables compared with meshes A and B.

Table 3.5 also shows the temperature and species flow rates at the outlet and the maximum temperature inside the furnace obtained for all meshes. From the axial and radial plots of velocities and temperatures as well as the values given in Table 3.5 a comparison was made between the meshes at the monitored locations, and



consequently mesh B, shown in Figure 3.2, was determined to yield a mesh independent solution and was chosen for carrying out all the subsequent simulations.

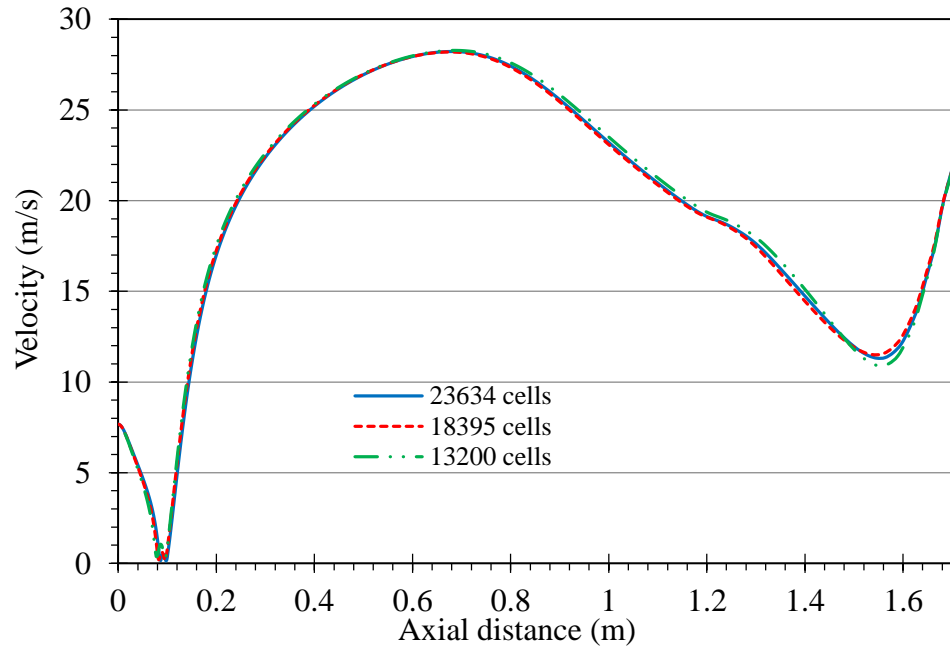


Figure 3.3: Velocity along the axial distance of the furnace for three different meshes.

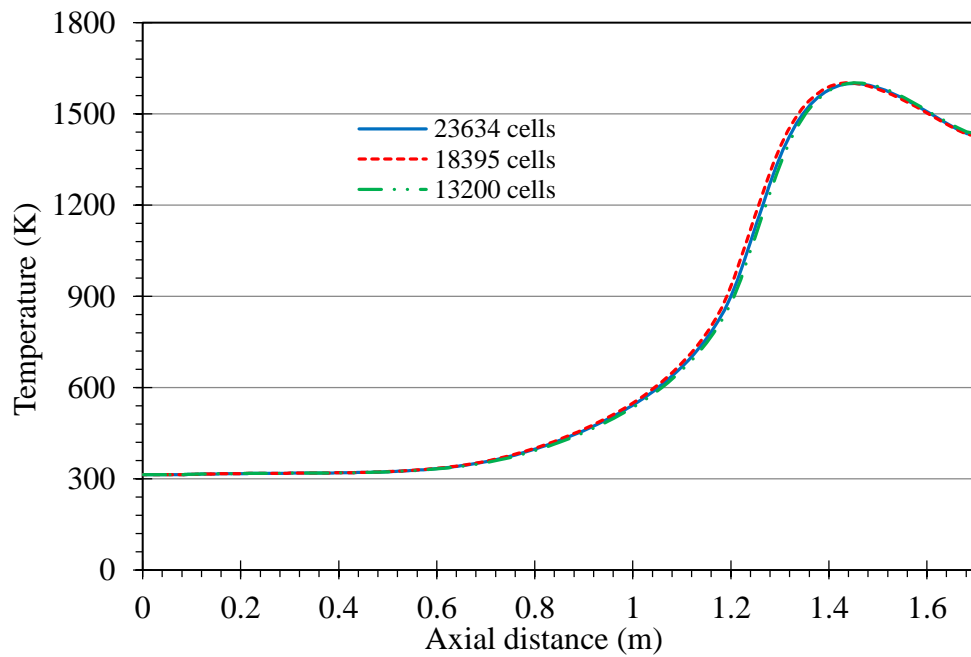


Figure 3.4: Temperature along the axial distance of the furnace for three different meshes.

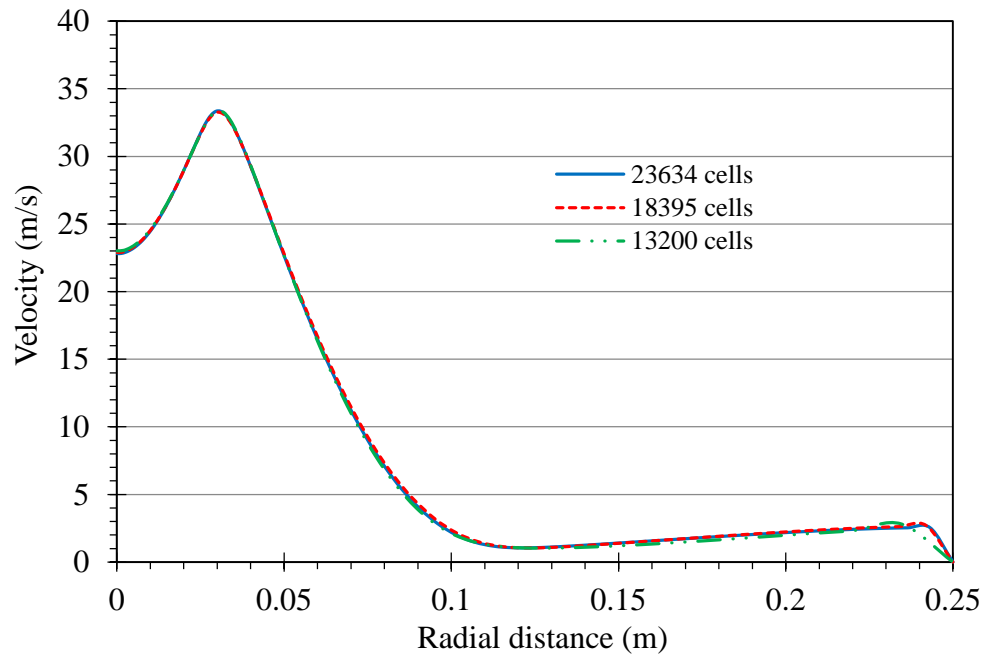


Figure 3.5: Radial profiles of velocity at  $x = 0.312$  m for three different meshes.

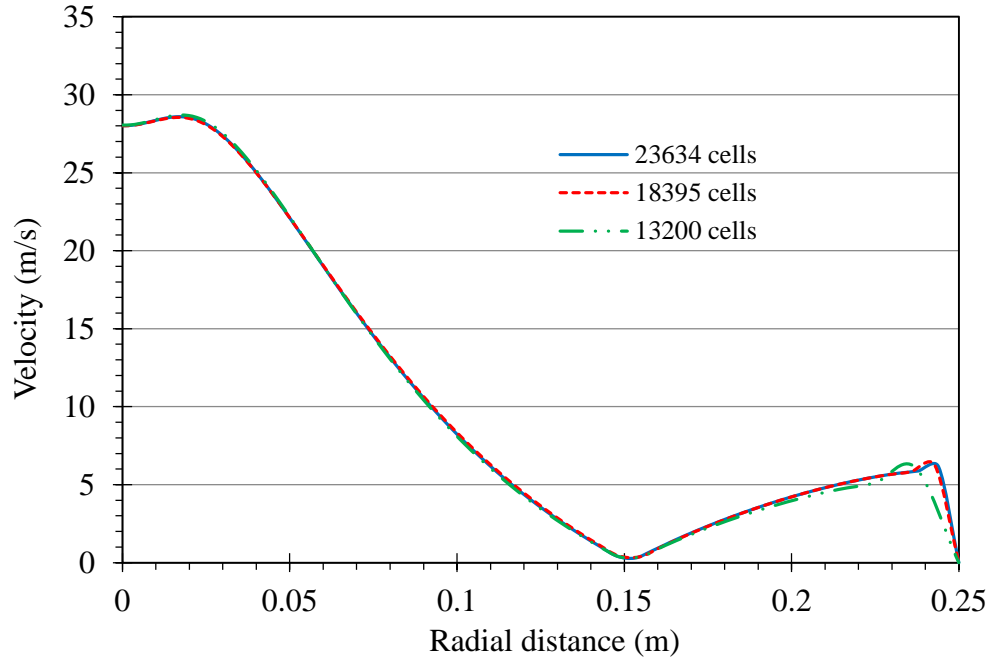


Figure 3.6: Radial profiles of velocity at  $x = 0.612$  m for three different meshes.

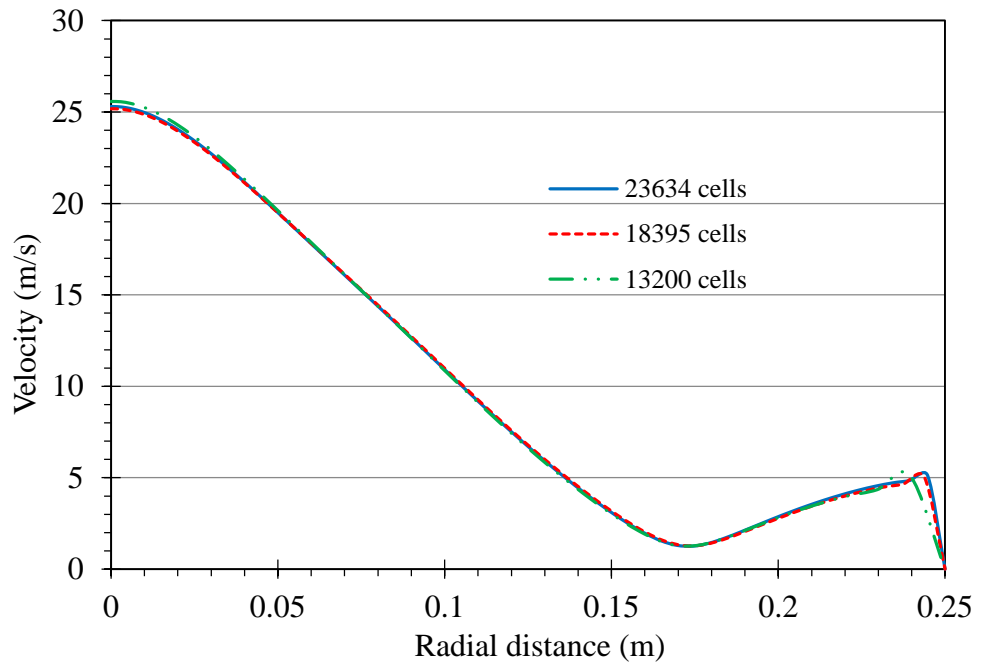


Figure 3.7: Radial profiles of velocity at  $x = 0.912$  m for three different meshes.

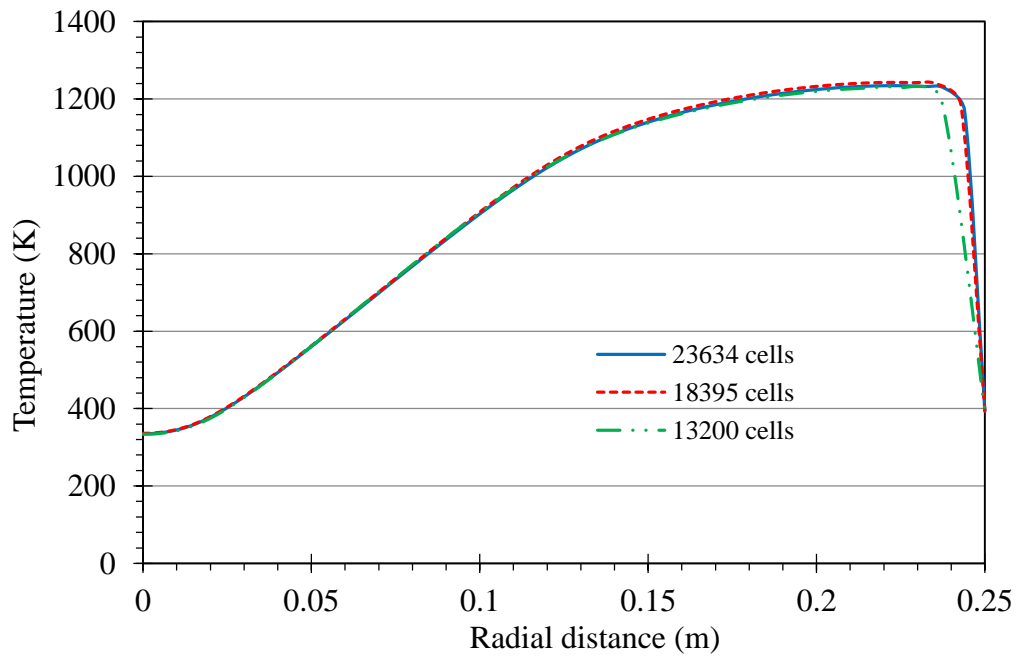


Figure 3.8: Radial profiles of temperature at  $x = 0.612$  m for three different meshes.

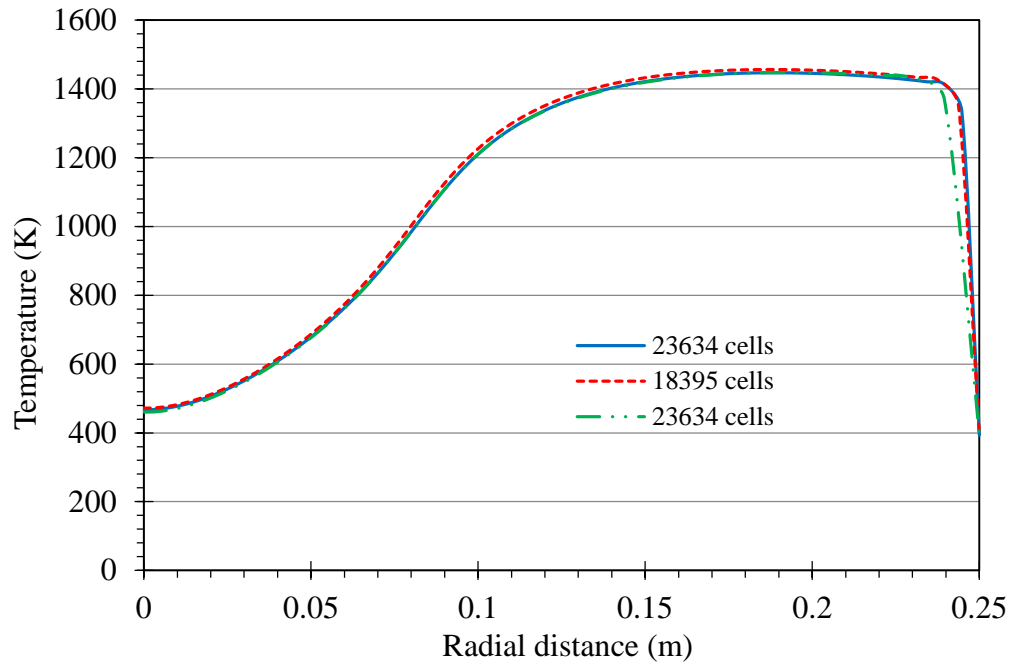


Figure 3.9: Radial profiles of temperature at  $x = 0.912$  m for three different meshes.

Table 3.5: Mesh independence temperature and flow rates at furnace outlet.

Mesh	A	B	C
Mass weighted average temperature [K]			
$T_{avg}$	1339.049	1336.4049	1347.5334
Species flow rate [kg/s]			
$\dot{m}_{CH_4}$	0.00071109226	0.00064929423	0.00061162794
$\dot{m}_{O_2}$	$0.66752805 \times 10^{-05}$	$1.203249 \times 10^{-05}$	$1.3592869e-05$
$\dot{m}_{CO_2}$	0.030436978	0.029913951	0.029893884
$\dot{m}_{CO}$	0.00081159326	0.0012321554	0.0012466239
$\dot{m}_{H_2O}$	0.025945209	0.026058445	0.026087508
$\dot{m}_{N_2}$	0.15501644	0.15506227	0.155074
$\dot{m}_{total}$	0.21292794	0.21292813	0.21292722
Maximum temperature inside the chamber [K]			
$T_{max}$	1600.338	1601.91	1602.871

## 3.10 Results and discussion

The results of CFD analysis are presented and discussed. These results include the effects of turbulence models, turbulence/ chemistry interaction and kinetic mechanisms on as well as the effects of mass fraction on the combustion process.

### 3.10.1 Mechanism one (M-I)

In this case, the chemical mechanism is the same mechanism used for grid independence analysis was employed to model the combustion of methane, which is mechanism (M-I). This mechanism consists of three reactions as shown in Table 3.2. For turbulence/chemistry interaction, the FR/ED model was used. To model the turbulence three models were utilized. They are the two-equation  $k-\epsilon$  models (standard, RNG and realizable). The constants of these models are mentioned in § 3.3. With regard to radiation modelling, P-1 model was used.

Numerical models on computational fluid dynamics and heat transfer can only be accepted if the results obtained from the simulations match quite well those obtained from the experimental work whether they are available in the literature or they are obtained from side by side experiments. In the case of this mechanism and the other mechanisms that will be presented in the next discussions, the model were validated by comparing the predictions against the experiments conducted by [20], the numerical results of Magel et al [183] and the numerical results obtained by [184] . In general, the results show good agreement with the experiments.

Figure 3.10, Figure 3.11 and Figure 3.12 show the velocity magnitude, axial velocity and velocity field vectors inside the chamber. The negative values of axial velocity indicate that there is an internal recirculation zone in front of the fuel inlet due to the sudden expansion.

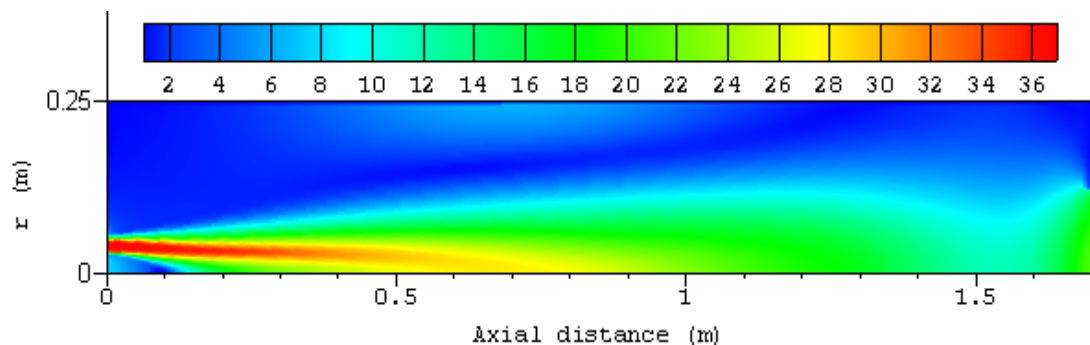


Figure 3.10: Velocity profile inside the chamber for  $k-\epsilon$  standard case (M-I).

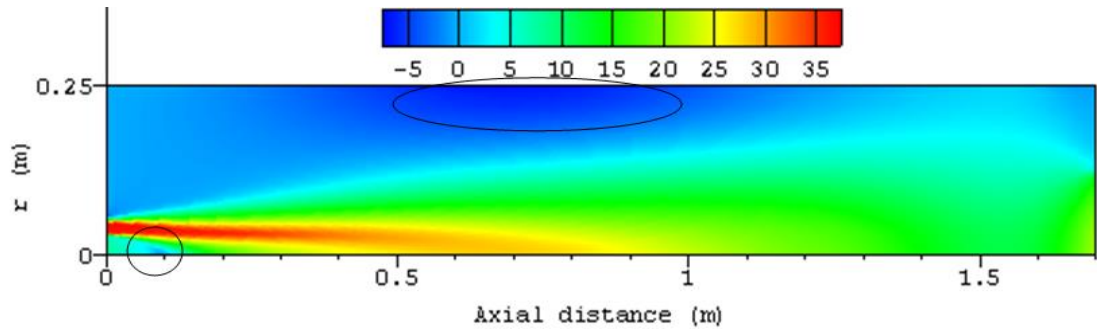


Figure 3.11: Axial velocity profile inside the chamber for  $k-\epsilon$  standard case (M-I).

From Figure 3.11, a recirculation region (circled) is observed at the entrance region near the fuel inlet. The creation of this recirculation leads to a premixing of air and fuel. The other recirculation region located close to the wall also enhances the mixing process and speeds up the reactions due to temperature increase. The variation of axial velocity along the radial direction at different axial locations is shown in Figure 3.13. It can be seen that there is a variation in positive and negative of axial velocity. This variation of velocity indicates the occurrence of recirculation zones which leads to good mixing of air and fuel.

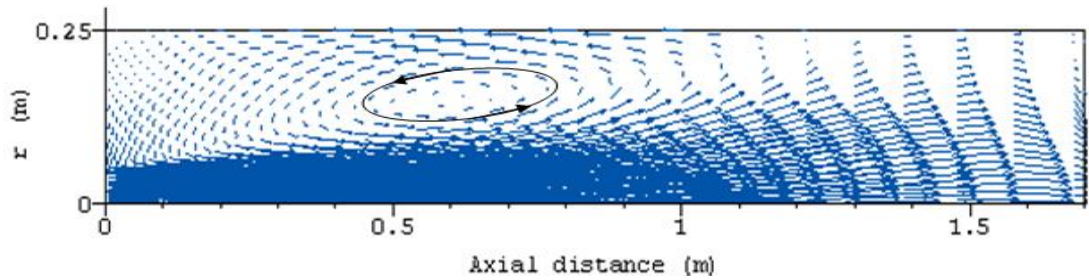


Figure 3.12: Velocity field vectors inside the chamber for  $k-\epsilon$  standard case (M-I).

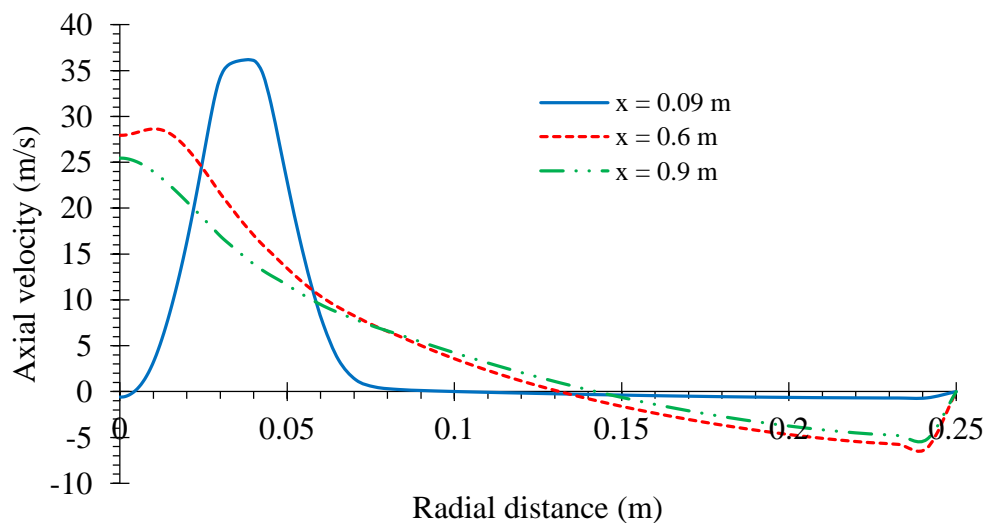


Figure 3.13: The variation of axial velocity along the radial direction at different axial locations  $k-\epsilon$  standard case (M-I).

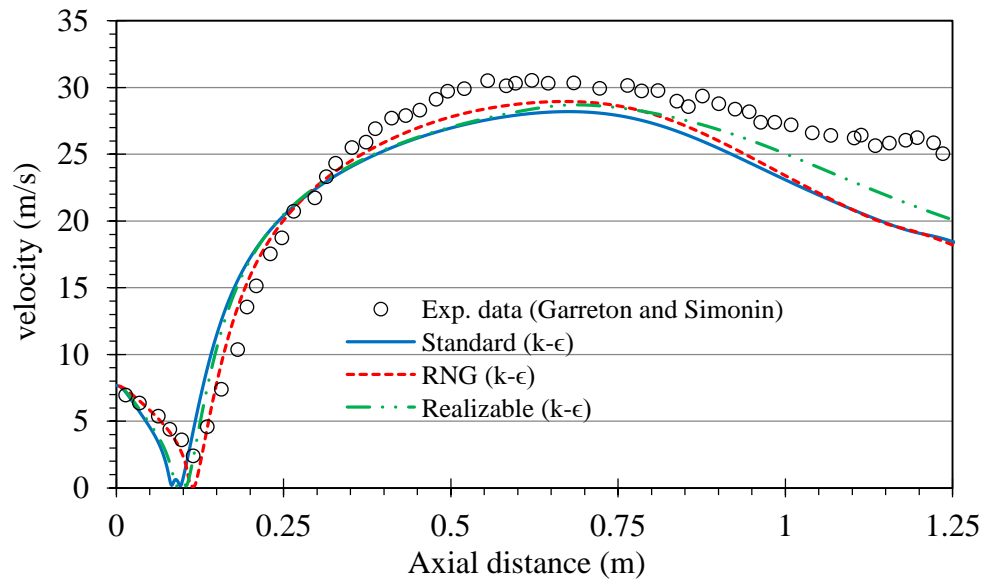


Figure 3.14: Velocity magnitude along the centreline of the chamber (M-I).

The velocity magnitude and the axial velocity along the centreline are shown in Figure 3.14 and Figure 3.15, respectively. It can be seen that the predicted values reasonably agree with the measured values. It is shown that all cases under-predict the experimental data in the axial distance lies between 0.4 and 1.25 m. This may attributed to mesh resolution in this region, which may need to be increased. From the figures, it can also be seen that RNG  $k-\epsilon$  case shows better agreement with the experimental data along the centreline at the axial distance lies between 0 and 0.4 m.

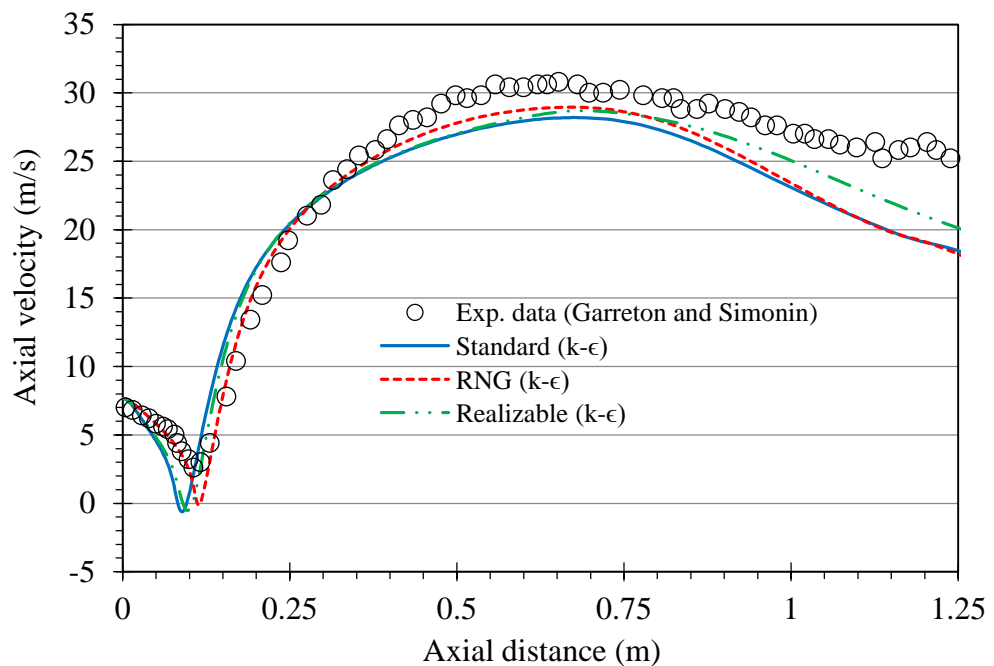


Figure 3.15: Axial velocity along the centreline of the chamber (M-I).

Figure 3.16 to Figure 3.19, show the difference between the temperature distributions for all present cases. They visualize the flame and its structure by means of the temperature distributions and show how these distributions are differing for all the cases. It is shown in the figures that the flame is blown further downstream of the chamber. For all cases, it can be also noted that the highest temperature zone occupies a wider span of the radial section. It can be seen from the figures that at the centre of the chamber the flame temperature increases very slowly along the axial distance till approximately half of the way then it starts to increase quite rapidly and reaches its maximum. This can be clearly seen in Figure 3.28 that will be presented next. It can also be seen from the figures that the temperature contours of standard  $k-\epsilon$  case are approximately the same as those of RNG  $k-\epsilon$  case and there is not a considerable difference between them. On the other hand, in comparison with standard  $k-\epsilon$  and RNG  $k-\epsilon$  cases, there is an obvious difference in the flame structure of the realizable  $k-\epsilon$ . It can be seen that the position of the highest temperature zone of gases for the realizable  $k-\epsilon$  shifts along the centreline of the chamber towards the exit. The contours of the case in which the radiation was not taken into account follow the same behaviour.

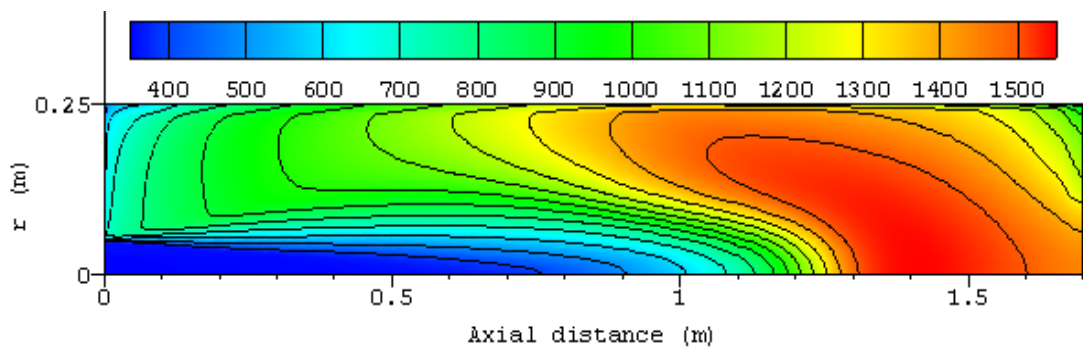


Figure 3.16: Temperature distributions for standard  $k-\epsilon$  case (M-I).

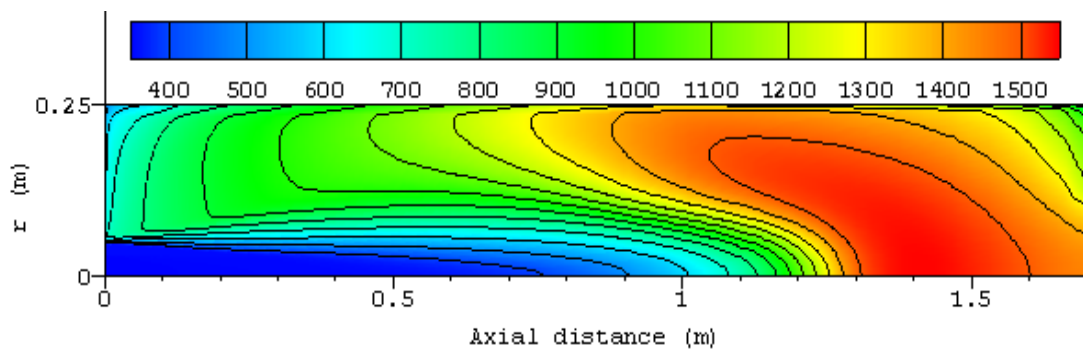


Figure 3.17: Temperature distributions for RNG  $k-\epsilon$  case (M-I).



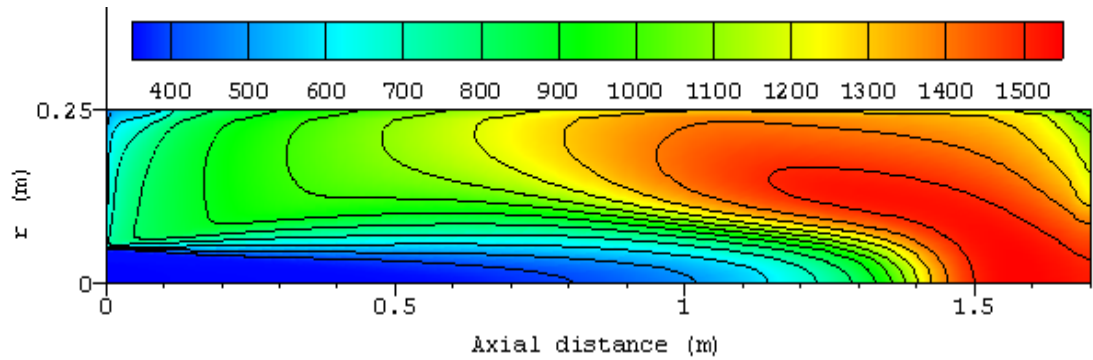


Figure 3.18: Temperature distributions for Realizable  $k-\epsilon$  case (M-I).

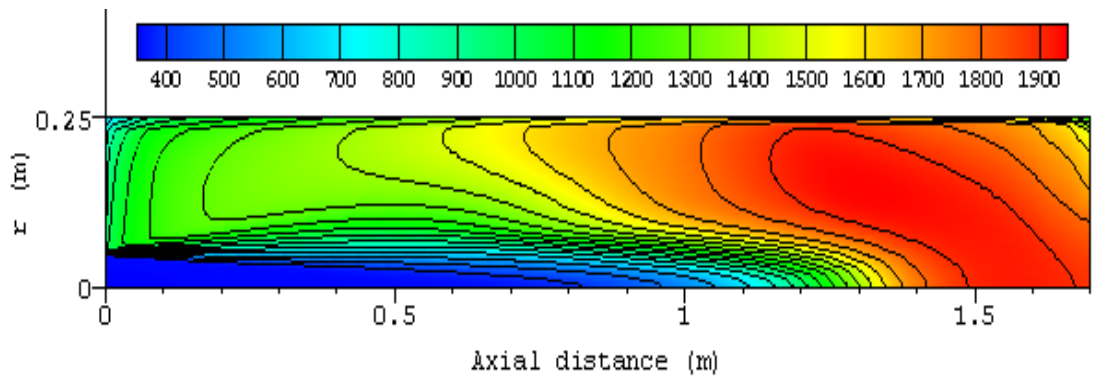
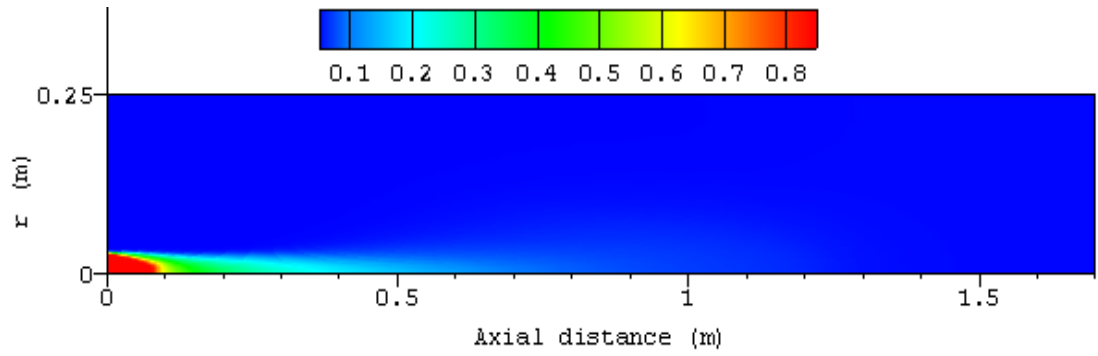
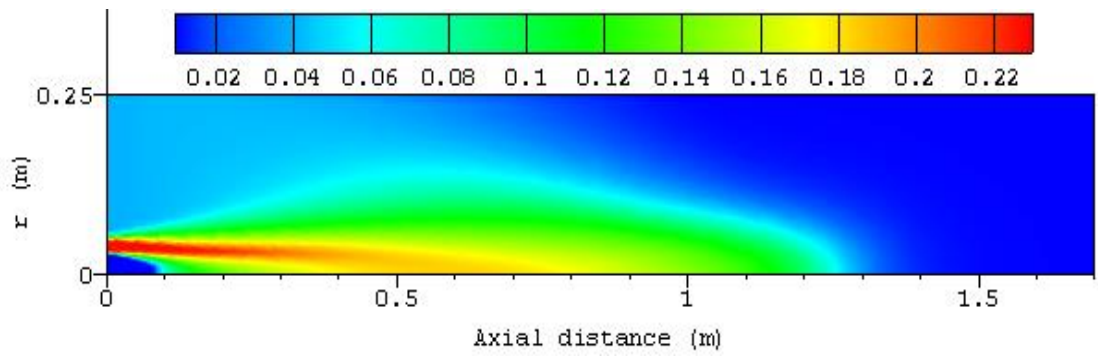
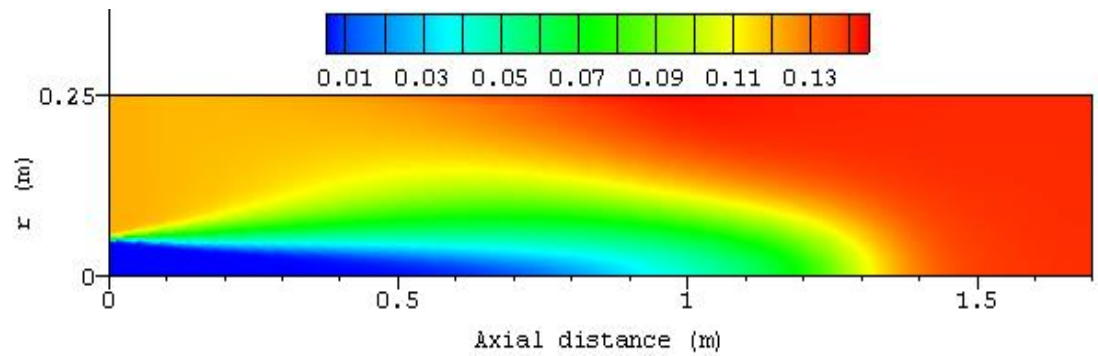
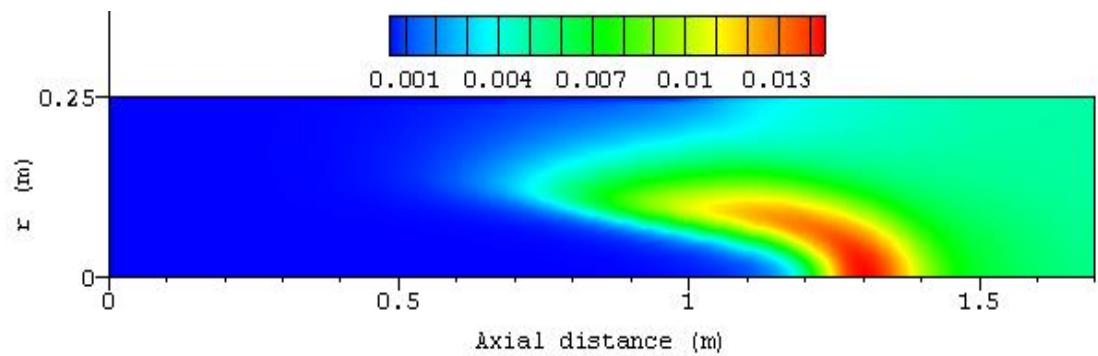


Figure 3.19: Temperature distributions for standard  $k-\epsilon$  case (without radiation) (M-I).

Figure 3.20 to Figure 3.23 show the contours of mass fraction of species  $\text{CH}_4$ ,  $\text{O}_2$ ,  $\text{CO}_2$  and  $\text{CO}$ , respectively. As shown in Figure 3.20, it is clear that  $\text{CH}_4$  is consumed in the reaction zone at the far side from the burner.  $\text{CH}_4$  has a mass fraction of 0.84 at the inlet which stays constant till the axial distance of 0.08 m where its consumption started. At this point there is a premixing of methane and air that takes place due to the recirculation of the gas flow as mentioned earlier when describing Figure 3.11 and Figure 3.13. The mass fraction of  $\text{CH}_4$  approximately becomes zero at the downstream region towards the exit of the chamber.

When having a look on the mass fraction distribution of  $\text{O}_2$  (see Figure 3.21), as expected, we can notice that the concentration of  $\text{O}_2$  is zero at both the inlet of fuel and the region near the exit of the chamber, which is consistent with the consumption of  $\text{CH}_4$ . The consumption of oxygen begins by the axial distance of 0.09 m.

From Figure 3.22 and Figure 3.23, it is clearly seen that the most  $\text{CO}_2$  and  $\text{CO}$  products are in the region where the combustion flame is indicated (see Figure 3.16).

Figure 3.20: CH<sub>4</sub> mass fraction for standard  $k-\epsilon$  case (M-I).Figure 3.21: O<sub>2</sub> mass fraction for standard  $k-\epsilon$  case (M-I).Figure 3.22: CO<sub>2</sub> mass fraction for standard  $k-\epsilon$  case (M-I).Figure 3.23: CO mass fraction for standard  $k-\epsilon$  case (M-I).

The rates of the reactions (r-2), (r-3) and (r-4) are shown in Figure 3.24, Figure 3.25 and Figure 3.26, respectively. As mentioned above, it is clearly seen that the flame is located at the region near the exit of the chamber where the reactions take place.

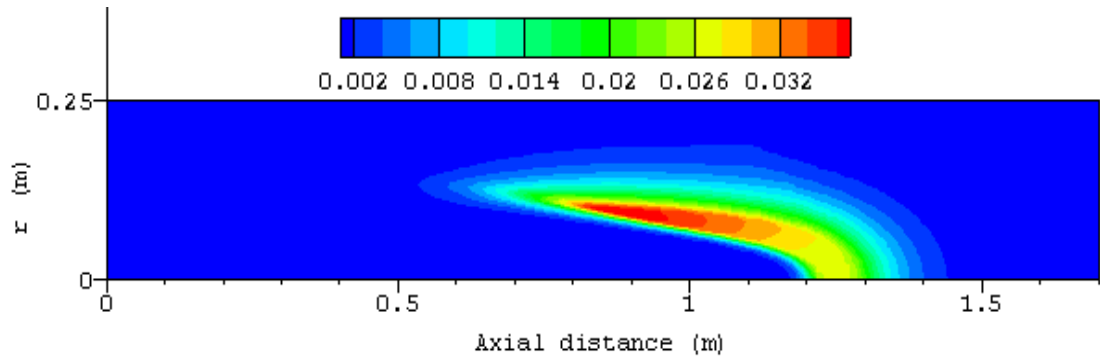


Figure 3.24: Rate of methane destruction reaction (r-2) in ( $\text{kmol}/\text{m}^3/\text{s}$ ) for standard  $k-\epsilon$  case (M-I).

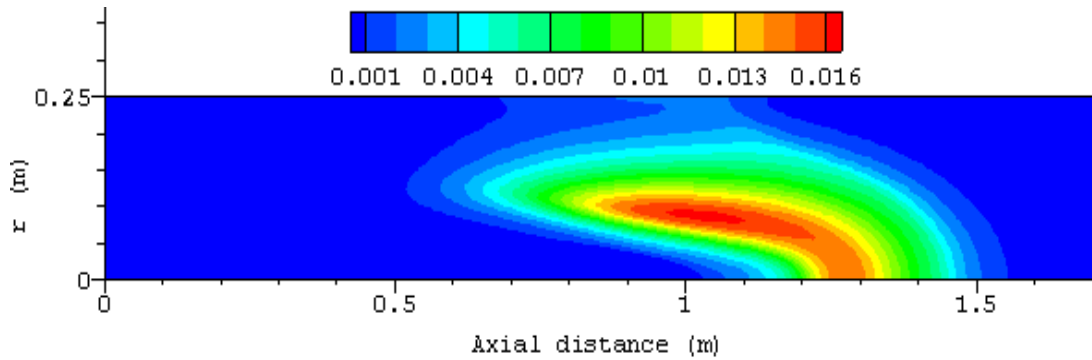


Figure 3.25: Rate of reaction (r-3) in ( $\text{kmol}/\text{m}^3/\text{s}$ ) for standard  $k-\epsilon$  case (M-I).

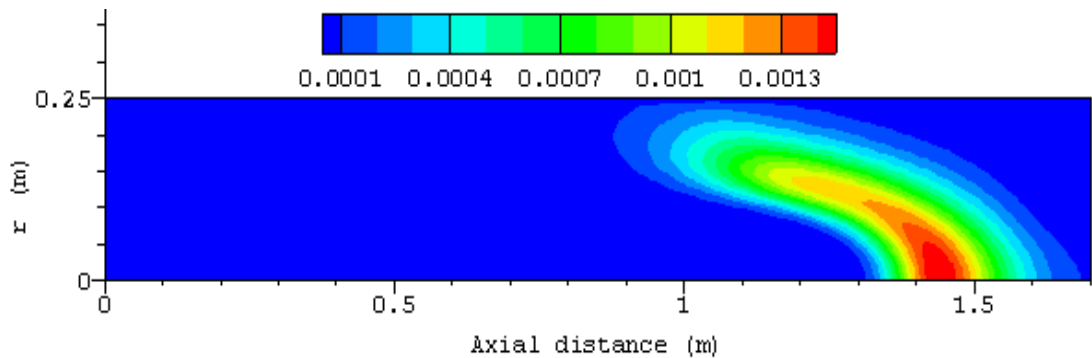


Figure 3.26: Rate of reaction (r-4) in ( $\text{kmol}/\text{m}^3/\text{s}$ ) for standard  $k-\epsilon$  case (M-I).

The profiles of the rate of reactions mentioned earlier along the centreline are shown in fig 3.26. It is shown that the combustion was not rapid. To view the gradients of temperature along the axial direction (x), the variations of the computationally predicted temperature compared with the experimental data along the chamber centreline are plotted in Figure 3.28.

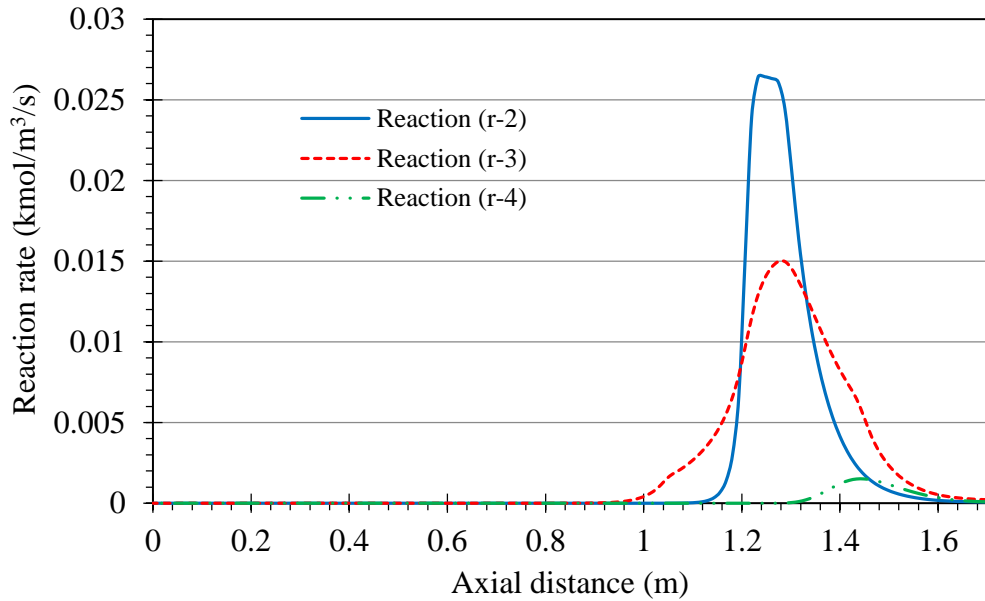


Figure 3.27: The profiles of reaction rate along the centreline of the chamber for standard  $k-\epsilon$  case (M-I).

All the cases exhibit the correct temperature trend as the experimental data by [20]. For all cases, the predicted temperature started to increase very slowly and as the combustion takes place it increases and achieves a maximum value of 1586 K (standard  $k-\epsilon$  case at  $x = 1.43$  m), 1617 K (RNG  $k-\epsilon$  case at  $x = 1.42$  m), 1548 K (realizable  $k-\epsilon$  case at  $x = 1.6$  m) and 1979 K (standard  $k-\epsilon$  case without radiation at  $x = 1.6$  m).

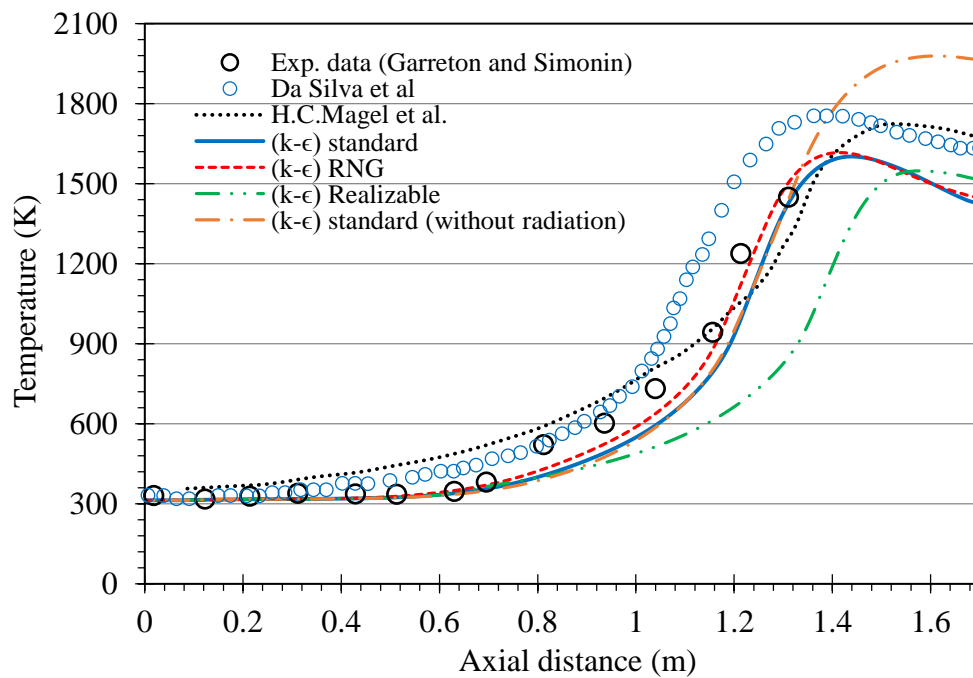


Figure 3.28: Gas temperature along the centreline of the chamber (M-I).

Unfortunately, there is no experimental data available beyond the axial distance of 1.3 m to validate the predicted results. It can be seen that larger temperature gradients occur along the centreline of the chamber between  $x = 1.3$  and  $x = 1.7$  m. At  $x < 0.7$  m, all the cases yield the correct temperature. Whereas, for  $x > 0.7$  m, RNG  $k-\epsilon$  and standard  $k-\epsilon$  cases show better results than the realizable  $k-\epsilon$  case when compared with the experimental data with the former one predicted the best results. The gas temperature predicted by realizable  $k-\epsilon$  case is significantly underestimated in comparison with the measured temperature. Radiation is a source of heat loss in flames and has a major influence on temperature distribution. Neglecting the radiative heat transfer generally causes over-prediction in temperature profile. As is evident from Figure 3.28, comparing the results of standard  $k-\epsilon$  case, including and excluding the radiation effects, with the experimental data indicates that maximum temperature obtained from the case without radiation was reduced by 19.8 % and the results are better fit to the experimental data. However, as shown in the figure, the effects of radiation are considerable at the exit of the chamber (at  $x > 1.3$  m) where the temperatures are higher, while for  $x < 1.3$  m, the temperatures are relatively lower and these effects appear to be very smaller and are neglected along the axial distance.

In order to further estimate quantitatively the difference between the experimental and numerically predicted results, a parity plot of the gas temperature at different axial locations lie between  $x = 0$  and  $x = 1.35$  m are presented in Figure 3.29.

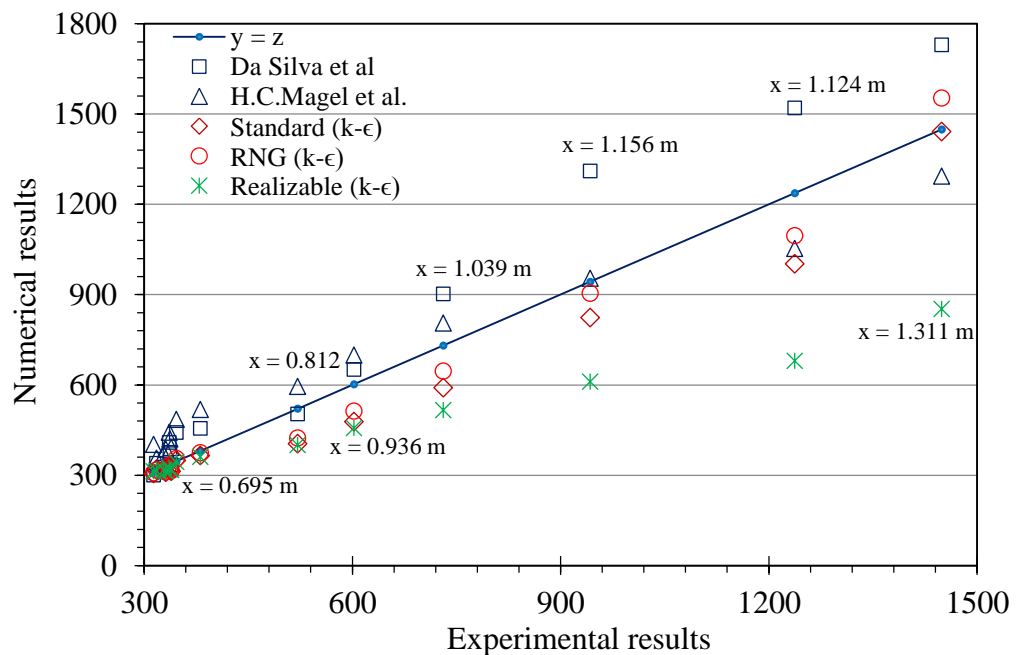


Figure 3.29: Comparison between the experimental and predicted data of gas temperature for all cases- (M-I). Ideal results lie on the line indicated by  $y = z$ .

The  $y = z$  line indicates the ideal results i.e. the simulated results are identical to those from the experiment. It is seen that all the results of the present cases lie very close to the line at the axial locations on the centreline for  $x < 0.7$  m, except for the results predicted by Silva et al. [184] and Magel et al. [183], which show slight difference above the line. At the axial locations for  $x > 0.7$ , it is shown that the results of Magel et al., standard  $k-\epsilon$  and RNG  $k-\epsilon$  cases lie closer to the line than the other two cases. Moreover, it is seen that RNG  $k-\epsilon$  case gives better results than Magel et al. case at the axial positions  $x \approx 1.124$  and  $1.311$  m.

The mass fraction of the species in the axial direction along the centreline is shown in Figure 3.30 to Figure 3.33. With respect to  $\text{CH}_4$  mass fraction along the axial direction, its variation along the centreline is illustrated by Figure 3.30. It shows that the trend of variation is almost the same for all the cases and in comparison with the experimental data  $\text{CH}_4$  is predicted very well. It is seen that mass fraction of  $\text{CH}_4$  decays slowly due to its consumption by chemical reactions and approximately reaches zero at the exit of the chamber. The slow decay can be attributed to the slow mixing which results in that the chemical reactions are quite slow leading to a slow rise in temperature (see Figure 3.28). Moreover, in terms of the effects of radiation on  $\text{CH}_4$  species, there is only a very slight difference between the mass fraction of both the standard  $k-\epsilon$  and standard  $k-\epsilon$  (without radiation). However, as it is seen, the radiation effect of non-gray gases of  $\text{CO}_2$  and  $\text{H}_2\text{O}$  changed the other species mass fractions and the results improved.

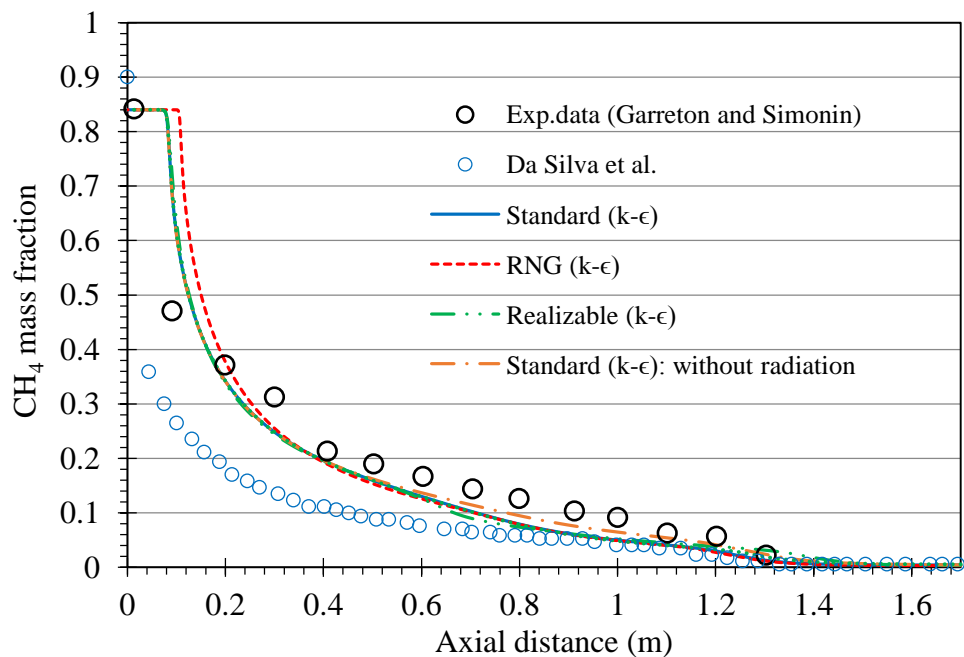


Figure 3.30:  $\text{CH}_4$  mass fraction along the central line (M-I).

The axial profile of mass fraction of  $O_2$  along the centreline of the chamber is depicted in Figure 3.31, which shows that the predictions of standard and RNG  $k-\epsilon$  cases are in good agreement with the experimental data. It is shown that the trend is well reproduced by all cases. It is also seen that  $O_2$  mass fraction of both the experimental and computational results increases from the inlet along the axial distance up to the axial position of approximately 0.6 m where it starts to decay till reaches the exit of the chamber where is totally consumed. From the figure, one can see that the mass fractions of realizable  $k-\epsilon$  and standard  $k-\epsilon$  (without radiation) are predicted well in the upstream distance of the chamber and they shifted towards the exit of the chamber in the downstream distance.

Figure 3.32 shows the variation of CO mass fraction along the chamber central line compared with the experimental data. All the cases predicted the correct results along the axial distance between 0 and 0.9 m. However, after this point a reliable comparison is not possible due to the absence of experimental data, except for that point which measured at axial position of 1.3 m. As seen from the figure, this point can be considered as the maximum value of the experimental data. According to this, it is seen that the CO peak concentrations are over-predicted in most cases. The reason for this may be the partial premixing of the fuel with air.

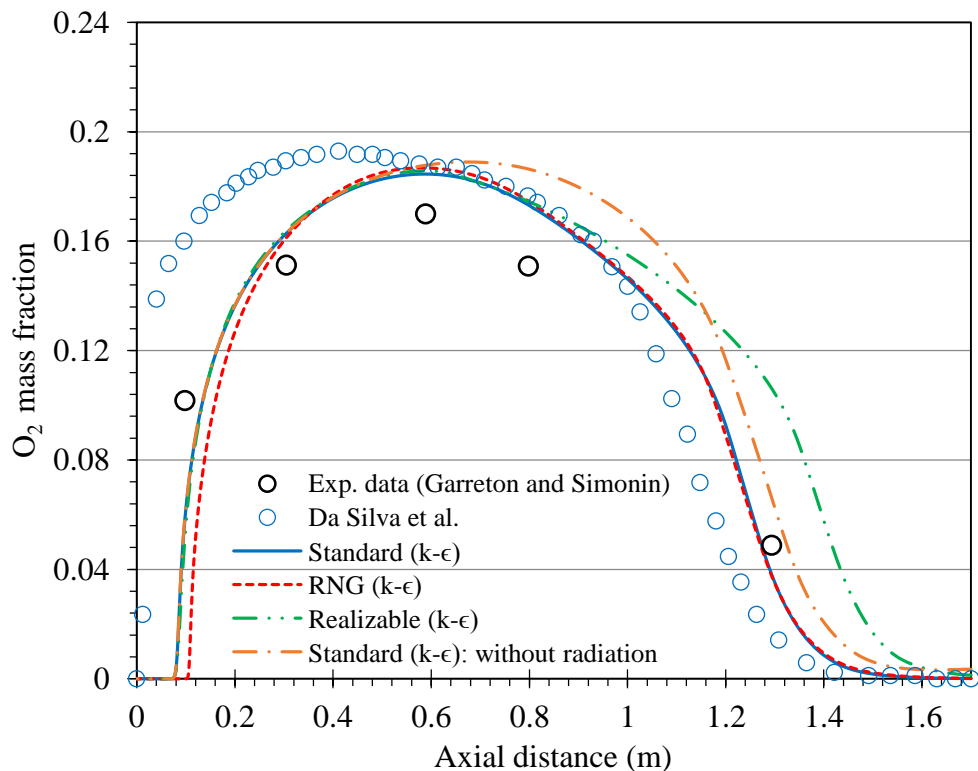


Figure 3.31:  $O_2$  mass fraction along the central line (M-I).

The figure also indicates that better results were obtained from standard and RNG  $k-\epsilon$  cases. It can be seen that realizable  $k-\epsilon$  case showed the same trend of the two cases, but the peak value shifted towards the outlet. Regarding the case in which the radiation was excluded, it can be seen that CO mass fraction was significantly over predicted in the downstream zone close to the outlet. This over-prediction was reduced and the results were improved when the reaction (r-4) (for  $\text{CO}_2$  decomposition) was excluded from the mechanism as shown in Figure 3.32.

Figure 3.33 depicts the comparison between the computationally predicted mass fraction of  $\text{CO}_2$  and the experimental data along the centreline of the chamber. It can be seen that realizable  $k-\epsilon$  case shows the best results when compared to the other cases, while no comparison is also possible beyond the axial position ( $x = 1.36$  m) due to the unavailability of the experimental data.

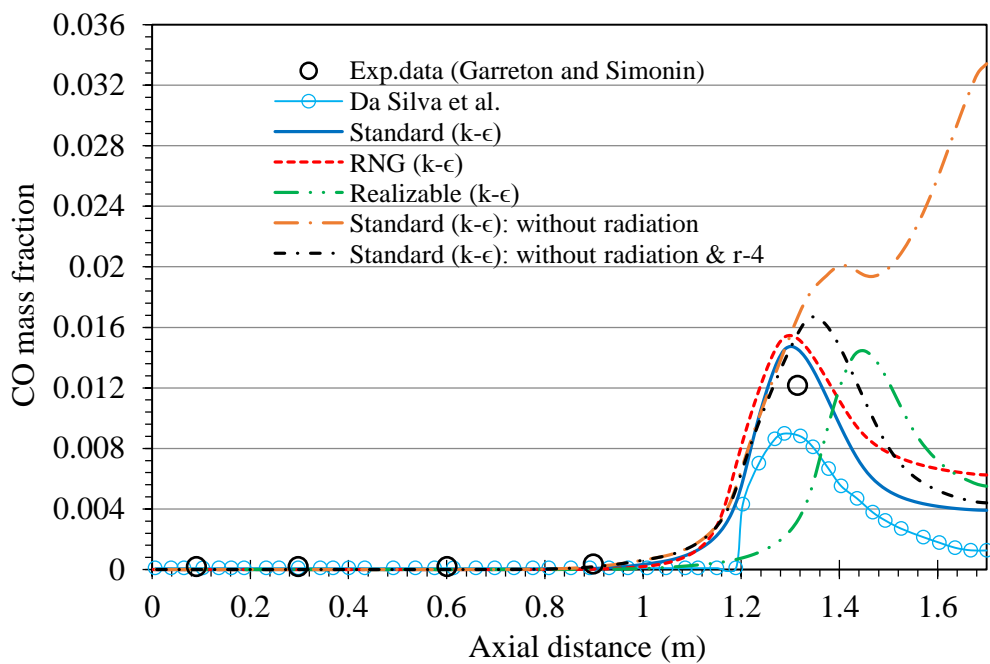


Figure 3.32: CO mass fraction along the central line (M-I).



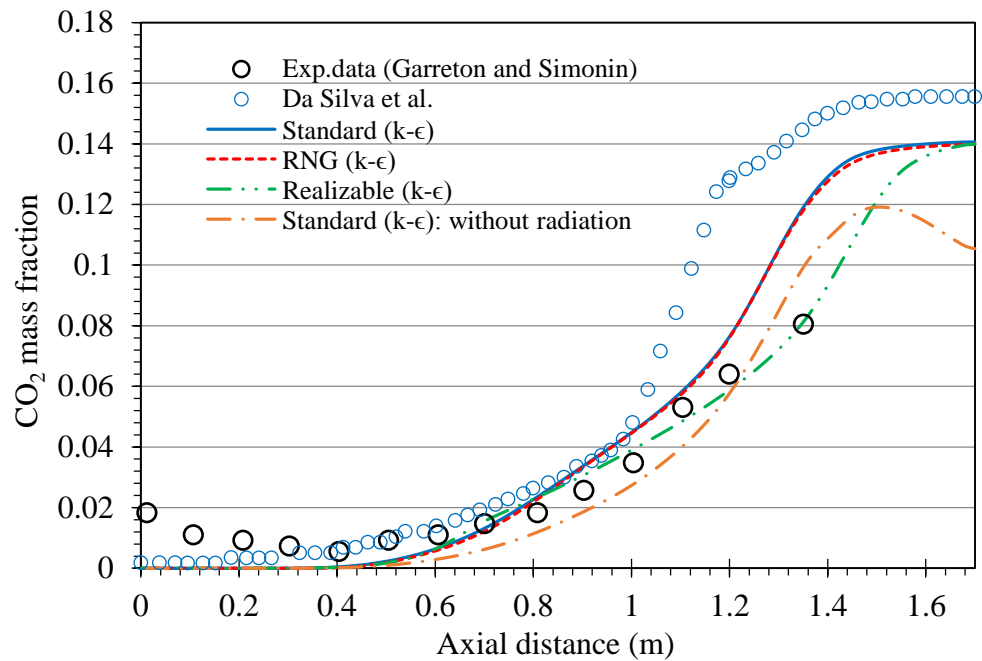


Figure 3.33: CO<sub>2</sub> mass fraction along the central line (M-I).

A selection of results obtained at various axial locations downstream from the burner for temperature and species mass fractions are plotted in Figure 3.34 to Figure 3.42. Generally, most of the predicted results are matched reasonably well with the experimental data and qualitatively they have good agreement implying some accurate predictions in some locations.

Figure 3.34, Figure 3.35 and Figure 3.36 show the profiles of gas temperature at axial locations (0.312, 0.912 and 1.312 m) downstream of the burner inlet as a function of radial distance from the centreline compared with the measurements, respectively. As it is evident from Figure 3.34, the heating up of the mixture started at radial distance of 0.03m. Further, the radial temperature increases due to the initiation of exothermic reactions as can be seen from Figure 3.35 and Figure 3.36. Apart from the case without radiation, it can be seen that the other three cases show reasonable agreement with the experimental data at axial locations  $x = 0.312$  and  $0.912$  m. At  $x = 0.312$ m, all cases under-predict the radial temperature excluding the case without radiation, which over-predicts the temperature at all selected axial locations. At  $x = 0.912$  m depicted by Figure 3.35, RNG and realizable  $k-\epsilon$  cases show very good agreement, whereas standard  $k-\epsilon$  case slightly over-predicts the temperature when compared with experimental data.

Concerning the axial location at  $x = 1.312$  m, it is shown in Figure 3.36 that standard and RNG  $k-\epsilon$  cases predicted the radial profiles of temperature excellently. It can be seen that the former one shows excellent agreement with the experiment in the zone around the centreline at a radial distance between 0 and 0.13 m. On contrary, the results of later one have excellent agreement with experiment in the zone far from the centreline at a radial distance between 0.13 and 0.25 m. Regarding realizable  $k-\epsilon$  case, it shows good agreement with the experimental data at radial distance lies between 0.14 and 0.25 m. Whereas, it under-predicts the radial temperature in the opposite direction at a radial distance lies between 0 and 0.14 m. This is due to the shift of the position of the increased temperature zone of gases along the centreline of the chamber towards the exit as mentioned before as shown in Figure 3.18. It is evident from the plots of radial profiles that effects of thermal radiation are so small around the centreline of the chamber and this is clear in Figure 3.28, which, as mentioned previously, shows that the thermal radiation is considerable at  $x > 1.3$  m. On the hand, it can be clearly seen that the effects of thermal radiation substantially reduces the flame temperatures along the radial distance ( $r > 0.03$  m).

Figure 3.37, Figure 3.38 and Figure 3.39 depicts the radial profiles of  $O_2$  mass fraction that show the comparisons of the predicted results against the experiment [20] and the computational results reported by Silva et al.[184]. As seen from the figures, the results obtained from the present cases agree well with the experimental data and follow the same trend. In Figure 3.37, it is seen that the maxima of  $O_2$  mass fraction are over-predicted compared with experiment and these maxima shifted to the left when referring to the maximum value of the experimental data. For all cases, there is a slight over-prediction in  $O_2$  mass fraction at the radial distance lies between 0 and 0.03 m. At the radial distance lies between 0.03 and 0.25 m, all the cases, except for the case without radiation, show good results in comparison with the experimental data. The effects of thermal radiation on the concentration of  $O_2$  can also be observed from the figure, since the over-prediction in  $O_2$  mass fraction (without radiation case) is reduced when these effects are taken into account (standard  $k-\epsilon$  case).

A part from the case without radiation, the obtained results from the cases are in good agreement with the experimental data as shown in Figure 3.38. However, it can be seen that they shows slight over-predictions in  $O_2$  mass fraction at the radial distance ( $r > 0.06$  m). The plots of radial profiles at the axial position  $x = 1.312$  m (see Figure 3.39) show that all cases significantly under-predict  $O_2$  mass fraction, except for realizable  $k-$

$\epsilon$  case, which shows very good agreement with the experimental data. It is also seen in the figure that excluding the thermal radiation effect (standard  $k-\epsilon$  case: without radiation) gives better results in terms of  $O_2$  mass fraction than those when including it (standard  $k-\epsilon$  case).

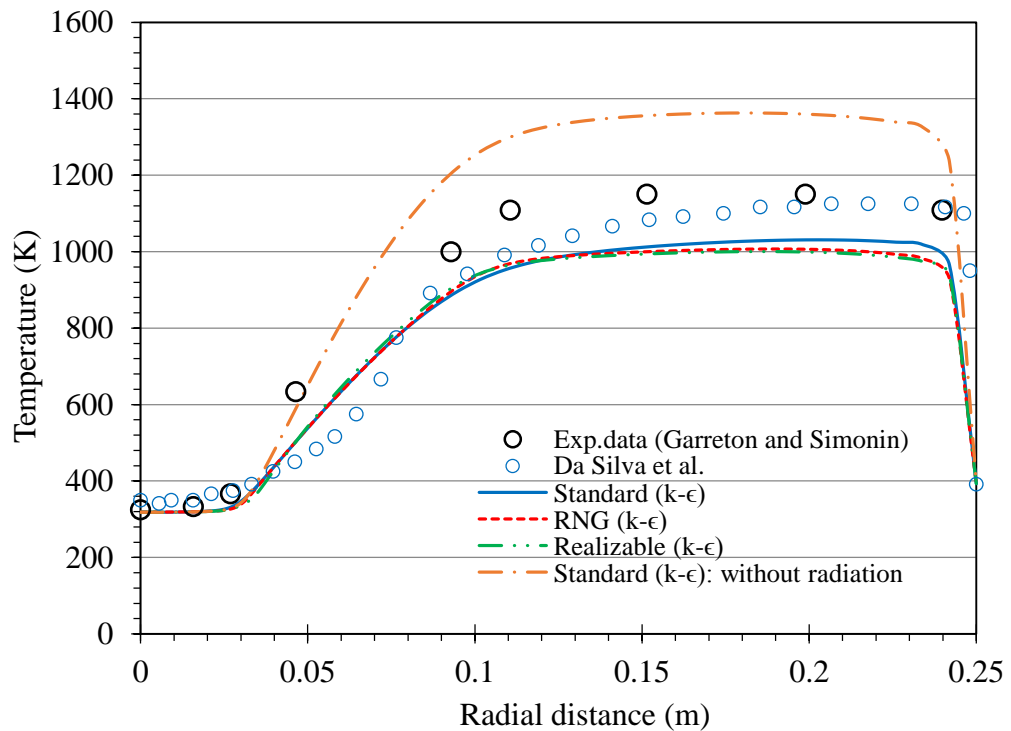


Figure 3.34: Radial temperature profile at axial location  $x = 0.312$  m, (M-I).

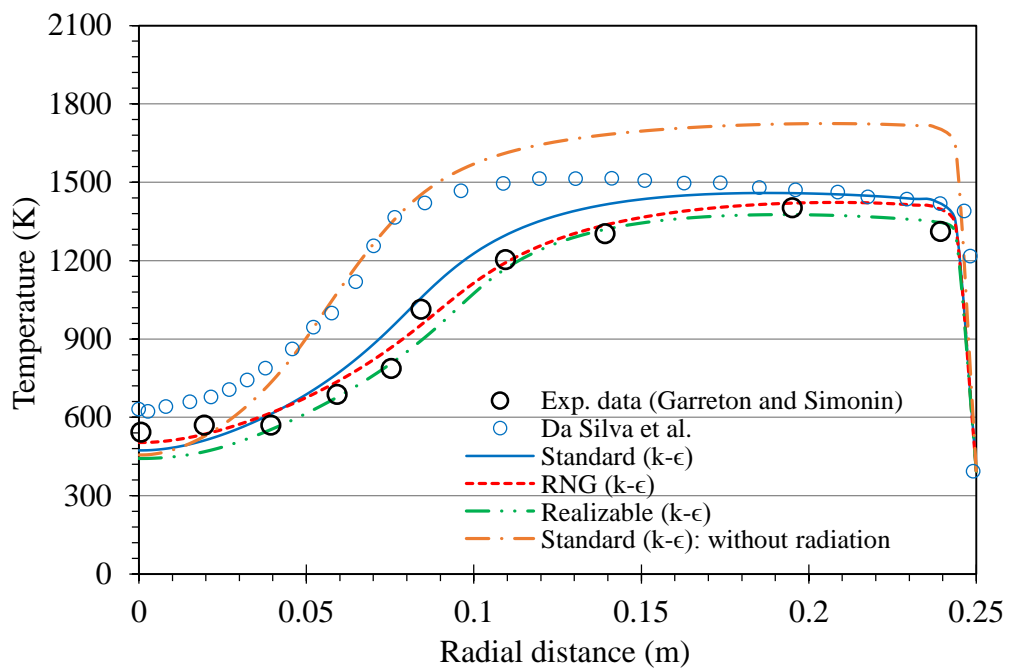


Figure 3.35: Radial temperature profile at axial location  $x = 0.912$  m, (M-I).

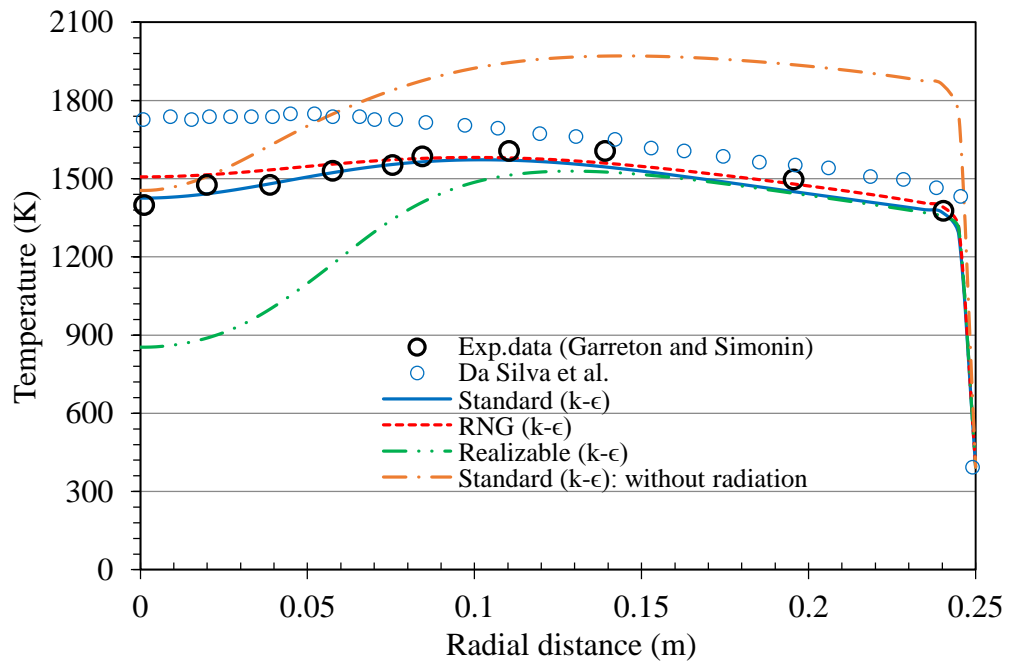


Figure 3.36: Radial temperature profile at axial location  $x = 1.312$  m, (M-I).

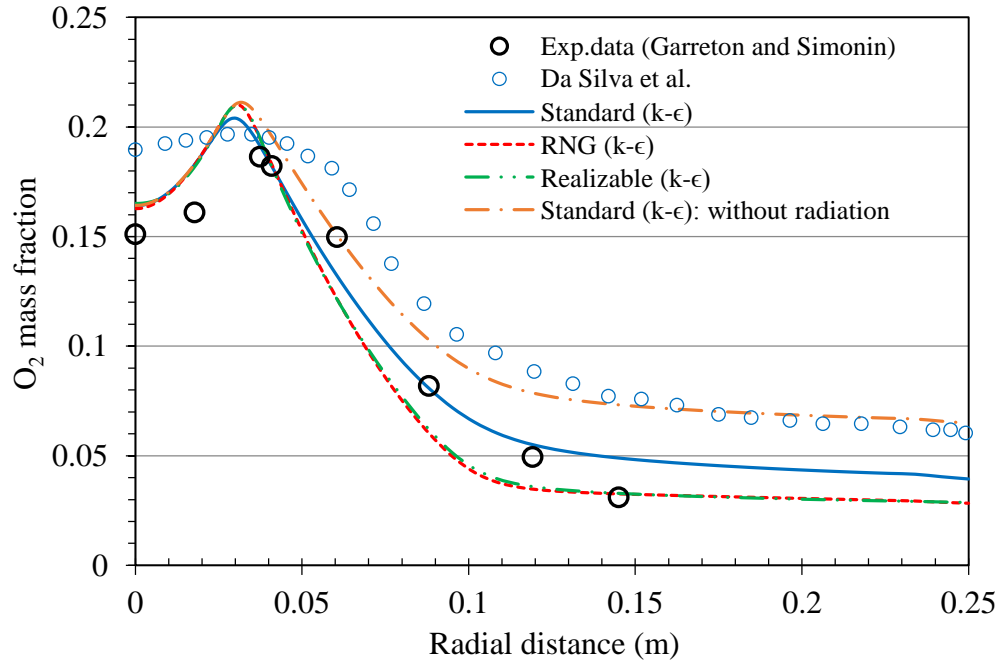


Figure 3.37: Radial profile of  $O_2$  mass fraction at axial location  $x = 0.312$  m, (M-I).

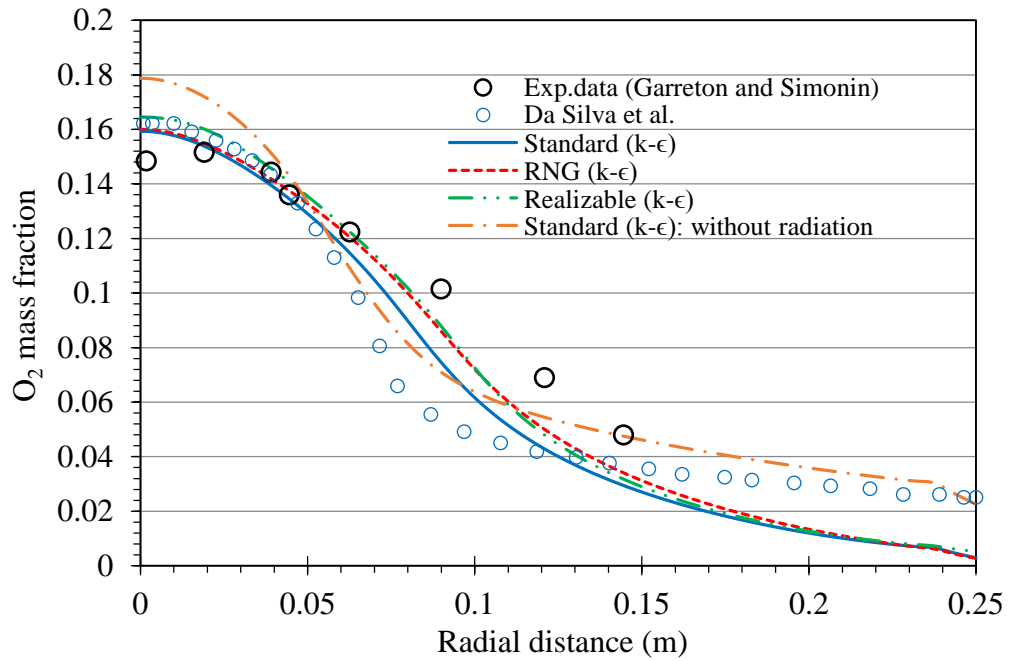


Figure 3.38: Radial profile of  $O_2$  mass fraction at axial location  $x = 0.912$  m, (M-I).

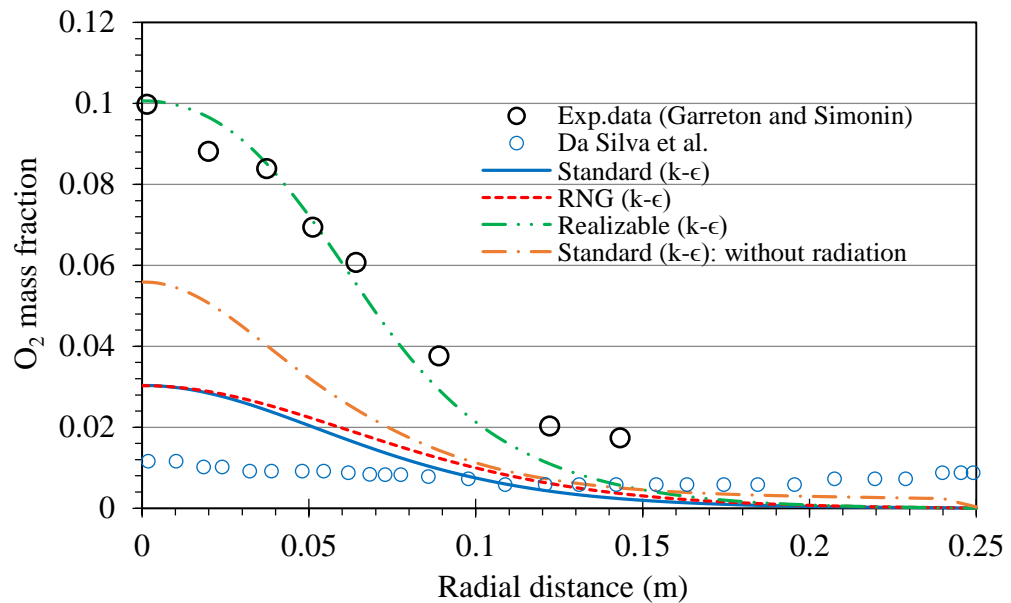


Figure 3.39: Radial profile of  $O_2$  mass fraction at axial location  $x = 1.312$  m, (M-I).

The radial distribution of  $CO_2$  mass fraction at the selected axial positions is depicted in Figure 3.40, Figure 3.41 and Figure 3.42. From these figures, in comparison with the experimental data, a part from the case without radiation at the axial location  $x = 0.312$  m, the numerical results of all present cases are over-predicted. The overall accuracy of the results is acceptable. It was also noticed that excluding reaction (r-4) (for  $CO_2$  decomposition) resulted in increasing  $CO_2$  mass fraction. As is seen in Figure 3.42, the results of realizable  $k-\epsilon$  case shows very good agreement with the experimental data in the radial distance lies between 0 and 0.06 m.

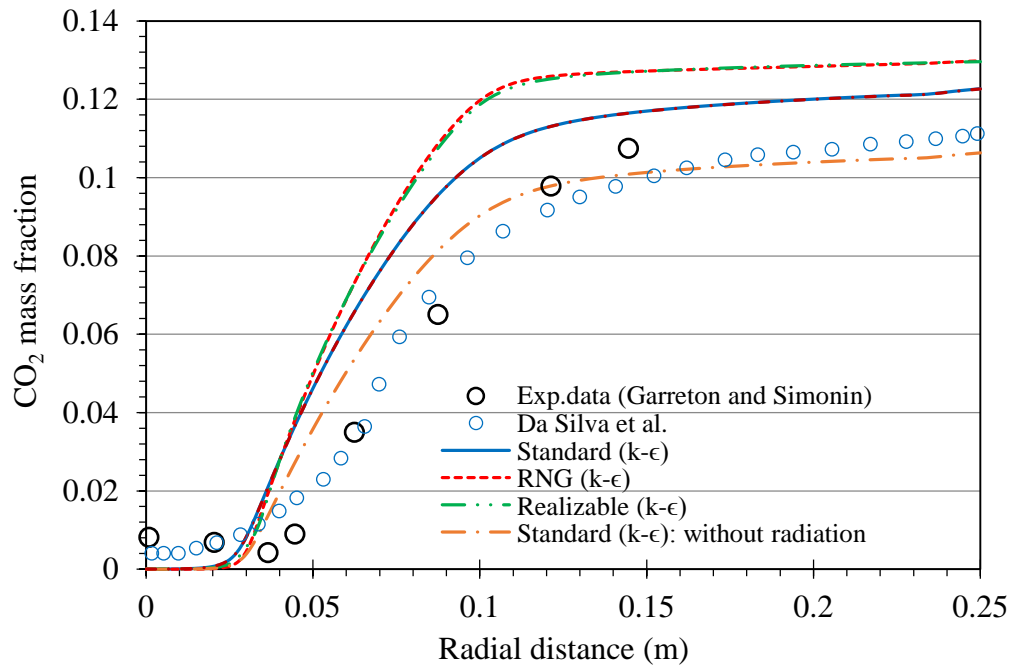


Figure 3.40: Radial profile of CO<sub>2</sub> mass fraction at axial distance  $x = 0.312$  m, (M-I).

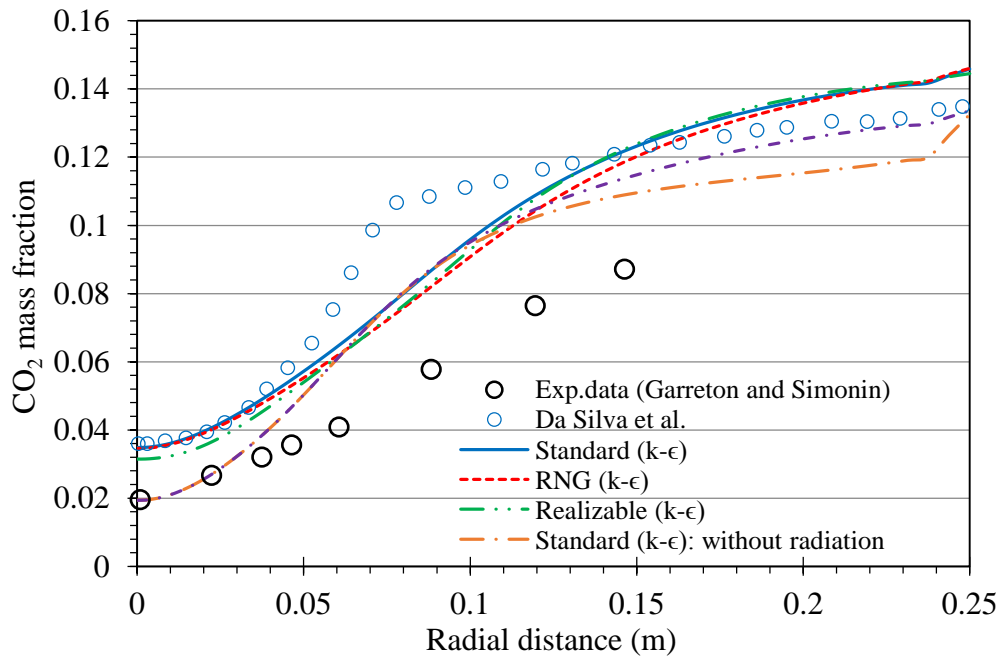


Figure 3.41: Radial profile of CO<sub>2</sub> mass fraction at axial distance  $x = 0.912$  m, (M-I).

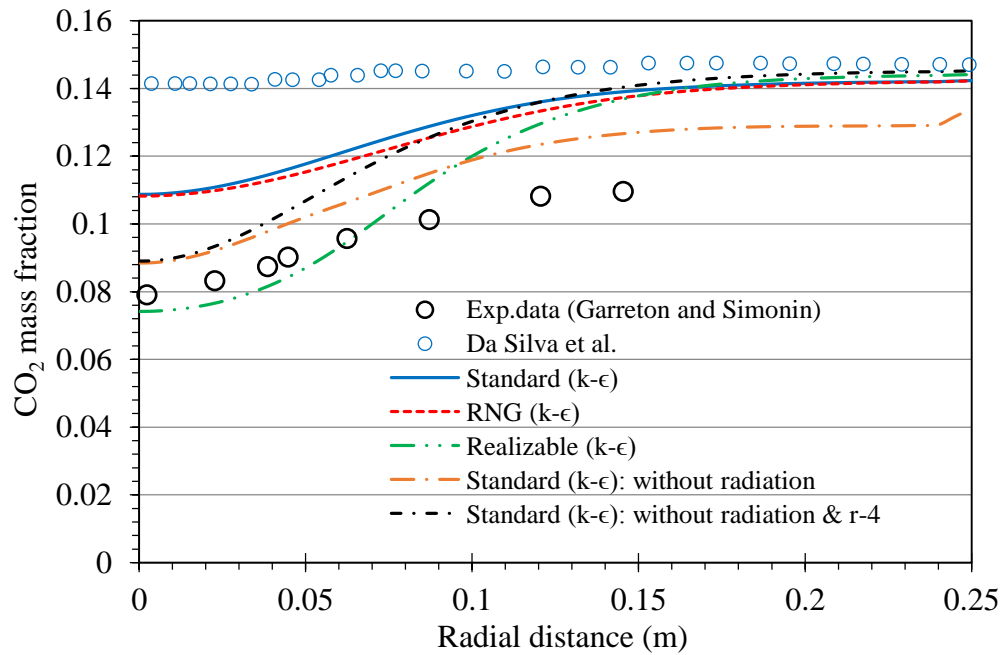


Figure 3.42: Radial profile of CO<sub>2</sub> mass fraction at axial distance  $x = 1.312$  m, (M-I).

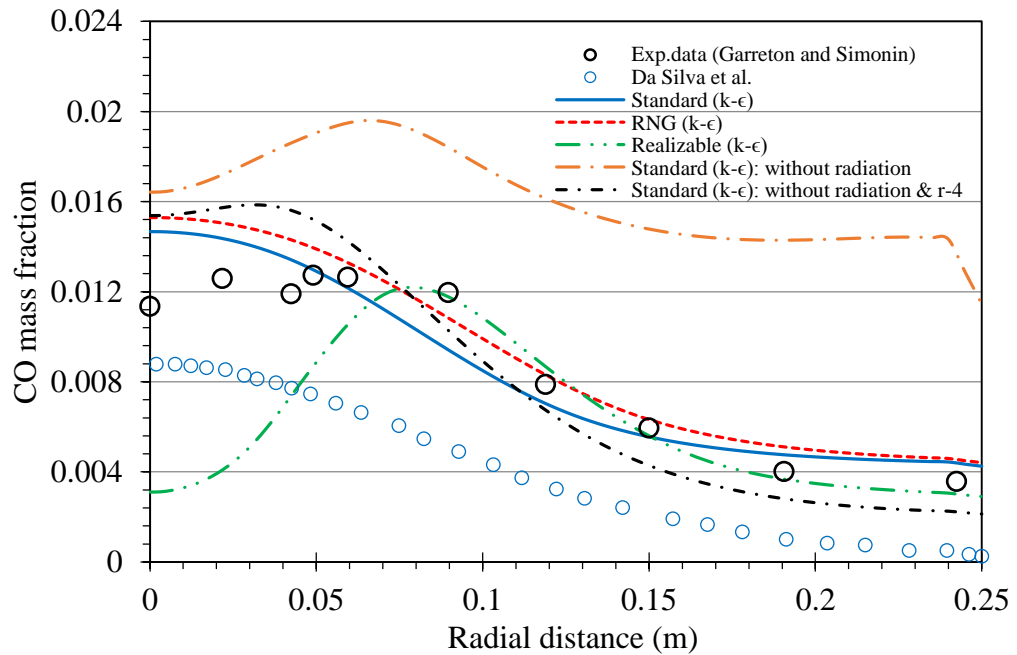


Figure 3.43: Radial profile of CO mass fraction at axial location  $x = 1.312$  m, (M-I).

Figure 3.43 above depicts the radial profile of CO mass fraction at the axial position ( $x = 1.312$  m). Compared with the experimental data, standard and RNG  $k-\epsilon$  cases give better results. Despite of the under-prediction at the radial distance near the centreline ( $r < 0.09$  m) realizable  $k-\epsilon$  case shows very good agreement with the experimental data beyond the radial distance of 0.09 m. It is seen that not taking the thermal radiation effects into consideration leads to a significant over-prediction of CO mass fraction, but

the results are improved and fit better with the experimental data by excluding the reaction (r-4) from the mechanism.

### 3.10.2 Mechanism (M-I) with modified turbulence model

In this case the same mechanism provided in Table 3.2 was used. Using this mechanism in this case is differ from its using in the previous case, discussed in § 3.10.1, in terms of turbulence modelling. In this case modified standard and realizable  $k-\epsilon$  models are adopted. The value of turbulent Schmidt number ( $Sc$ ) is modified from 0.7 to 0.85. The effects of the modification will be seen in the next figures.

Figure 3.44 shows the axial profiles of gas temperature inside the chamber along the centreline of the chamber. It can be seen that there is no difference between the standard and realizable  $k-\epsilon$  cases (base case with the default value) and the modified standard and realizable cases (base case with the new value) along the centreline of the chamber up to the value ( $x = 1$  m). Beyond this point and up to the axial value of 1.36 m for standard  $k-\epsilon$  cases and 1.48 m for realizable  $k-\epsilon$  cases, there is a slight difference in temperature. After these two points, the temperature increased. The same behaviour is seen in Figure 3.45. Compared with the base cases, It can be seen that  $O_2$  mass fraction resulted from the modified cases are slightly shifted to the right along the axial distance till the axial location ( $x = 0.7$  m), where this difference after this point became bigger.

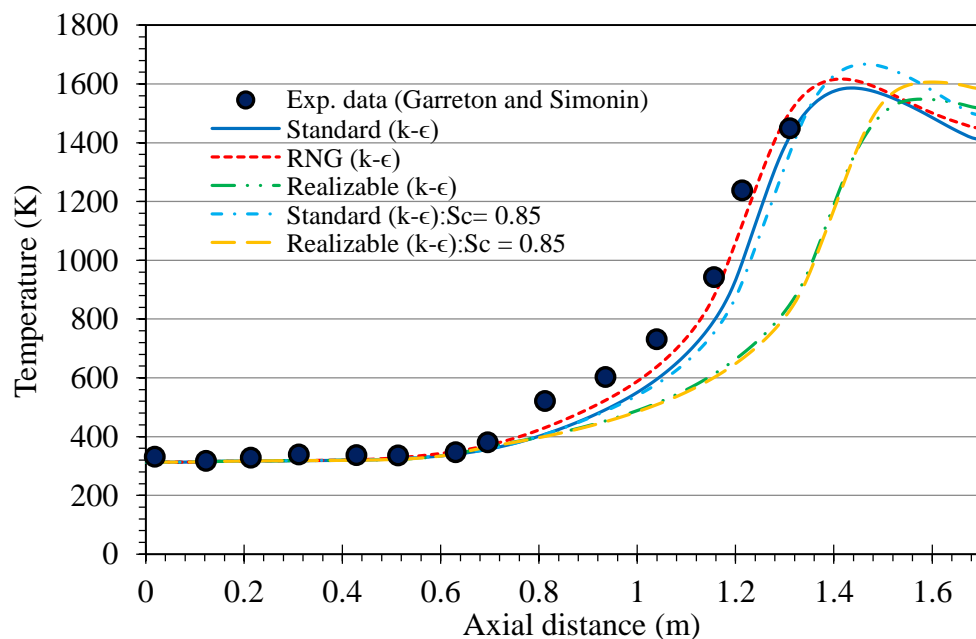


Figure 3.44: Gas temperature along the centreline of the chamber (M-I with modified turbulence models).



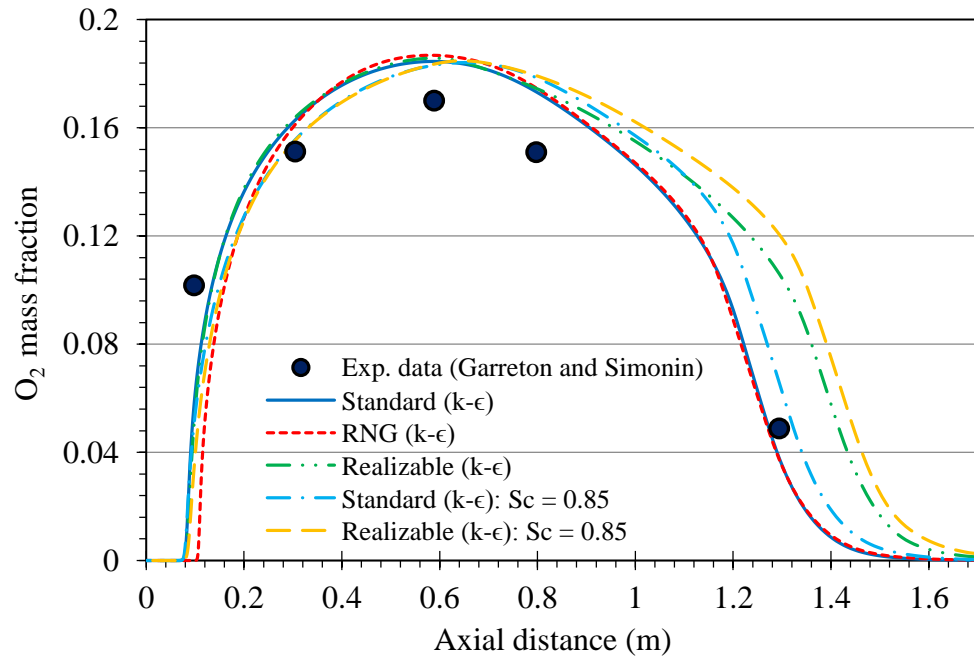


Figure 3.45:  $O_2$  mass fraction along the centreline of the chamber (M-I with modified turbulence models).

The axial profile of CO mass fraction along the centreline of the chamber is illustrated in Figure 3.46. As is shown in the figure, the maximum values of the two modified cases are increased and shifted to the right. It is also seen that the cases with the modified turbulence models predicted the same results as the experiments and the other two base cases along the axial distance up to the value of 0.96 m.

In Figure 3.47, the variation of  $CO_2$  mass fraction is also shown along the centreline of the chamber. It appears in the figure that the predicted results of the case with the modified standard  $k-\epsilon$  model fits the experimental data better than the base case (with the default standard  $k-\epsilon$  model) and shows very good agreement in the axial distance, which lies between 0.8 and 1.2 m. The results obtained from the case with modified realizable model also show very good agreement with the experimental results in some axial distance. It is also noticed that all the Figure 3.44 to Figure 3.47 indicate that the effects of the modified turbulence models on the results clearly appear in the axial distance above 1 m.

The radial profiles of the results obtained from the case with the modified standard  $k-\epsilon$  model are compared with the ones which have been generated from the case with the default standard  $k-\epsilon$  model as will be shown the next figures. These figures depict the distribution of temperature and species mass fraction as a function of the radial distance at various axial positions which are  $x = 0.312, 0.912$  and  $1.312$  m.

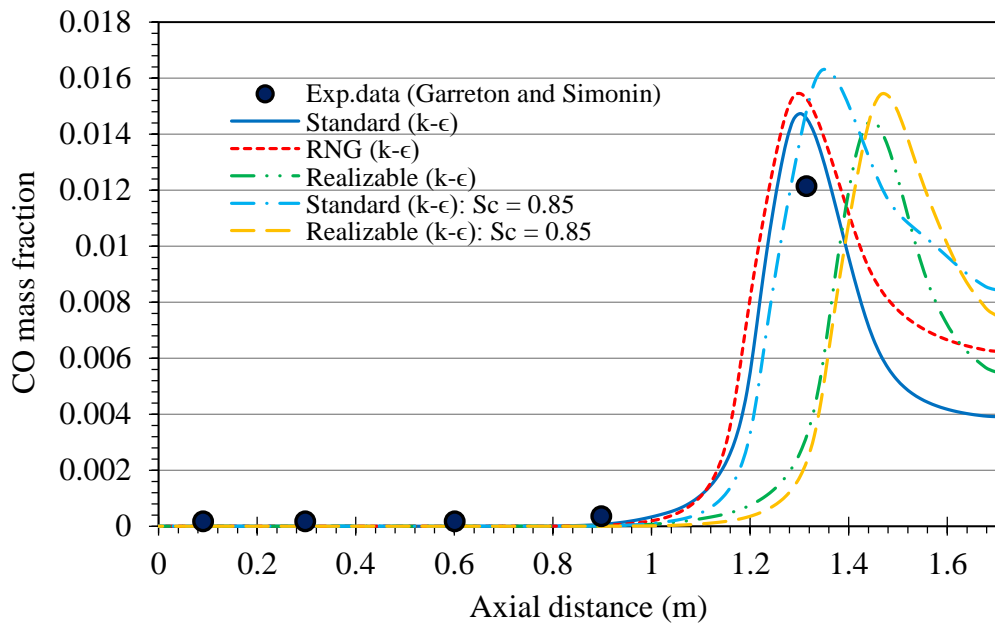


Figure 3.46: CO mass fraction along the centreline of the chamber (M-I with modified turbulence models).

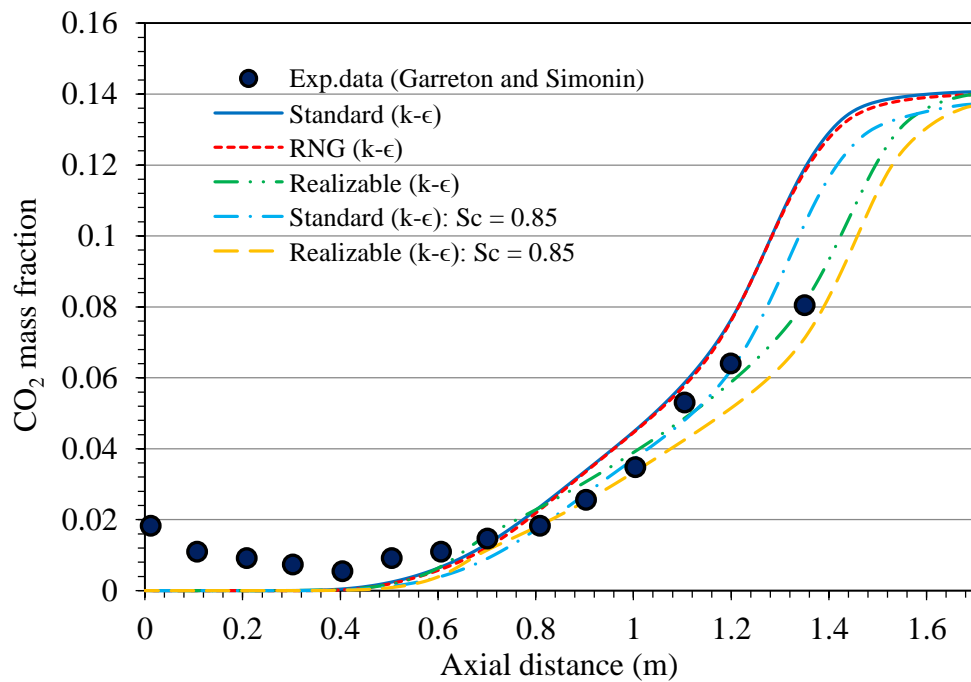


Figure 3.47: CO<sub>2</sub> mass fraction along the centreline of the chamber (M-I with modified turbulence models).

Figure 3.48, Figure 3.49 and Figure 3.50 show the radial profiles of gas temperature at these axial positions, respectively. It can be seen that the predicted results of the case with standard  $k-\epsilon$  model were improved by increasing the value of turbulent Schmidt number ( $Sc$ ). The computationally predicted results of the case with modified standard  $k-\epsilon$  model has very good agreement with the experimental data in the radial distance at the axial locations  $x = 0.912$  and  $x = 1.312$  m. For the same case, at the axial location  $x = 0.312$  m, it is appeared from Figure 3.48 that the temperature decreased slightly when compared with the base case and the predicted radial temperature of case with modified realizable  $k-\epsilon$  model also does the same in comparison with the base case.

The radial variation of  $O_2$  mass fraction is shown in Figure 3.51, Figure 3.52 and Figure 3.53. Better improvement in results is obtained from the case with the modified standard  $k-\epsilon$  model as shown in Figure 3.52 and Figure 3.53. Modified realizable  $k-\epsilon$  turbulence model case also shows very good improvements in results in the radial distance far from the centreline as is shown in Figure 3.52. Regarding the radial variation at the axial position ( $x = 0.312$  m), it can be seen from Figure 3.51 that there is a slight difference between the base and modified cases.

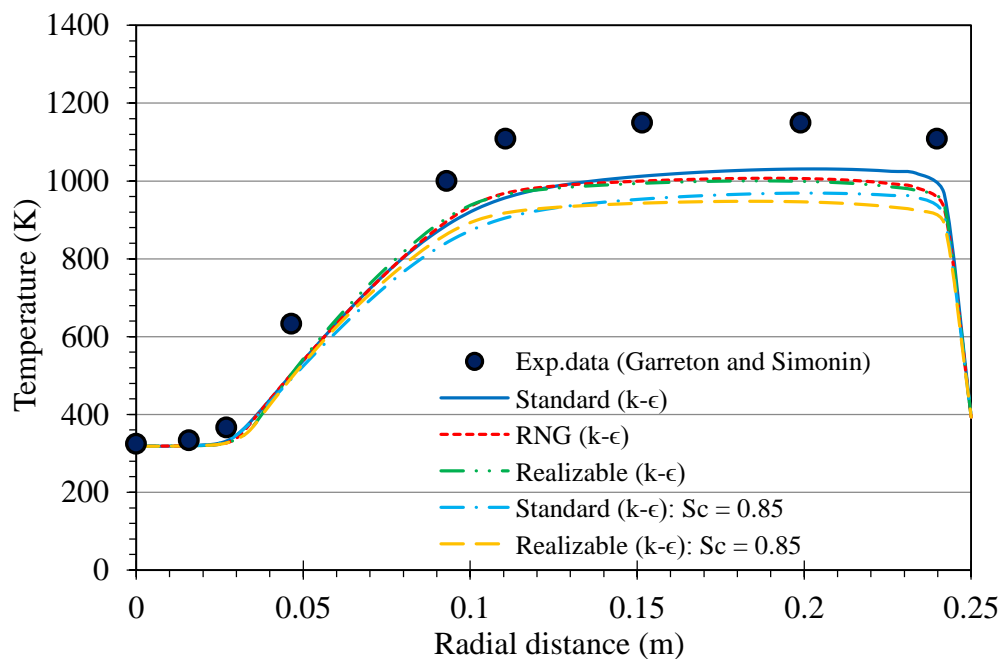


Figure 3.48: Radial temperature profile at axial location  $x = 0.312$  m, (M-I with modified turbulence models).

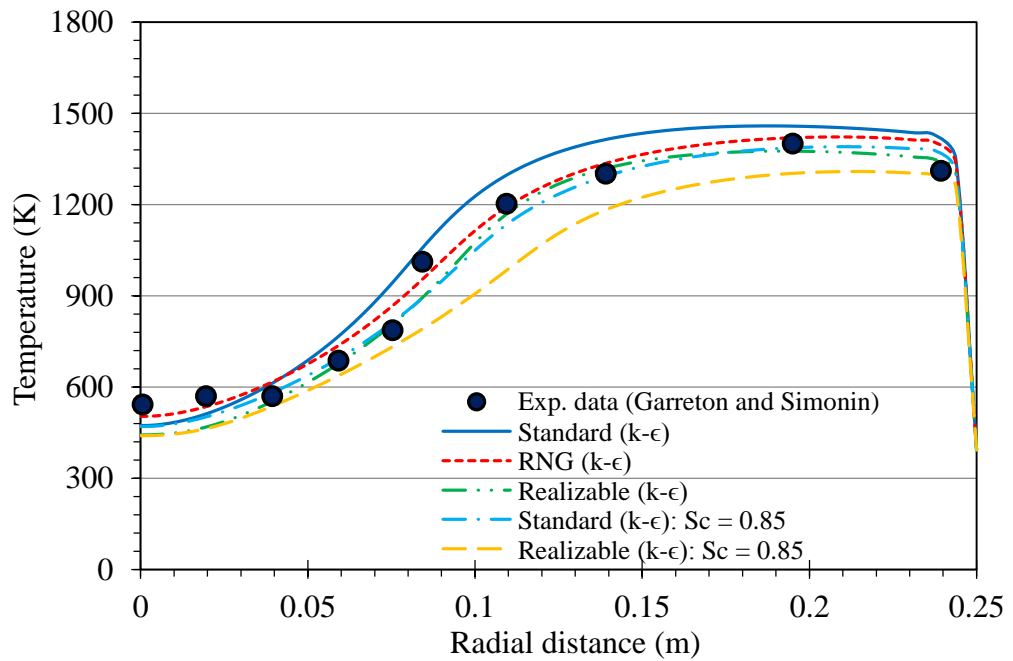


Figure 3.49: Radial temperature profile at axial location  $x = 0.912$  m, (M-I with modified turbulence models).

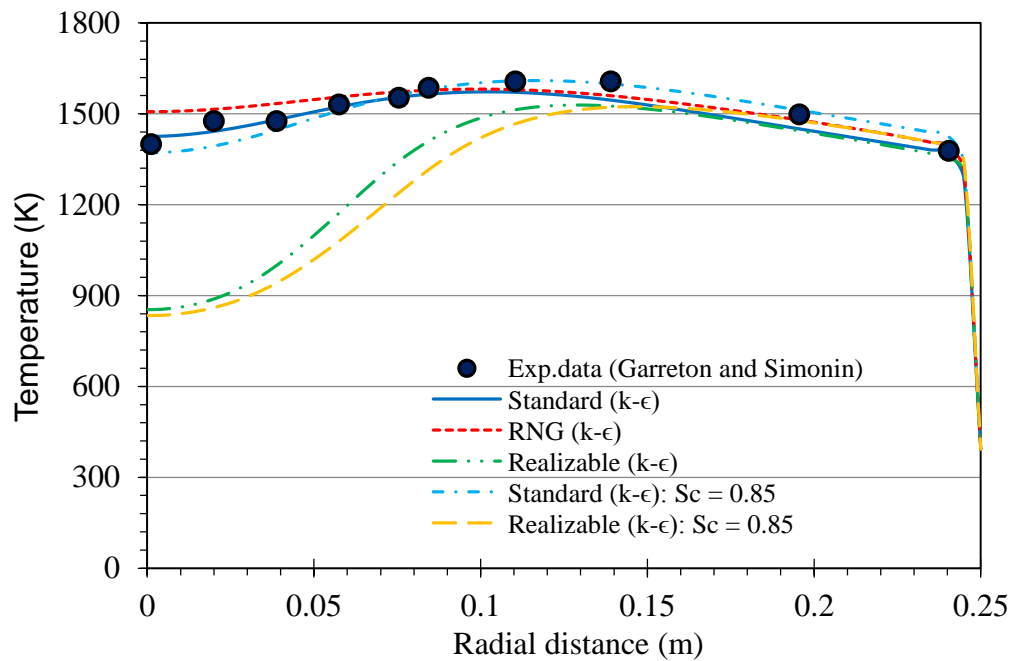


Figure 3.50: Radial temperature profile at axial location  $x = 1.312$  m, (M-I with modified turbulence models).

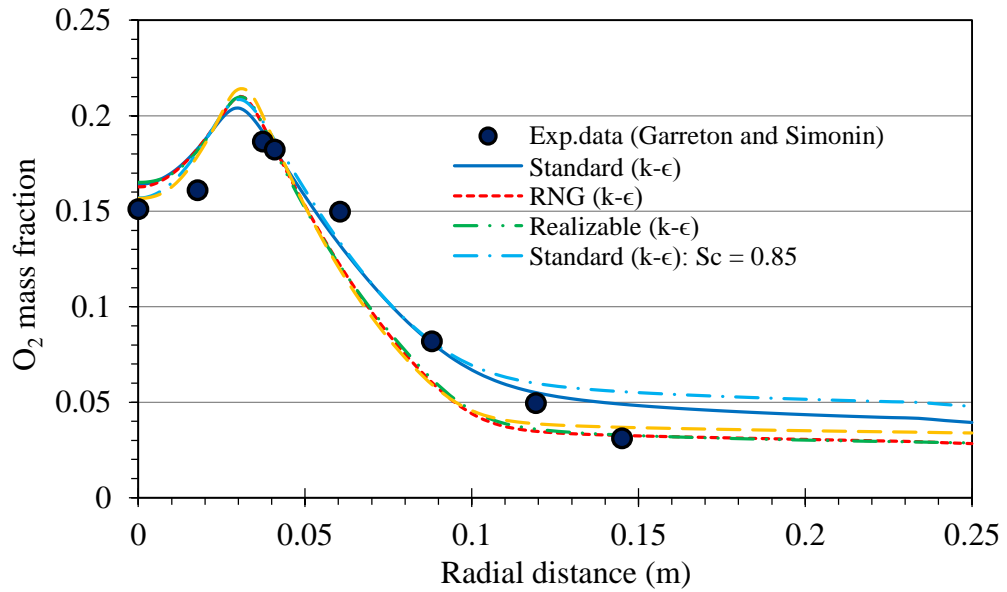


Figure 3.51: Radial profile of  $O_2$  mass fraction at axial location  $x = 0.312$  m, (M-I with modified turbulence models).

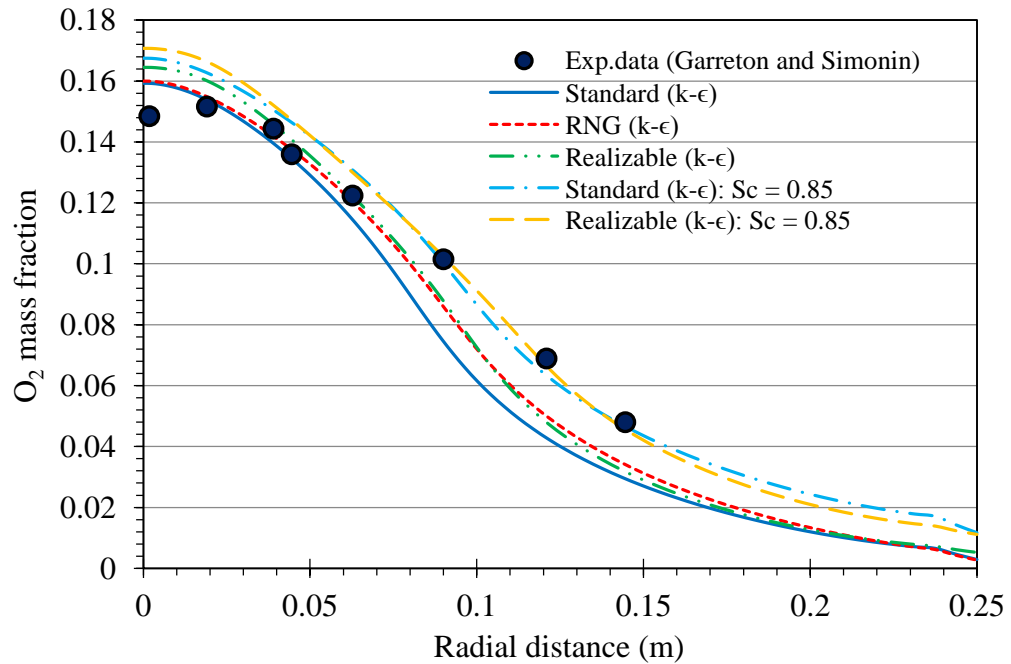


Figure 3.52: Radial profile of  $O_2$  mass fraction at axial location  $x = 0.912$  m, (M-I with modified turbulence models).

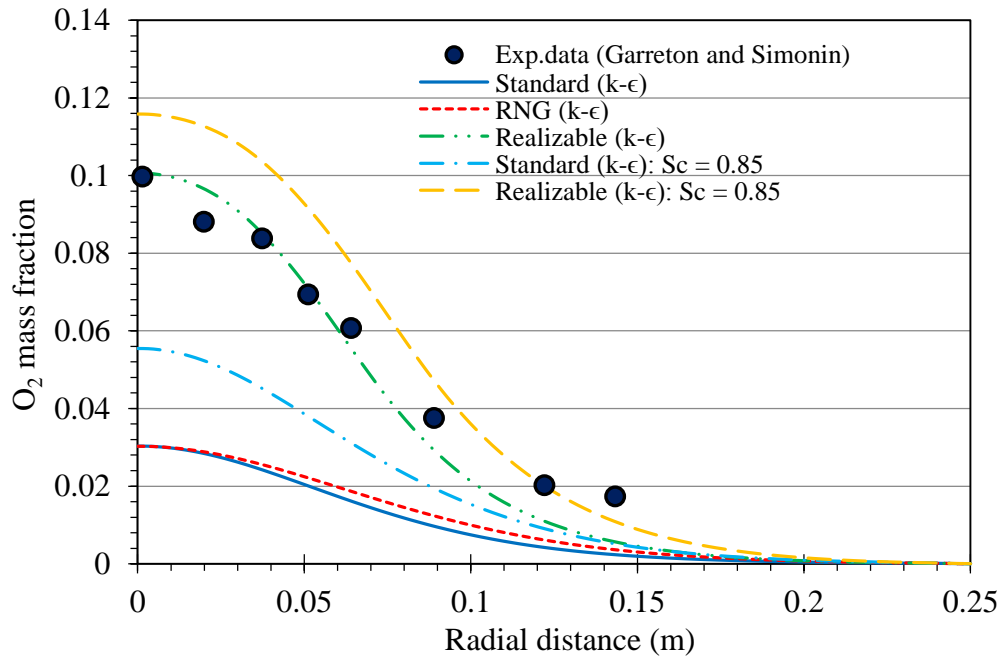


Figure 3.53: Radial profile of  $O_2$  mass fraction at axial location  $x = 1.312$  m, (M-I with modified turbulence models).

$CO_2$  mass fraction is illustrated in Figure 3.54, Figure 3.55 and Figure 3.56. From these figures, it is seen that better results are also obtained from the case with the modified standard  $k-\epsilon$  turbulence model when compared with those of base case. As is evident from Figure 3.57, contrary to the base case, the case with the modified standard  $k-\epsilon$  over predicts the experimental data in terms of the mass fraction of carbon monoxide  $CO$ , but it shows the same trend.

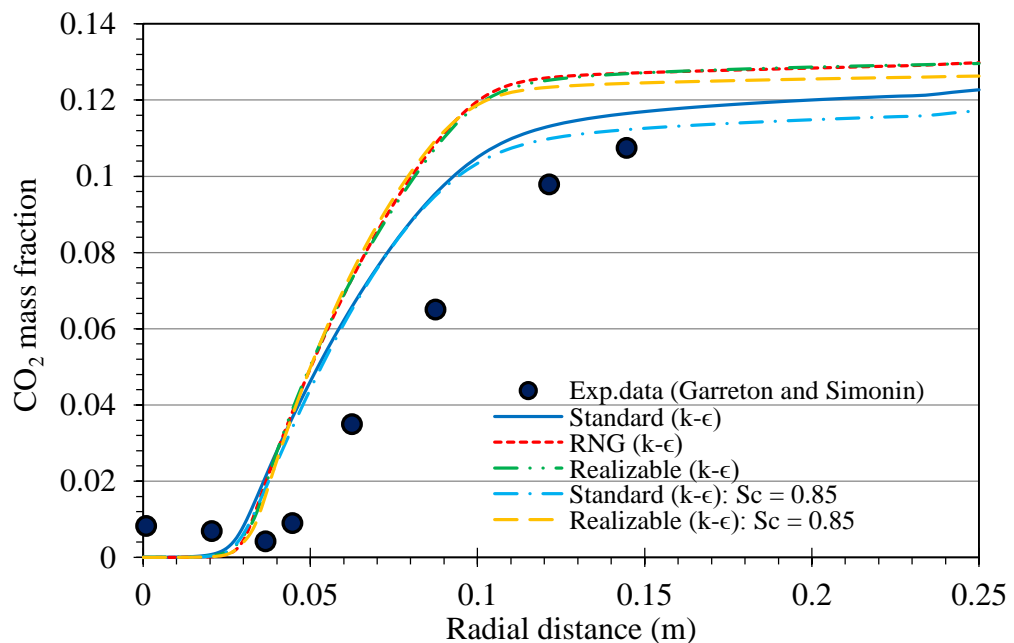


Figure 3.54: Radial profile of  $CO_2$  mass fraction at axial location  $x = 0.312$  m, (M-I with modified turbulence models).

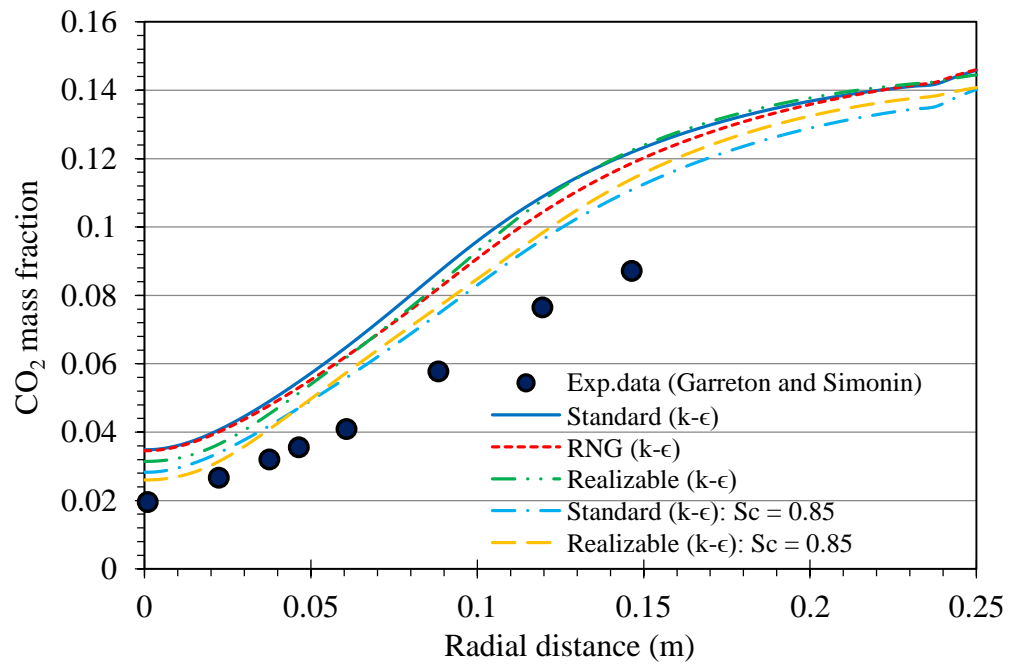


Figure 3.55: Radial profile of CO<sub>2</sub> mass fraction at axial location  $x = 0.912$  m, (M-I with modified turbulence models).

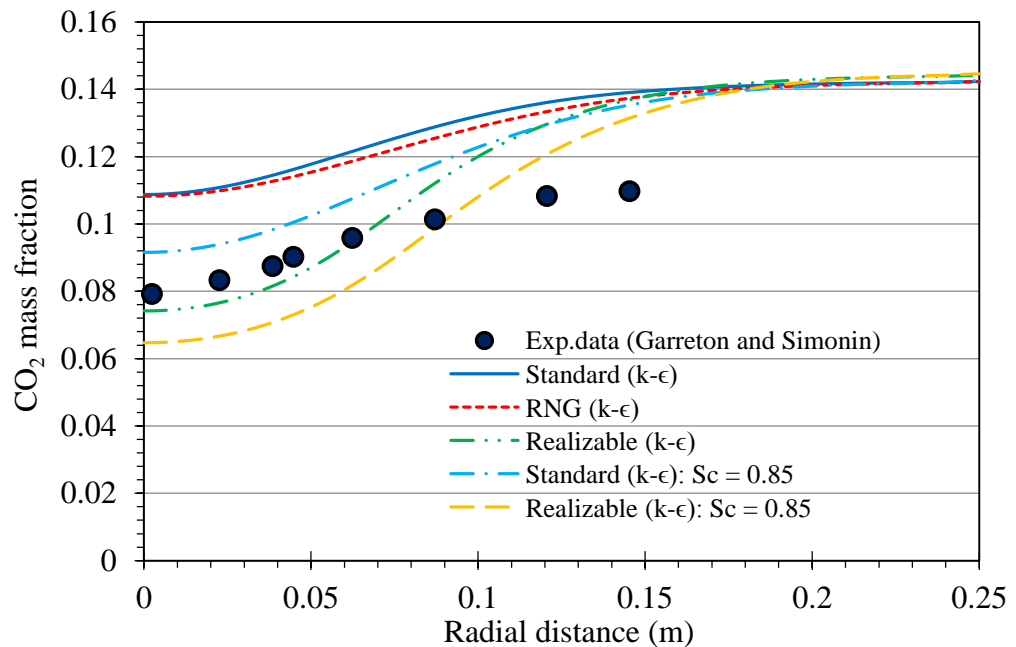


Figure 3.56: Radial profile of CO<sub>2</sub> mass fraction at axial location  $x = 1.312$  m, (M-I with modified turbulence models).

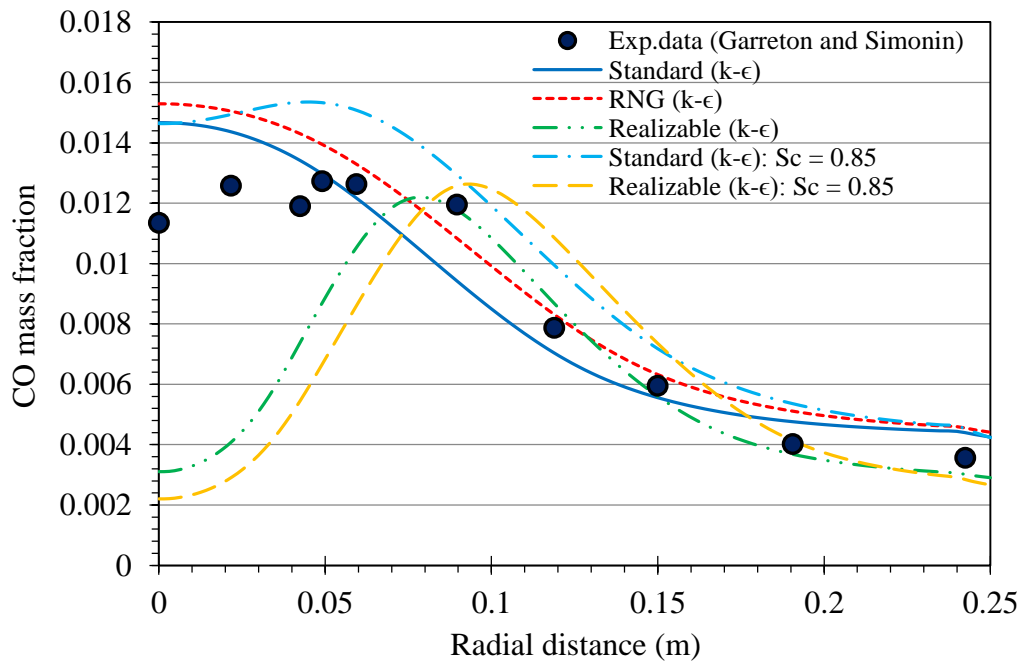


Figure 3.57: Radial profile of CO mass fraction at axial location  $x = 1.312$  m, (M-I with modified turbulence models).

### 3.10.3 Mechanism two (M-II)

In the following cases, the reaction mechanism (M-II) by Westbrook and Dryer (WD) [165], which is shown in Table 3.2, was used. Three cases were suggested in this section. The kinetics of the reactions for case 1 (the base case) are provided in Table 3.6. This chemical reaction mechanism is already built in FLUENT. Regarding the other two cases, (cases 2 and 3), the activation energy ( $E_m$ ) of reaction (r-2) was optimized. The values of the activation energy for the reaction (r-2) are given in Table 3.6. In these cases, the standard  $k-\epsilon$  turbulence model was also modified by changing the turbulent Schmidt number. The default value was 0.7 and was changed to 0.85 which also resulted in better results as will be seen in the next figures.

Table 3.6: Optimized values of activation energy for reaction (r-2).

Case	Activation energy $E_m$ (J/kmol)
Case 1(base case)	$2 \times 10^8$ [165]
Case 2	$1.7 \times 10^8$
Case 3	$1.6 \times 10^8$

Figure 3.58 depicts the gas temperature along the centreline of the chamber. As it is evident from the figure, all the cases give the same results along the axial distance up to



1.1 m and when comparing them with the experimental data, they show very good agreement along the axial distance from 0 to 0.66 m. It is also shown that case 1 shows a great difference in comparison with the experimental data. It is seen that decreasing the activation energy of reaction (r-2) in cases 2 and 3 improves the results and gives better fit with the experimental data along the axial distance above 1.1 m. With respect to the variation of oxygen species  $O_2$  along the centreline, it is also seen in Figure 3.59 that decreasing the activation energy leads to improve the predicted results, which give better fit with the experiment measurements. Figure 3.60 shows the effect of decreasing the activation energy on the concentration of  $CO_2$ . It can be seen that case 1 has very good agreement with experimental data. The other two cases also have very good agreement in comparison with experimental data along the axial distance lies between 0.6 and 1.2 m, but there is an over-prediction of the results after that. CO mass fraction along the centreline of the chamber for the three cases is plotted in Figure 3.61. For case 1, it is seen that the maximum value is 0.0128 for case 1, which is nearly the same as that of the experiments and located at the axial distance of 1.5 m.

Unfortunately, there is not experimental data available beyond the axial distance of 1.3 m to compare the results that lie beyond this point with it. It is also indicated that the maximum concentration of CO shifted towards the burner for cases 1 and 2 and the results are better fit with the experimental data, though the maximum value is increased.

The gas temperature and species concentrations at 0.312, 0.912 and 1.312 m downstream of the burner as a function of radial distance from the centreline compared with measurements are shown in Figure 3.62 to Figure 3.71. At 0.312 m (see Figure 3.62) the results obtained from the cases are the same, even though there is an under-prediction in comparison with the experimental data. At 0.912 m it is evident from Figure 3.63 that case 3 agreed well with the experimental data and so it does at 1.312 m as shown in Figure 3.64. From Figure 3.65, which depicts the radial variation of  $O_2$  mass fraction at axial distance of 0.312 m, it is also seen that all cases produced the same results and have the same trend of the experimental data. At the axial distance of 0.912 m illustrated in Figure 3.66 cases 2 and 3 have very good agreement with the experimental data. Figure 3.67 shows that case 1 has better agreement with the experimental data than case 2 and case 3 which significantly under-predict  $O_2$  mass fraction. Concerning the concentration of  $CO_2$  species, the radial variation of  $CO_2$  mass fraction is shown in Figure 3.68, Figure 3.69 and Figure 3.70. At axial distance of

0.312 m all the cases approximately produced the same results, but at 0.912 m case 1 agreed well with the experimental data. At 1.312 m it is seen that case 2 is in closest agreement with the experimental data. On contrary to the other two cases, case 1 failed to predict the correct results CO concentration at the axial distance of 1.312 m. Cases 2 and 3 show the same trend of the experimental data. The latter one provides very good agreement with the experimental data along the radial distance above 0.09 m.

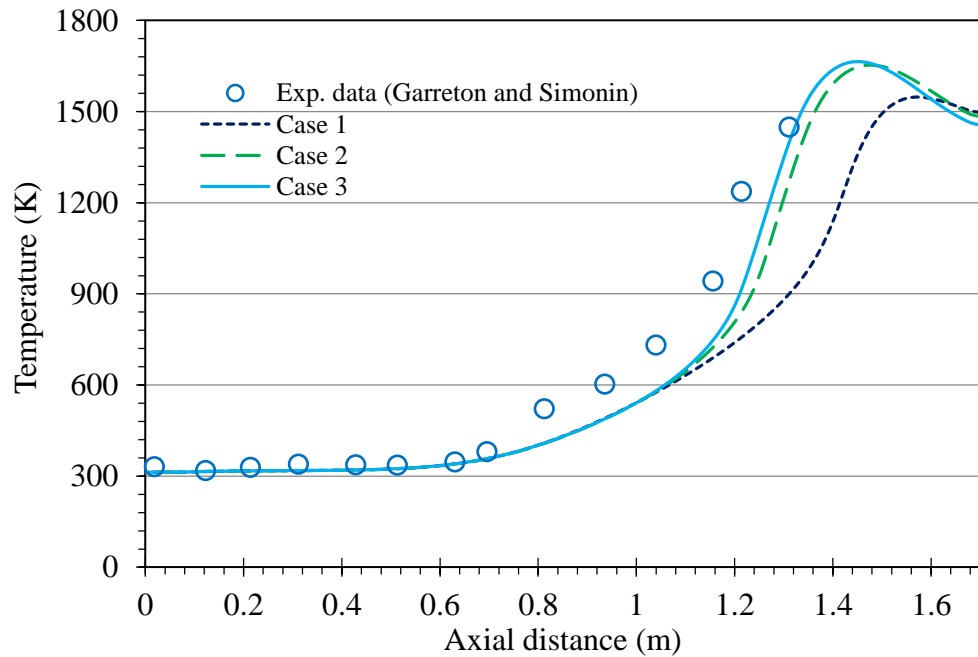


Figure 3.58: Gas temperature along the centreline of the chamber, (M-II).

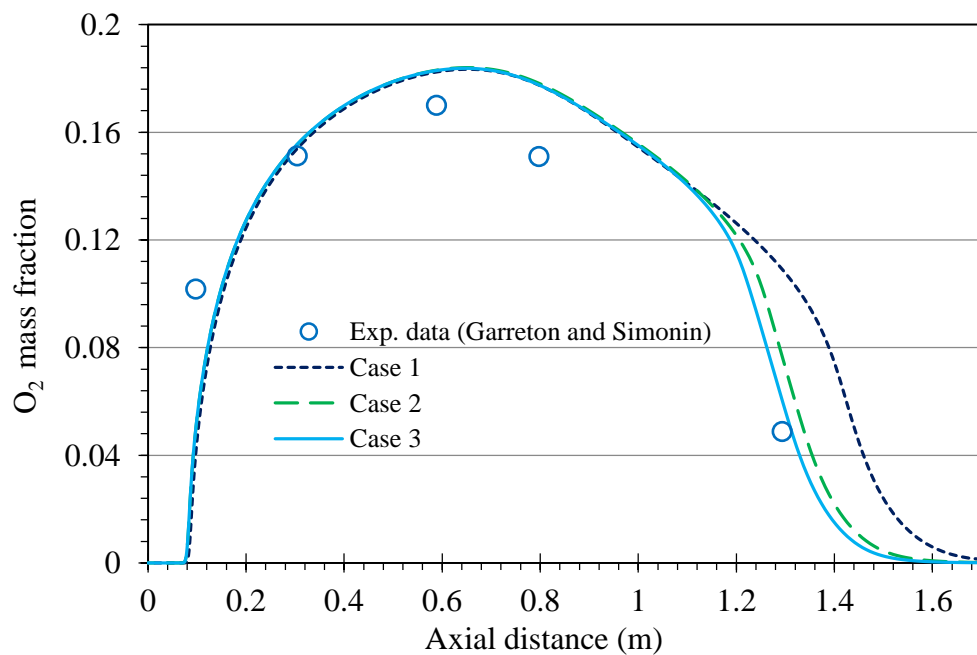


Figure 3.59: O<sub>2</sub> mass fraction along the centreline of the chamber, (M-II).

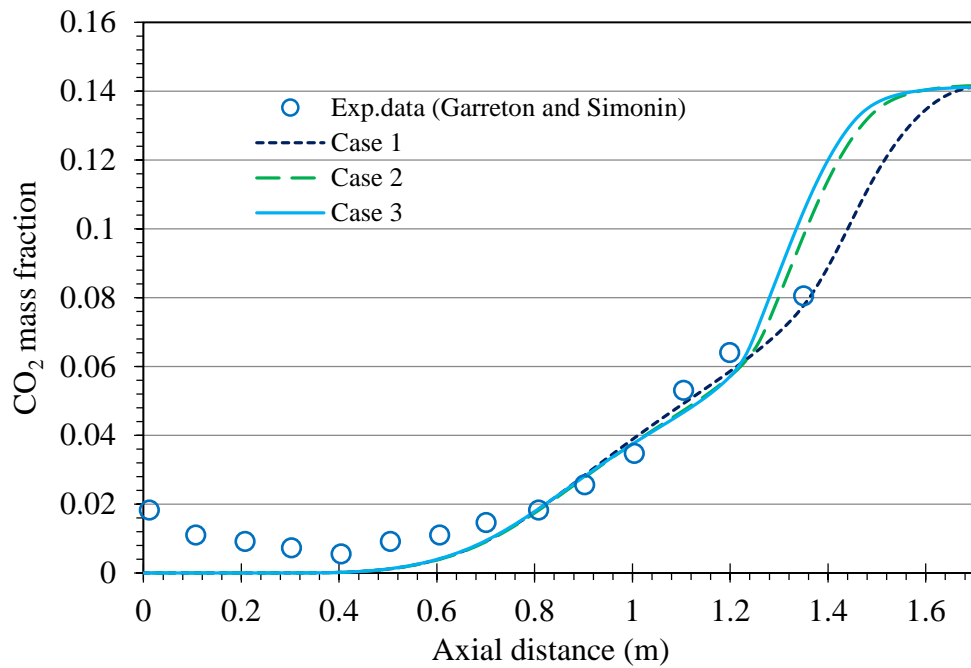


Figure 3.60: CO<sub>2</sub> mass fraction along the centreline of the chamber, (M-II).

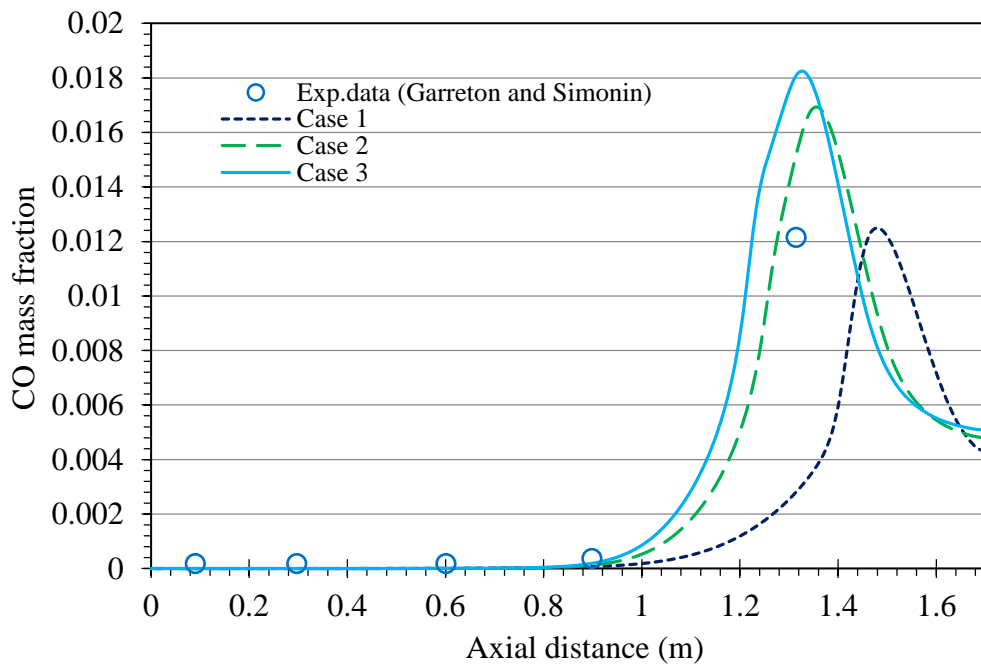


Figure 3.61: CO mass fraction along the centreline of the chamber, (M-II).

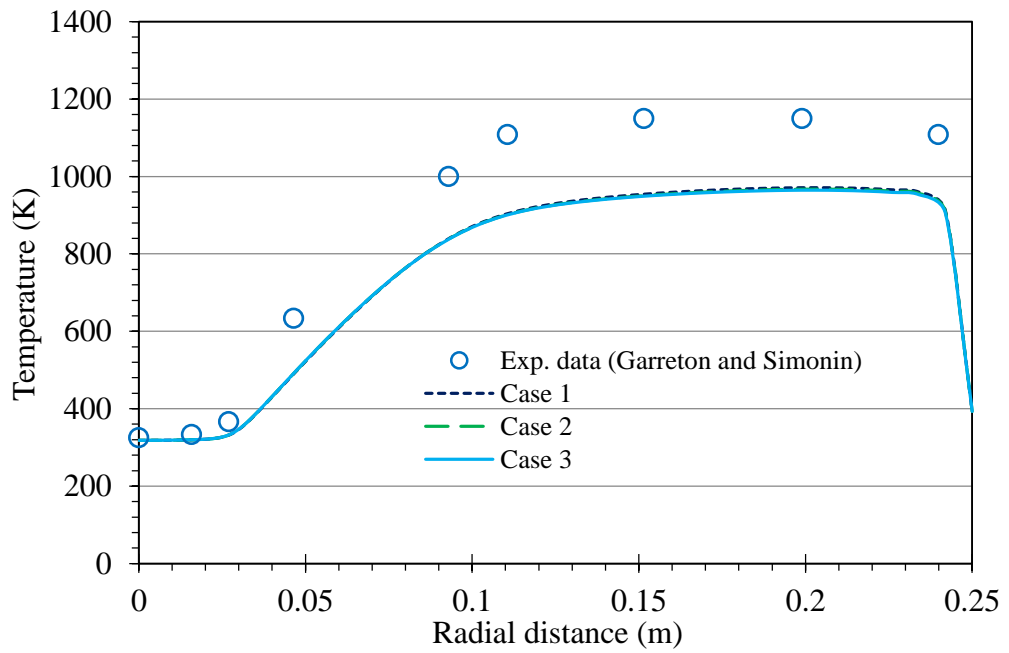


Figure 3.62: Radial temperature profile at axial location  $x = 0.312$  m, (M-II).

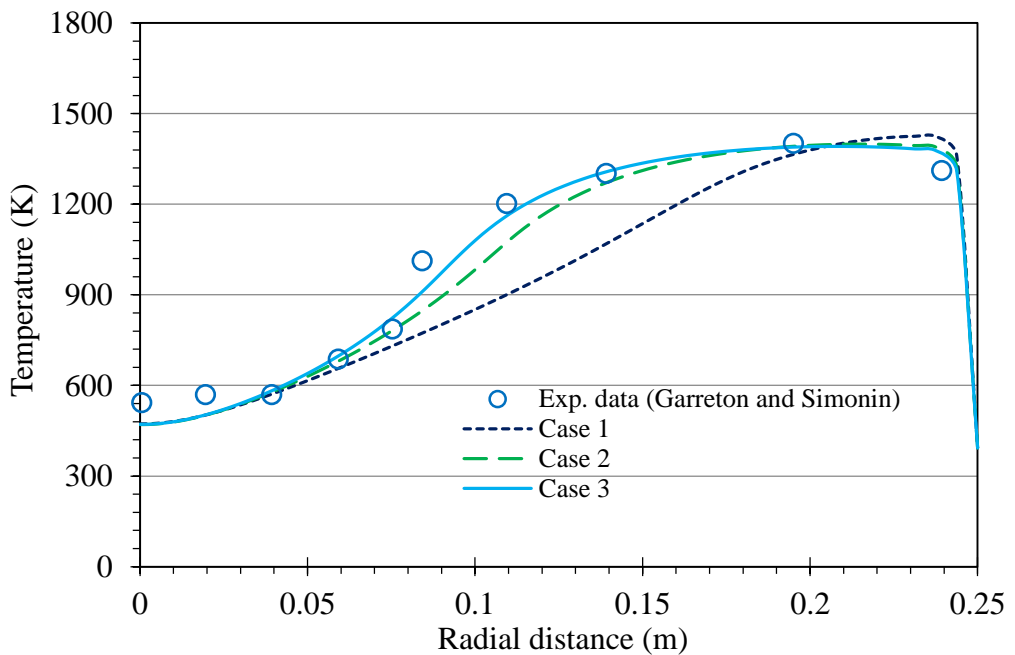


Figure 3.63: Radial temperature profile at axial location  $x = 0.912$  m, (M-II).

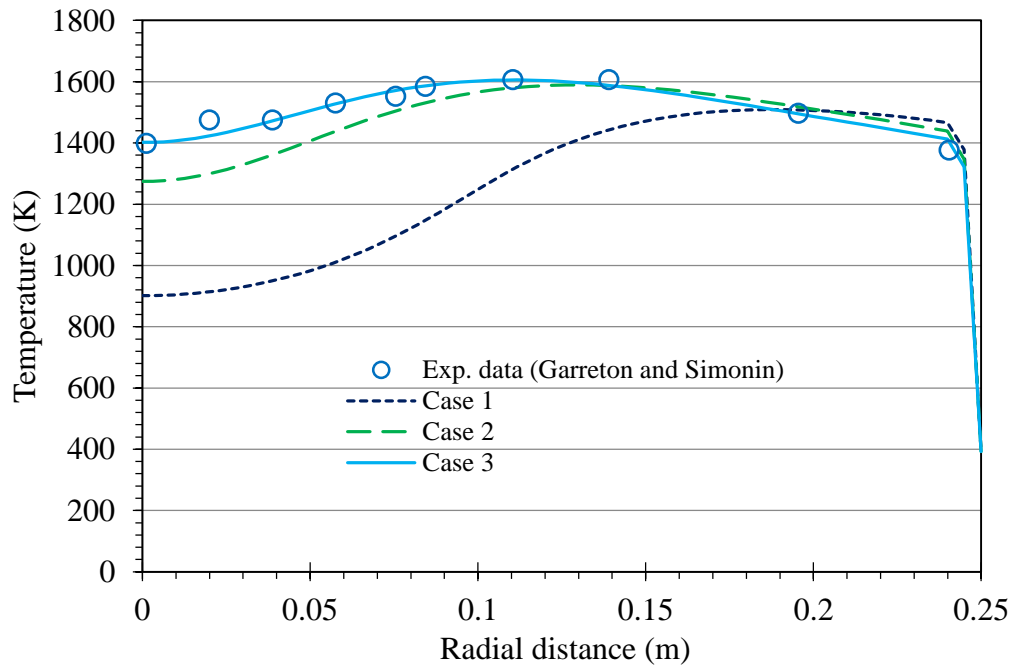


Figure 3.64: Radial temperature profile at axial location  $x = 1.312$  m, (M-II).

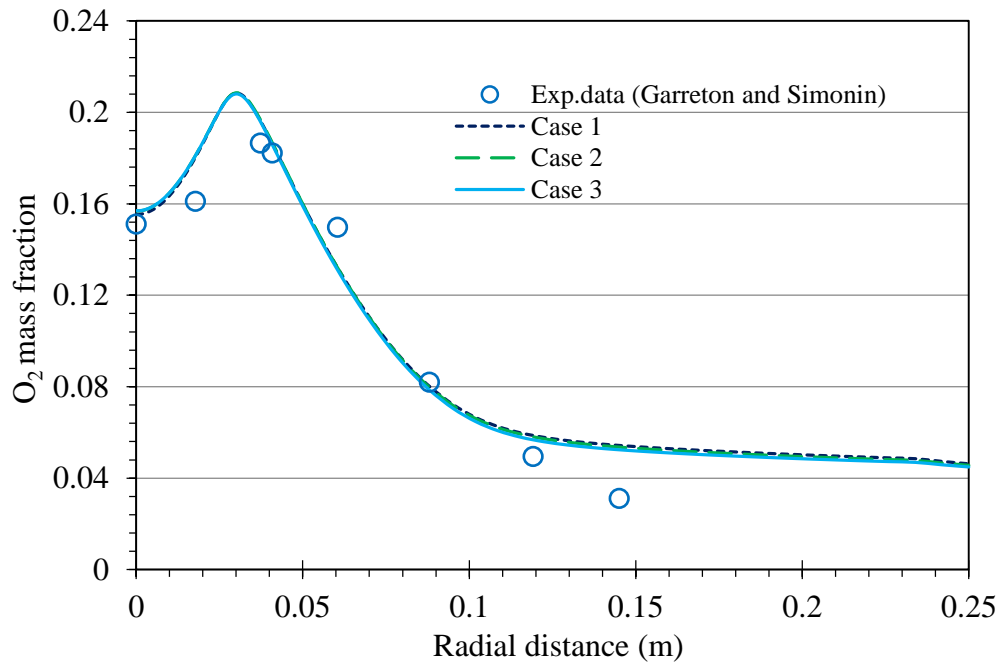


Figure 3.65: Radial profile of  $O_2$  mass fraction at axial location  $x = 0.312$  m, (M-II).

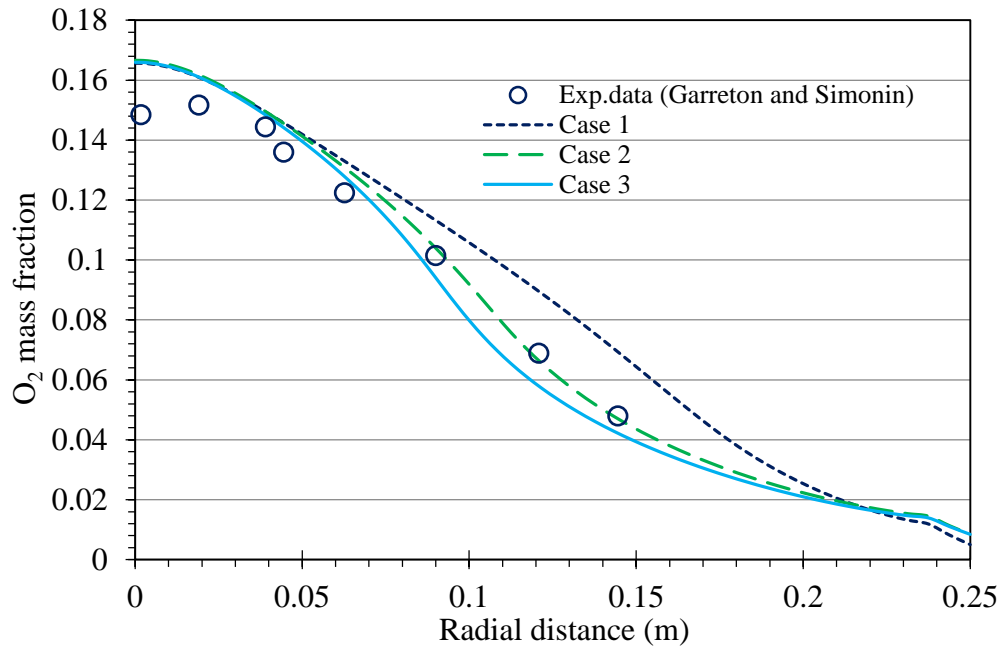


Figure 3.66: Radial profile of O<sub>2</sub> mass fraction at axial location  $x = 0.912$  m, (M-II).

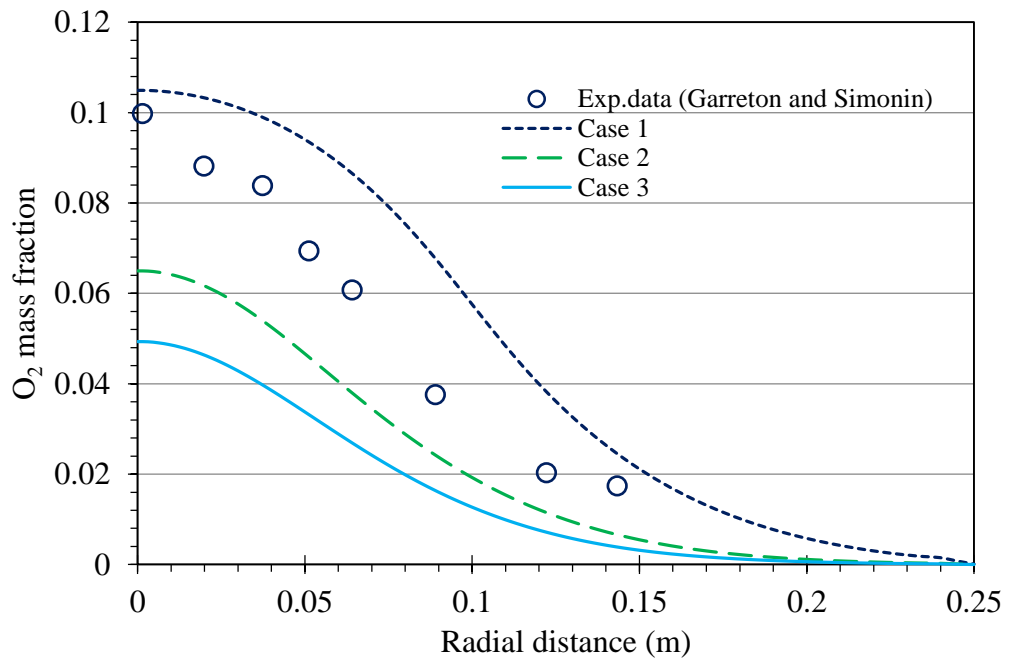


Figure 3.67: Radial profile of O<sub>2</sub> mass fraction at axial location  $x = 1.312$  m, (M-II).

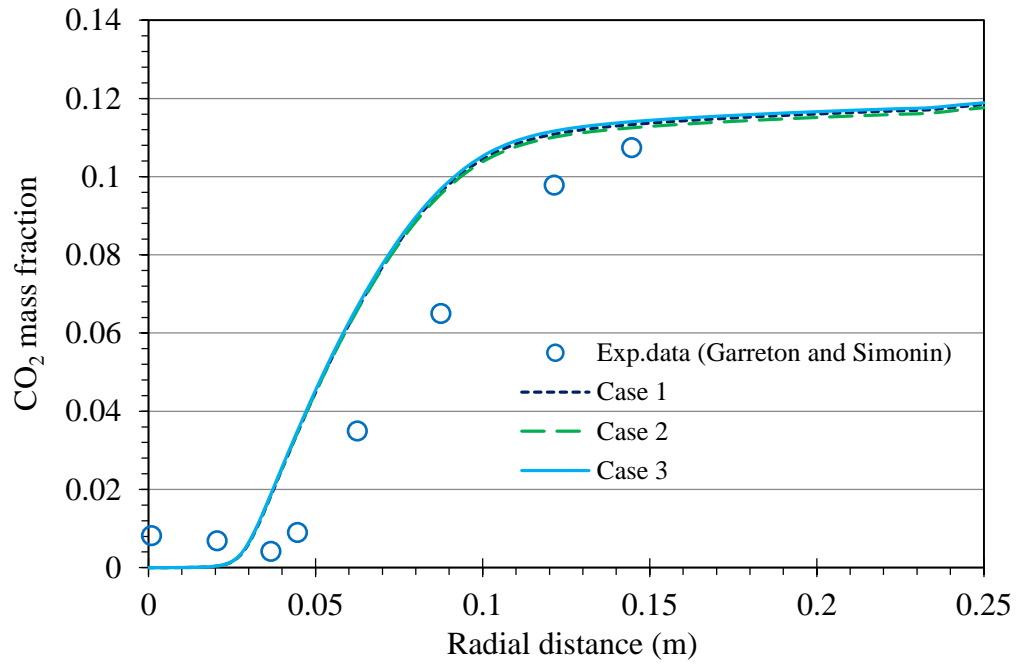


Figure 3.68: Radial profile of CO<sub>2</sub> mass fraction at axial location  $x = 0.312$  m, (M-II).

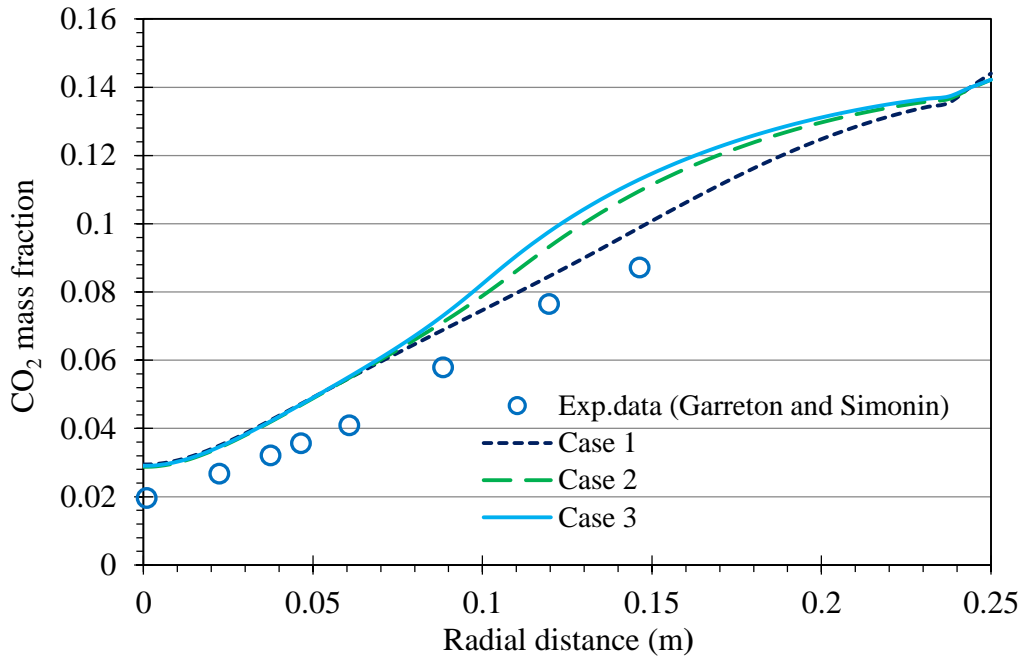


Figure 3.69: Radial profile of CO<sub>2</sub> mass fraction at axial location  $x = 0.912$  m, (M-II).

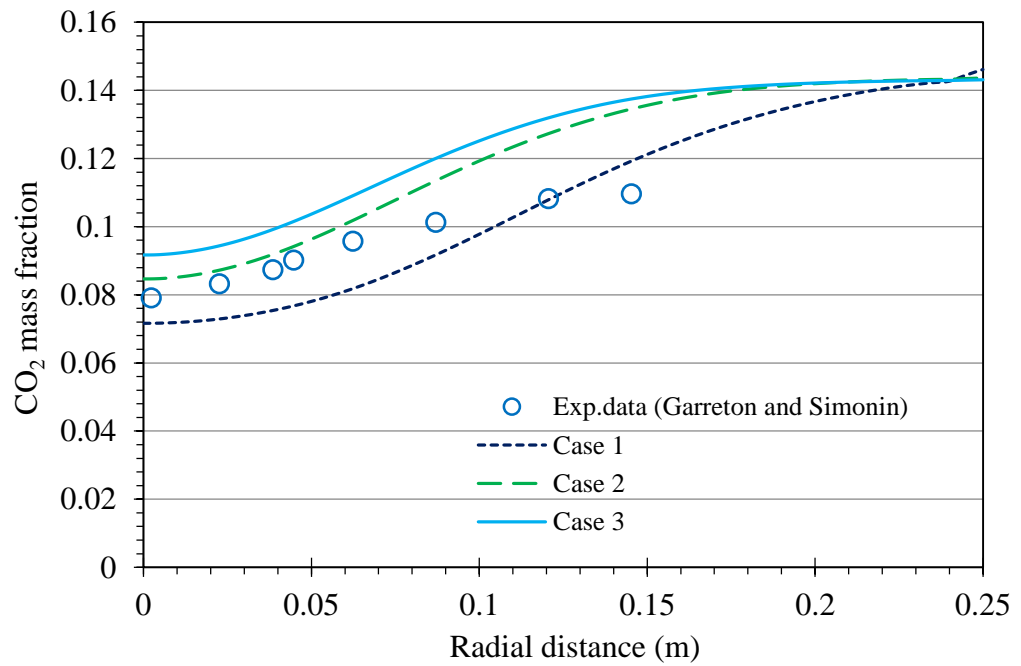


Figure 3.70: Radial profile of CO<sub>2</sub> mass fraction at axial location  $x = 1.312$  m, (M-II).

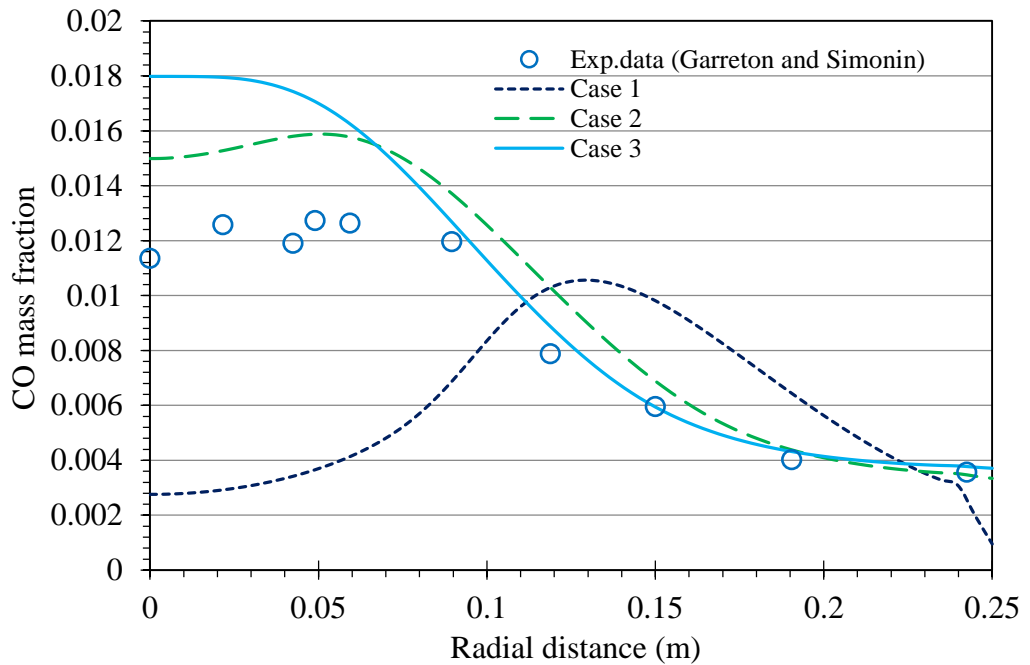


Figure 3.71: Radial profile of CO mass fraction at axial location  $x = 1.312$  m, (M-II).



### 3.10.4 Mechanisms M-III and M-IV

In the present cases, another two reaction mechanisms were selected for the simulations. One of them is a one-step reaction mechanism [180] and the other one is the five-step reduced mechanism, which was developed by Nicol et al. [167]. The chemical kinetics of the reactions involved in these two mechanisms are also provided in Table 3.2. In these two cases, the turbulence was modelled using the standard  $k$ - $\epsilon$ . The FR/ED model was also used to model the interaction between the chemistry and turbulence.

The axial variations of temperature and species mass fraction at the centreline of combustion chamber are shown in Figure 3.72 to Figure 3.75. It can be seen from the figures that there are only slight differences between the predicted results of the two cases and the experimental data as well as the other cases, except for the axial variation of CO mass fraction (see Figure 3.75) which shows that the maximum value was shifted to the left in the direction towards the burner. However, the figure shows that all the cases have very good agreement with the experimental data along the axial distance from 0 to 0.9 m. Unfortunately, after this point, as mentioned in § 3.10.1, there is only one measured value available which appears to be the maximum value of CO mass fraction, and this point is not enough to compare the obtained results from the various cases with. The radial profiles of temperature at axial distances 0.312, 0.912 and 1.312 m are depicted in Figure 3.76, Figure 3.77 and Figure 3.78, respectively. At 0.312 m, as is evident from Figure 3.76, the two cases under-predict the experimental data and fit better with the other cases. Regarding the axial location at axial distance of 0.912 m, it is seen from Figure 3.77 that both cases over predict the experimental data. For one-step case, the over-prediction is far from the centreline of chamber and lies in the radial distance between 0.11 and 0.24 m. On the other hand, along the radial distance less than 0.11 m this case has very good agreement with the experimental data. The five-step case shows an over-prediction along the almost radial distance, except for the radial distance that are very close to both the centreline and the wall, where it shows good agreement with the experiments. At 1.312 m, it is shown that the two cases generated very good results at some radial distance when comparing them with the experimental data and the previous cases that are discussed before. The one-step case has very good agreement with the experiments along the radial distance close to the centreline up to 0.06 m and beyond this point there is a small over-prediction. On contrary, the results of the five-step case agrees well with the experimental data along

the radial distance far from the centre line and over-predicts them along the radial distance close to the centreline (less than 0.07 m). Radial profiles of mass fraction of  $O_2$  at different downstream positions are plotted in Figure 3.79, Figure 3.80 and Figure 3.81. The two cases agree very well with the experimental data and the other cases as shown in Figure 3.79 for the axial location at ( $x = 0.312$  m). For ( $x = 0.912$  m) shown in Figure 3.80, it is seen that one-step case show better results than five-step case when comparing them with the experimental data. Figure 3.81 depicts the radial variation at ( $x = 1.312$  m). It is also seen that the two cases under-predict the experimental data significantly with better results of one-step case than five-step case. The radial profiles of  $CO_2$  mass fraction are shown in Figure 3.82, Figure 3.83 and Figure 3.84. It is seen that the two cases over-predict the experimental data as the other cases did. In terms of CO mass fraction, its radial variation at the axial distance of 1.312 m is shown in Figure 3.85. It can be seen that the five-step case approximately has the same trend of the experimental data. However, it predicts a significantly lower CO concentration along the radial distance near the centreline of the chamber and a higher concentration along the radial distance far from it.

Although, it was mentioned in [158] that allowing multi-step reaction mechanisms with this model will likely lead to incorrect solutions, the results obtained from the five-step reaction mechanism show a reasonable fit with experimental data as well as the other cases. Generally, in comparison with the results presented in the previous sections, the one-step and five-steps cases show good results as will be seen in the next figures.

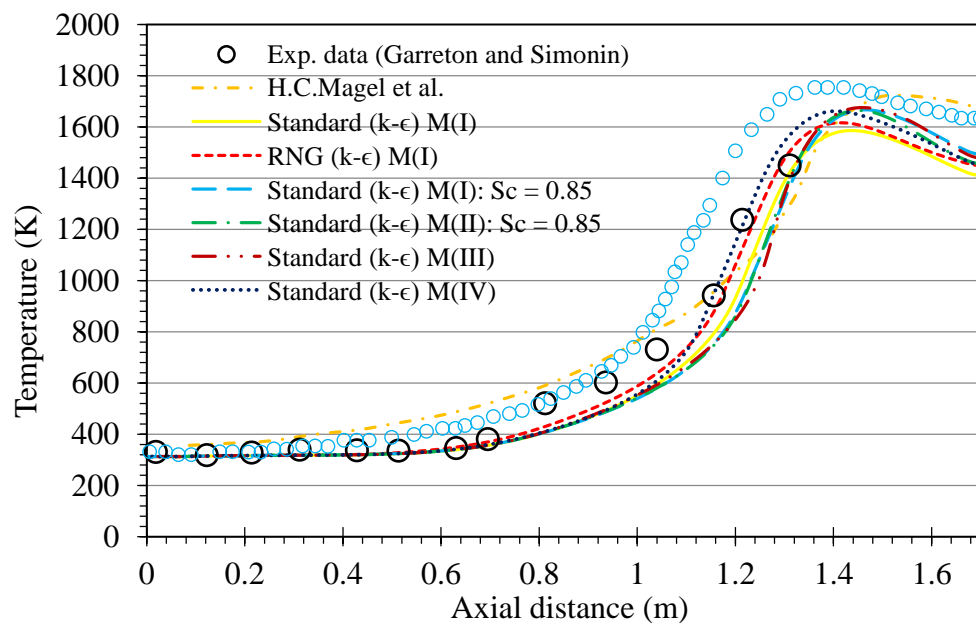


Figure 3.72: Gas temperature along centreline of the chamber for all cases.

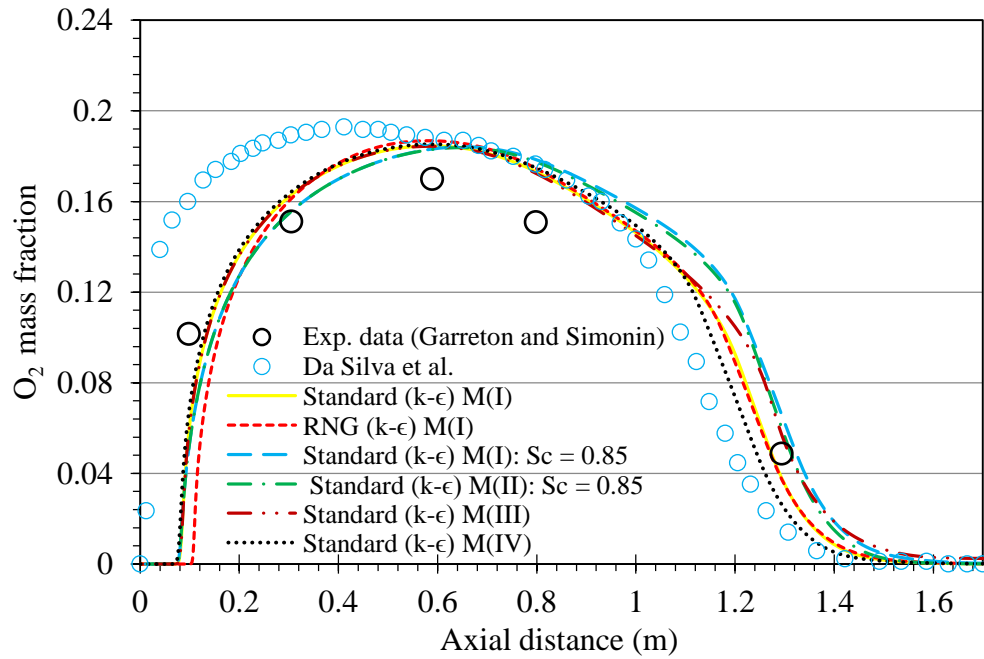


Figure 3.73:  $O_2$  mass fraction along the centreline of the chamber for all cases.

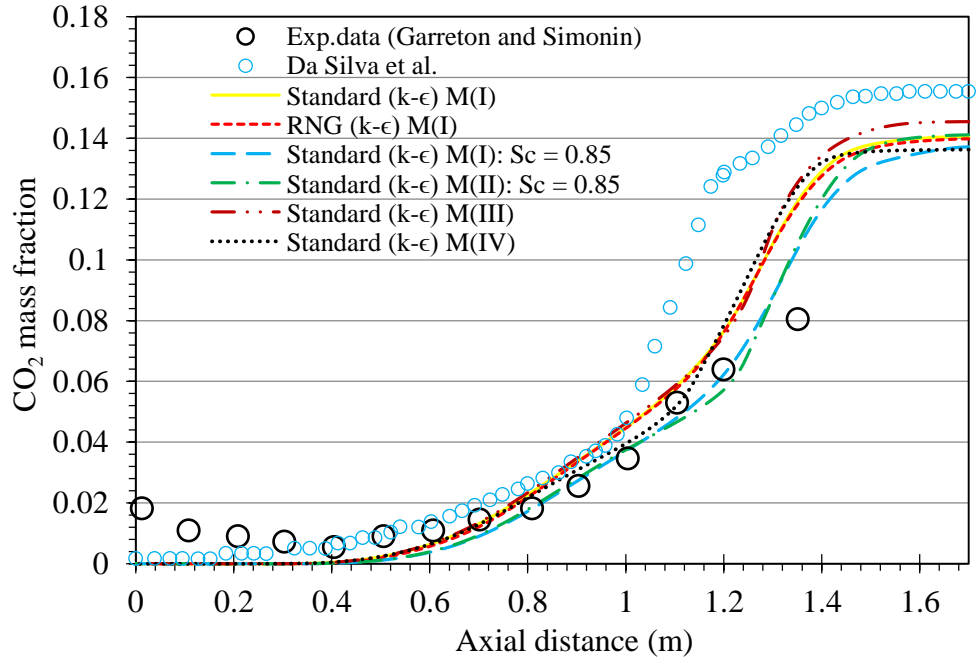


Figure 3.74:  $CO_2$  mass fraction along the centreline of the chamber for all cases.

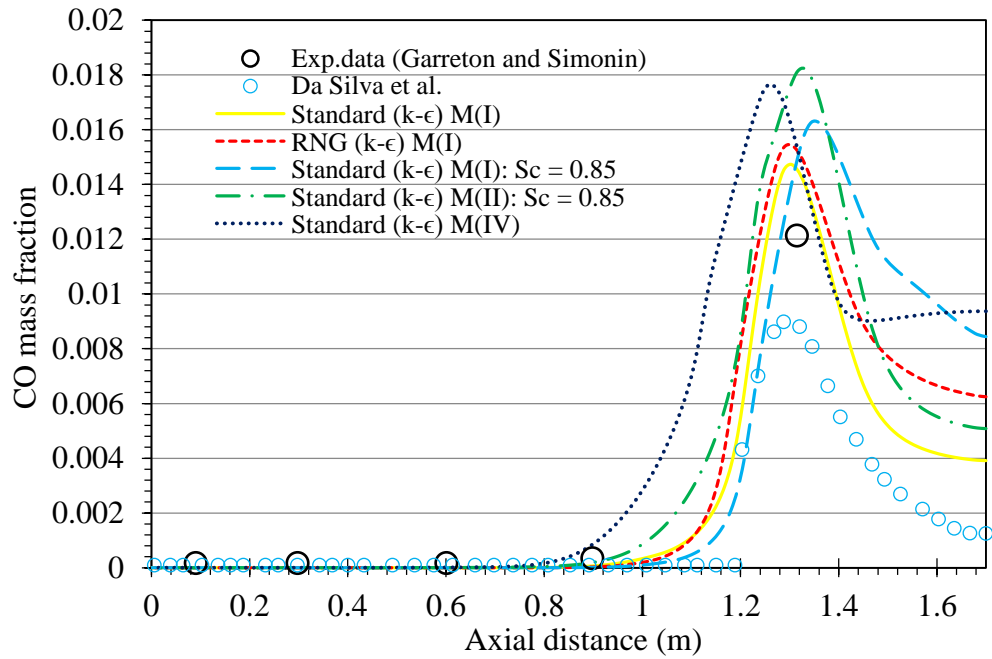


Figure 3.75: CO mass fraction along the centreline of the chamber for all cases.

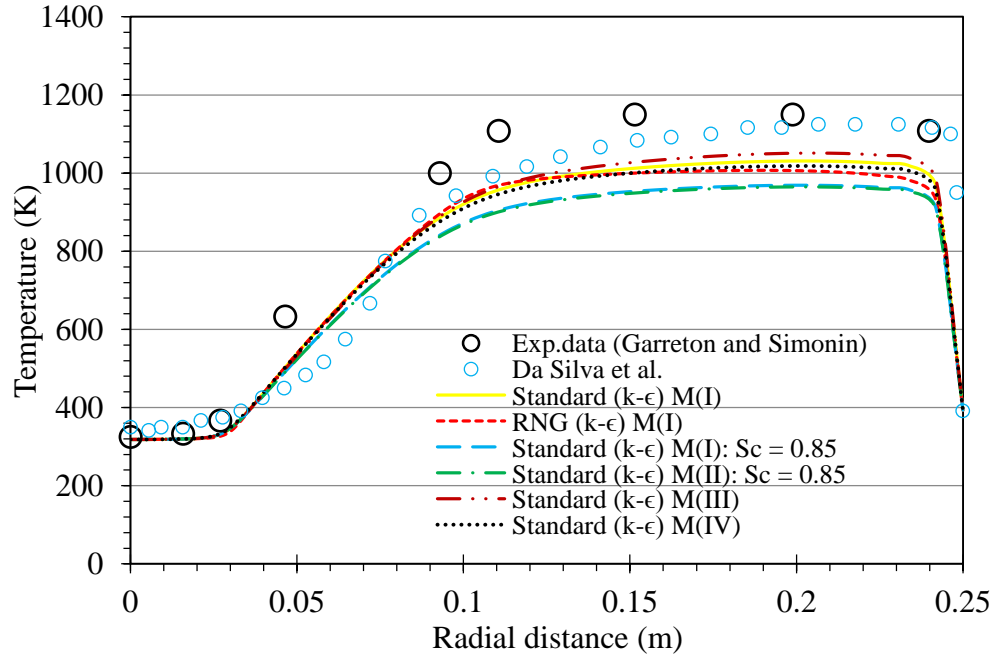


Figure 3.76: Radial temperature profiles at axial location  $x = 0.312$  m for all cases.

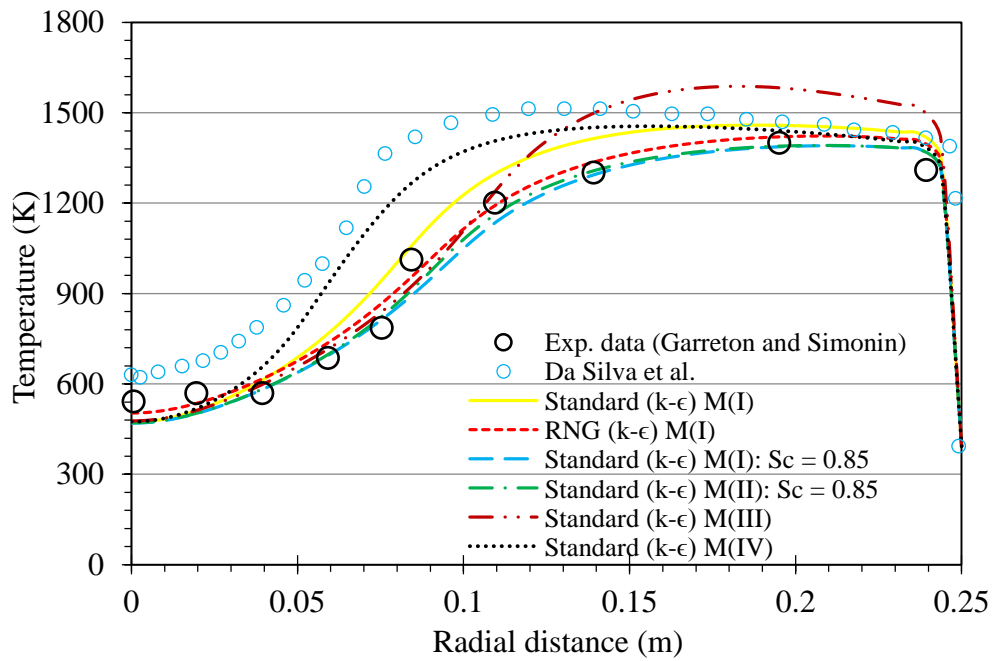


Figure 3.77: Radial temperature profile at axial location  $x = 0.912$  m for all cases.

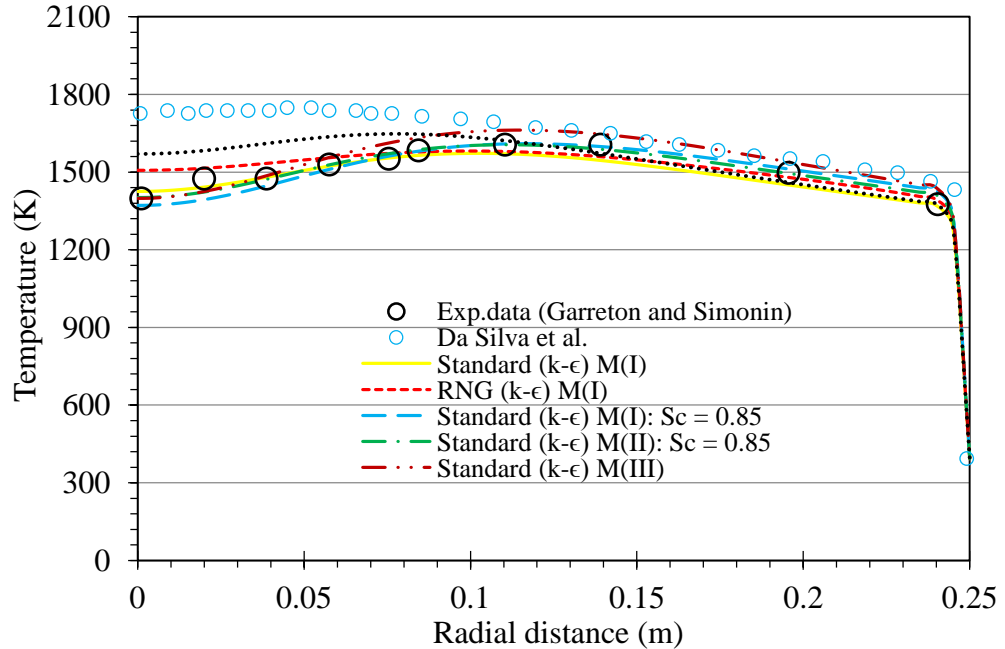


Figure 3.78: Radial temperature profile at axial location  $x = 1.312$  m for all cases.

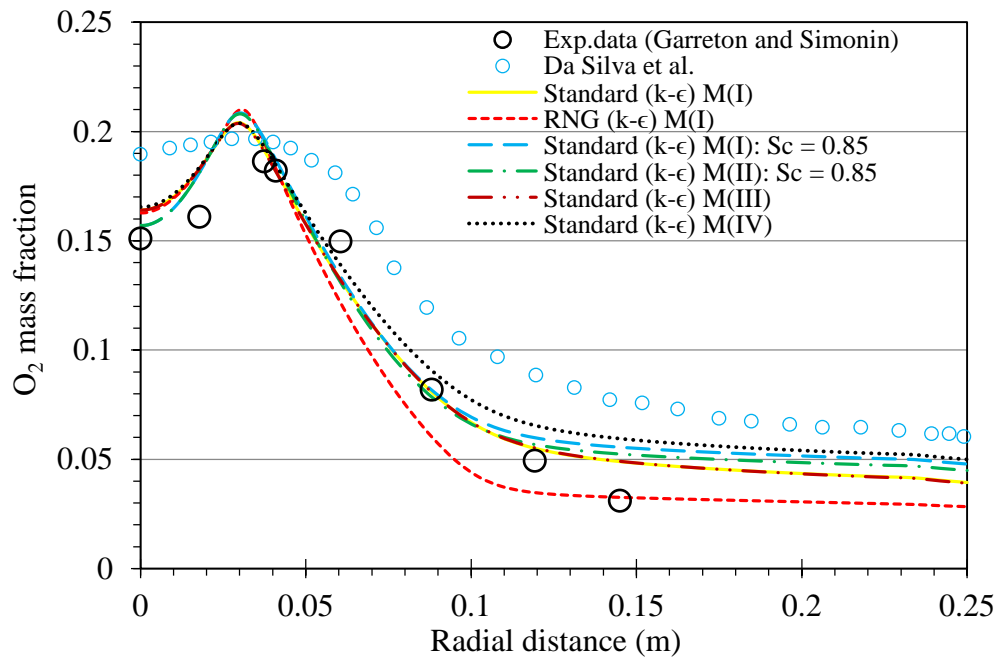


Figure 3.79: Radial profile of  $O_2$  mass fraction at axial location  $x = 0.312$  m for all cases.

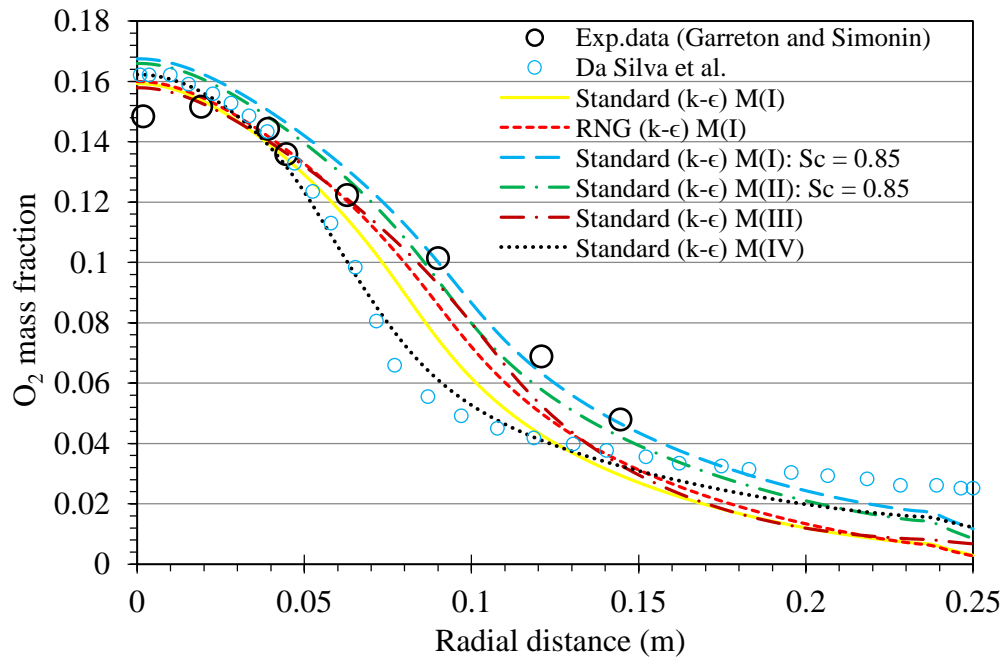


Figure 3.80: Radial profile of  $O_2$  mass fraction at axial location  $x = 0.912$  m for all cases.

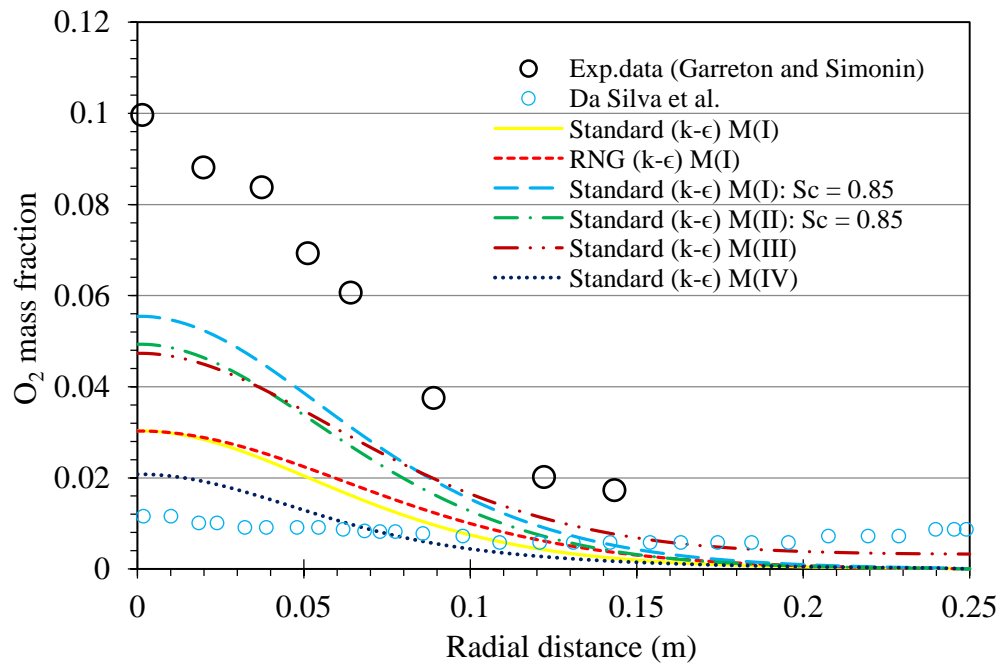


Figure 3.81: Radial profile of  $O_2$  mass fraction at axial location  $x = 1.312$  m for all cases.

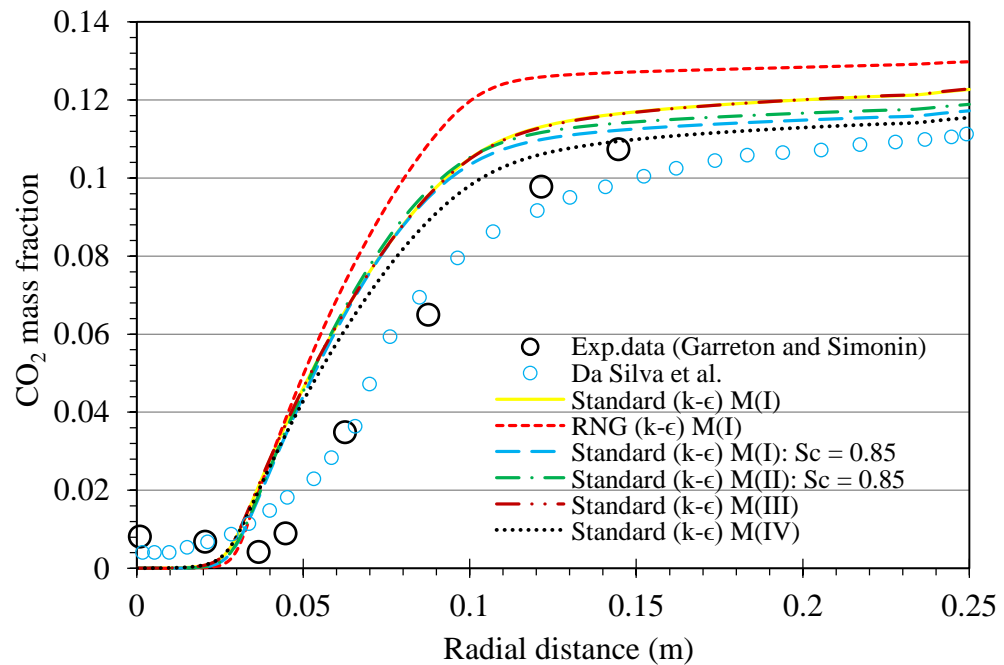


Figure 3.82: Radial profile of  $CO_2$  mass fraction at axial location  $x = 0.312$  m for all cases.

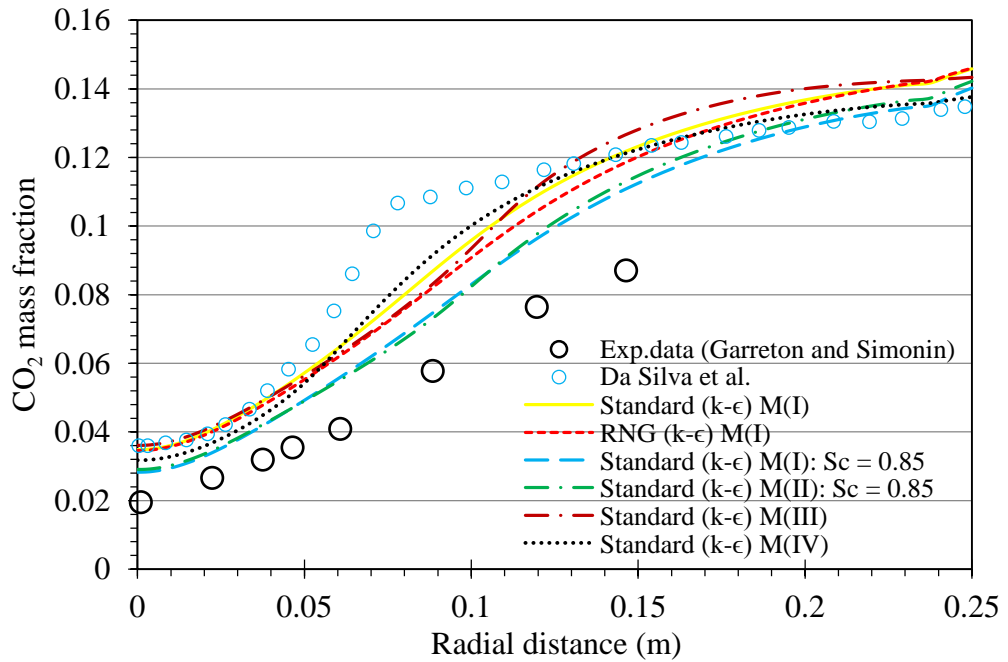


Figure 3.83: Radial profile of CO<sub>2</sub> mass fraction at axial location  $x = 0.912$  m for all cases.

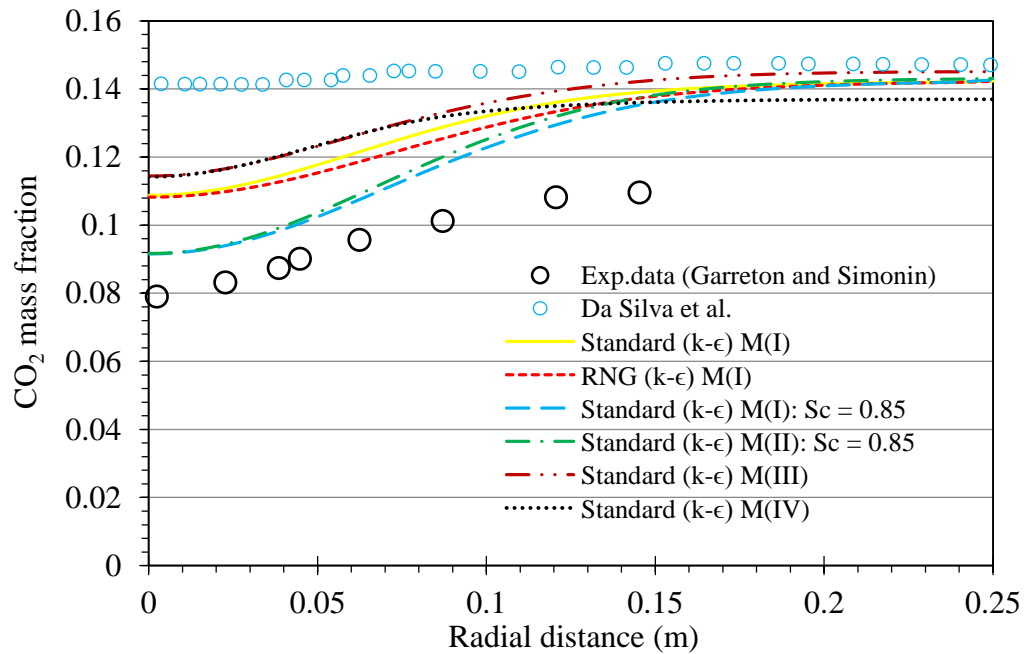


Figure 3.84: Radial profile of CO<sub>2</sub> mass fraction at axial location  $x = 1.312$  m for cases.



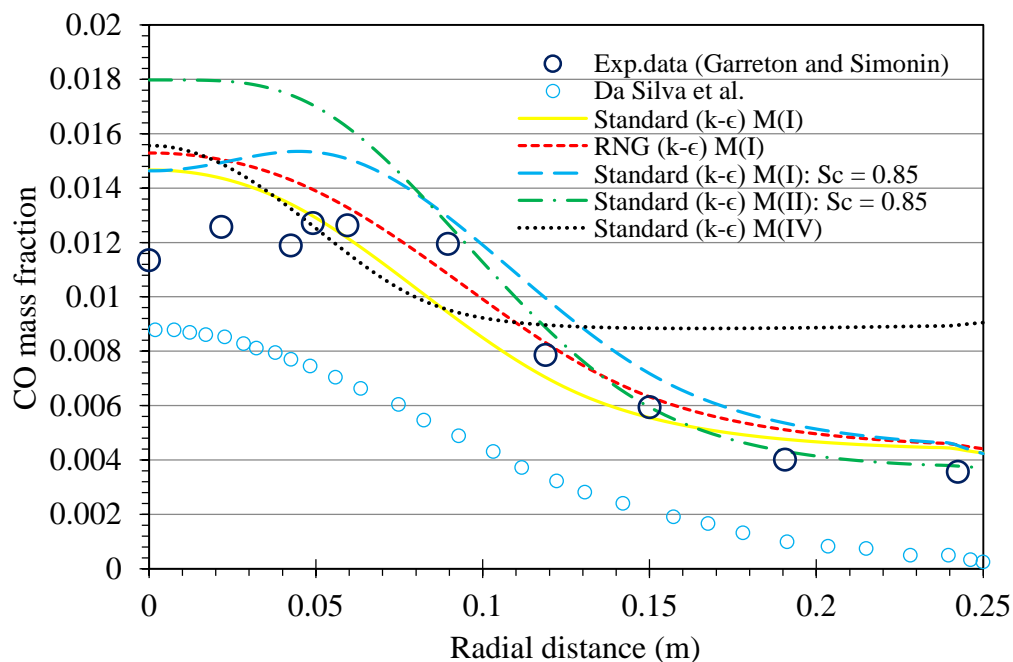


Figure 3.85: Radial profile of CO mass fraction at axial location  $x = 1.312$  m for all cases.

### 3.10.5 The effect of fuel concentration

The combustion of various fuel concentrations was simulated i.e. the fuel is diluted. The chemistry mechanism used in the simulations is M-I and the modified standard  $k-\epsilon$  turbulence model was also adopted. The axial temperature profile along the centreline of the chamber for the base case ( $\text{CH}_4$  90 %,  $\text{N}_2$  10 % by volume) and the other case ( $\text{CH}_4$  100, 85, 80, 70 %) is plotted in Figure 3.86. As it is shown in the figure, the predicted temperature is the same for all cases along the axial distance up to 1 m. It is also indicated that the peak temperature is decreased for all cases even for the case with pure methane as a fuel (fuel rich case with equivalence ratio  $\phi = 1.1556$ ). The peak temperature position at centreline of the base case lies between that of pure methane and 85% methane cases. It is clearly shown that the base case produces the highest temperature. Figure 3.87 depicts the axial variation of  $\text{CH}_4$  mass fraction along the centreline of the chamber. It is shown that methane decays slowly for all cases and this, as mentioned previously, can be attributed to the slow mixing which results in that the chemical reactions are quite slow leading to a slow rise in temperature. It can be also seen that  $\text{CH}_4$  mass fraction is a little bit higher than the other cases at the exit of the chamber. The mass fractions of species  $\text{O}_2$ ,  $\text{CO}_2$  and CO are shown in Figure 3.88, Figure 3.89 and Figure 3.90, respectively.

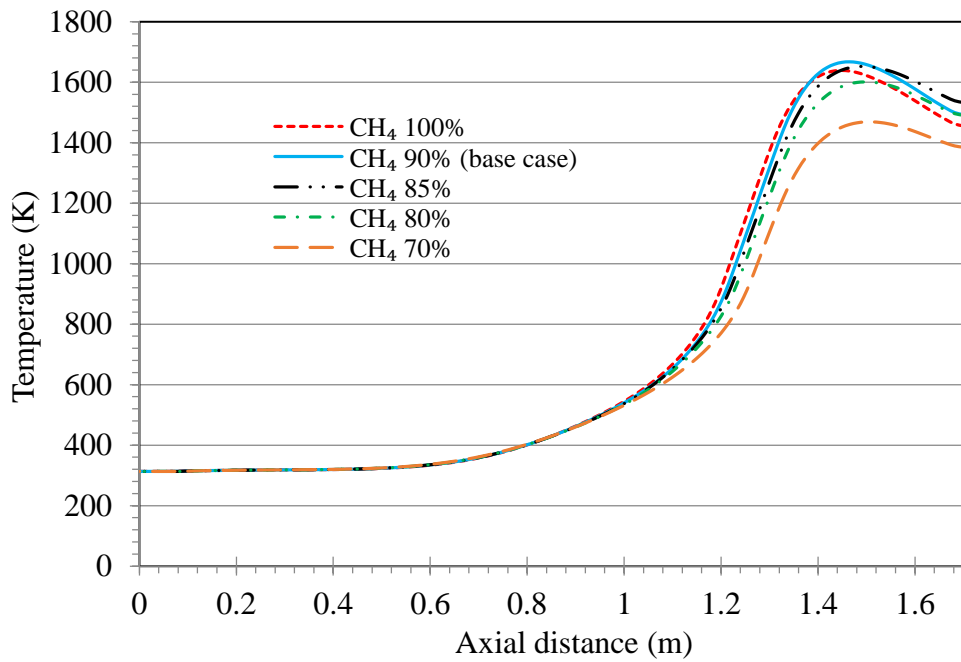


Figure 3.86: Gas temperature along centreline of the chamber for different cases with different percentages of CH<sub>4</sub> (volume basis).

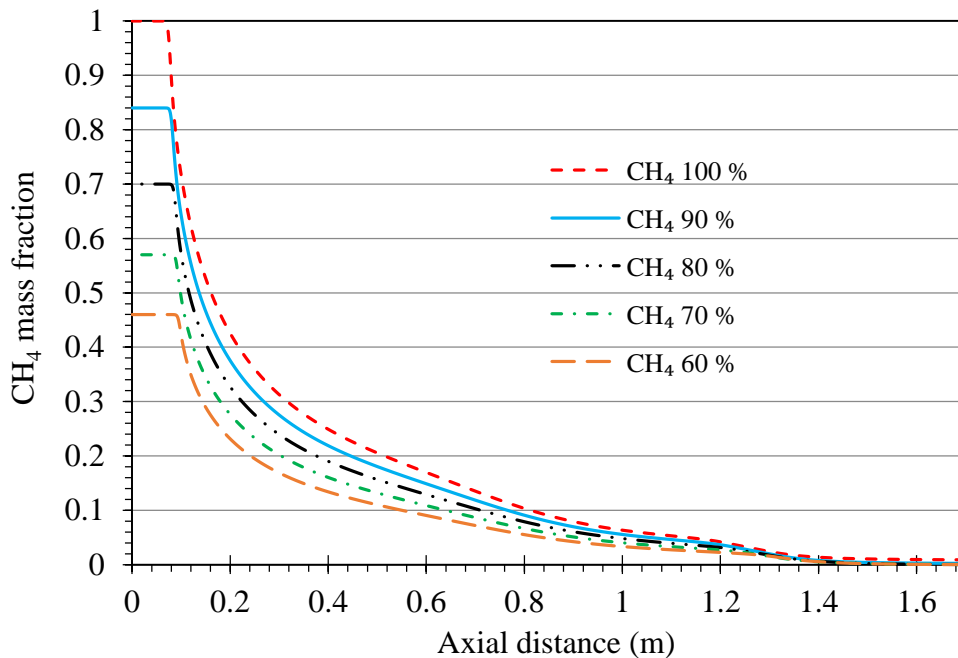


Figure 3.87: CH<sub>4</sub> mass fraction along the centreline of the chamber for different cases with different percentages of CH<sub>4</sub> (volume basis).

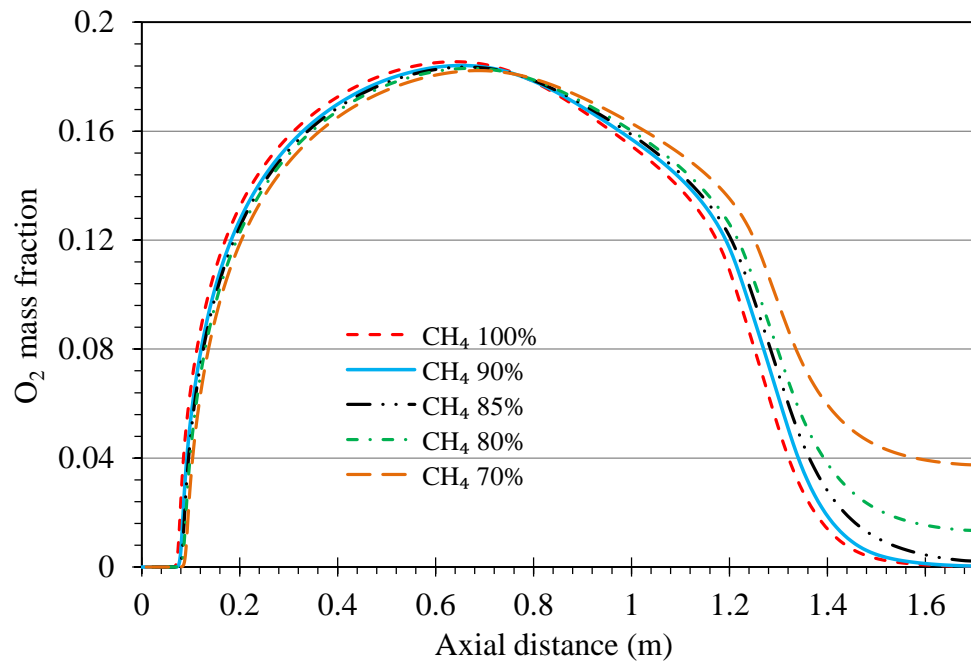


Figure 3.88: O<sub>2</sub> mass fraction along the centreline of the chamber for different cases with different percentages of CH<sub>4</sub> (volume basis).

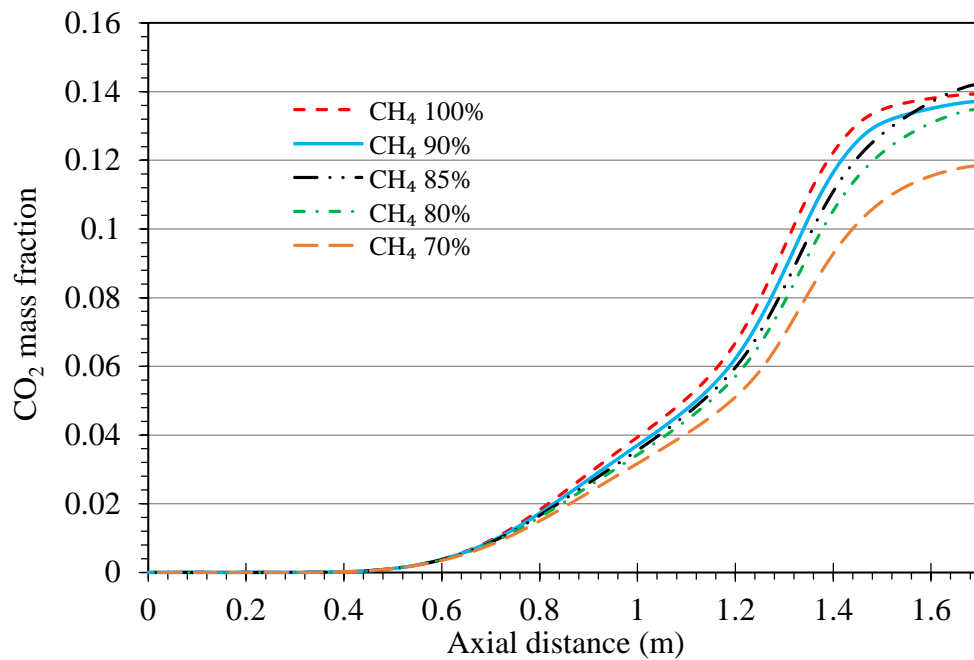


Figure 3.89: CO<sub>2</sub> mass fraction along the centreline of the chamber for different cases with different percentages of CH<sub>4</sub> (volume basis).

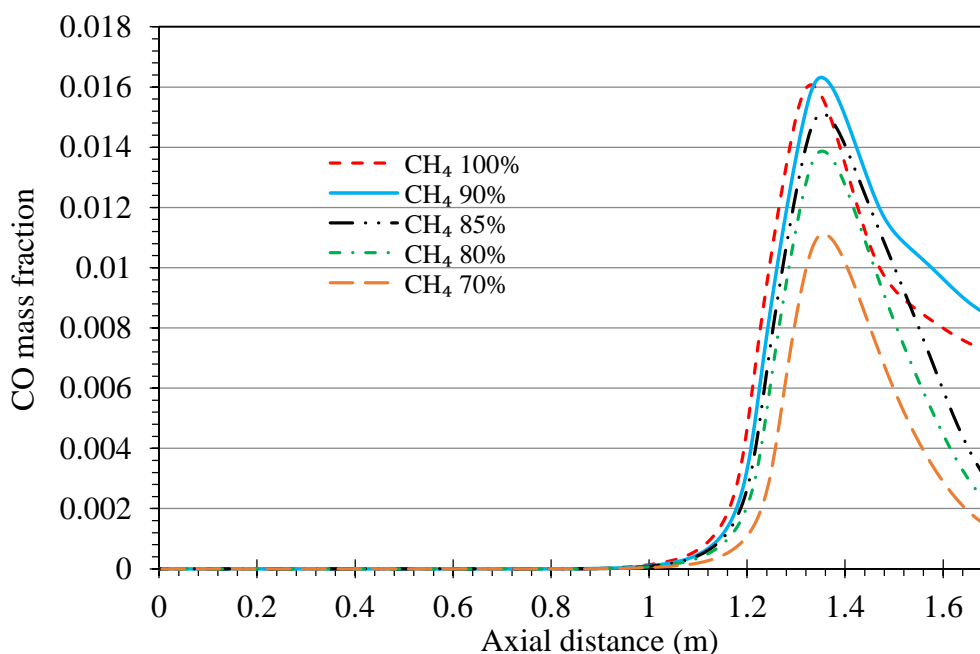


Figure 3.90: CO mass fraction along the centreline of the chamber for different cases with different percentages of CH<sub>4</sub> (volume basis).

### 3.11 Conclusion

In this chapter, the investigations have sought to determine the accuracy of CFD simulations using RANS approach. The simulations are based on the finite volume solution procedure, including sub-models for turbulent flow, radiative heat transfer and combustion. The purpose is to analyse the turbulent flow, species concentrations and temperature arising in the turbulent non-premixed combustion of natural gas (90% methane and 10% nitrogen by volume) in a cylindrical combustor. Experimental data of existing study [20] has been utilized for comparisons. For the combustion modelling the FR/ED model was considered. This model has the advantage that it is computationally inexpensive and simple to use. The flow field was calculated using the standard  $k-\epsilon$ , RNG  $k-\epsilon$  and realizable  $k-\epsilon$ . For chemical reactions, four global mechanisms were employed. For radiation modelling, P-1 method was applied for investigating the radiative heat transfer from the flame. A mesh independence study was performed for the aim of identifying which of the meshes constructed lead to a mesh independent solution. It was found that mesh B fulfils this requirement and has been chosen to perform all the subsequent simulations. The trends of all cases are well reproduced in comparison with the experiment. Despite some disagreement with the experimental data at some locations, good agreement is achieved in both quantitative and qualitative aspects. In comparison with the experimental data, it is shown that one-step reaction mechanism (M-III) can provide satisfactory estimate of maximum

temperature in the reaction zone. For the case of M-I, it is observed that the results of all turbulence models show very good agreement with the experimental data in terms of temperature along the centreline in the half of the chamber close to the burner. In the direction towards the exit of the chamber the results obtained from standard  $k-\epsilon$  case are almost close to that obtained from RNG  $k-\epsilon$ . The inclusion of radiative heat losses reduced the temperature inside the chamber and this is noticed in the region near the exit of the chamber. When applying the modified standard  $k-\epsilon$  it is observed that obtained results were improved. The optimization of kinetic energy of reaction (r-2) in mechanism (M-II) also improved the results. Regarding the case (M-IV) in which a five-step reaction mechanism was employed, the predicted results shows a reasonable agreement with the experiments in terms of temperature. In some locations especially for the predicted concentration of carbon monoxide CO along the centreline and at the axial location of  $x = 1.312$  m there is an over-prediction, though, the trend is similar to that of experimental data. It is seen that peak temperatures obtained from both the combustion of pure methane (100% CH<sub>4</sub>) and the combustion of diluted methane (85% CH<sub>4</sub>, 15% N<sub>2</sub>) are less than that of the base case (90% CH<sub>4</sub>, 10% N<sub>2</sub>) at the same operating conditions. This leads to conclude that the best compromise of methane and nitrogen is that of the base case. To sum up, in comparison with the experimental data and the predicted results reported by Magel et al [183], which were obtained by using EDC, the FR/ED model proved to capture the features of combustion process with sufficient accuracy. The numerical simulations indicate that the cases with the modified standard  $k-\epsilon$  lead to generally best predictions.

## 4 Pulverized combustion

This chapter presents a CFD modelling study of pulverized combustion of coal and biomass as well as the co-firing of both. It provides the basis for a comprehensive model. Some assumptions to simplify the modelling process are considered. The simulations of pulverized combustion are based on the Euler-Lagrange approach. The discrete phase model (DPM) is used. The first part of this chapter starts with modelling the pulverized combustion of two types of bituminous coal. It presents three cases using three different char oxidation models. Cases 1 and 2 use diffusion and kinetics/diffusion models, respectively. Case 3 uses the multi-surface reaction model, where a UDF is used to define the rate of heterogeneous reactions between both the gas and particulate phases. Modelling of  $\text{NO}_x$  is also presented. The models are validated with the available experimental data in the literature. The results show good agreement with the experiments. The combustion model of case 3 is then used to model the pulverized combustion of straw particles and the co-firing of pulverized coal and straw particles. Finally, a conclusion of the predicted results is given.

### 4.1 Introduction

Chemical compositions and molecular structures in any carbonaceous fuel, such as coal or biomass, are very complex. The main elements present in biomass, determined by ultimate analyses, are usually carbon (C), hydrogen (H), oxygen (O) and nitrogen (N). Other elements also found include sulphur, chloride and other impurities. The difference in this composition and particle size distribution results in different characteristics of combustion for biomass and coal as discussed in § 2. One of the combustion technologies that have a great of importance in generating power is the pulverized combustion of solid fuels. This technology is based on the pneumatic conveying system, since the fuel particles are carried by the air. Therefore, it is considered as one of the typical examples of particle-laden flows.

Despite the general similarities between the pulverised combustion of coal and that of biomass, there is a difference between their chemical compositions. Biomass has significantly lower fractions of carbon, while its oxygen content exceeds that of coal. The hydrogen fraction is also somewhat higher than that of coal. The typical weight percentages for C, H and O, respectively are 30 to 60 %, 5 to 6 % and 30 to 45 % [1].

For coal, the typical compositions (mass percentages) include 65 to 95% C, 2 to 7% H, up to 25% O and 1 to 2% N [45]. Moreover, there is also a difference between biomass and coal regarding their devolatilization. Compared to coal, biomass has a much higher amount of volatile matter leading to a dominating role of devolatilization in the overall conversion process of biomass particles. The volatiles fraction in biomass is usually 70-80%, whereas the fraction in coal is 10-50%. The high level of volatiles makes biomass a combustible fuel which means that it is easier to ignite even at low temperature. However, it has lower energy content due to the higher O/C and H/C atomic ratios when compared to coal. With anthracite less than 10% and bituminous from 5 to 6%, biomass fuels can lose up to 90% of their masses during the process of devolatilization [1]. The heating value of biomass fuels is significantly lower than that of coal requiring a large amount to be injected in furnaces compared to coal firing and this also suggests that less excess air is needed for biomass combustion. Moreover, biomass fuels begin to release volatiles at a lower temperature and in a more rapid way than coal does.

Regarding the devolatilization kinetics, the sensible prediction of the rate of release of volatile matter is of importance for the success of any computational model. Devolatilization process plays an important role in coal and biomass combustion. Determination of devolatilization rates is typically done by means of thermo-gravimetric analysis. In these analyses, small samples of solid fuel are ground so fine that the size dependence is not a factor which is to be considered and heated up with different temperature slopes. Using the thermo-gravimetric analyser, in a well-controlled atmosphere, the change in sample weight is measured. A number of kinetic models have been developed for the devolatilization of various coals and the models that are relatively simple include the single kinetic rate model and the two competing rates model. Models that are applicable over a wide range of coal types, but they are complex and difficult to use for practical applications include the functional group model, the flashchain model and the chemical percolation devolatilization model. The devolatilization of biomass and coal has been extensively investigated in [186-189].

In numerical simulations, most researchers for simplicity considered the combustion of solid fuels occurring in two individual steps. The first one is the combustion of volatiles and the second one is the combustion of char, neglecting the interaction between the two steps. But, for any two-phase flow, such as pulverized coal combustion, the interactions between the gaseous and solid phases needs to be taken into account because such a type of flow is characterized by non-linear coupling between the two

phases such as gas turbulence influencing both the particle motion and heat up. This requires an accurate description of both continuous gas phase and dispersed particle phase. This may be studied by using the Euler-Lagrange or Euler-Euler modelling approaches and it is crucial for practical application of prediction of solid fuels combustion for different technologies. The former one is the basis for the discrete phase model (DPM) in FLUENT.

When carrying out numerical simulations of particle-laden flows, it needs to bear in mind that there are different flow regimes which are classified in dilute and dense flow regimes. Therefore, to decide which regime is the case to be simulated is determined by the volume fraction of the dispersed (particulate) phase.

$$\alpha_p = \frac{V_p}{V} \quad (4.1)$$

where  $V_p$  is the volume of the dispersed phase in a specific volume  $V$ . This volume fraction has an upper threshold that is given by maximum value of 0.64 in a packed bed of particles (mono-dispersed spherical particles) [190]. In DPM, the assumption made is that the particles take up a negligible volume in the fluid phase. Practically, this limits the particulate phase to around 10-12%. The other thing that needs to be mentioned is the turbulent dispersion. Although the calculation of particle trajectories from the mean continuous phase velocities is valid for an individual particle, unrealistic results will be produced when considering an ensemble of similar particles. Therefore, to account for turbulence a term which is stochastic can be added to the calculation.

Pulverized combustion is characterized by small volume fraction of the dispersed particle phase and therefore, in this study, the Euler-Lagrange approach has been used to model the pulverized coal and biomass combustion, whereas, the other approach has been applied in another model that will be presented in the next chapter.

In the simulation of pulverised combustion of coal or biomass, the mathematical model needs to describe a number of phenomena such as multi-phase turbulent fluid mechanics (particle dispersion and exchange of mass, momentum and energy between phases), turbulent mixing, particle devolatilisation, volatiles combustion, char oxidation and radiative heat transfer.

Many models adopted Lagrangian approach in treating the particle phase when modelling pulverized coal combustion [191-193]. Concerning biomass combustion, the



Lagrangian approach was used by Fletcher [194] to simulate the flow and reactions inside an entrained biomass gasifier and the numerical results showed the capability of the Lagrangian model to optimise the design of such gasifiers. Another study regarding the modelling of pulverized wood combustion was carried out in which the Lagrangian manner was also adopted [195]. In this chapter, two firing scenarios have been simulated including pulverized coal combustion and pulverized biomass combustion.

## 4.2 Governing equations and used models

### 4.2.1 Gas phase

The governing equations of the conservation of mass, momentum, chemical species, energy as well as the equations of the turbulent kinetic energy and its rate of dissipation for the steady incompressible flow in 2d axisymmetric takes the general form as presented in equation (3.40). The turbulence model used in the current simulation is the standard  $k$ - $\epsilon$ , which has been outlined in § 3.3. Unfortunately, the optimized standard  $k$ - $\epsilon$  considered in ch.3, which shows better results when modelling the combustion of methan is not used in these simulations.

### 4.2.2 Modelling of the particulate phase

Besides the modelling of turbulent and reactive gaseous flow, pulverized fuel combustion also includes solid fuel particles which are dispersed into it. In the Euler-Lagrange approach, the dispersed phase is solved by the DPM, in which a large amount of particles is tracked. However, it is computationally expensive. In the application of pulverised fuel, the discrete phase is considered to be dilute and its volumetric fraction is neglected [158, 196]. The dilute dispersed flows are defined as those in which the particle motion is controlled by the hydrodynamic forces (drag and lift forces) [197]. Therefore, the motion of particles mainly depends on drag forces. On the other hand, it is controlled by the collisions of particles in dense flow systems. Coupling between the two phases accounts for the exchange of mass, momentum and heat as shown in Figure 4.1. Generally, the coupling between the gas and particulate phases can be found in different ways which include one-way coupling, two-way coupling and four-way coupling (related only to dense flows) as shown in Figure 4.2. For volume fraction less than  $10^{-6}$  (very dilute flows), the particulate phase has negligible effects on the gas phase. Regarding the Larger volume fraction ( $<10^{-3}$ ), a two-way coupling is required. A

four-way coupling should be used for larger volume fraction ( $>10^{-3}$ ). FLUENT provides only the first two types of coupling. The motion of fuel particles is modelled according to the differential equations for mass, momentum and energy. These equations predict the change in particle trajectory as it moves through the gas phase taking into account the interaction between the two phases by treating the heat and mass losses of the particles as the source terms in the governing equations.

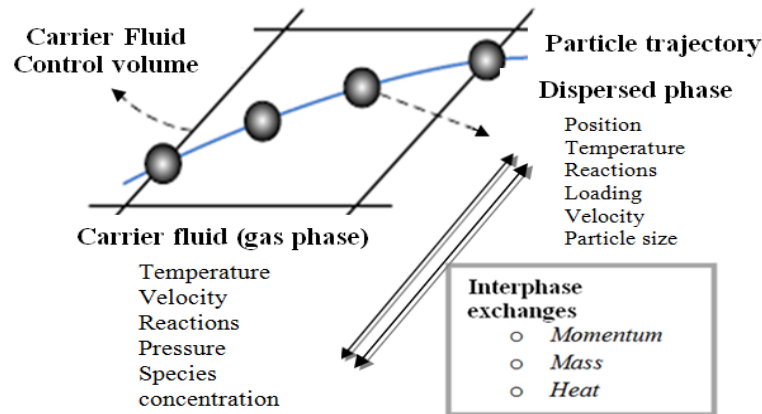


Figure 4.1: The interaction between gas phase and particulate phase [158].

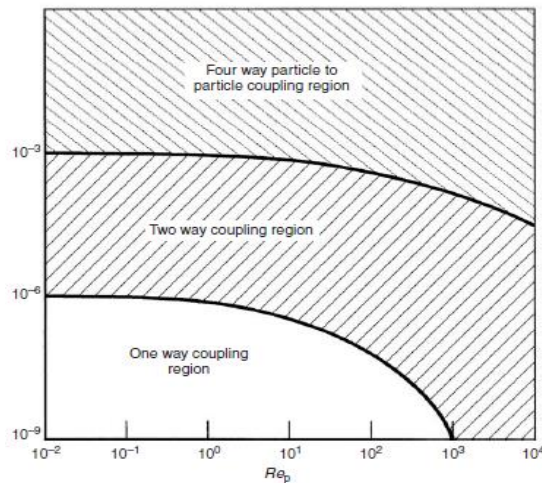


Figure 4.2: Coupling regions for particle-fluid turbulence interaction [198].

#### 4.2.2.1 The particle equation of motion

The trajectory of each discrete phase particle is calculated by solving its equation of motion, whose theory is based on Newton's second law. For the x-direction, it is given by:

$$m_p \frac{du_p}{dt} = \sum F_p \quad (4.2)$$

where  $m_p$  and  $u_p$ , respectively are the mass and instantaneous velocity of the particle and  $F_p$  represents different forces acting on the particle which, depending on the characteristics of the particles and the continuous phase (gas phase), some of them have various relevance and some of them can be neglected.

$$m_p \frac{du_p}{dt} = \sum F_p = F_d(u - u_p) + g_x(\rho_p - \rho)/\rho_p + F_x \quad (4.3)$$

where  $F_d$  and  $g_x$  are the drag force and acceleration gravity, respectively and  $\rho_p$ ,  $u$ , and  $F_x$  are the particle density, the instantaneous gas velocity and additional forces that can be important, respectively. The other forces that are represented by  $F_x$  may include pressure gradient force, virtual mass force, lift force (see for [158] more details). If the fluid-particle density ratio is very small ( $\sim 10^{-3}$ ), all the forces are neglected, apart from the drag force and the gravity force. The drag force  $F_d$  is the only one taken into account in this model and calculated as following:

$$F_d = \frac{3\mu}{\rho_p d_p^2} \frac{C_D Re_p}{4} \quad (4.4)$$

where  $d_p$  is the particle diameter and  $Re_p$  is the relative Reynolds number which is calculated using the following equation:

$$Re_p = \frac{\rho d_p |u_p - u|}{\mu_g} \quad (4.5)$$

where  $\mu_g$  is the gas viscosity. To calculate the drag coefficient  $C_D$  for spherical particles, FLUENT uses the correlations developed by Morsi and Alexander [199].

$$C_D = a_1 + \frac{a_2}{Re_p} + \frac{a_3}{Re_p^2} \quad (4.6)$$

where  $a_1$ ,  $a_2$ , and  $a_3$  are constants.

#### 4.2.2.2 Heat and mass transfer to and from particles calculations

The thermal energy conservation equation can be written as following:

$$\frac{d(m_p h_p)}{dt} = \sum \dot{Q}_p \quad (4.7)$$

where  $\dot{Q}_p$  is the sum of energy sources, such convection from the gas phase, radiative energy transport and heat of reaction and  $h_p$  is the particle enthalpy.

The particle enthalpy per unit mass is

$$h_p = h_{pf}^\circ + \int_{T_o}^{T_p} c_{p,p} dT_p \quad (4.8)$$

where  $c_{p,p}$  is the heat capacity of the particle,  $T_p$  is the particle temperature,  $T_o$  is the temperature at standard conditions (298 K) and  $h_{pf}^\circ$  is the enthalpy of formation ( $h_{pf}^\circ = 0$ ). The particle temperature is governed by a heat balance of different heat fluxes that involve convective heat transfer, radiative heat transfer, the heat loss due to evaporation of moisture and the devolatilization reaction in the particle and the heat of char combustion. Mathematically, the particle heat balance can be represented as

$$m_p c_{p,p} \frac{dT_p}{dt} = \pi d_p \lambda Nu (T_g - T_p) + A_p \varepsilon_p s_b (\theta_R^4 - T_p^4) + \frac{dm_p}{dt} h_{fg} - f_h \sum_i \frac{dm_p}{dt} H_{reac_r} \quad (4.9)$$

where  $d_p$  is the particle diameter,  $\lambda$  is the thermal conductivity of gas phase,  $T_g$  is the temperature of the gas phase,  $A_p = \pi d_p^2$  is the surface area of the particle,  $\varepsilon_p$  is the particle emissivity,  $s_b$  is the Stefan-Boltzman constant ( $5.67032 \times 10^{-8} \text{ W/m}^2 \cdot \text{K}^4$ ),  $\theta_R$  is the radiation temperature,  $\left(\frac{G}{4s_b}\right)^{1/4}$ ,  $f_h$  is the fraction of heat absorbed by the particle and takes the value of 0.3,  $H_{reac_r}$  is the enthalpy of reaction  $r$  (the heat gain/loss by heterogeneous reactions including the heat gain due to char combustion reactions and the heat loss due to the gasification reactions),  $h_{fg}$  is the latent heat of devolatilization and  $Nu$  is the Nusselt number. ( $G$ ) is the incident radiation in  $\text{W/m}^2$ :

$$G = \int_{\Omega=4\pi} I d\Omega \quad (4.10)$$

where  $I$  is the radiation intensity and  $\Omega$  is the solid angle.

The convective heat transfer coefficient  $\hat{h}$  is evaluated using the correlation of Ranz and Marshall:

$$Nu = \frac{\hat{h} d_p}{\lambda} = 2.0 + 0.6 Re_p^{1/2} Pr^{1/3} \quad (4.11)$$

and

$$Pr = C_p \mu_g / \lambda \quad (4.12)$$

where  $Pr$  is Prandtl number of the gas phase. In equation (4.9), the first term in the right hand side represents the heat transfer due to convection, the second term is the heat transfer caused by radiation, the third term is the heat of reaction and the last one is the heat transfer results from evaporation. The heat of evaporation is not included in this model as the coal was considered to be dry-ash-free (DAF). The heat of

devolatilization is neglected in this work, firstly, due to the difficulties and uncertainty of measurements [200] and secondly, because it is much less than the heat transferring from the gas phase to the particle. It is negligible as compared to the heat due to convection and radiation. Moreover, the latent heat is normally small for coals.

#### 4.2.2.3 Thermally-thin assumption

Equation (4.9) assumes that the internal resistance to heat transfer is negligible, i.e., the particles are at a uniform temperature throughout (thermally-thin assumption is considered). If the temperature is uniform throughout the particles, the stages of fuel particle combustion such as heating, devolatilization and char oxidation occur in a sequence way and the current study is based on this assumption. On the other hand, when temperature gradients are present, they may occur simultaneously. The temperature distribution in a particle is generally characterized by means of Biot number ( $Bi$ ), which relates the internal heat transfer resistance (internal conduction resistance) to the external resistance (surface convection). When the Biot number is very small the internal heat transfer due to conduction is fast. Therefore, temperature gradients are negligible inside the particle and the temperature of the particle can be regarded as uniform, which means that the combustion and gasification will depend on the external heat transfer and chemical reactions. On contrary, if the number is large, the external heat transfer due to convection is faster than that due to conduction. This means that the particle size will be a limiting factor.

$$Bi = \frac{\hat{h}L_c}{\lambda_s} \quad (4.13)$$

Where  $\hat{h}$  is the convective heat transfer coefficient,  $\lambda_s$  is the thermal conductivity of the particle, and  $L_c$  is the ratio of particle volume to its surface area ( $L_c = V_p/A_p$ ). In the current study, either pulverised combustion of coal and biomass are modelled by using the discrete phase model which is based on the assumption that the particles are thermally-thin and the particles are tiny in size. Therefore, under the conditions of all cases, the Biot number is so small that the uniformity of temperature within the particle phase due to the small size and large thermal conductivity of the particles has been considered.

#### 4.2.3 Combustion stages of fuel particle

The general model used for many solid fuels involves three stages of combustion:

1. Fuel heating and drying.
2. Devolatilization of particle to produce volatile and char.
3. Volatile combustion in the gas phase and char oxidation and gasification.

The inert heating is applied as long as the particle temperature is less than the vaporization temperature (devolatilization temperature) and after the volatile fraction of the particle has been released ( $T_p < T_{vap}$ ). During this stage, the fuel particle is heated rapidly by both the convective heat and absorption of radiation at the surface and equation (4.9) becomes as

$$m_p c_{p,p} \frac{dT_p}{dt} = \pi d_p \lambda Nu (T_g - T_p) + A_p \varepsilon_p S_b (\theta_R^4 - T_p^4) \quad (4.14)$$

When the temperature of the particle reaches the vaporization temperature, the combusting particle may proceed to obey the devolatilization and surface combustion laws and returns to the inert cooling law when the volatile fraction has been consumed ( $m_p < (1 - f_{v,o})m_{p,o}$ ). In this study, it is assumed that all the particle combustion stages take place in sequence way. In this process, devolatilization refers to the release of volatile matter by thermal decomposition, while it is termed pyrolysis when it takes place under inert conditions. The devolatilization law is applied to the combusting particle when ( $T_p \geq T_{vap}$ ) and stays effective while the mass of the particle  $m_p$  exceeds the mass of non-volatile in the particle ( $m_p > (1 - f_{v,o})m_{p,o}$ ). The particle temperature during this stage is described by equation (4.15).

$$m_p c_{p,p} \frac{dT_p}{dt} = \pi d_p \lambda Nu (T_g - T_p) + A_p \varepsilon_p S_b (\theta_R^4 - T_p^4) + \frac{dm_p}{dt} h_{fg} \quad (4.15)$$

After a complete evolve of the volatile component the surface reactions, which consumes the combustible fraction ( $f_{comb}$ ), begin. At this point, ( $m_p < (1 - f_{v,o})m_{p,o}$ ). At this stage, the combustion of char starts and continues until it is consumed and the particle temperature is described by equation (4.9).

#### 4.2.4 Turbulent dispersion in gas-solid flow

Commonly, turbulent dispersion is a term used to describe the transport phenomena of the particles in the carrier phase, whilst the flow is turbulent. In the analysis of gas-solid flows, coupling between the gas phase and the particulate phase is an important concept. It describes the effects of one phase on the other as shown in Figure 4.1. The

combination of the stochastic change in velocity and the misalignment of particles and fluid trajectories are the ways in which the turbulence is felt by the dispersion phase.

When considering a turbulent flow, we must take into account the effect of a random fluctuating velocity. The effects of turbulence are accounted for by predicting the trajectories of particles using the mean gas phase velocity ( $\bar{u}$ ) in the trajectory equations. The model of particle motion given by equations ((4.2)-(4.6)) needs the instantaneous local value of the velocity of the gas mixture.

$$u = \bar{u} + u' \quad (4.16)$$

In the current work, the standard  $k$ - $\epsilon$  model is used for estimating the turbulence properties. Thus, the mean velocity,  $\bar{u}$ , is calculated by solving the Favre averaged Navier-Stokes equations for the gas phase and the fluctuating velocity,  $u'$ , is assumed to follow a Gaussian probability distribution and determined in a stochastic manner within a turbulent eddy. Therefore, the instantaneous gas velocity is calculated as

$$u = \bar{u} + \xi (\overline{u'^2})^{1/2} = \bar{u} + \xi (2k/3)^{1/2} \quad (4.17)$$

where  $\xi$  is a normally distributed random number.

For this purpose the dispersion of the particles due to turbulence in the gas phase is predicted using a stochastic tracking approach. The turbulent dispersion of particles is predicted by integrating the trajectory equations for individual particles using the instantaneous fluid velocity along the particle path during the integration. The particle position at any given instant of time, the density, the temperature and the sources to the gas phase are computed for a sufficient number of representative particles (number of tries) with different sizes, dropped from each cell of the inlet as shown in Figure 4.3. In the present investigations, the discrete random walk (DRW) [201] model is used. In this model, the fluctuating velocity components are discrete piecewise constant functions of time and their random value is kept constant over an interval of time given by the characteristic lifetime of eddies.

The eddy lifetime is expressed as a constant:

$$\tau_e = 2T_L \quad (4.18)$$

where  $T_L$  is the fluid Lagrangian integral time and given as

$$T_L = 0.15 \frac{k}{\epsilon} \quad (4.19)$$

To cross an eddy, the particle requires time is given by

$$\tau_{cross} = -\tau_p \log \left( 1 - \frac{l_e}{\tau_p |u - u_p|} \right) \quad (4.20)$$

where  $\tau_p$  is the particle relaxation time,  $l_e$  is the eddy length scale, and  $|u - u_p|$  is the magnitude of the relative velocity. It is assumed that the particle interacts with the gas phase over the smaller of  $\tau_e$  and  $\tau_c$  and therefore a new value of instantaneous velocity has to be calculated.

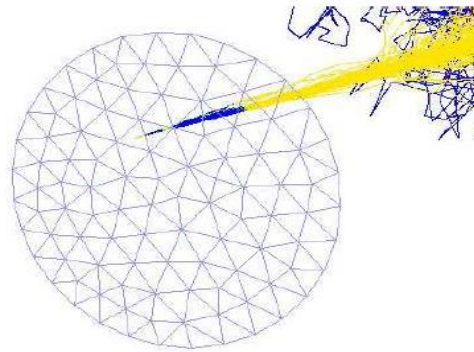


Figure 4.3: Trajectories of particles for a single cell [202].

### 4.2.5 Particle size distribution

The size of particles injected into the reactor is one of the important parameters when modelling multiphase systems such as pulverised fuel combustion. The pulverized fuel composed of particles with different sizes. Therefore, the particle size distribution needs to be measured. It is normally obtained by a standard laboratory screening method. In FLUENT, it is possible to simulate pulverized fuel flow with using various sizes of particles with the assumption that the particle size distribution follows a Rosin-Rammler distribution curve i.e. in the form of Rosin-Rammler type. The Rosin-Rammler distribution function is based on the assumption that an exponential relationship exists between the particle diameter  $d_p$  and the mass fraction of particles  $Y_d$  with diameter greater than  $d_p$ :

$$Y_d = e^{-(d_p/\bar{d})^n} \quad (4.21)$$

where  $\bar{d}$  is the mean diameter and  $n$  is the spread parameter. Therefore, the measured particle size distribution is transferred to the Rosin-Rammler distribution. Then, the



average particle diameter is calculated. Finally, the spread parameter is calculated. The particle size distribution of the fuels used in the current study will be presented next.

### 4.2.6 Radiation

The distribution and concentrations of products are strongly influenced by heat transfer in combustion systems. Therefore, its proper prediction is essential. In pulverised coal combustion systems and combustion reactors with heated walls, radiation is the dominating heat transfer mechanism [203]. Several radiation models have been developed as outlined in § 3.4. For comprehensive combustion modelling, the P-1 radiation model has employed for the heat transfer of radiation [17]. This radiation model has been successfully used by several researchers [204-206]. The weighted-sum-of gray-gases model (WSGGM) is used for determining the absorption coefficient of the gas phase. The WSGGM-cell based method, which calculates the mean beam length based on a characteristic cell size from the CFD model has been used.

## 4.3 Pulverized coal combustion

In the current work, the combustion of pulverized coal is modelled in an electrically heated reactor which will be described in § 4.3.1. To validate how well the CFD models capture the physical and chemical process taking place inside the reactor, the predictions are compared with the relevant experimental data.

### 4.3.1 Model geometry and operating conditions

The basic geometry of the reactor considered for this study is taken from literature [207]. The reactor is 2.5 m in length with an internal diameter of 200 mm. The axis-symmetric computational domain and the burner of the reactor that consists of three concentric tubes are as shown in Figure 4.4. The coal particles are injected centrally through an 8 mm diameter inner tube. A concentric tube with a diameter of 18 mm makes an annular gap that admits the primary air through it. The secondary air is supplied through another annular gap made by a concentric tube with a diameter of 34 mm. The operating conditions are provided in Table 4.1. Some assumptions are made in order to simplify the modelling. It is assumed that the gas phase can be treated as an ideal-gas mixture.

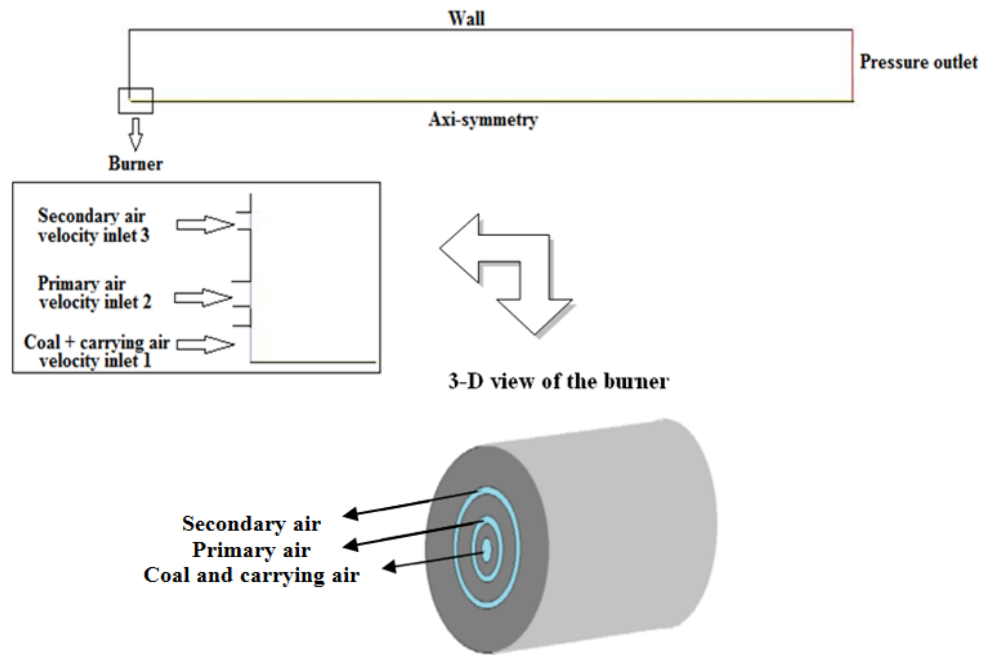


Figure 4.4: Geometry of the axisymmetric combustor.

The coal particles are assumed to be spherical in shape and enter the combustor at the same velocity as the carrying air. It is also assumed that the particles are dry with a temperature of 300 K. The side walls are modelled as having a constant temperature maintained by electrical heater. For the discrete phase, the particles parameters including the mass flow rate, temperature, velocity and diameters were specified at the inlet. The interaction between the particles was neglected.

Table 4.1: Operating conditions of pulverized coal combustion.

Parameters	Units	Values
Coal mass flow	kg/hr	1
Wall temperature	K	1523
Volume flow rate of coal carrying air	m <sup>3</sup> /hr	2.38
Temperature of coal carrying air	K	473
Volume flow rate of primary air	m <sup>3</sup> /hr	4.68
Temperature of primary air	K	523
Volume flow rate of secondary air	m <sup>3</sup> /hr	11.15
Temperature of secondary air	K	623

Table 4.2: Coal analysis data.

Proximate analysis (wt%, raw basis)					Ultimate analysis (wt%, raw basis)				
	Moisture	Volatile	Fixed carbon	Ash	C	H	O	N	S
Coal 1	1.57	30.46	62.87	6.67	78.9	4.9	7.6	1.3	0.6
HHV = 35084.16 [KJ/Kg]					LHV = 33930.32 [KJ/Kg]				
Coal 2	1.69	31.94	57.32	10.74	74.2	4.4	8.2	1.2	1.1
HHV = 34210.764 [KJ/Kg]					LHV = 33127.25 [KJ/Kg]				
Particle size distribution									
Average particle size				[ $\mu\text{m}$ ]	16, 52, 160, 350				
Mass fraction of particle diameters				%	30, 35, 25, 10				
Rosin-Rammler particle size distribution		Min $d_p$ [ $\mu\text{m}$ ]	Max $d_p$ [ $\mu\text{m}$ ]	$\bar{d}$ [ $\mu\text{m}$ ]	$n$ [-]				
		16	350	48	0.747				

## 4.4 Chemistry of coal

The simulations of pulverised coal combustion have been carried for two types of bituminous coal. The proximate and ultimate analysis and the particle size distribution data of the two coals fired in the pulverised combustion reactor are shown in Table 4.2.

It appears that the low heating value is higher than that of pure carbon (around 33 MJ/kg) because the high heating value was estimated on the DAF basis using the correlation given in [208].

### Reaction kinetics

The combustion of solid fuels is a complicated process that includes several physical and chemical phenomena. This makes combustion modelling to be a time-consuming challenging task. Therefore, the combustion phenomena need to be considerably simplified for CFD modelling and a reduced combustion mechanism is used. The combustion mechanism used in the current work is explained below.

#### 4.4.1.1 Devolatilization

The pulverized coal combustion model proposed in this simulation involves devolatilization, volatile combustion, char combustion and other gas phase reactions. In

this study, volatiles release is described by the single rate model [128]. It assumes that the rate of devolatilization is first-order dependent on the amount of volatiles remaining in the particle and employs global kinetics. The reaction and its rate constant are:



where  $\alpha$  is the distribution coefficient.

$$k_d = A \exp(-E/RT) \quad (4.22)$$

#### 4.4.1.2 Heterogeneous reactions

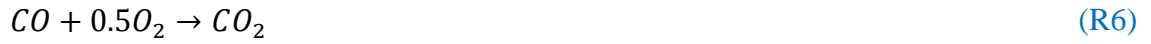
Four well-defined steps are usually involved in the chemical processes of solid fuel combustion as mentioned above: drying, devolatilization, volatile combustion and char oxidation. Once solid fuels are injected into a combustion chamber, they are heated up and the drying process (the release of moisture) occurs immediately, followed by the rapid devolatilization process (the release of volatiles) which occurs due to high temperatures. Char produced through the volatilization process is consumed by heterogeneous processes of combustion and gasification and its combustion yields carbon monoxide (CO) and carbon dioxide (CO<sub>2</sub>) according to the following reactions:



Reactions (R2) and (R3) are exothermic and will occur very rapidly but reaction (R4) is endothermic. In general, a dominating heterogeneous reaction is related to whether the char combustion rate is limited by either the diffusion of oxygen through the boundary layer surrounding particles or the kinetic rate of carbon oxidation reactions. Heterogeneous reactions can also include the following endothermic reaction:



where the carbon monoxide (CO) and hydrogen (H<sub>2</sub>) resulting from reactions (R4), (R5) and (R6) are incorporated to the gas phase and oxidized to CO<sub>2</sub> and H<sub>2</sub>O according to the following homogeneous reactions:



Three cases are considered in the present work. The heterogeneous reaction begins after the volatile fraction of coal particles is completely evolved. In case (1) and case (2), the initial reaction considered in this simulation is the oxidation of combustible fraction of coal particle (char) to carbon dioxide (R2). The models that are applied to calculate the reaction rate, described in § 2.7.3, are the diffusion model [127] for case (1), and the kinetics/diffusion model [133] for case (2). It assumes that the heterogeneous reaction rate is determined by the diffusion of the gaseous oxidant to the surface of the particle in the former model, and is determined either by the diffusion rate or by a chemical reaction, presumed to be first order in oxidant partial pressure and occurring entirely at the particle surface, in the latter one. With regard to case (3), the multiple-surface reaction model was used. Surface reactions are modelled by the implicit relationship proposed by Smith [135]. According to this model, the rate of particle species depletion for any reaction is given by

$$\bar{r}_{het} = A_p \eta Y_i R_{i,r} \quad (4.23)$$

where  $A_p$ ,  $\eta$ ,  $Y_i$  and  $R_{i,r}$  are the particle surface area [ $m^2$ ], effectiveness factor, mass fraction of surface species  $i$  in the particle and rate of particle species depletion [ $kg/m^2 s$ ], respectively.

$$R_{i,r} = \mathcal{R} \left( P_n - \frac{R_{i,r}}{D_o} \right)^N \quad (4.24)$$

where  $P_n$ ,  $D_o$ ,  $\mathcal{R}$  and  $N$  are bulk partial pressure of the gas phase species (pa), the diffusion and kinetic rate and apparent order of reaction, respectively.

$$D_o = C_1 \frac{[(T_p + T_g)/2]^{0.75}}{d_p} \quad (4.25)$$

where  $C_1$  is the mass diffusion limited rate constant ( $C_1 = 5 \times 10^{-12} m^3/K^{0.75}s$ ).

$$\mathcal{R} = AT^\beta e^{-(E/R_u T)} \quad (4.26)$$

Then, the rate of particle surface species depletion for a reaction with order ( $N = 1$ ) is given by

$$\bar{r}_{het} = A_p \eta Y_i P_n \frac{\mathcal{R}D_o}{\mathcal{R}+D_o} \quad (4.27)$$

and for a reaction with order ( $N = 0$ ),

$$\bar{r}_{het} = A_p \eta Y_i \mathcal{R} \quad (4.28)$$

In case 3, the combustion of char was assumed to follow the reactions (R2)-(R5). To determine the rates of these reactions, a user-defined function (UDF), given in appendix (B), was written and exported to the solver. The other processes were modelled using sub-models which are readily available in fluent such as turbulence, turbulence-chemistry interaction, radiation, particles initial heating up, particles devolatilization, and NO<sub>x</sub> models.

Summary of the three cases and the heterogeneous reactions and the models used to determine their rates are provided in Table 4.3.

Table 4.3: Devolatilization and char oxidation models used in the simulation cases.

	Case 1	Case 2	Case 3
Devolatilization	Single rate model	Single rate model	Single rate model
Char oxidation	diffusion model	kinetics/diffusion model	multiple surface reaction model
Heterogeneous reactions	(R2)	(R2)	(R2), (R3), (R4), (R5)

#### 4.4.1.3 Gas phase reactions

In the gas phase reactions, the yields of gases and tars combined are known as the volatile matter ( $hv\_vol$ ) which will evolve during the devolatilization process. This volatile matter, for simplicity in this study and also because the detailed chemical species in it are not completely understood due to the complexity of the chemical structure of coal and biomass, was generally treated as a single species which varies depending on the type of solid fuel whether it is coal or biomass and comprising carbon, hydrogen and oxygen ( $CH_xO_y$ ) in a ratio determined from the ultimate analysis of the solid fuel. Moreover, the formation of volatile products consists of individual time-dependent species release, but this takes place so rapidly that for most modelling application they can be treated as a single time-dependent variable. For the description of the gas composition inside the furnace the species transport approach in FLUENT

has been used and for this purpose six species have been defined:  $CH_xO_y$ ,  $O_2$ ,  $CO_2$ ,  $CO$ ,  $H_2O$  and  $N_2$ . For all the cases, the homogeneous reactions (R6) and (R8) are included.



where  $x$  and  $y$  represent the composition of the chemical elements based on the type of solid fuel. Thus, equating the numbers of atoms of each element in the reactants to the number in the products gives:

$$a = (1 + x/4 - y/2) \quad (4.29)$$

$$b = x/2 \quad (4.30)$$

For coal and biomass types used in the current study, the volatile gas species are represented in the CFD predictions as will be presented later which was calculated from the coal's ultimate and approximate analysis. The FR/ED model that calculates both the Arrhenius kinetic and eddy-dissipation [142] rates was applied in the simulations to account for the turbulence/chemistry interaction and the net reaction rate is chosen as the minimum of the two rates depending on which one is dominating the local reactions as outlined in chapter § 3.5.3.2.

$$r_i = \min(r_{Arr}, r_{Edd}) \quad (4.31)$$

The Arrhenius kinetic and eddy-dissipation rates are, respectively, given as

$$r_{Arr} = AT^\beta \exp\left(-\frac{E}{R_u T}\right) [C_R]^d [C_{ox}]^e \quad (4.32)$$

where  $C_R$  and  $C_{ox}$  are reactant and oxidant concentrations, respectively.

$$r_{Edd} = 4v'_{i,r} M_{w,i} \rho \frac{\epsilon}{k} \min\left[\min\left(\frac{Y_R}{v'_{R,r} M_{w,R}}\right), \frac{\sum_{\mathcal{P}} Y_{\mathcal{P}}}{2 \sum_j^N v''_{j,r} M_{w,j}}\right] \quad (4.33)$$

where  $M_{w,i}$  is the molecular weight of species  $i$ ,  $Y_{\mathcal{P}}$  is the mass fraction of any product species,  $Y_R$  is the mass fraction of a particular reactant  $R$ ,  $N$  is the number of species,  $v'_{i,r}$  is the stoichiometric coefficient for reactant  $i$ , and  $v''_{j,r}$  is the product species stoichiometric coefficient and it will be zero for any species that is not a product in the reaction.

For the chemical reactions considered: the heterogeneous ones (R2) through (R5) and the gaseous reactions (R6) and (R8), a summary of the kinetics data used in the present combustion modelling and the values of  $d$  and  $e$  are provided in Table 4.4.

Table 4.4: Kinetic constants of reactions.

Type of reaction	Reaction. no.	Kinetic parameters			$d$	$e$	Ref.
		$A$ (units vary)	$E$ (J/kmol)	$\beta$			
Devolatilization	(R1)	3.12E+05	7.4E+07	-	-	-	[128]
Heterogeneous	(R2)	0.002	7.9E+07	0	-	-	[158]
Heterogeneous	(R3)	0.052	1.33E+08	0	-	-	[209]
Heterogeneous	(R4)	4.4	1.62E+08	1	-	-	[210]
Heterogeneous	(R5)	1.33	1.47E+08	1	-	-	[210]
Homogeneous	(R6)	1.30E+11	1.26E+08	-	0.5	0.5	[211]
Homogeneous	(R8)	2.119E+11	2.027E+8	-	0.2	1.3	[158]

#### 4.4.2 Coal volatile elemental composition and enthalpy of formation

The molecular formulas of the two coals used in the model have been simplified in a form that makes the numerical simulations simpler. The contents of Sulphur (S) and Nitrogen (N) have been neglected.

For (coal 1) on DAF basis, the proximate analysis is 32.6% volatile and 67.4% fixed carbon (char). The elemental composition of the coal 1 on DAF basis is 86.32% C, 5.36% H and 8.32% O. The relative proportion composition of the volatile is determined by assuming that its mass is to be 32.6% of 1kg of the DAF composition.

thus

$$0.326 = (x/100)C + (5.36/100)H + (8.32/100)O$$

then

$$x = 18.92\%$$

The elemental composition of volatile is  $C_{18.92/12}H_{5.36}O_{8.32/16}$  and this leads to  $C_{1.58}H_{5.36}O_{0.52}$ .



The volatiles of (coal 1) has the simplified molecular formula “ $CH_{3.392}O_{0.33}$ ” with the molecular weight of 20.672 kg/kmol.

The lower heating value of volatile ( $LHV_{vol}$ ) is calculated using the following formula:

$$LHV_{vol} = \frac{LHV_{coal} - F_c * LHV_c}{F_{vol}} \quad (4.34)$$

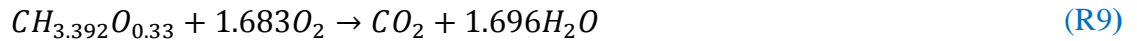
where  $F_c$  is the mass fraction of char in coal [kg/kg-coal],  $F_{vol}$  is the mass fraction of volatiles in coal [kg/kg-coal] and  $LHV_c$  is the lower heating value of char which is regarded to be equal to that of fixed carbon (32900 KJ/Kg).

$$LHV_{vol} = \frac{33930.32 - 0.674 \times 32900}{0.326} = 36060.5 \text{ kJ/kg}$$

then

$$LHV_{vol} = 36060.5 \times 20.672 = 745442.4658 \text{ kJ/kmol}$$

The oxidation of volatiles of coal 1 is represented by the following reaction:

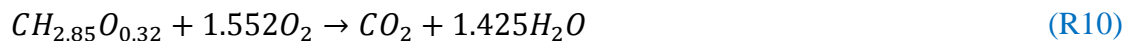


The formation of enthalpy of the volatile is calculated by the following equation:

$$H_{reac} = \sum h_{f,products}^\circ - \sum h_{f,reactants}^\circ \quad (4.35)$$

where  $H_{reac}$  is heat of reaction (745442.4658 kJ/kg), and  $h_{f,products}^\circ$  and  $h_{f,reactants}^\circ$  are the enthalpy of formation of products and reactants in [kJ/kmol], respectively. The enthalpy of information of the species  $O_2$ ,  $CO_2$  and  $H_2O$  are obtained from FLUENTdatabase. Solving equation (4.35) resulted in the enthalpy of formation of the volatiles of (coal 1),  $h_{f,vol_1}^\circ$  that have the value of  $(-5.824 \times 10^7 \text{ J/kmol})$ .

The same steps above have been followed to obtain the enthalpy of formation of the volatiles of (coal 2),  $h_{f,vol_2}^\circ$  which has the molecular formula “ $CH_{2.85}O_{0.32}$ ” with the molecular weight of 19.97 kg/kmol. The obtained enthalpy of formation has the value of  $(-6.8462068 \times 10^7 \text{ J/kmol})$ , which is based on the following reaction:



## 4.5 Mesh-independence study

The mesh for the geometry shown in Figure 4.4 is generated using GAMBIT. A steady-state computation was initially carried out with a grid resolution having a total of 48,000 control volumes, which is shown in Figure 4.5. For proving that the solution is independent of the mesh used in the simulations, it is important to carry out a grid-independence study. Therefore, the grid density was slightly reduced to 37,500, and then symmetrically increased to 52,000, 61,000 control volumes to check their sensitivity on simulated results. Figure 4.6 shows the temperature inside the reactor along the mid-line for the four grids and the predicted results show reasonably good agreement with small variation at the upstream of the reactor. Moreover, Figure 4.7 shows the variation of the temperature along the axial line at an outer radius (i.e.,  $y = 70$  cm). It is shown that the simulation results based on the four meshes are very close to each other except for the small discrepancies in the upstream region. Therefore, the grid that has a total number of cells of 48000 was sufficient for obtaining a grid-independent CFD solution and used for carrying out the further simulations.

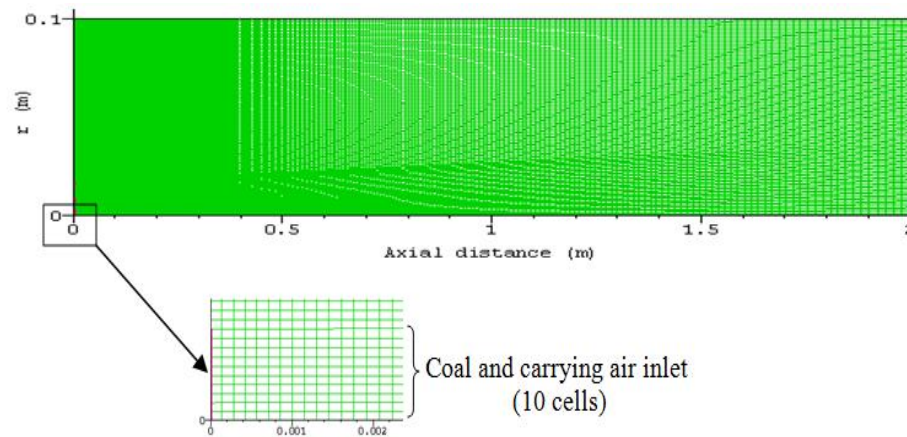


Figure 4.5: The grid of the computational domain.

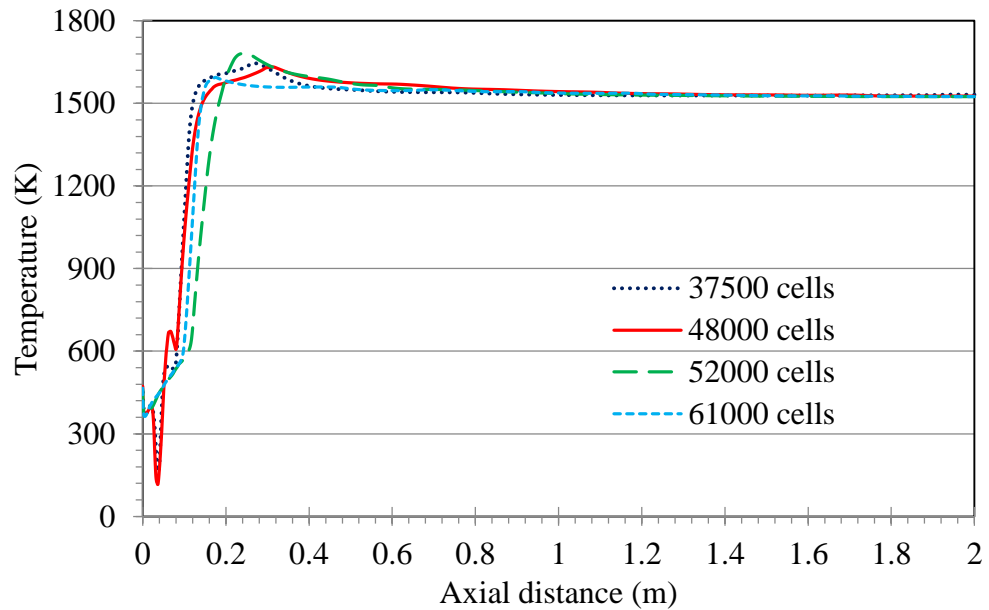


Figure 4.6: The variation of temperature predicted along the centreline of the reactor with different grids (coal 1).

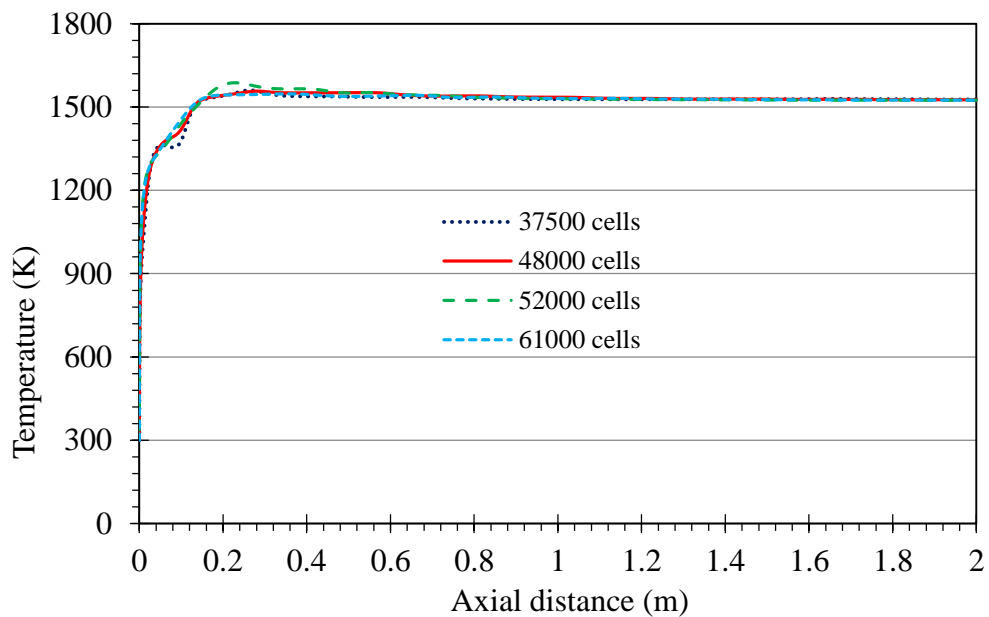


Figure 4.7: The variation of temperature predicted along the line ( $y = 70$  cm) of the reactor with different grids (coal 1).

## 4.6 Numerical methods

Solving the governing equations of two phases during the course of simulations has been carried out using the implicit finite volume method. ANSYS FLUENT 6.2 software has been used for solving the equations. The steady state segregated solver has been employed with a pressure-velocity coupling derived by the SIMPLE (Semi-Implicit Method for Pressure linked equations) algorithm [24]. The discretisation process is second order upwind scheme and the evaluation of gradients and derivatives is carried out by Green-Gauss cell based Gradient Evaluation method. For getting a

stable solution, the relaxation factors have been adjusted and the residual for all the variables converged to  $10^{-3}$  but for the energy and radiation to  $10^{-6}$ . Six discrete particle sizes are considered to be released from each cell of the injection surface. The particles enter the computational domain through the coal burner. The total number of particles tracked depends on the number of tries of DRW model (see § 4.2.4), which have been set to the value of 10. Number of cells in the injection's surface is 20. Therefore, there are 1200 particles, which are tracked during the simulations. They are tracked cell by cell through the volume. They are subjected to devolatilization and combustion and exchange of heat with the gas phase as well. Tracking these particles takes place till they either burn out or pass out the reactor exit.

## 4.7 Modelling of $\text{NO}_x$ chemistry

### 4.7.1 Mechanisms of $\text{NO}_x$ formation

In combustion systems including pulverized combustion, the formation and destruction of nitrogen oxides ( $\text{NO}_x$ ) emissions are influenced by several factors as fuel properties and combustion conditions such as the temperature of combustion zone and the fuel-air ratio [212, 213]. Understanding the chemistry of nitrogen in solid fuel burned systems mainly can help to improve the measures of  $\text{NO}_x$  control.

The nitrogen from combustion air and solid fuel are converted to pollutants comprise various nitrogen compounds such as nitric oxide (NO), nitrogen dioxide ( $\text{NO}_2$ ), nitrous oxide ( $\text{N}_2\text{O}$ ), ammonia ( $\text{NH}_3$ ) and hydrocyanide (HCN).  $\text{NO}_x$  oxides can include mostly NO and too much lower the contributions from  $\text{NO}_2$  and  $\text{N}_2\text{O}$ . So, the focus of  $\text{NO}_x$  models is only on predicting the concentration of NO in the reactive field of interest.

Without considering the nitrogen contained in the fuel, these emissions are formed at high temperatures from the combustion air nitrogen and can be limited by combustion engineering measures to a permitted values. On the other hand, when using nitrogenous fuels and low combustion temperatures, the formation of  $\text{NO}_x$  is mainly due to the conversion of fuel nitrogen partially or totally into nitrogen oxide [115].

During devolatilization, the nitrogen in the solid fuel is released as the nitrogen in the volatiles (volatile-N), such as Tar-N, HCN,  $\text{NH}_3$  and  $\text{N}_2$  and the remainder is retained as the nitrogen in the char, which is called (char-N). Most coals contain 0.5-2.0%

nitrogen by weight with bituminous coals generally have high nitrogen levels and anthracite low nitrogen levels. The split of nitrogen in the fuel into volatile-N and char-N is important for  $\text{NO}_x$  formation. Consequently, nitrogen release from both coal pyrolysis and char oxidation must be considered when modelling  $\text{NO}_x$  reactions in coal combustion systems.

Different mechanisms during the combustion of solid fuels cause the formation of  $\text{NO}_x$  oxides. In combustion field, there are four different mechanisms, which are identified in the formation of  $\text{NO}_x$  nitrogen oxides can be formed [213] and briefly described as following:

1. Thermal-NO, which is simply formed by the high-temperature oxidation of atmospheric nitrogen and determined by a set of chemical reactions, which take place in a few tens of microseconds, and are highly temperature-dependent.
2. Prompt-NO, which is first postulated by Fenimore [214]. It is another way in which the atmospheric nitrogen can participate in the formation of NO. In this mechanism, the molecular nitrogen is attacked by hydrocarbon radicals produced at high temperature in fuel-rich regions of flames when hydrocarbon fuels or coal are burned, producing atomic nitrogen, which is subsequently oxidized to NO. Therefore, Prompt-NO is only important in very fuel-rich regions with high hydrocarbons concentration. Due to reason that the presence of hydrocarbons is only in the devolatilization zone of the coal flames with a concentration that is much lower than that in methane flames, it is likely to make only a small contribution to the total NO formation in industrial combustion systems. Therefore, it is usually negligible in the combustion of solid fuels. In pulverized coal combustion, it was estimated that the amount of NO is less than 10 ppm [115]
3. In the combustion of solid fuels, fuel-NO is the principle source of the  $\text{NO}_x$ . It describes the formation of NO from the nitrogen, which is chemically bounded in the fuel during the combustion process. As mentioned earlier, Fuel-NO is namely composed of volatile-NO and char-NO and typically accounts to more than ~ 80% [215]. The formation of NO is usually assumed to proceed through the formation of HCN and/ or  $\text{NH}_3$  which are oxidized to NO.
4. In addition to the above mechanisms, there is another mechanism that could be considered which is nitrous oxide  $\text{N}_2\text{O}$  intermediate mechanism. In this mechanism and with the presence of a third body, the molecular nitrogen is

attacked by the O atom to form  $N_2O$ , which subsequently reacts with O atom to form NO.

In solid fuel combustion systems, the oxidation of fuel-NO is typically the most significant source produced during the combustion process with some contribution from thermal-NO. It has been shown in [216-218] that over 80% of the NO formed in pulverised coal combustion derives from the coal, i.e. they results from the oxidation of nitrogen in the coal (coal-N), and the remainder is due to thermal and prompt NO. In addition, the experimental work carried out by Pershing and Wendt [215] demonstrated that the contributions of thermal NO become significant when the temperatures in the coal flames are greater than 1650 K.

### 4.7.2 Kinetics of $NO_x$ reactions

Table 4.5: Rate constants for thermal NO chemical reactions,  $k = AT^\beta \exp(-E/R_uT)$ .

Rate constant	A	$\beta$	E
$k_1$	$1.8 \times 10^8$	0	38370
$k_2$	$3.8 \times 10^7$	0	425
$k_3$	$1.8 \times 10^4$	1	4680
$k_4$	$3.8 \times 10^3$	1	20820
$k_5$	$7.1 \times 10^7$	0	450
$k_6$	$1.7 \times 10^8$	0	24560

In this work, thermal-NO and the fuel-NO were considered. For the former one, NO is predicted by using the Zelovich [219] mechanism with the partial equilibrium approach for radicals O and OH concentrations. It incorporates the following reactions:



where:  $k_1, K_3, K_5$  stands for the forward and  $K_2, K_4, K_6$  for the backward rate constants of the reactions and  $O, N$  and  $OH$  are oxygen radical, nitrogen radical and hydroxyl radical. Fluent uses the values compiled by Hanson and Salimian [220] as shown in Table 4.5.

The net rate of NO production is:

$$\frac{d[NO]}{dt} = k_1[O][N_2] + k_3[N][O_2] + k_5[N][OH] - k_2[NO][N] - k_4[NO][O] - k_6[NO][H] \quad (4.36)$$

where all concentrations have units  $\text{mol}/\text{m}^3$ .

In order to compute the concentrations of NO, the concentrations of N,  $N_2$ , O, H and OH radicals must be known. It is useful to assume that the rate of consumption of free nitrogen atoms becomes equal to the rate of its formation and therefore a quasi-steady state can be established. This assumption is valid for most of the combustion cases except in those of extreme fuel-rich conditions. Hence the formation rate of NO can be expressed as following [221]:

$$\frac{d[NO]}{dt} = 2[O] \left\{ \frac{k_1[N_2] - \frac{k_2 k_4 [NO]^2}{k_3 [O_2]}}{1 + \frac{k_2 [NO]}{k_3 [O_2] + k_5 [OH]}} \right\} \quad (4.37)$$

If the reverse reactions and the third reaction of the above mechanism are neglected, the following simplified expression can be obtained:

$$\frac{d[NO]}{dt} = 2k_1[O][N_2] \quad (4.38)$$

The  $[O]$  and  $[OH]$  are estimated by the partial equilibrium approach as following:

$$[O] = K_1 T^{1/2} [O_2]^{1/2} \quad (4.39)$$

$$[OH] = K_2 T^{-0.57} [O_2]^{1/2} [H_2O]^{1/2} \quad (4.40)$$

where the equilibrium constants  $K_1$  and  $K_2$  are as follows:

$$K_1 = 36.64 \exp\left(\frac{-27123}{T}\right) \quad (4.41)$$

$$K_2 = 2.129 \times 10^2 \exp\left(\frac{-4595}{T}\right) \quad (4.42)$$

With regard to fuel-NO, most coals contain 0.5-2.0% nitrogen by weight with bituminous coals generally have high nitrogen levels and anthracite low nitrogen levels. It was assumed that the nitrogen contained in the coal is completely devolatilized during the simulations and distributed between the volatiles and the char when a coal particle is heated. This distribution is indicated by most experimental studies of coal pyrolysis [222]. The split of nitrogen in the fuel into volatiles and char is important for  $NO_x$  formation. Consequently, nitrogen release from both coal pyrolysis and char oxidation must be considered when modelling  $NO_x$  reactions in coal combustion systems. The key issue is the knowledge of partitioning of the nitrogen between them. The fraction of nitrogen released with the volatiles depends on the fuel type, the temperature, and the residence time [217]. The increase in temperature and residence time favours the conversion of coal-N to volatile-N. On contrary, low temperature favours the preferential retention of nitrogen in char, which is greater for biomass [217].

In some studies [223-225], it was assumed that fuel nitrogen is distributed evenly between the volatiles and the char, whereas, a parameter  $\gamma$  (char nitrogen as a fraction of total nitrogen) is introduced to describe this distribution in this analysis as follows:

$$m_{vol}^N = (1 - \gamma) * \frac{m_{tot}^N}{F_{vol}} \quad (4.43)$$

$$m_{char}^N = \gamma * \frac{m_{tot}^N}{F_c} \quad (4.44)$$

where  $\gamma \in \langle 0,1 \rangle$ :  $m_{vol}^N$ ,  $m_{char}^N$ ,  $m_{tot}^N$ ,  $F_{vol}$  and  $F_c$  are the mass fraction of nitrogen in volatiles, the mass fraction of nitrogen in char, the total mass fraction of nitrogen in DAF coal, mass fraction of volatiles in DAF coal and mass fraction of char in DAF coal, respectively.

The transformation of nitrogen to pollutants takes place via intermediates HCN and  $NH_3$ . For both of them, two variations of fuel  $NO_x$  pathways are included as shown in Figure 4.8 [218, 226].

The reactions considered for NO formation and the ones that leads to the reduction of NO are as follows:



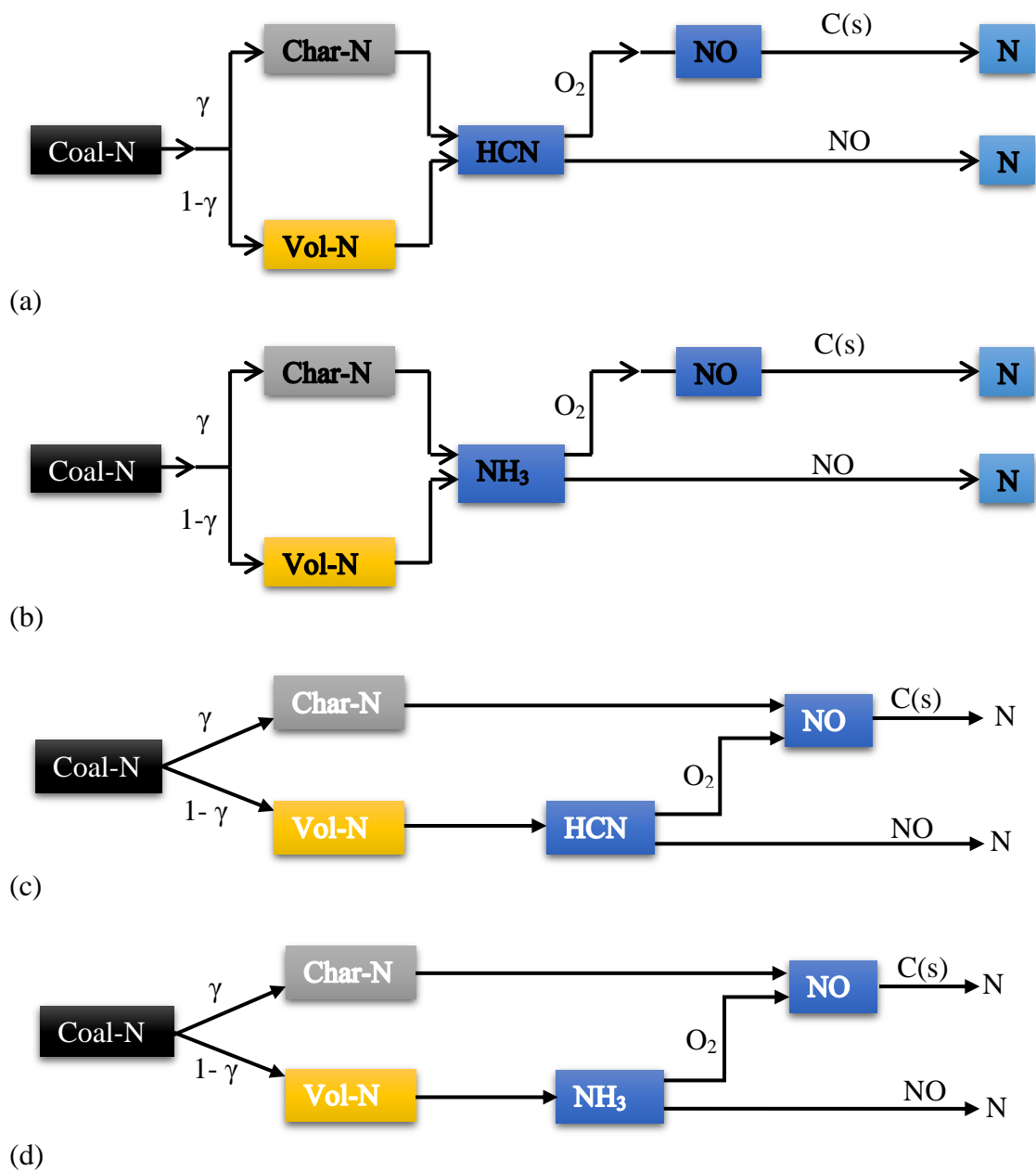


Figure 4.8: Fuel-NO pathways: (a), (b) [227], (c) and (d) [218].

The rate of conversion of HCN and  $NH_3$  are given by De Soete [228] as the following:

$$\mathcal{R}_1 = A_1 X_{HCN} X_{O_2}^a \exp(-E_1/RT) \quad (4.45)$$

$$\mathcal{R}_2 = A_2 X_{HN_3} X_{O_2}^a \exp(-E_2/RT) \quad (4.46)$$

$$\mathcal{R}_3 = A_3 X_{HCN} X_{NO} \exp(-E_3/RT) \quad (4.47)$$

$$\mathcal{R}_4 = A_4 X_{HN_3} X_{NO} \exp(-E_4/RT) \quad (4.48)$$

where  $X$  is the mole fraction (1/s),  $a$  is the oxygen reaction order and  $T$  is the instantaneous temperature (K).

The kinetics of these reactions are given in Table 4.6 and the oxygen reaction order is taken from Table 4.7. Regarding NO reduction on char surface, the heterogeneous reaction by which the reduction of NO occurs on the char surface is given as



Levy [229] who uses pore surface area (BET) to define the rate of NO consumption due to this reaction which will then be:

$$S_{NO-5} = c_s A_{BET} M_{w,NO} \mathcal{R}_5 \quad (4.49)$$

where  $A_{BET}$  is BET surface area ( $m^2/kg$ ),  $c_s$  is the concentration of the particles and  $S_{NO-5}$  is NO consumption ( $kg/m^3/s$ ).

Table 4.6: Reaction kinetics.

Rate of reaction	$A$ (1/s)	$E$ (J/mol)
$\mathcal{R}_1$	$1.0 \times 10^{10}$	280451.95
$\mathcal{R}_2$	$4.0 \times 10^6$	133947.2
$\mathcal{R}_3$	$3.0 \times 10^{12}$	251151
$\mathcal{R}_4$	$1.8 \times 10^8$	113017.95

Table 4.7: Oxygen reaction order.

Oxygen mole fraction	$a$
$X_{O_2} \leq 4.1 \times 10^{-3}$	1
$4.1 \times 10^{-3} \leq X_{O_2} \leq 1.11 \times 10^{-2}$	$-3.95 - 0.9 \ln X_{O_2}$
$1.11 \times 10^{-2} \leq X_{O_2} \leq 0.03$	$-0.35 - 0.1 \ln X_{O_2}$
$X_{O_2} \geq 0.03$	0

For coal, typically, the BET area is 25000 m<sup>2</sup>/kg. This value is used as the default in FLUENT. The reaction rate ( $\mathcal{R}_5$ ) is modelled as

$$\mathcal{R}_5 = A_5 \exp(-E_5/RT) P_{NO} \quad (4.50)$$

where  $\mathcal{R}_5$  is the rate of NO reduction (mol/s/m<sub>BET</sub><sup>2</sup>),  $P_{NO}$  is NO partial pressure calculated using Dalton's law:  $P_{NO} = X_{NO}P$  and  $T$  is the mean temperature (K). The kinetic constants of this reaction are  $A_5 = 2.27 \times 10^{-3}$  (mol/pa/s/m<sub>BET</sub><sup>2</sup>) and  $E_5 = 142737.485$  J/mol.

### 4.7.3 Numerical procedure

Due to the reason that the concentration of NO formed is so small compared with the concentration of other species of interest in the combustion process, the reactions included in the NO chemistry have been decoupled from the pulverized coal combustion process, i.e. the models of nitrogen pollutants are de-coupled from the combustion model and executed after the flame structure has been predicted. Thus, the method used for NO<sub>x</sub> modelling in RANS simulations and particularly in Fluent is the one by which the chemical formation and reduction rates of NO are calculated by post-processing data obtained from previously reacting flow simulations. Another advantage of this method is the computational efficiency. Standard Fluent NO-post-processing models considering thermal-NO and fuel-NO formation were used and the specie transport equations for the mass fraction of NO, HCN, and NH<sub>3</sub> were solved.

$$\frac{\partial}{\partial x}(\rho u Y_i) + \frac{\partial}{\partial r}(\rho v Y_i) = \frac{\partial}{\partial x}(\rho D_i \frac{\partial Y_i}{\partial x}) + \frac{\partial}{\partial r}(r \rho D_i \frac{\partial Y_i}{\partial r}) + S_i \quad (4.51)$$

where  $Y_i$  is the mass fraction of NO, HCN, and NH<sub>3</sub> and  $S_i$  is the source term of the production and reduction of NO.

As mentioned above, thermal NO is calculated according to the extended Zedovich mechanism with the partial equilibrium approach for the radicals O and OH. On the other hand, some assumptions are made to calculate fuel-NO.

Moreover, during the process of pulverized combustion, devolatilization takes place rapidly, followed by the oxidation of the devolatilized products (volatiles) such as tar and light gases. When these volatiles are released much of the nitrogen contained in the coal particles is also released. However, the nitrogen contained in the fuel is partially released in both the volatiles and the char. The split of nitrogen in the fuel into volatile-N and char-N is potentially important for  $\text{NO}_x$  formation.

It is assumed that fuel nitrogen is distributed between the volatiles and char according to the parameter  $\gamma$ , which takes the value of 0.2. This assumption has been made because the conversion of the nitrogen released in the volatiles to  $\text{NO}_x$  is predominant during pyrolysis in pulverized fuel flames. As mentioned in § 4.7.2 the nitrogen is depleted at high temperatures but at low temperatures it is retained in the char. In particular, at higher temperatures (above 1500 K), up to 70-90% of coal nitrogen is devolatilized [230]. Pulverized furnaces produce high temperature which results in releasing most of the coal nitrogen with the volatiles.

In regular pulverized coal combustion, about 60-80% of  $\text{NO}_x$  is resulted from the volatile-N [231]. Thus, by using the value  $\gamma = 0.2$  the mass fractions of nitrogen in both the volatiles and char are calculated using the equations (3.43) and (4.44). Furthermore, the type of coal used in this study is bituminous which yields large amount of tar when compared with the other types of coals [232].

Yang et al. [233] showed that volatile matter for bituminous coals is the most important  $\text{NO}_x$ -forming property, and the volatile-N consists mostly of tarry compounds that at high temperatures decay rapidly to HCN. In addition, the combustion of the bituminous coals show more HCN formation than  $\text{NH}_3$  [234-236], thus leading to the assumption that the nitrogen is released via the intermediates HCN and  $\text{NH}_3$  with higher percentage of the former one. The percentages used for different simulation runs for the two species are shown in Table 4.8 and, depending on the local conditions, these two species will react to form either NO or  $\text{N}_2$ . For char-N path way, it is assumed that all the nitrogen is released via the intermediate HCN [218, 237].

Table 4.8: Partition of volatile nitrogen via the intermediates HCN and NH<sub>3</sub>.

Run	volatile nitrogen (volatile-N) partitioning		
	% HCN	% NH <sub>3</sub>	% NO
1	60	10	30
2	55	10	35
3	52	10	38
4	50	10	40
5	48	10	42
6	45	10	45

## 4.8 Results and discussion of coal combustion model

### 4.8.1 Combustion model

Three cases were simulated for both types of coals: In the first two cases, the char was assumed to be only oxidized to CO<sub>2</sub> according to reaction (R2). The char oxidation model used in the first case (Case 1) was the diffusion model while in the second case (Case 2) was the diffusion-kinetics model. In the third case (Case 3), the combustion of char was assumed to follow the reactions (R2)-(R5).

#### 4.8.1.1 Model validation

In order to validate the model, the simulation results are compared with the experiment data [207] as shown in Figure 4.9 and Figure 4.10 for coal 1 and in Figure 4.11 and Figure 4.12 for coal 2. It can be seen that the predictions of O<sub>2</sub> and CO<sub>2</sub> concentrations have a good agreement with the experimental data. In particular, the mass fraction of oxygen along the axial distance of the reactor in Figure 4.9 for coal 1 and Figure 4.11 for coal 2 show that the results predicted by Case 3 are more close to the experimental data near the burner than the other two cases, while Case 1 results for coal 1 show better agreement at the exit of the reactor. In terms of coal 2, case 2 show better results at the exit of the reactor in comparison with the experimental data. The mole fractions of carbon dioxide in Figure 4.10 for coal 1 and Figure 4.12 for coal 2 also show that the Case 3 results have very good agreement with the experimental data.

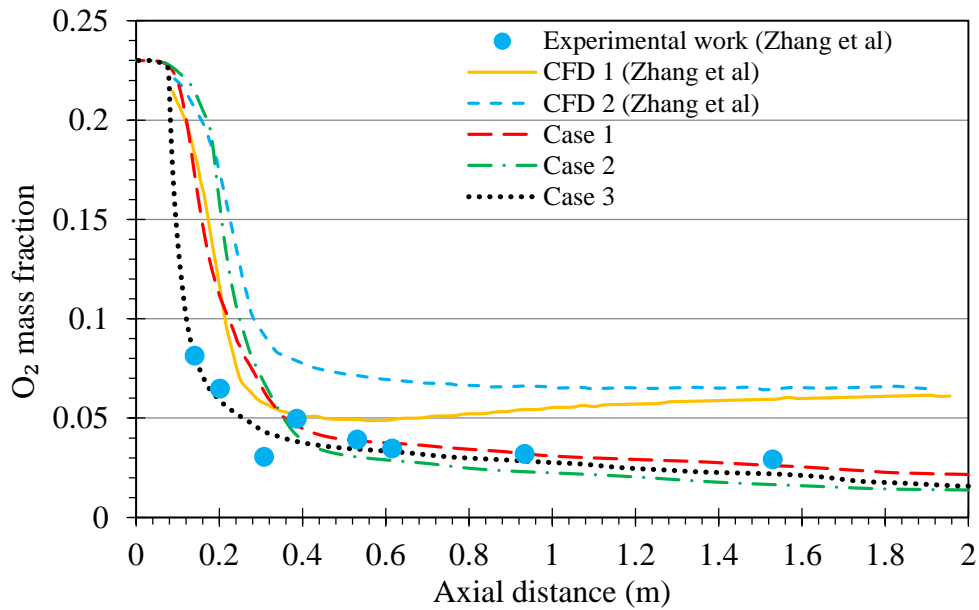


Figure 4.9: Mass fraction of  $O_2$  for coal 1 along the axial distance of the reactor.

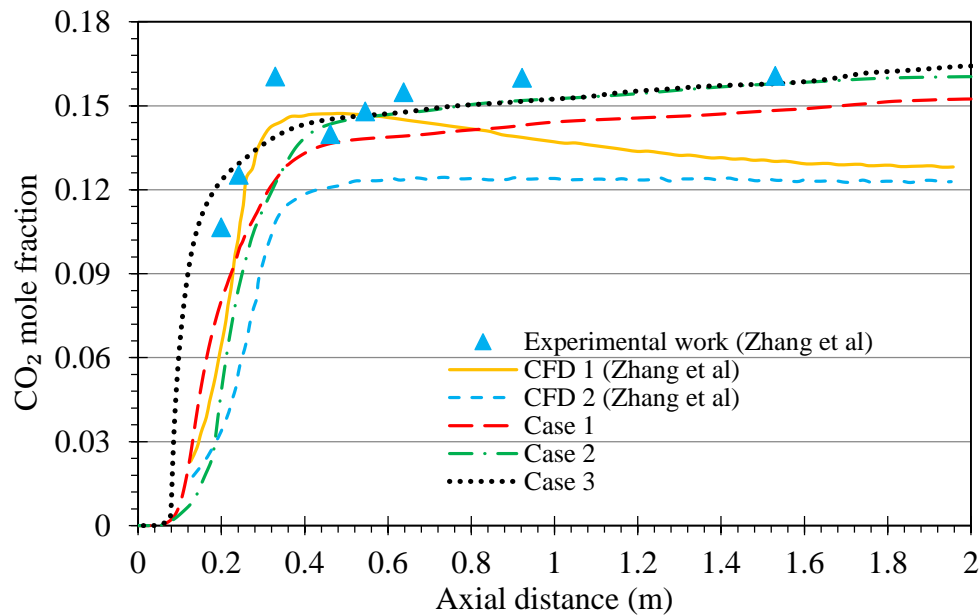


Figure 4.10: Mole fraction of  $CO_2$  for coal 1 along the axial distance of the reactor.

We note that Zhang et al. [207] also performed CFD investigations in the same combustion chamber, and the results predicted by the current simulation approaches are far better than their results. CFD 2 means an algebraic unified second-order moment (AUSM) turbulence/chemistry model of char combustion that takes into account the influence of temperature fluctuation on char combustion rate, which is totally eliminated by CFD 1 model (the old char combustion model). For more details one can refer to reference [207]. They used an Eulerian-Eulerian model while the current

simulations results proved that the discrete phase Eulerian-Lagrangian model is a better suited method for this particular application of modelling coal combustion.

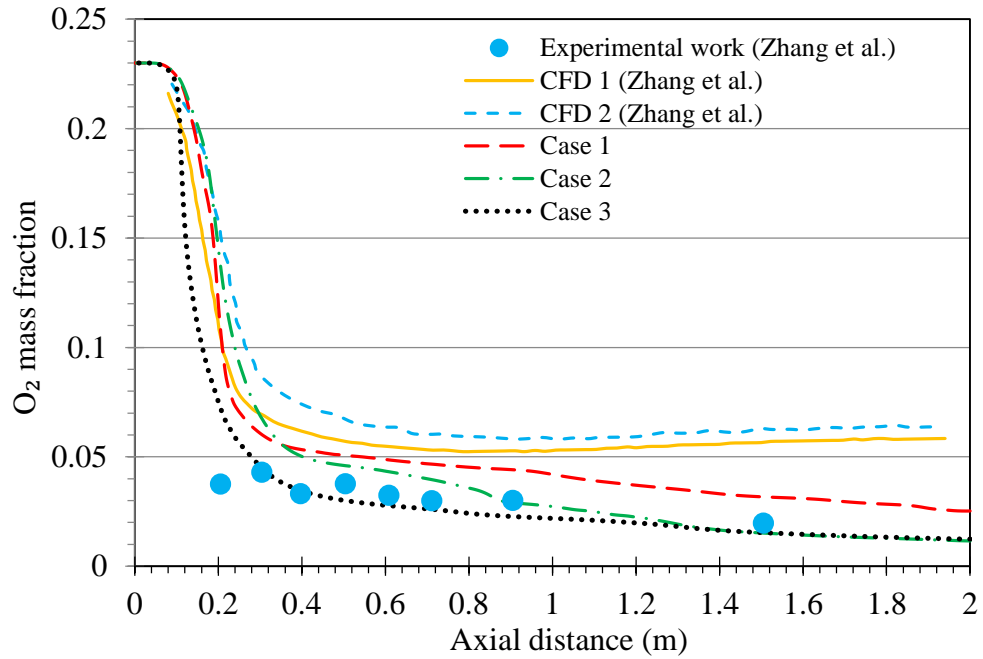


Figure 4.11: Mass fraction of  $O_2$  for coal 2 along the axial distance of the reactor.

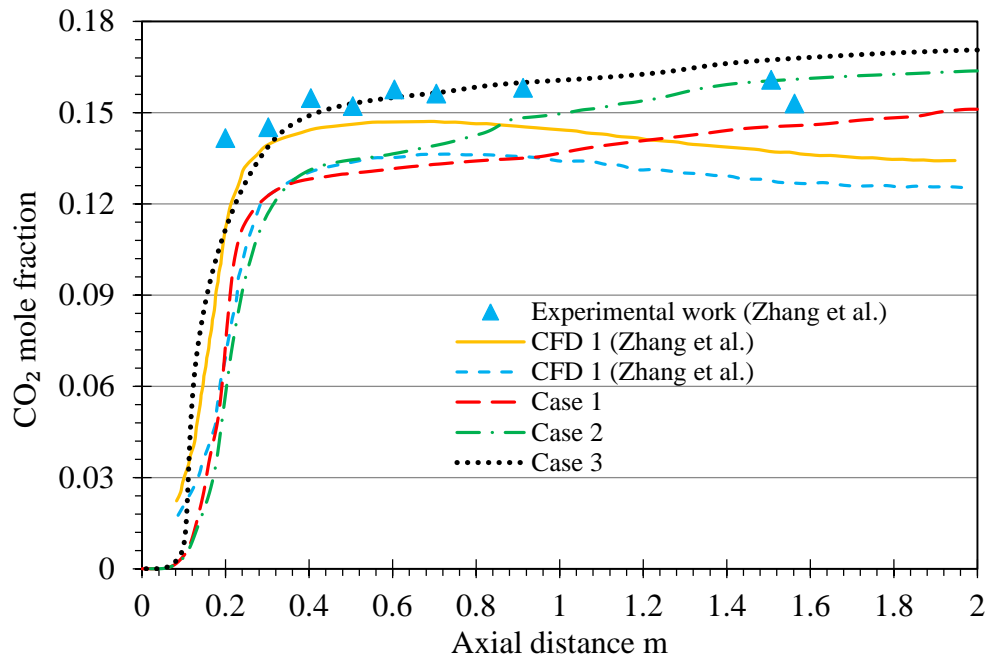


Figure 4.12: Mole fraction of  $CO_2$  for coal 2 along the axial distance of the reactor.

In order to further estimate quantitatively the difference between the experimental and numerically predicted results, a parity plot of the  $O_2$  mass fraction and  $CO_2$  mole fraction for coal 1 at the different axial locations are presented in Figure 4.13. The  $y = z$

line indicates the ideal results i.e. the simulated results are identical to those from the experiment.

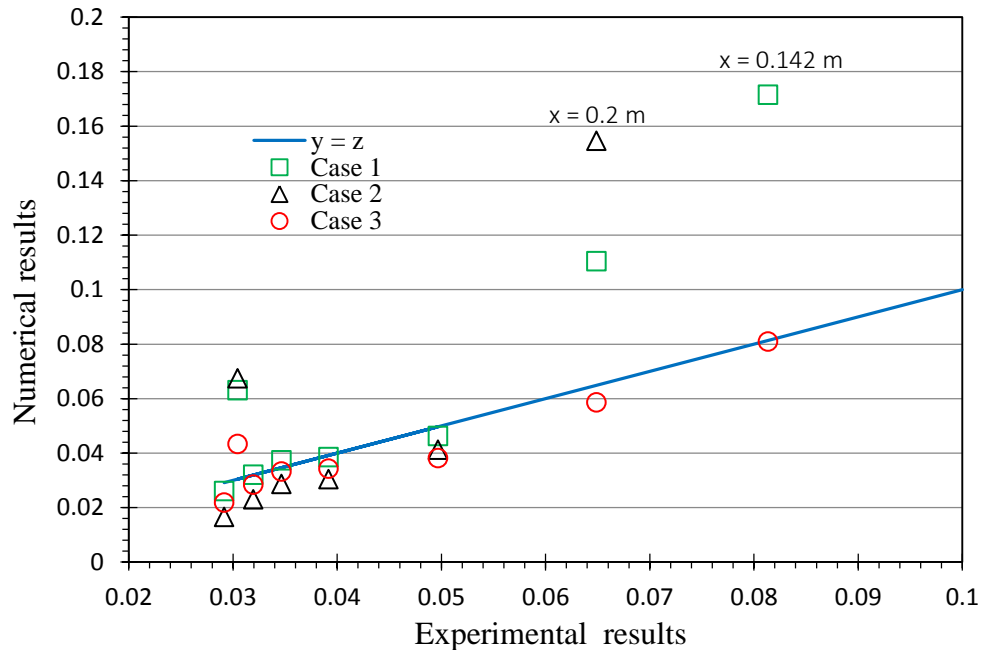


Figure 4.13: Comparison between the experimental and simulated data of  $O_2$  mass fraction for coal 1. Ideal results lie on the line indicated by  $y = z$ .

From Figure 4.13 above for the oxygen mass fraction, it can be seen that the results of Case 3 have good agreement as most of the data points lie very close the line when compared with the other cases. Results of Cases 1 and 2 have good agreement with the experiment towards the downstream of the reactor but failed to achieve better accuracy near the burner region as can be seen at the axial distances  $x \approx 0.142$  m and  $x \approx 0.2$  m where the data placed far from the line.

The same is seen in Figure 4.14 for the carbon dioxide mole fraction. However, we further emphasise that no information is available in Zhang et al. [207] on the standard deviation of these experimental data and in practice this has to be taken into account in any comparative plot, and overall, as already mentioned, Case 3 produces the best agreed results.

#### 4.8.1.2 Temperature and mass fractions of combustion species

The volatile mass fraction for coal 1 is illustrated in Figure 4.15. It is seen that the behaviour of the volatile release is almost the same in general for all the cases but the start of volatile release shifts to a downstream location of the reactor for case 1 and



case 2 in comparison with case 3. This can also be seen in Figure 4.16, which shows the distribution of the volatile mass fraction.

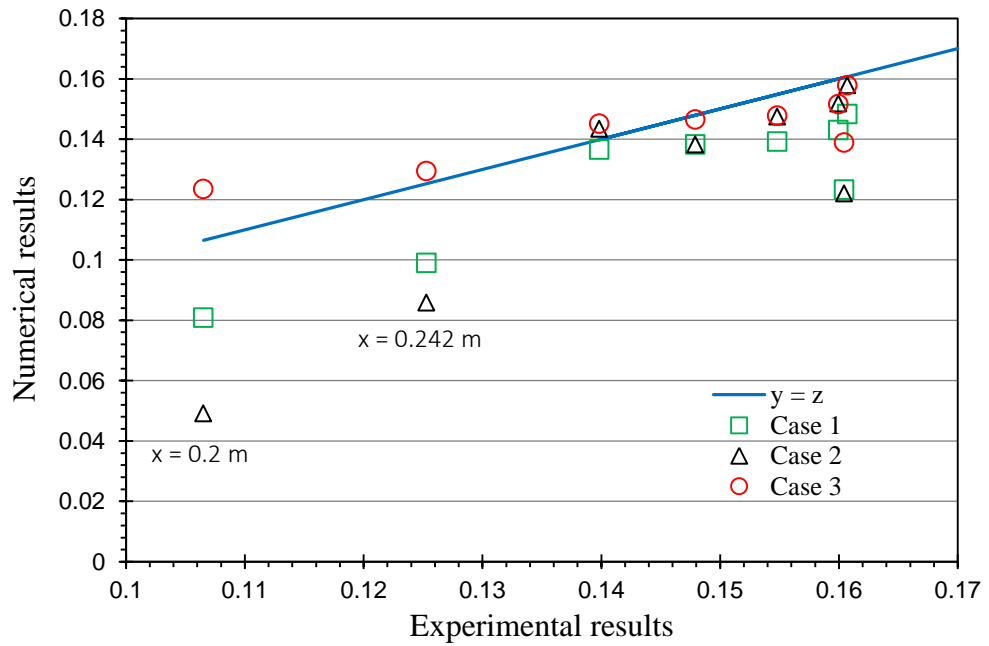


Figure 4.14: Comparison between the experimental and simulated data of  $\text{CO}_2$  mole fraction for coal 1. Ideal results lie on the line indicated by  $y = z$ .

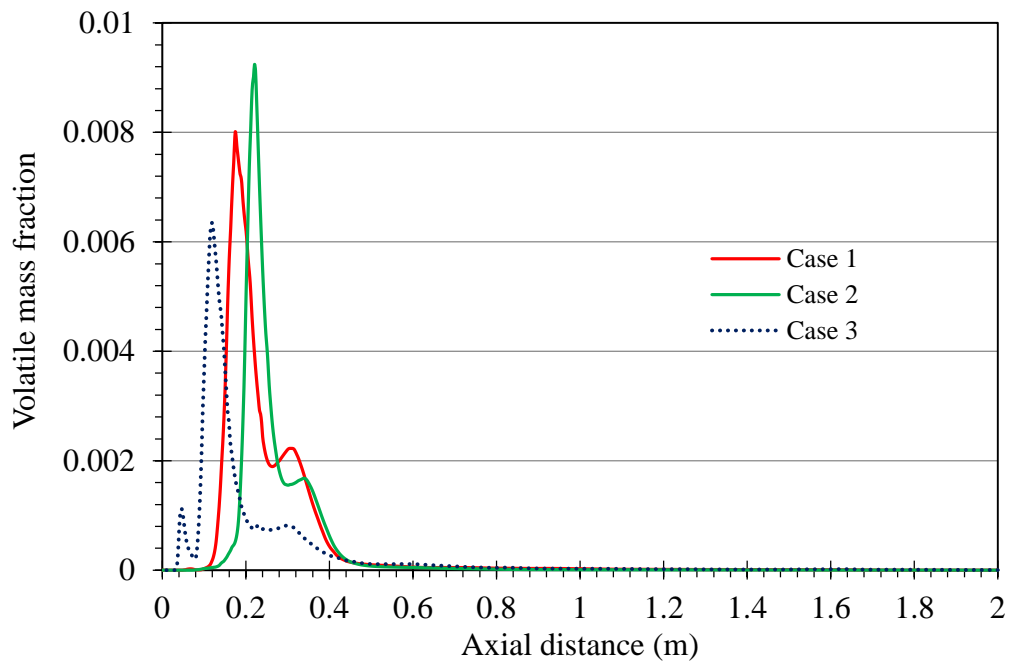


Figure 4.15: The variation of volatile mass fraction for coal 1 in the axial direction of the reactor.

The release of volatiles takes place while coal particles are entrained by the carrier gas (air), which mixes with the inlet gas (air) supplied through the primary and secondary

inlets. Therefore, the release and combustion of volatiles mainly occurs at the centre of the reactor as can be seen in Figure 4.16.

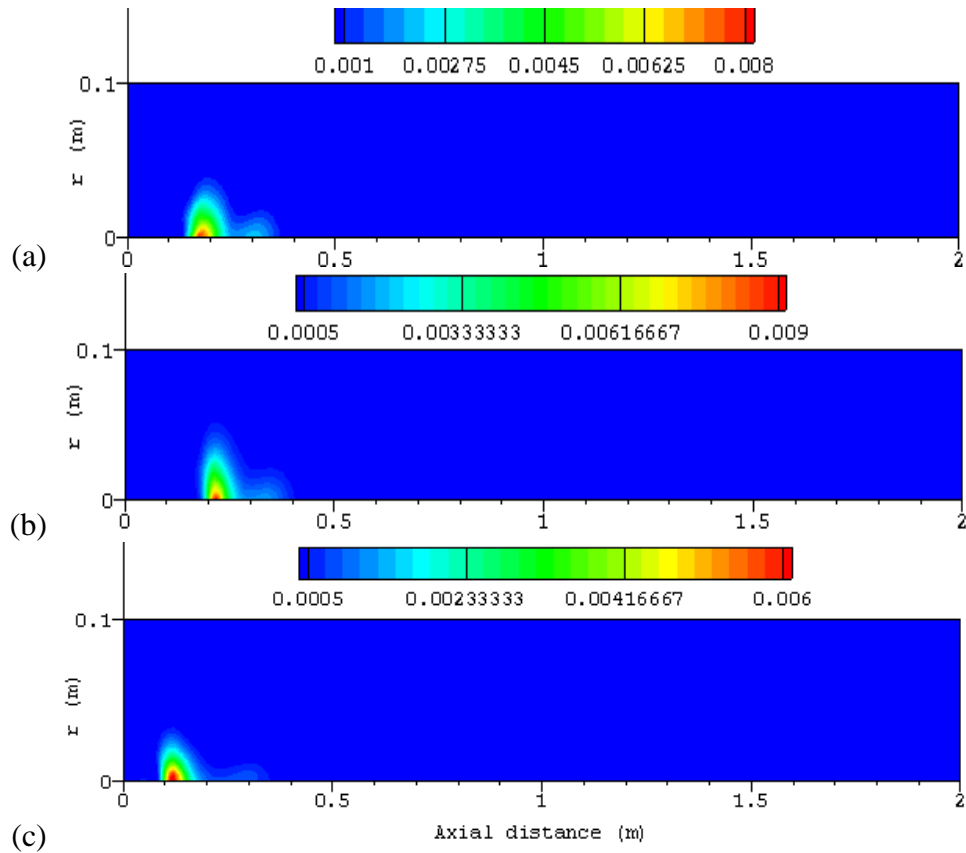


Figure 4.16: Volatile mass fraction distribution for coal 1: (a) case 1, (b) case 2 and (c) case 3.

The variation of gas temperature inside the reactor along the centreline for all the cases is depicted by Figure 4.17. It is shown that the high temperature occurs in the region where the volatiles combustion takes place which can be identified by the release of volatiles shown in Figure 4.15 and Figure 4.16. It can be seen that case 3 gives higher temperature than that of the other cases.

Figure 4.18 demonstrates the isothermal contours of the gas phase in the reactor. The maximum temperature of case 3 is 1632 K. The maximum temperature of both case 1 and case 2 are 1604.77 K and 1602.967 K, respectively. The high temperature zone at the upstream where the release of volatile takes place is due to the exothermic coal combustion. Despite the difference in the temperature distribution at the part near the coal inlet, it can be seen that it is almost the same near the exit of the reactor. The variation of temperature inside the reactor indicates the process of the coal combustion when referring to Figure 4.17. For all the cases, once the particles of coal mix with the air at the feed point, the mixture temperature initially increased due to the process of

heating up till the point where the release of volatiles started. At this location the temperature dropped down due to the heat taken by the coal particles for the devolatilization process then went up gradually. After a gradual increase, the temperature rapidly increases as a result of the combustion of volatiles followed by the combustion of char. The gas phase reactions have rates that are known to be much faster than those of the char combustion reactions and therefore they are dominant in the presence of  $O_2$ . The peak temperature occurs at the instant when most of the oxygen is depleted (see Figure 4.9). When the peak temperature is reached the gasification reactions become more important and their effectiveness depends on the operating conditions. It is clearly seen from Figure 4.17 that when the peak temperature is achieved the temperature of gas phase begins to decrease due to commence of the gasification reactions.

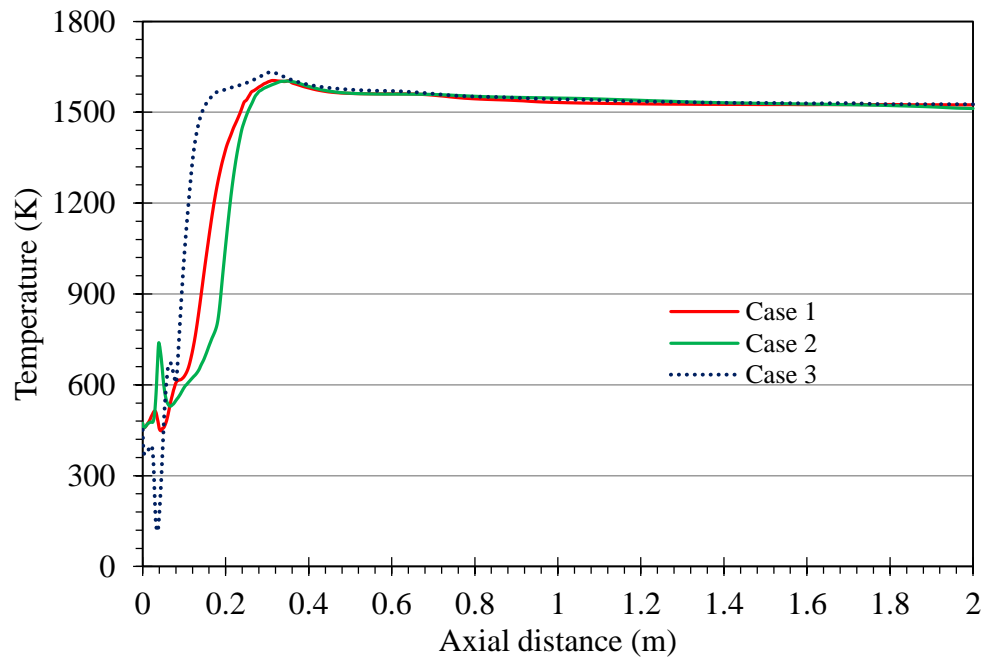


Figure 4.17: Gas temperature variation for coal 1 along the axial distance of the reactor.

Figure 4.19 shows the char burnout rates. From this figure and both Figure 4.15 and Figure 4.16, it can be seen that both the process of char combustion and the process of release and combustion of volatile for the whole combustion process take place in the same time. The coal particles injected into the reactor have different particle sizes and some particles are so smaller and some are bigger. Therefore, the smaller particles release their volatile content faster than the bigger ones and their char content is combusted while the bigger ones are still releasing their volatile content. When

considering only the combustion of one coal particle, it will take place in a sequence way based on the assumption made earlier (see § 4.2.2.3).

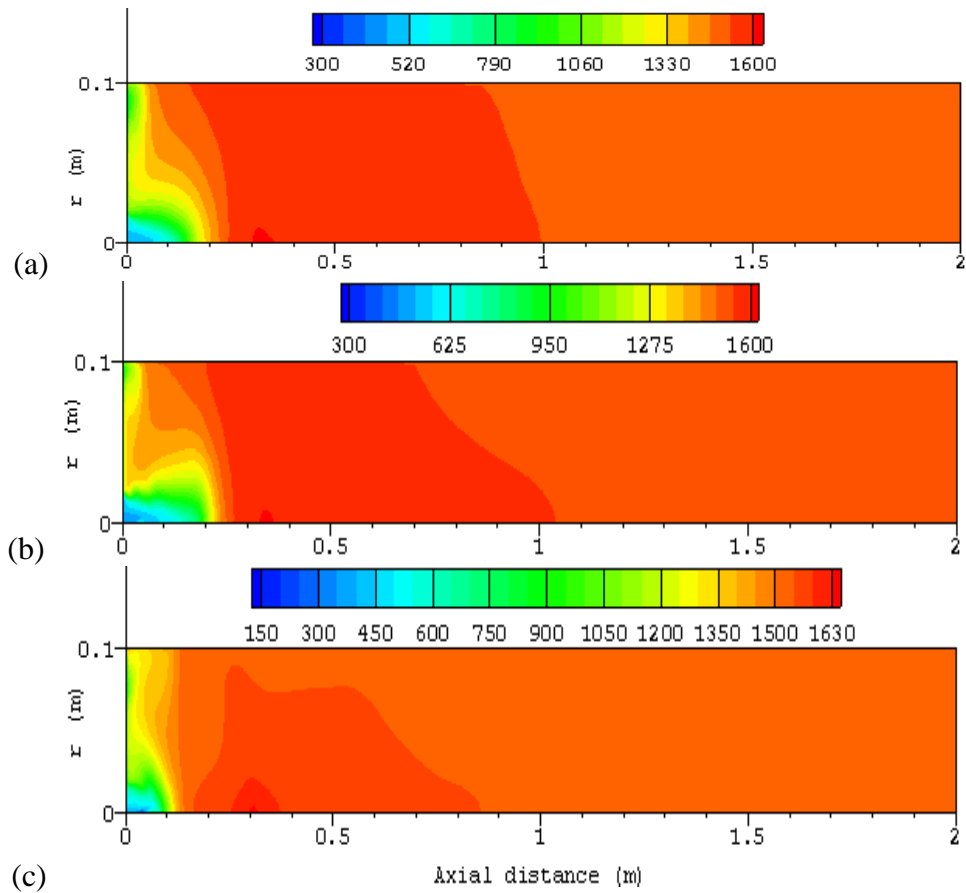


Figure 4.18: Predicted temperature distribution for coal 1: (a) Case 1, (b) Case 2 and (c) Case 3.

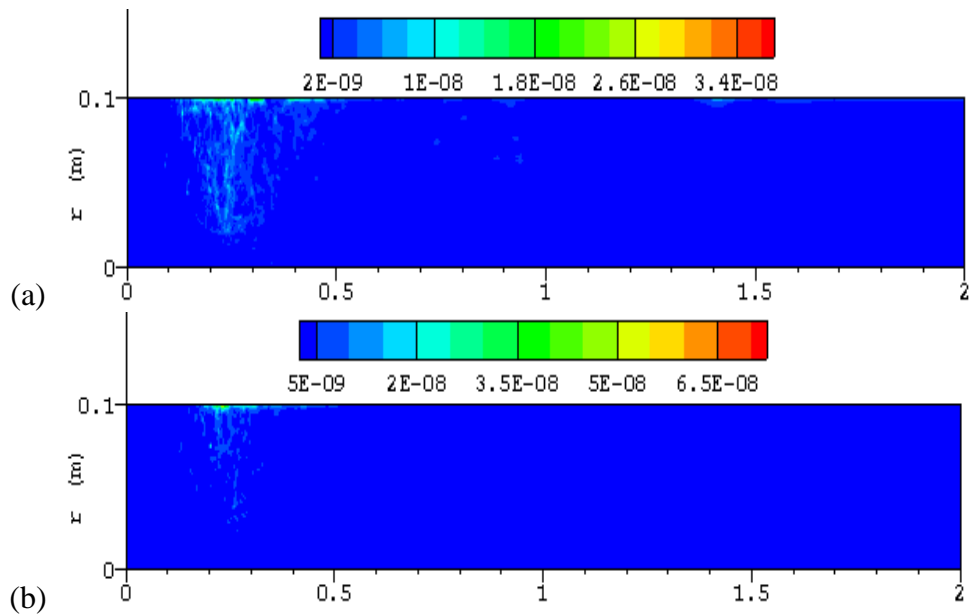


Figure 4.19: Particles burnout for coal 1.

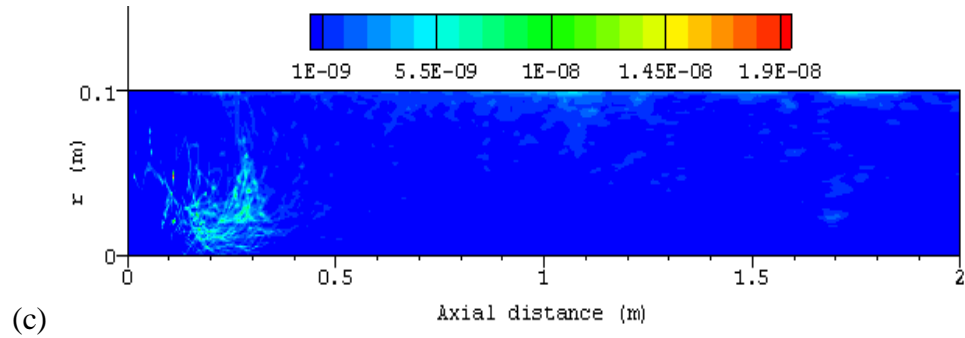


Figure 4.19: continued.

The distribution of mass fractions of combustion species for the three cases of coal 1 is shown in Figure 4.20 through Figure 4.23 for  $O_2$ ,  $CO_2$ ,  $H_2O$  and  $N_2$ , respectively. From Figure 4.20, it can be seen that  $O_2$  is available in the vicinity of the burner. For case 1,  $O_2$  is available in the first 10 cm of the reactor for case 1 and in the first 8 cm. For case 2, the availability of  $O_2$  is in the first 15 cm of the reactor. These sections represent the drying zones and the earlier devolatilization zones. The distribution of  $O_2$  in these zones is fairly uniform ( $O_2$  does not vary along the axial direction). For all cases, as  $O_2$  moves further it is consumed by the combustion of volatiles and char till the exit of the reactor where only a very small fraction is available as can be seen in Figure 4.9. The concentration of  $O_2$  in these stages depends on the devolatilization rate, the mixing rate of volatiles and air due to the turbulence and the particles residence time. It is seen that the rapid consumption of  $O_2$  is mainly due to the combustion of volatiles.

From Figure 4.21 and Figure 4.22, it can be seen that the concentration of  $CO_2$  and  $H_2O$  increase showing high quantities just after the rapid decrease of  $O_2$ . The concentration of  $CO_2$  reaches the maximum value at the outlet as can be seen in Figure 4.10, which gives an indication that the gasification reaction (R4) is not effective. The mass fractions of the species  $CO$  and  $H_2$  for case 3 are plotted respectively in Figure 4.24 and Figure 4.25. It is observed that the concentrations of  $CO$  and  $H_2$  are very small within the char combustion zone.  $CO$  produced is immediately consumed in the gas phase. There is only very little of  $CO$  appearing in the downstream region which resulted from the reduction reaction (R4). This is consistent with what mentioned above regarding the ineffectiveness of this reaction. Regarding  $H_2$ , it increases monotonically along the length of the reactor as can be clearly seen in Figure 4.26, which illustrates the variation of mass fractions of species  $CO$  and  $H_2$  along the centreline of the reactor.

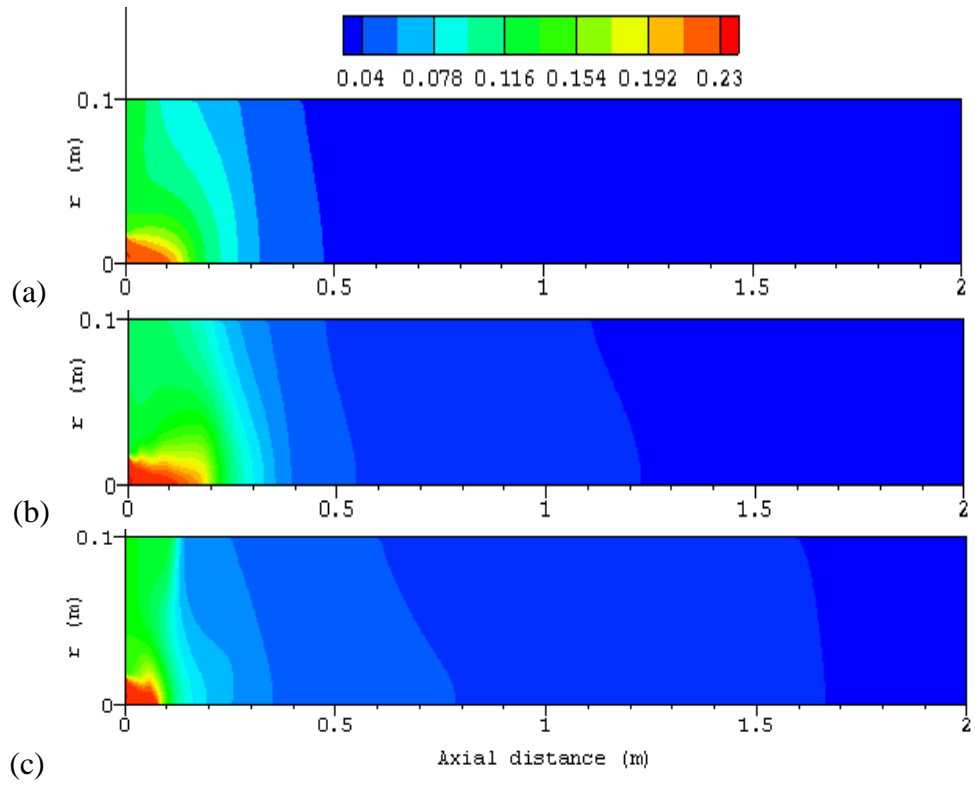


Figure 4.20: Mass fraction of  $O_2$  distribution for coal 1: (a) case 1, (b) case 2 and (c) case 3.

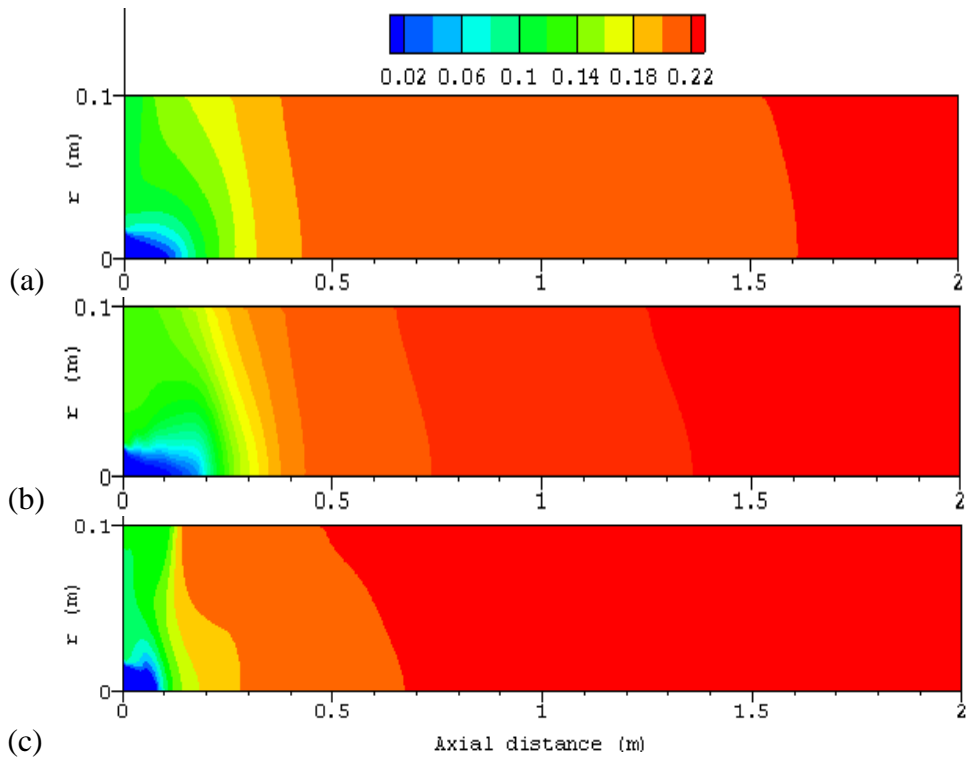


Figure 4.21: The distribution of  $CO_2$  mass fraction for coal 1: (a) case 1, (b) case 2 and (c) case 3.

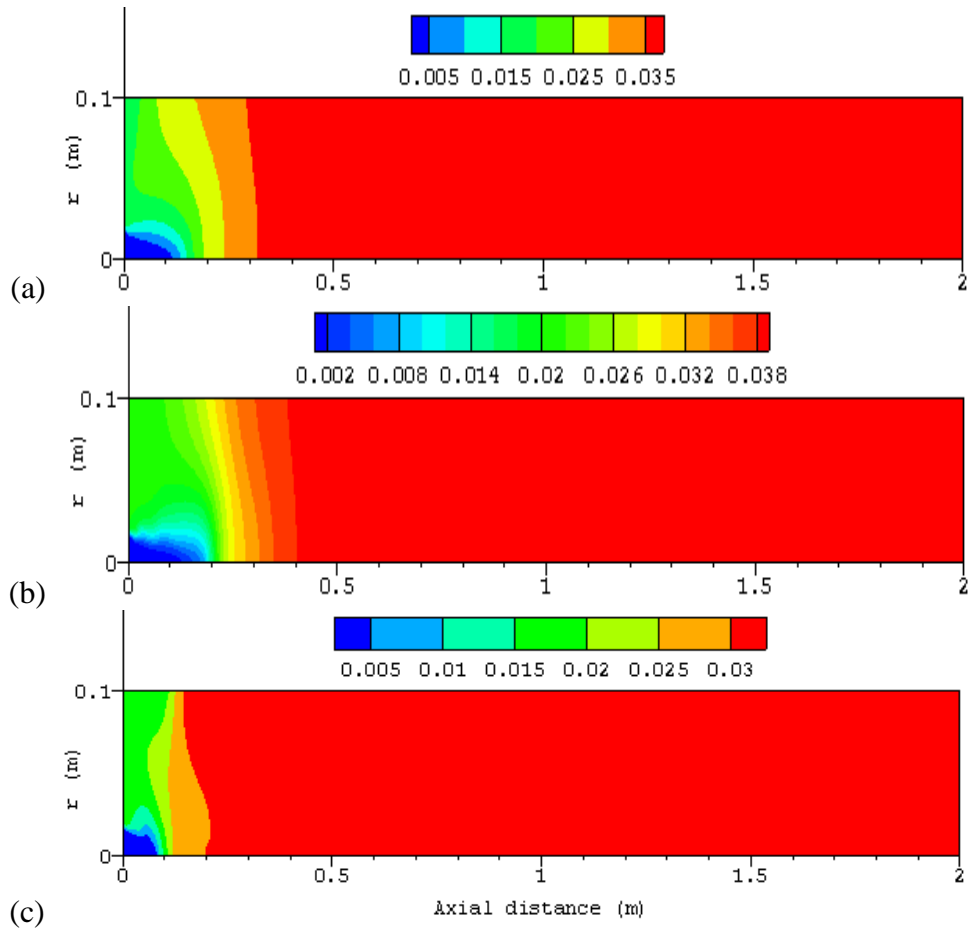


Figure 4.22:  $\text{H}_2\text{O}$  mass fraction distribution for coal 1: (a) case 1, (b) case 2 and (c) case 3.

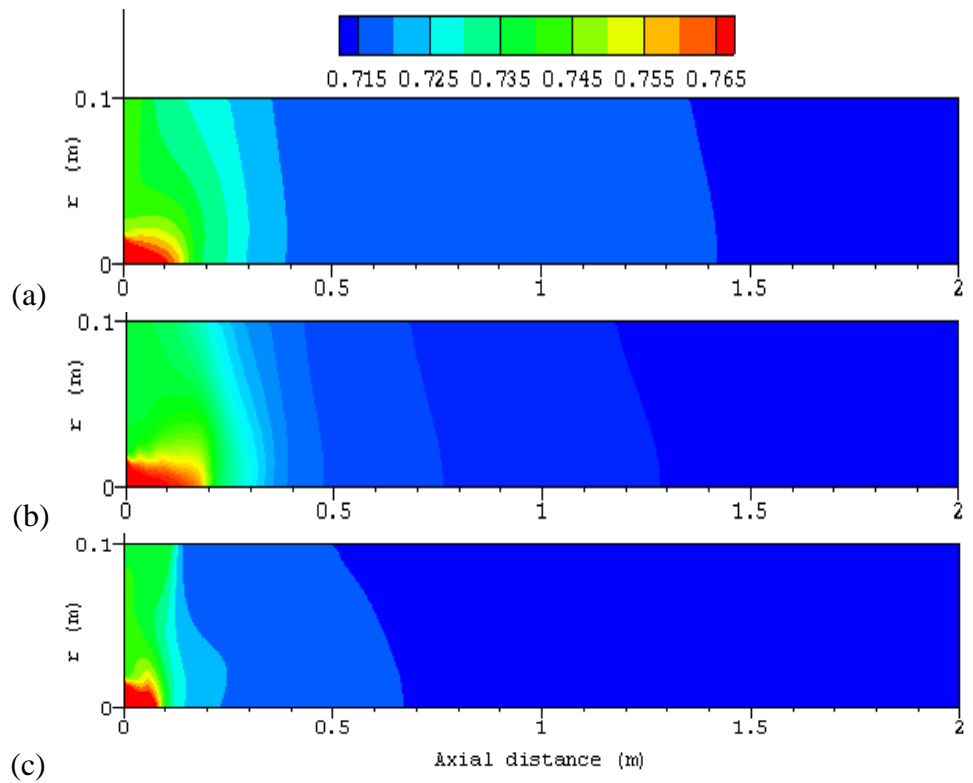


Figure 4.23: The distribution of  $\text{N}_2$  mass fraction for coal 1: (a) case 1, (b) case 2 and (c) case 3.

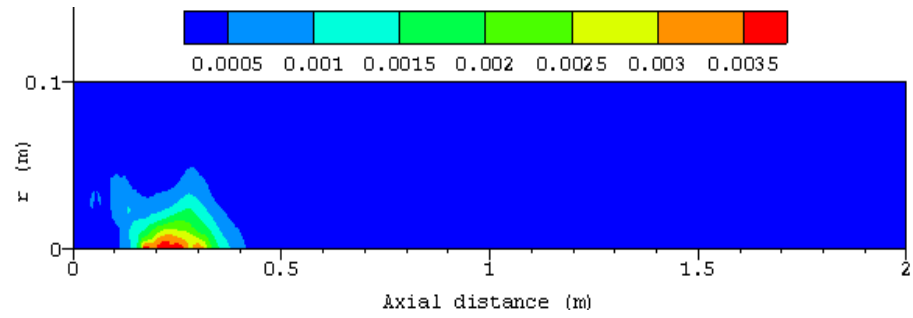


Figure 4.24: The distribution of CO mass fraction for coal 1 (case 3).

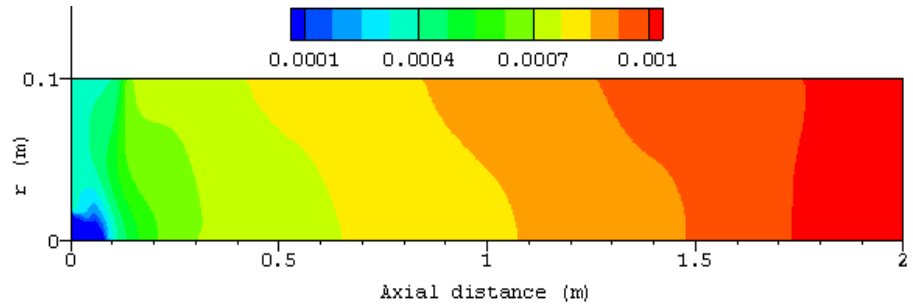


Figure 4.25: The distribution of H<sub>2</sub> mass fraction for coal 1 (case 3).

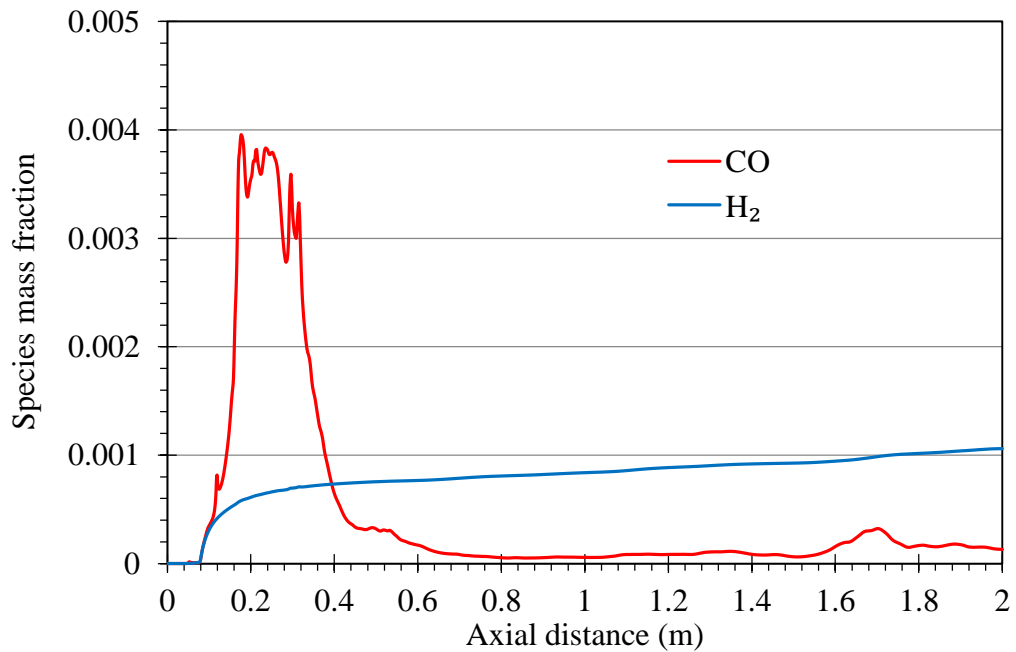


Figure 4.26: Mass fraction of CO and H<sub>2</sub> for coal 1 along the axial distance of the reactor.

#### 4.8.1.3 Particles depletion and burnout

From Figure 4.27 that depicts the mass change of coal particles along the axial distance of the reactor it can be seen that there is a flat part of the curves at the beginning for each particle, which means that there is no mass change takes place and the particles only undergo a heating process. It can also be seen that the larger particles need longer



period of time than that of the smaller particles to be heated up. Then, there is a decrease in the mass due to the particles devolatilization which takes place rapidly for the small particles and becomes slower near the exit of the reactor as the particle size increases. During the devolatilization the volatile matter is released. Figure 4.27 also shows that whole volatile matter was almost released and the char reactions began. From the properties of the coal the solid combustible fraction of coal on DAF basis was approximately 67 % and it is seen that the decrease in mass reached this value means that nearly the total volatile matter was released. This reduction in mass is accompanied by the volatile combustion and this can be identified when referring to Figure 4.17, where it was found that the highest rate of change of temperature occurred in the region between 0.1 m and 0.4 m due to the rapid change of mass of the small particles. This effect is now clearly examined from Figure 4.27, where the results show that the particles with smaller diameters (e.g. 16 and 84  $\mu\text{m}$ ) rapidly lost their mass, at a faster rate than the larger particles. For the larger particles, the heat release by combustion is taken up by the endothermic reactions, causing a slower decrease in their mass. Furthermore, when the heat is released by combustion and the oxygen is almost depleted, the gas temperature decreases gradually.

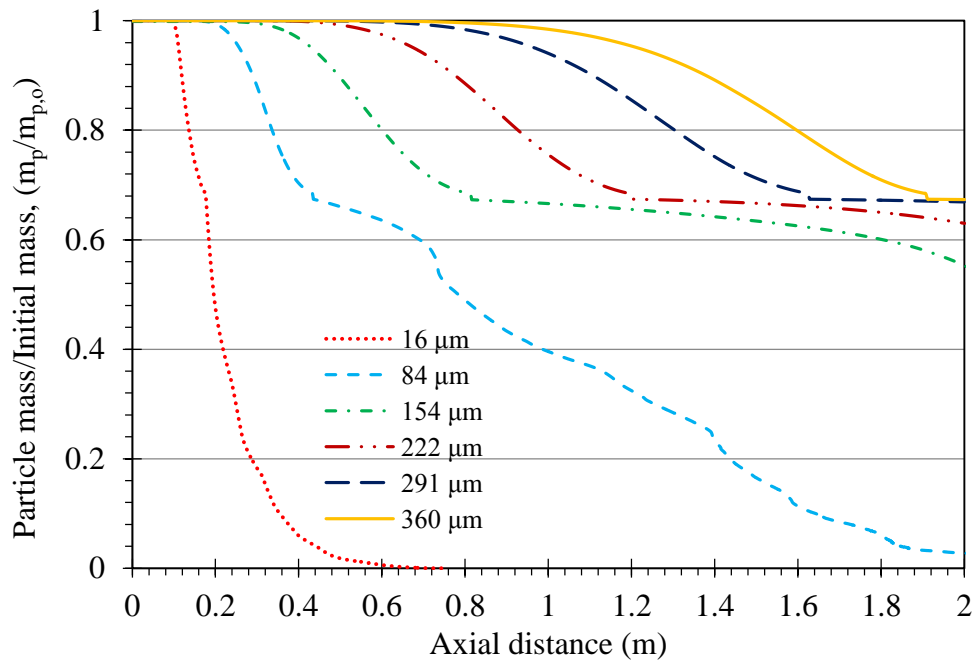


Figure 4.27: Mass depletion of particles with different sizes for case 3.

Figure 4.28 shows the burnout of the particles. The burnout of the particles is a measure of the extent of coal particles combustion. It can be seen that the particle size has a great effect on the coal burnout. The burnout of the particle with a diameter of 16  $\mu\text{m}$  is

100%. Whereas, the burnout of the particles with diameters of 84, 154, 222, 291  $\mu\text{m}$  at the exit of the combustion domain is approximately 86, 75, 35, 33, 29 %, respectively. This leads to the conclusion that when the particle size increases the burnout decreases.

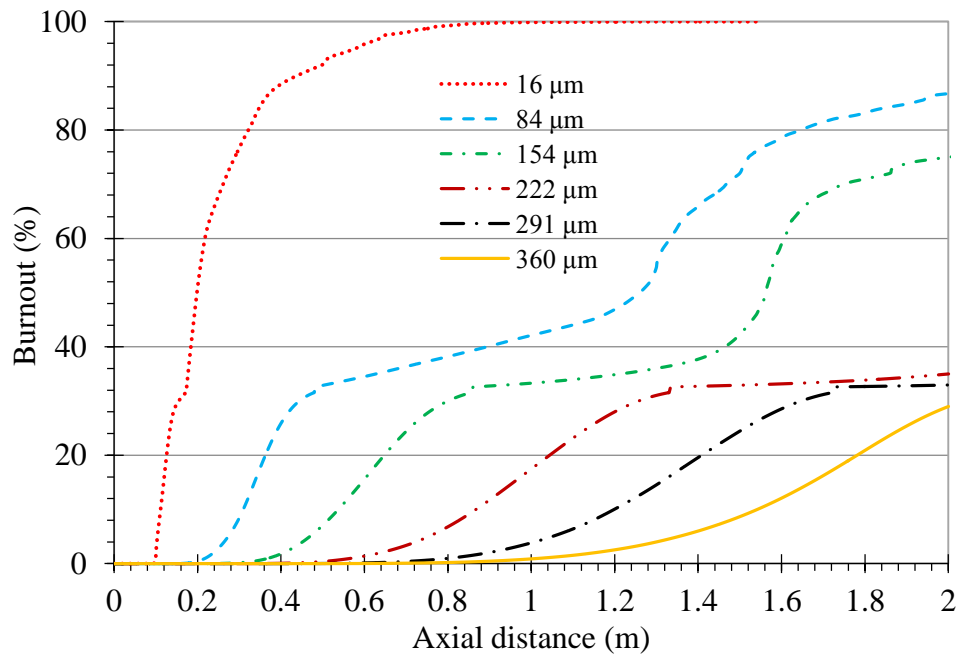


Figure 4.28: Burnout of particles with different sizes for Case 3.

### 4.8.2 $\text{NO}_x$ model

Figure 4.29 shows the calculated NO emissions for the third case of pulverized combustion modelling (Case 3) for different runs. It shows the effect of the intermediates on the formation of NO. All the runs gave the same trend, but it is clear that the run with the assumptions: 52% HCN, 10%  $\text{NH}_3$  and 38% NO has good agreement with the experiment data available in [238]. Further, it can be seen that the calculated profile of NO concentration is rather smooth except at the upstream where there is a slight difference found between the measured and calculated values. On the other hand, it gives good agreement in the downstream towards the exit of the reactor. Referring to Figure 4.29, it is seen that the variation of intermediate percentages has an influence on the formation of NO. Thus, the decrease of the assumed HCN percentage results in increasing the mass fraction of NO.

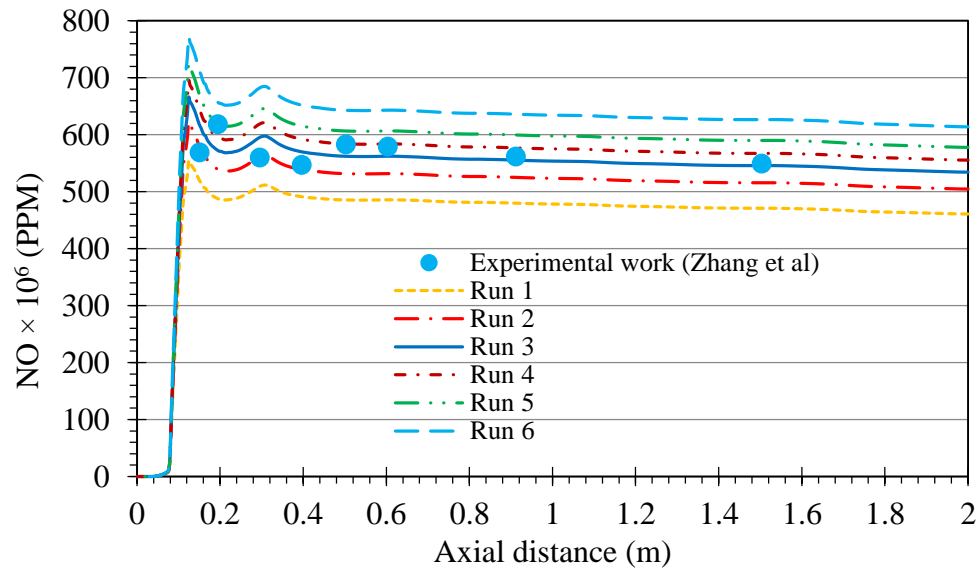


Figure 4.29: NO weight fraction for various runs along the axial distance of the reactor.

### 4.8.3 Effects of wall temperature

Figure 4.30 through Figure 4.36 show the effects of the variation of wall temperature on the temperature of gas phase and the species concentrations. In Figure 4.30, the variation of gas temperature along the centreline of the reactor is plotted. It can be seen that the gas temperature increases as the wall temperature increases. It is also seen that the trends are similar. The other important thing that can be extracted from Figure 4.30 is the heat needed to the process of char gasification. It is seen that at wall temperature of 1800 K, more heat is taken for the char gasification than the other cases as can be identified from the decrease of gas temperature after reaching the maximum value.

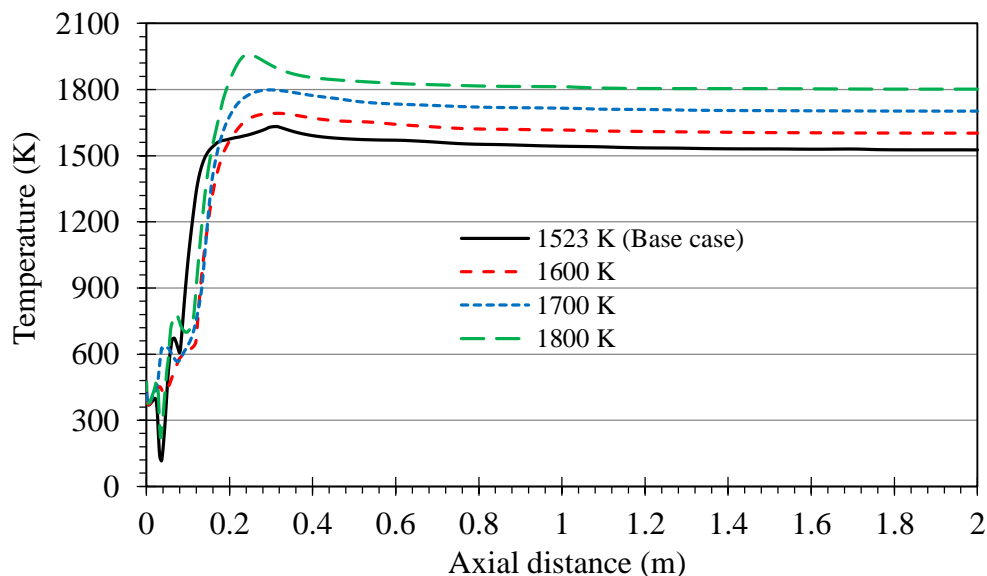


Figure 4.30: The variation of gas temperature along the centreline for various wall temperatures.

From Figure 4.31, it can be seen for all case that the release of volatile takes place in the same region, but the maxima of volatile mass fraction increases as the wall temperature increases.

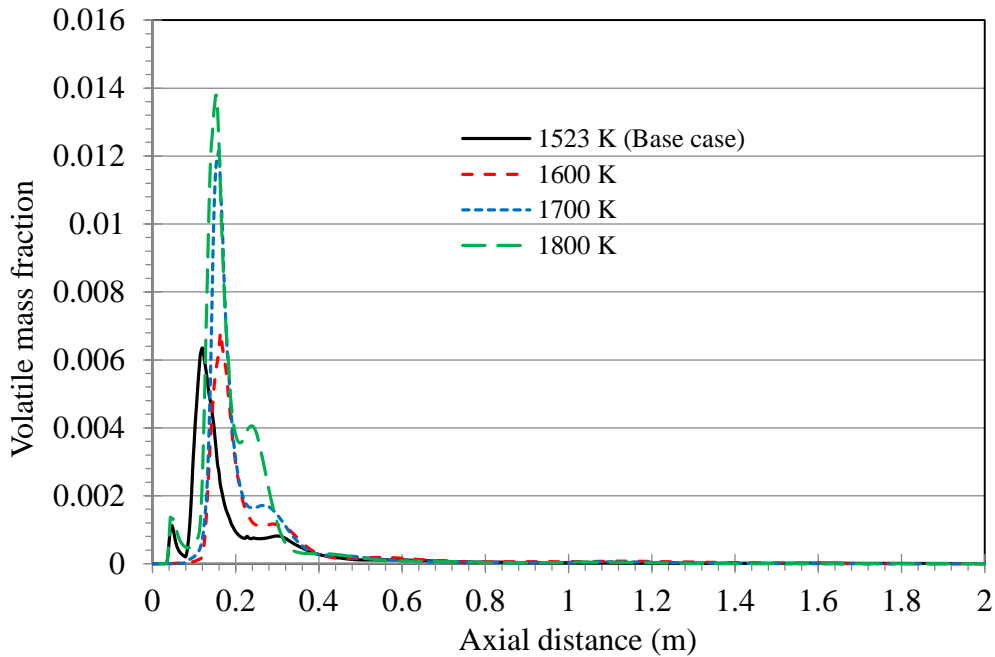


Figure 4.31: The variation of volatile concentration along the centreline for various wall temperatures.

With regard to  $O_2$  concentration, it can be seen from Figure 4.32 that there is no much change in it due to the increase of wall temperature. This is also seen in Figure 4.33, which depicts the variation of  $CO_2$  mass fraction along the centreline of the reactor. Moreover, it is also seen that  $CO_2$  mass fraction for each case increases along the axial distance especially in the region where there is only little oxygen is available (see Figure 4.32). This means that reaction (R4) is not effective.

On contrary, it can be seen that the mass fraction of  $H_2O$  decreases as the wall temperature decreases. Moreover, for wall temperature of 1523 K (base case) and the other cases, it is also seen that the concentration of  $H_2O$  along the axial direction reached its maxima then started to decrease at a certain axial location. For the former case, the decrease in  $H_2O$  concentration started the axial location ( $x = 1.6$  m), whereas the axial locations for wall temperatures 1600 K, 1700 K and 1800 K where the decrease of the concentration of  $H_2O$  is obvious are 1.04, 1.04 and 0.96 m, respectively. For all cases, this decrease of  $H_2O$  is due to the heterogeneous reaction (R5).

The mass fractions of CO and  $H_2$  are plotted in Figure 4.35 and Figure 4.36, respectively. As mentioned in § 4.8.1.2, since the CO produced due to the

heterogeneous reaction (R3) is immediately consumed in the gas phase due to the presence of  $O_2$ , only a small amount of CO is seen within the char combustion zone as shown in Figure 4.35. It is seen from the figure that the concentration of CO increases with increasing the wall temperature. It can be also seen that by increasing the wall temperature very small amounts of CO started to appear according to the reaction (R4) along the axial distance between the axial location ( $x > 1$  m) and the exit of furnace.

$H_2$  mass fraction increases with increasing the wall temperature as depicted in Figure 4.36. It can be also noticed that the concentration of  $H_2$  for all cases increases along the axial distance of the reactor due to the heterogeneous reaction (R5). Furthermore,  $H_2$  mass fraction increases as  $O_2$  mass fraction decreases because of the reason that the heterogeneous reaction (R5) becomes more active and this is consistent with the decrease in  $H_2O$  at the region near the exit of the furnace (see Figure 4.34). Figure 4.37 shows the composition of gas products at the reactor exit.

Regarding the influence of wall temperature on the concentration of pollutant NO, Figure 4.38 depicts the variation of NO emissions along the centreline of the reactor, which is plotted by different wall temperatures. The figure shows that increasing the wall temperature increases the concentration of NO. Apart from that the peak of the case for wall temperature 1600 K, which is lower than that for the base case, the same behaviour is visible for all graphs.

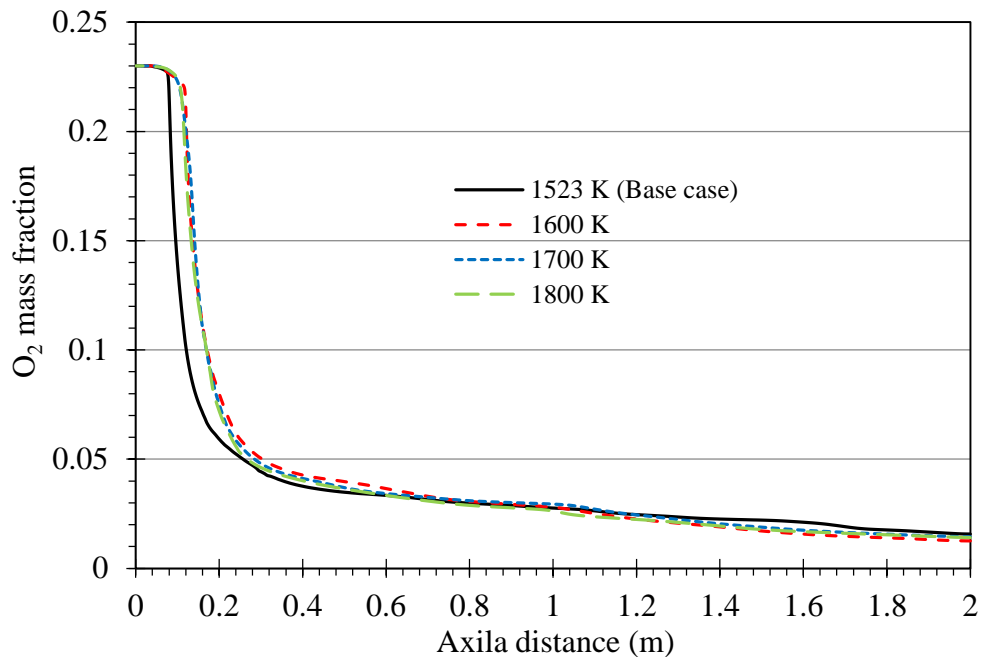


Figure 4.32: The variation of  $O_2$  concentration along the centreline for various wall temperatures.

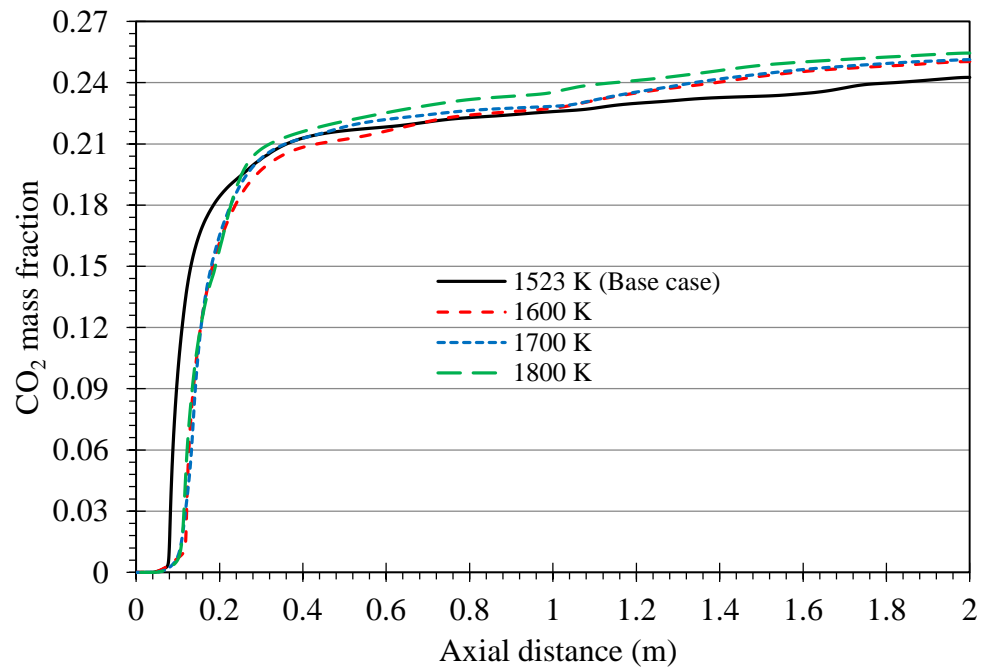


Figure 4.33: The variation of  $\text{CO}_2$  mass fraction along the centreline for various wall temperatures.

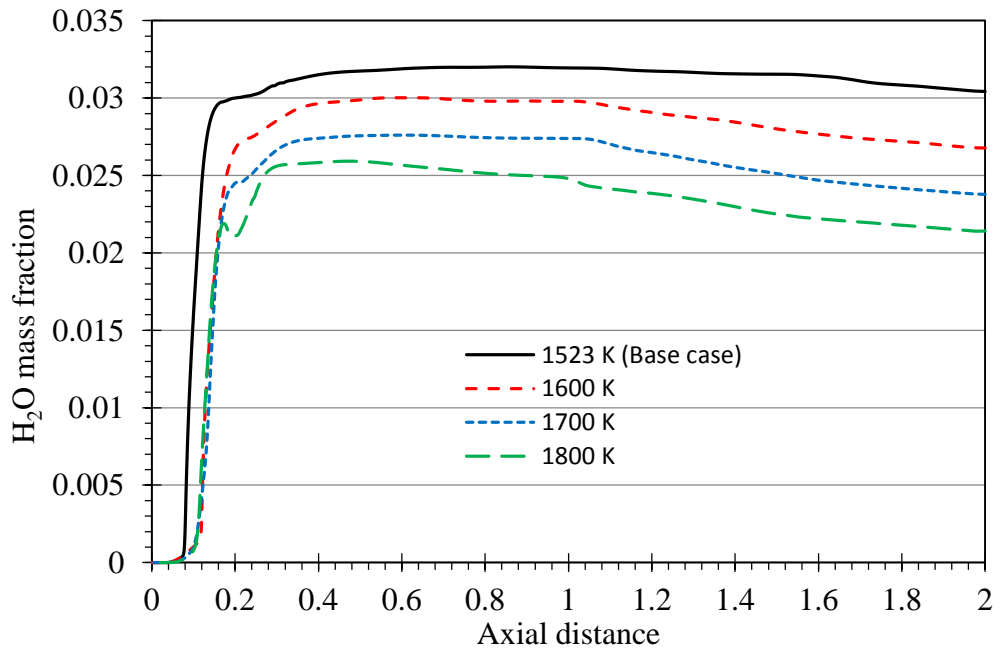


Figure 4.34: The variation of  $\text{H}_2\text{O}$  mass fraction along the centreline for various wall temperatures.

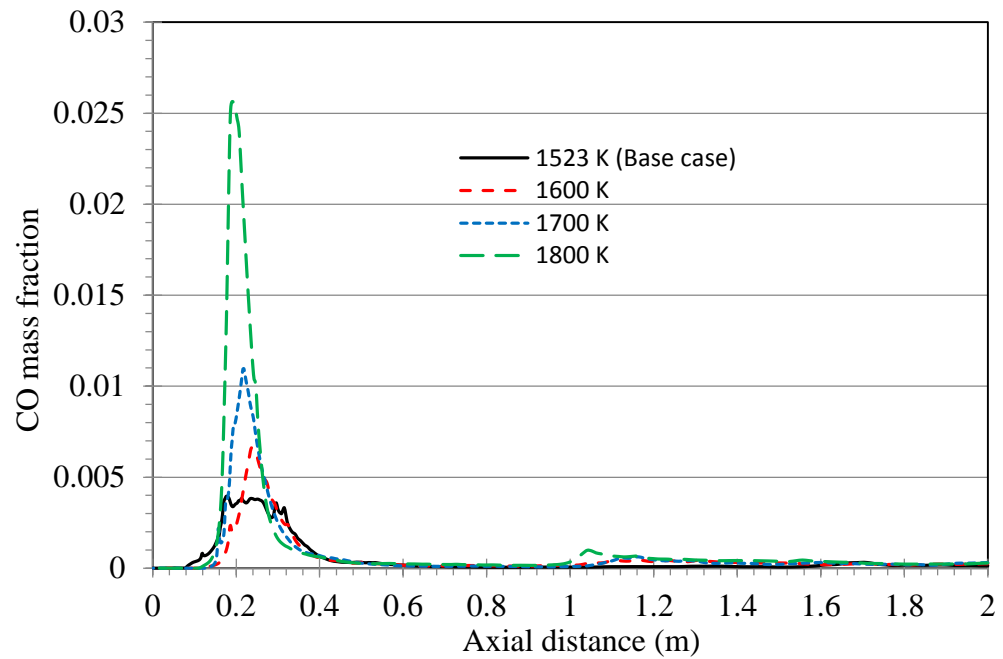


Figure 4.35: The variation of CO mass fraction along the centreline for various wall temperatures.

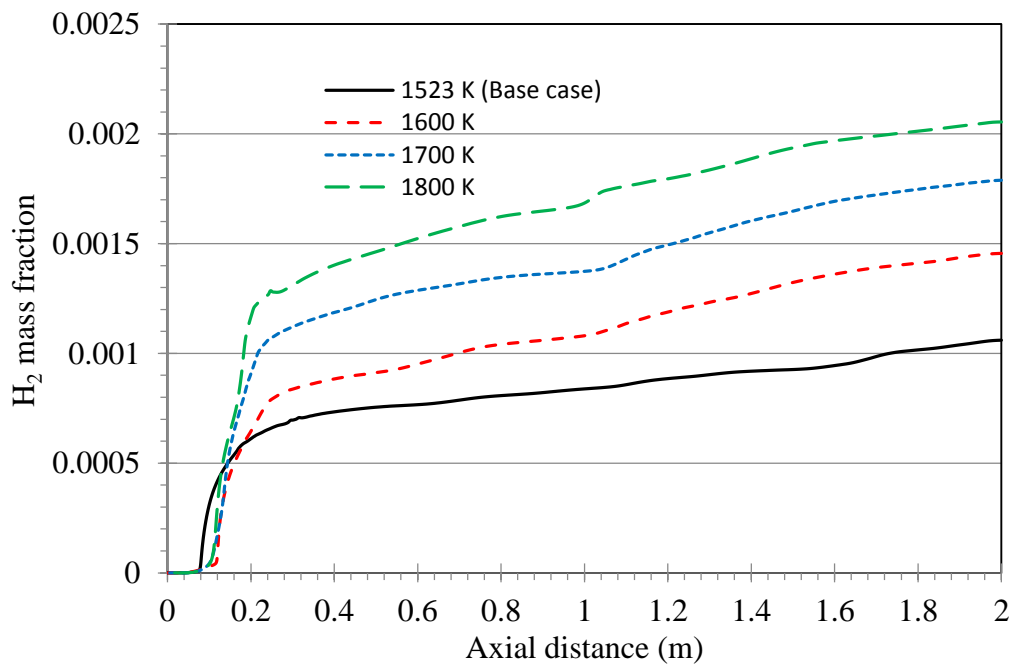


Figure 4.36: The variation of H<sub>2</sub> mass fraction along the centreline for various wall temperatures.

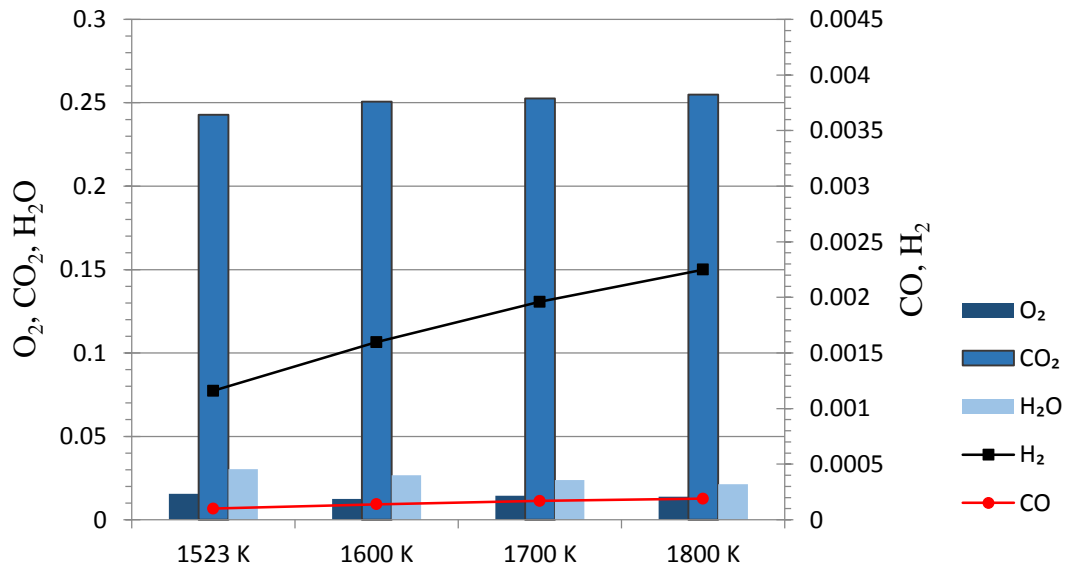


Figure 4.37: Variation of species mass fraction at the exit of the reactor for various wall temperatures.

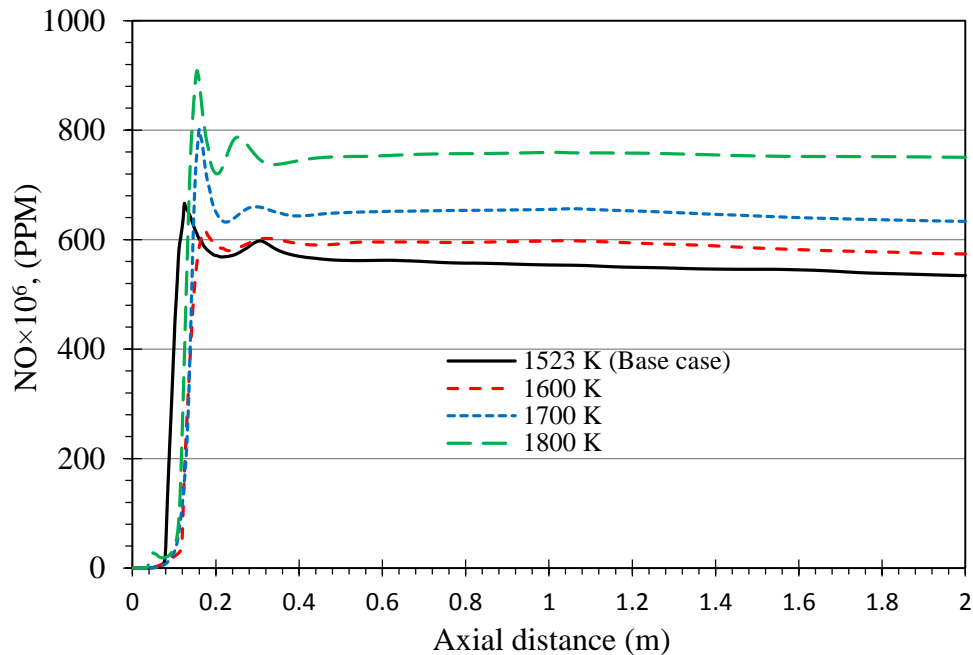


Figure 4.38: NO weight fraction along the axial distance of the reactor for various wall temperatures.

#### 4.8.4 The influence of air inlet rate

The effects of air inlet on the combustion process have been investigated. The inlet velocity of the air supplied through the secondary air inlet has been varied. The secondary air velocity takes the values of 11.5 m/s, 13.5 m/s, 15.5 m/s (base case) and 17.5 m/s. Figure 4.39 shows the variation of gas temperature axial direction. Compared with the base case, it can be seen that the gas temperature for the other cases increases and reaches a peak value in the region where the combustion of volatiles (large energy



release rate of the gas phase combustion reactions) and char takes place. For the secondary inlet velocity of 11.5 m/s the maximum temperature is about 2250 K and for the other two case it is ~ 1850 K for the inlet velocity of 13.5 m/s and ~ 1790 for the inlet velocity of 17.5 m/s. For all cases, the figure shows that the gas temperature reaches its maximum value then, later in the gasification process, it begins to decrease gradually due to the reduction reaction (the endothermic nature of the gasification reactions). It is also seen that the gas temperature is almost the same for all case in the region between the axial locations ( $x = 0.6$  m) and ( $x = 2$  m). In this region, the rate of decrease in temperature is too slow. The influence of gasification reactions on the gas phase temperature is clearly seen in the case with the secondary inlet velocity of 11.5 m/s. The variation of the released volatiles along the centreline of the reactor is plotted in Figure 4.40. It can be noticed that decreasing the velocity of the secondary air leads to that the particles will spend more time inside the reactor. Therefore, the residence time increases and as a result more volatiles will be released as can be seen for 11.5 m/s case in Figure 4.40. Moreover, It is also seen that a small portion of the volatiles appears in the region by the axial distance of 0.68 m till the exit of the reactor, which is attributed to that there is no more oxygen left for it to be oxidized (see Figure 4.41).

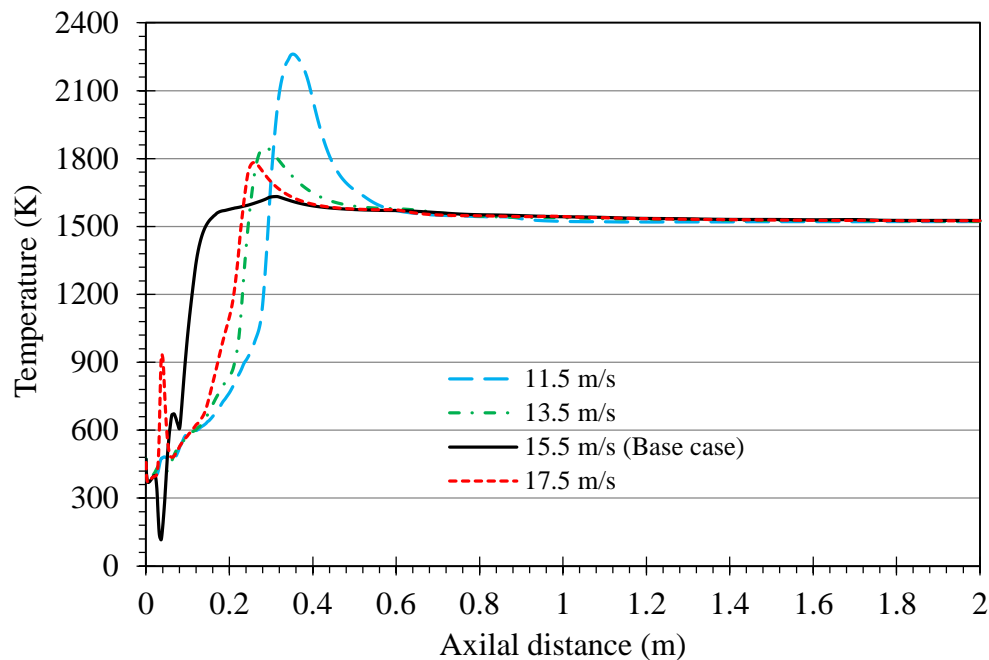


Figure 4.39: The variation of gas temperature along the centreline at different secondary air inlet velocities.

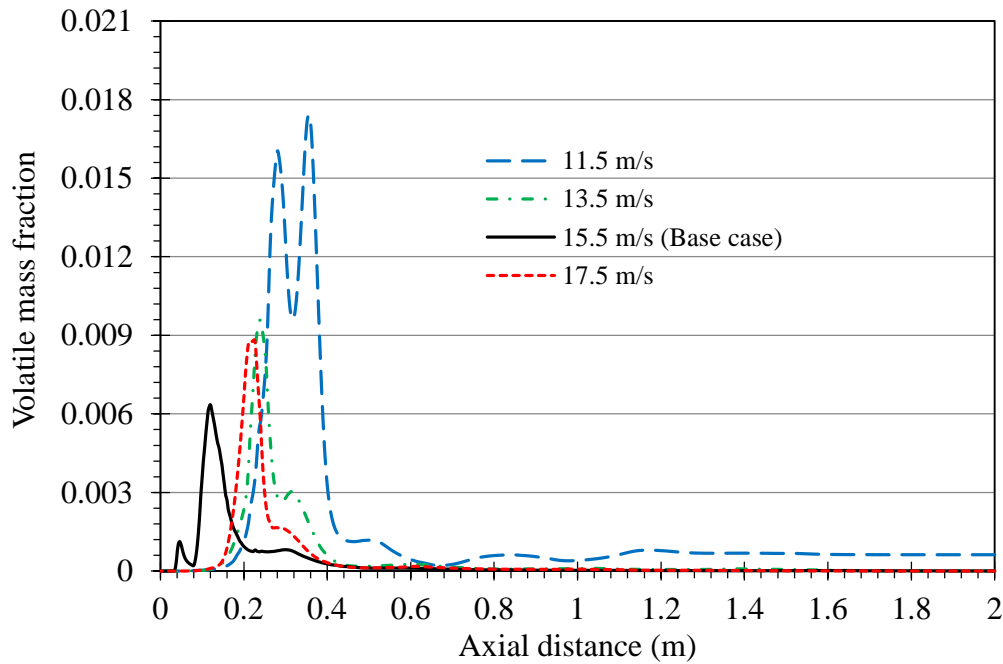


Figure 4.40: The variation of volatile concentration along the centreline at different secondary air inlet velocities.

The effects of varying the inlet velocity of the secondary air on gas phase species  $O_2$ ,  $CO_2$ ,  $H_2O$ ,  $CO$  and  $H_2$  is illustrated in Figure 4.41, Figure 4.43, Figure 4.44, Figure 4.45 and Figure 4.46, respectively. As it is evident from Figure 4.41 the oxygen is completely depleted at the axial location ( $x = 80$  cm) for the case with the secondary air inlet velocity of 11.5 m/s and at the axial location ( $x = 1.8$  m) for the case with the secondary air inlet velocity of 13.5 m/s. Compared with the base case (15.5 m/s) there is more  $O_2$  available at the exit of the reactor. It is also seen from the figure that the depletion of  $O_2$  for the base case begins at axial distance of 8 cm and takes place in a region close to the burner. Whereas, increasing the secondary inlet velocity to 17.5 m/s results in a depletion of  $O_2$ , which slightly shifts in a direction away from the burner. As it can be seen from Figure 4.42, which shows the flow stream lines, the secondary air effects on the mixing process. For the base case, it is shown that there is a vortex structure due to the secondary air in the region close to the burner inlet which enhances the mixing process and leads to the rapid depletion of  $O_2$ . Increasing the secondary inlet velocity to 17.5 m/s results in a vortex structure in the region between  $x = 20$  cm and  $x = 30$  cm. Figure 4.41 shows that the rapid depletion of  $O_2$  for the case of 17.5 m/s begins in the region where this structure vortex is formed. The same behaviour is seen for the other two cases of 11.5 m/s and 13.5 m/s. It is seen that the  $O_2$  is consumed rapidly where the vortex structures are created (see Figure 4.42) because of the reason that these vortex structures enhanced the mixing process.

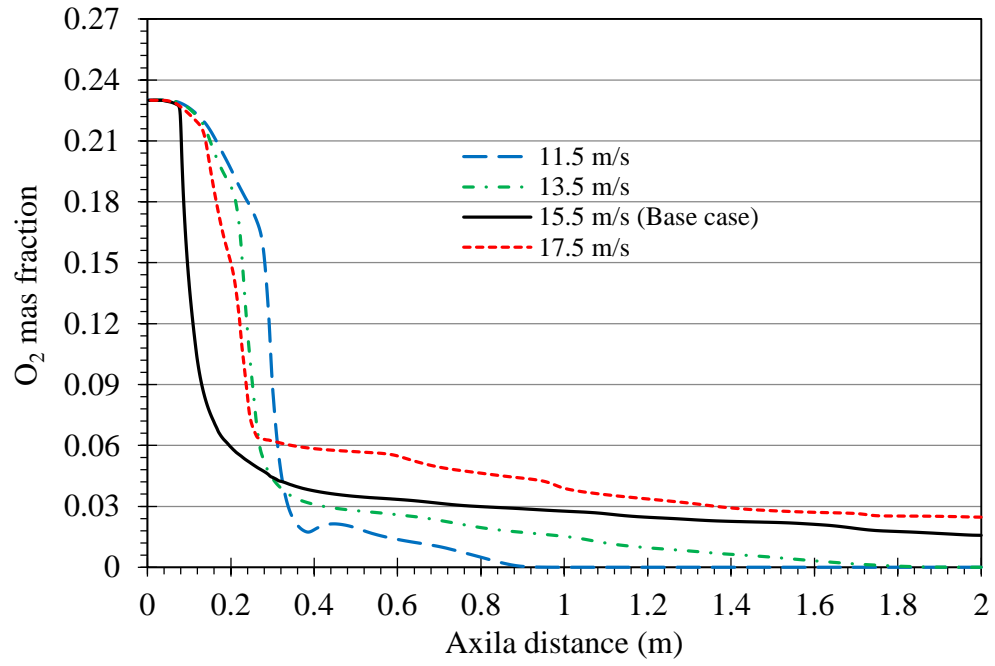


Figure 4.41: The variation of  $O_2$  concentration along the centreline at different secondary air inlet velocities.

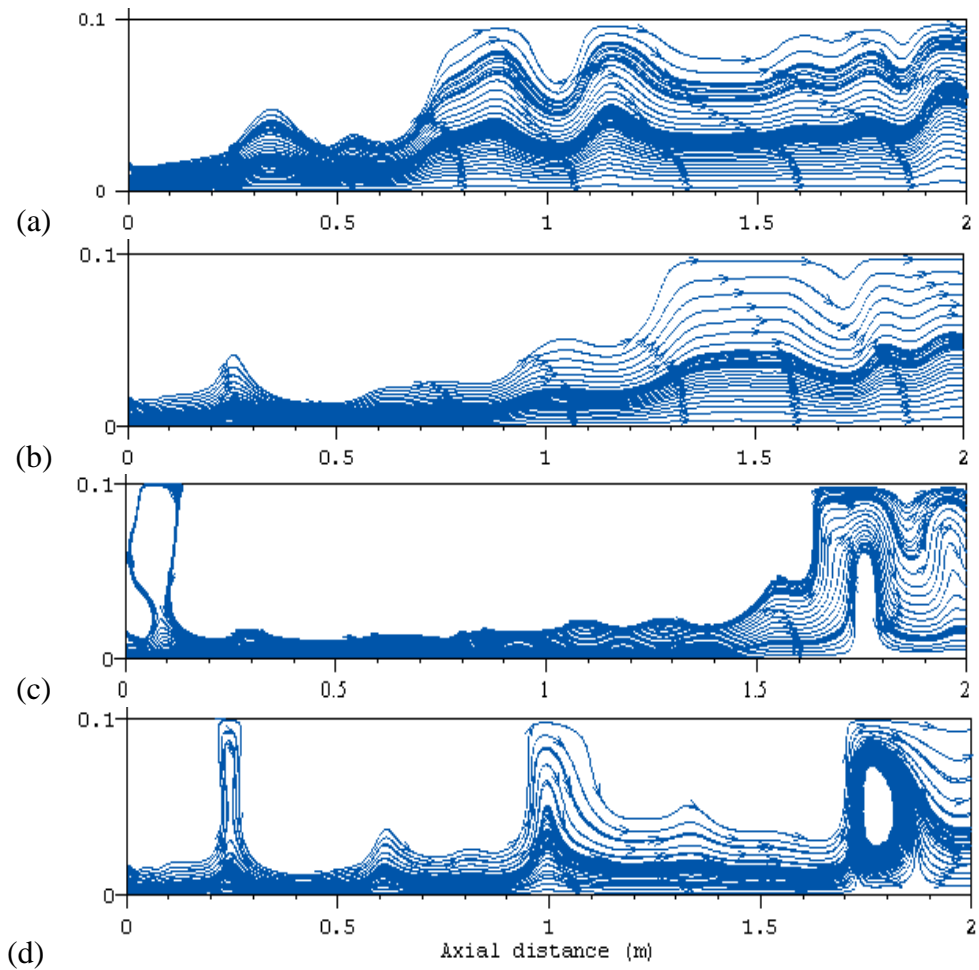


Figure 4.42: Stream lines: (a) 11.5 m/s, (b) 13.5 m/s, (c) 15.5 m/s and (d) 17.5 m/s.

Figure 4.43 and Figure 4.44 show the variation of  $\text{CO}_2$  and  $\text{H}_2\text{O}$  along the axial direction of the reactor. From Figure 4.43, it is shown that the concentration of  $\text{CO}_2$  for the cases with velocities of 11.5 m/s and 13.5 m/s increased when compared with the base case. For the former one, it is also shown that the concentration of  $\text{CO}_2$  reached its peak by axial distance of 0.88 m then it began to decrease along the axial towards the exit of the reactor because of the heterogeneous reaction (R4).  $\text{CO}_2$  mass fraction for the case with the velocity of 13.5 m/s reached its peak value in the region close to the exit of the reactor at the axial location ( $x \approx 1.88$  m). Compared with the base case, the case with the velocity of 17.5 m/s shows low concentration of  $\text{CO}_2$ . It can also be noticed that the heterogeneous reaction (R4) is not activated in this case due to the availability of  $\text{O}_2$ .

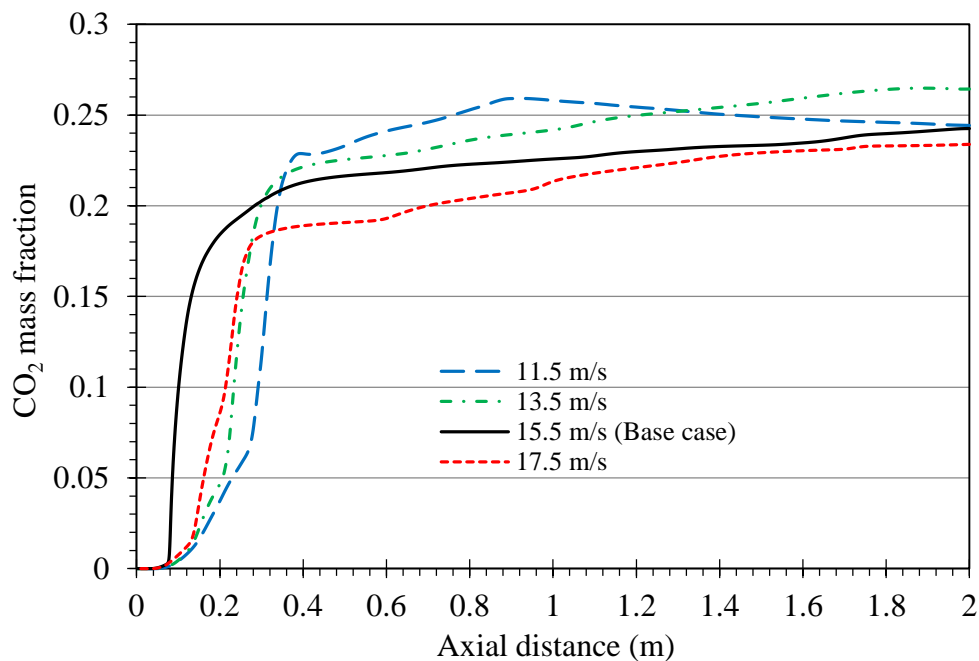


Figure 4.43: The variation of  $\text{CO}_2$  mass fraction along the centreline at different secondary air inlet velocities.

The concentration of  $\text{H}_2\text{O}$  along the axial direction of the reactor is shown in Figure 4.44. For the cases with velocities lower than that of the base case, it is shown that the concentration of  $\text{H}_2\text{O}$  is higher than the latter one the region between ( $x = 32$  cm) and ( $x = 88$  cm). The variation of the mass fraction of  $\text{CO}_2$  for case with secondary inlet velocity of 11.5 m/s reached the maximum value, which is 0.0365, then started to decrease along the axial distance towards the exit of the reactor. Such a decrease in  $\text{H}_2\text{O}$  mass fraction is attributed to the heterogeneous reaction (R5) which became a dominant in the combustion process besides the heterogeneous reaction (R4). Figure 4.44 also shows that the case with secondary velocity of 17.5 m/s produced lower

concentration of  $\text{H}_2\text{O}$  than that of the base case. It is also seen that the concentration of  $\text{H}_2\text{O}$  began to decrease along the centreline of the reactor towards its exit.

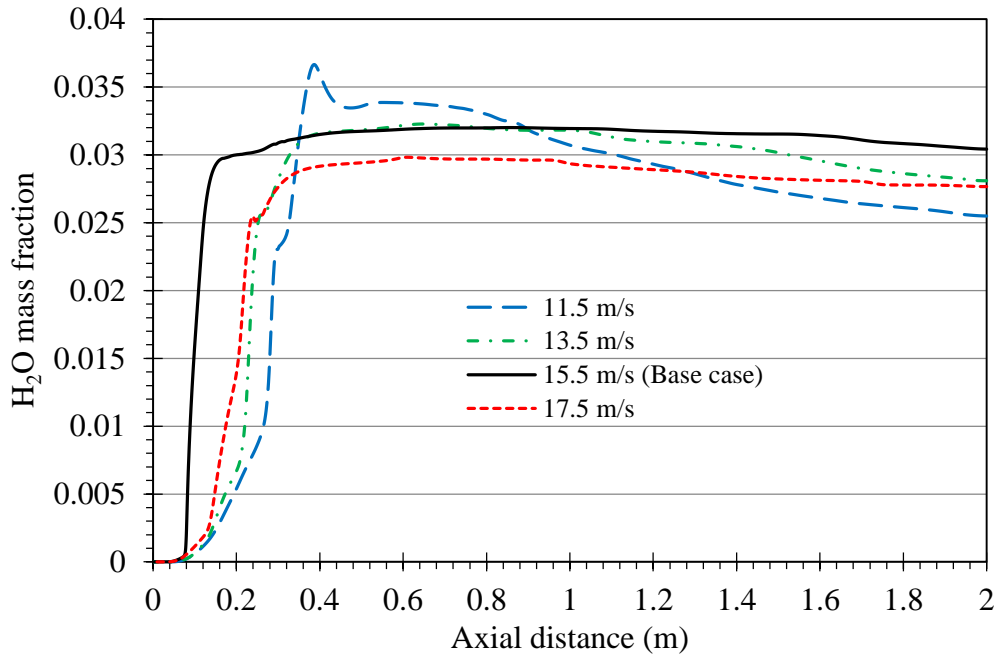


Figure 4.44: The variation of  $\text{H}_2\text{O}$  mass fraction along the centreline at different secondary air inlet velocities.

The mass fraction of  $\text{CO}$  and  $\text{H}_2$  is plotted in Figure 4.45 and Figure 4.46, respectively. The behaviour of the variation of  $\text{CO}$  and  $\text{H}_2$  concentration along the axial distance is similar to that discussed in § 4.8.3 except for that the mass fraction of  $\text{CO}$  for the case with the secondary inlet velocity of 11.5 m/s, which shows a monotonic increase along the axial distance immediately at the axial location ( $x = 64$  cm) where the concentration of  $\text{O}_2$  falls to zero. This monotonic increase in  $\text{CO}$  concentration is due to the gasification reaction (R4) and is consistent with the decrease in  $\text{CO}_2$  as shown in Figure 4.43. The mass fraction of  $\text{CO}$  for the case of 13.5 m/s also shows a small increase at the exit of the reactor. The increase of  $\text{H}_2$  mass fraction for all cases is due to the heterogeneous reaction (R5) and also consistent with the decrease of the mass fraction  $\text{H}_2\text{O}$ . It can be seen that the variation of  $\text{H}_2$  mass fraction along the axial direction for the case of 17.5 becomes higher than that for the base case (15.5 m/s) from the axial location of ( $x \approx 1$  m) till the exit of the furnace. This can be attributed to the structure vortex (see Figure 4.42 (d)) that enhances the mixing process in this region.

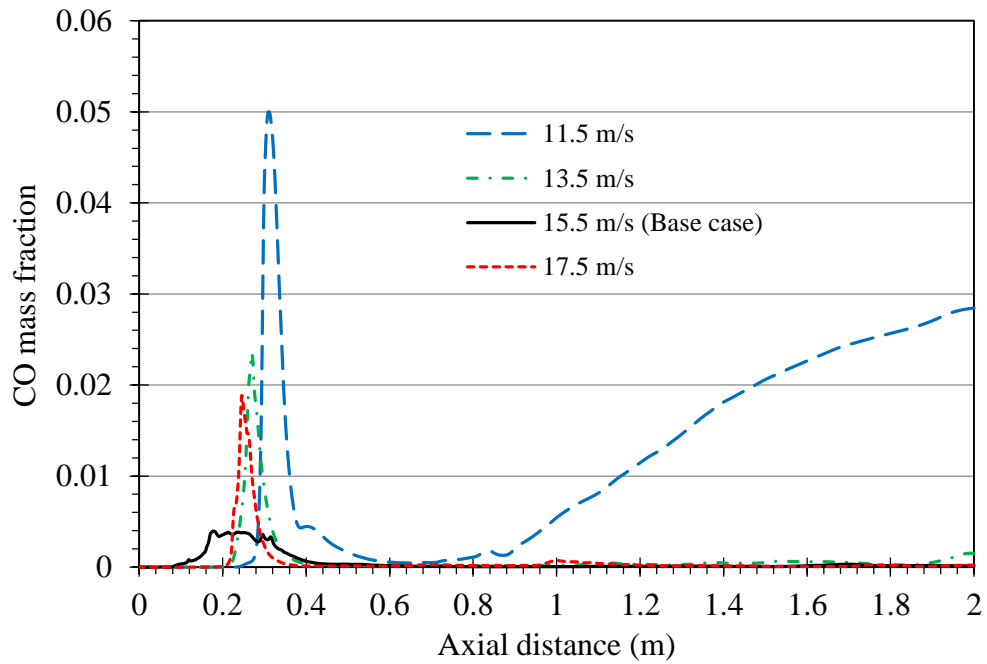


Figure 4.45: The variation of CO mass fraction along the centreline at different secondary air inlet velocities.

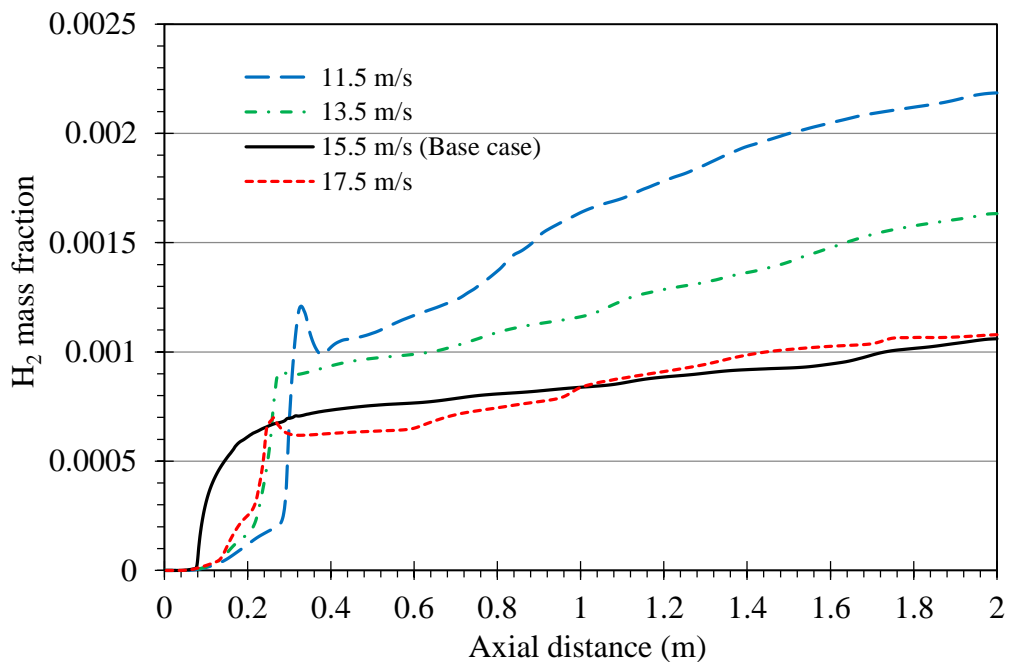


Figure 4.46: The variation of H<sub>2</sub> mass fraction along the centreline at different secondary air inlet velocities.

Figure 4.47 shows a comparison between the base case (15.5 m/s) and the case with the velocity of 11.5 m/s in terms of the change of the coal particle mass along the axial distance of the reactor. From this figure the coal combustion process for the two cases can be seen. In general, the figure gives an indication that the mass loss improved by decreasing the inlet velocity of the secondary air. It is indicated that by decreasing the

inlet velocity of the secondary air the particles stays longer inside the reactor. When decreasing the inlet velocity of the secondary air the slopes of the curves of mass change become steeper which indicate that more char conversion takes place inside the reactor. Therefore, their mass loss is improved. It is shown that all the particles end their release of volatile matter in the case with the velocity of 11.5 m/s by an axial distance that is shorter than that they do in the base case except for the particle with size of 16  $\mu\text{m}$ . In comparison with the base case, it can be seen that the heating up stage in the case of 11.5 m/s, which is represented by the flat part of the curve, for the particles 16  $\mu\text{m}$ , 84  $\mu\text{m}$  and 154  $\mu\text{m}$  increased. This means that the heating period increased. For the particle with the size of 16  $\mu\text{m}$ , it can be seen that the whole mass loss stages takes place in the upstream region of the reactor, but it ends by the axial distance of  $\sim 0.4$  m for the case with 11.5 m/s, which is shorter than that of the base case ( $\sim 0.75$  m). As indicated in the figure, the mass of the particles of sizes 84, 154, 222 and 291  $\mu\text{m}$  decreased at the exit of the reactor in the case of 11.5 m/s when is compared with base case. The particle with the size of 154  $\mu\text{m}$  shows the highest percentage of decrease of  $\sim 31$  %. This decrease in mass ratio ( $m_p/m_{p,0}$ ) at the exit of the reactor for the case with the velocity of 11.5 m/s when compared with the base case is due to the commence of reduction reactions which can be identified the rapid decrease in gas temperature (Figure 4.39) due to the heat taken for such endothermic reactions. Figure 4.47 (f) shows the ratio of mass loss of the particle with size of 360  $\mu\text{m}$ . It indicates that the conversion of the char does not occur for both cases. It can be noticed that period of heating is the same for the two case which is the same for the particles with sizes of 222 and 291  $\mu\text{m}$  as shown in Figure 4.47 (d) and (e).

The variation of pollutant NO along the centreline of the reactor is depicted in Figure 4.48. As it is evident from the figure, all the cases show higher concentration of NO along the axial direction when compared with the base case, but the trend is similar. It seen that the case with the velocity of 11.5 m/s shows the highest concentration, which is mainly due to the conversion of fuel-N. As mentioned in § 4.7.3 that Yang et al. [233] showed that volatile matter of bituminous coals is the most important  $\text{NO}_x$ -forming property and when referring to Figure 4.40, it can be seen that more volatiles are released during the devolatilization process which as a result contributed to the higher increase of NO. The same is for the case with the velocity of 13.5 m/s. It is also shown that the slopes of the curves for the cases with the inlet secondary air velocities of 11.5 and 13.5 m/s are steeper when compared with other two cases. For the former, this

becomes more obvious along the axial distance beyond the axial location ( $x = 0.8$  m). This is because  $O_2$  in this region is consumed (refer to Figure 4.41) and therefore, the concentration of the NO-intermediate products, which are HCN and  $NH_3$  increase because the reactions (R14) and (R15) become ineffective i.e. they are impeded. In turn, the rates of the reactions (R16) and (R17) become higher due to the increase of HCN and  $NH_3$  concentrations resulting in lower concentrations of NO. On contrary, the increase of NO concentration for the case with the velocity of 17.5 m/s, firstly, can be attributed to the reason that more  $O_2$  is available and therefore the reactions (R14) and (R15) become more active and, secondly, may result from the conversion of thermal-N, since more nitrogen is supplied in the inlet air.

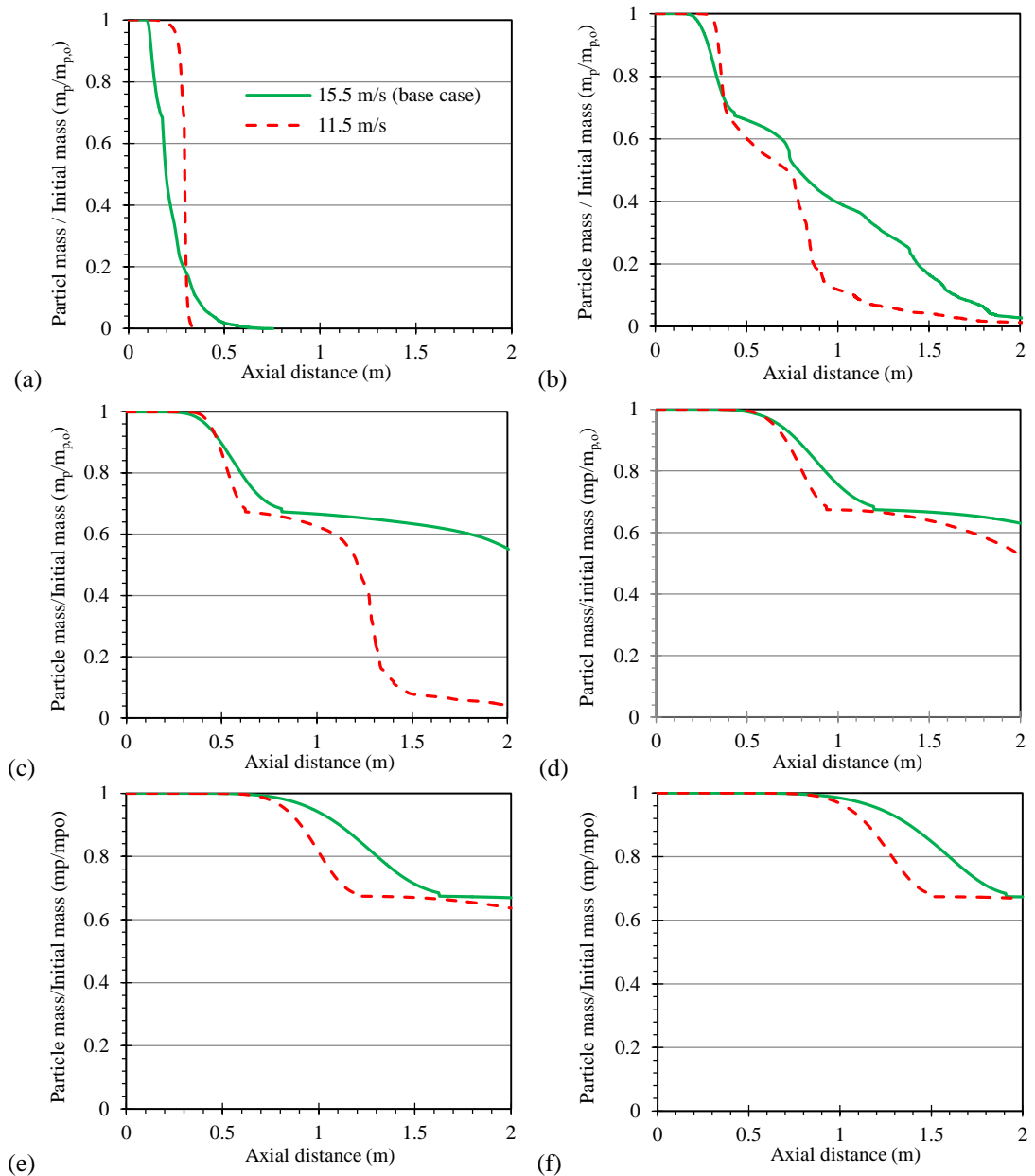


Figure 4.47: Mass depletion of particles: (a) 16  $\mu\text{m}$ , (b) 84  $\mu\text{m}$ , (c) 154  $\mu\text{m}$ , (d) 222  $\mu\text{m}$ , (e) 291  $\mu\text{m}$  and (f) 360  $\mu\text{m}$  at two secondary air inlet velocities.



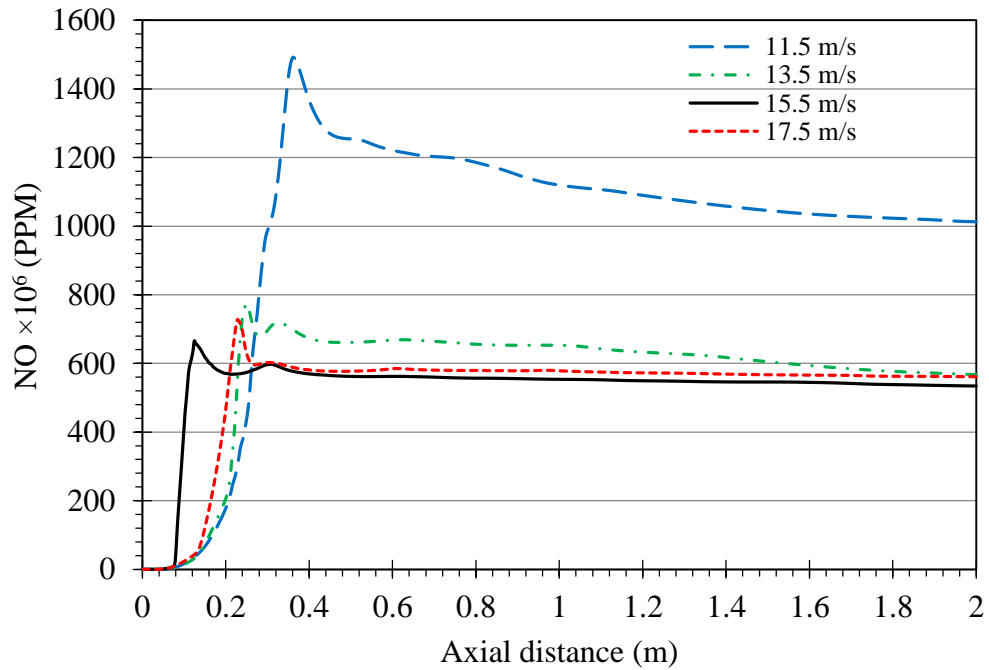


Figure 4.48: NO weight fraction along the centreline at different secondary air inlet velocities.

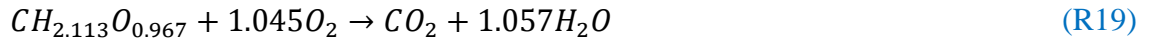
## 4.9 Biomass pulverized combustion

Pulverized coal combustion is a main source to produce energy in power section, but in the recent years there has been a development towards finding alternatives to be fired either alone or with coal for supplying energy. Therefore, biomass is the only alternative that can replace coal and regarded as the most important of renewable energy sources as discussed in chapter (2). In this part of the current work, an attempt has been made to deal with the development of modelling the combustion of biomass, which is represented by the pulverized combustion of straw. Despite the general similarities between the pulverised combustion of coal and that of biomass, there is a difference between their chemical compositions (see § 2.2). The volatile content of straw is significantly higher than that of coal. In addition, the release of volatile matter of straw starts at a lower temperature and more rapidly than coal.

### 4.9.1 Chemistry of straw and chemical reactions

The straw used in this work in terms of the ultimate and proximate analysis has the chemical composition that is shown in Table 4.9. The combustion of volatiles released during devolatilization, which has the molecular formula  $CH_{2.113}O_{0.967}$  (molar mass = 29.585 kg/kmol) based on the ultimate and proximate analysis, is also treated in the similar way of coal volatiles (see § 4.4.2).

The stoichiometric combustion reaction of the straw volatiles is as following:



The enthalpy of formation of straw volatiles was calculated according to equation (4.35) and found to be  $(-2.2983193 \times 10^8 \text{ J/kmol})$ .

Table 4.9: The chemical composition of straw.

Ultimate analysis		Proximate analysis			
		Moisture (wt%, AR <sup>1</sup> )	Volatiles (wt%, D <sup>2</sup> )	Char (wt%, D)	Ash (wt%, D)
C (wt%, D)	47.3	7.7	79.5	15.6	4.91
H (wt%, D)	5.68	HHV (kJ/kg, D)		18.493	
O (wt%, D)	41.6	LHV (kJ/kg, DAF <sup>3</sup> )		17.244	
N (wt%, D)	0.54	Particle density ( $\rho_p$ ), kg/m <sup>3</sup>		600	
S (wt%, D)	< 0.01	Particle size distribution		considered as coal	
		Operational conditions		considered as coal	

The bases: (1) AR = as received, (2) D = Dry, and (3) DAF = dry ash-free, wt% on mass.

For the simulation of gas phase, reactions (R6) and (R19) are considered. In terms of char oxidation, the heterogeneous reaction (R2)-(R5) of case 3 of pulverized coal combustion were considered. Regarding the devolatilization process, since there is little direct experimental information on the behaviour of the reaction rates of biomass in furnace flames where the heating-up rate is important, the present simulation is limited to selected works that use a single kinetic rate model according to reaction (R1) and Equation (4.22). The kinetic parameters,  $A$  and  $E$  used in Equation (4.22) are taken from [158] and the work of Zhou et al. [188] and shown in Table 4.10.

Table 4.10: Constants of single rate devolatilization model.

Reference	$A$ [s <sup>-1</sup> ]	$E$ [J/kmol]
Fluent [158]	$3.12 \times 10^5$	$7.4 \times 10^7$
Zhou et al. [188]	$1.56 \times 10^{10}$	$1.38 \times 10^8$

## 4.9.2 Numerical solution

Some assumptions have been made in the current simulations which involve that the biomass particles are assumed to be spherical and dry and they are thermally thin. The conversion of straw particles is solved by the default DPM laws as has been done for coal combustion presented earlier. The FR/ED model is used to model the turbulence-chemistry interaction in gas phase. For modelling radiation heat transfer, the P-1 radiation model is used. In terms of turbulence modelling, standard  $k$ - $\epsilon$  model is used.

## 4.10 Results and discussion of straw combustion

### 4.10.1 Combustion results of pulverized straw

Two cases were performed to model the pulverised coal combustion of straw in the same reactor shown in Figure 4.4. The first one (case I) uses the default kinetics for modelling the devolatilization and the second (case II) uses the kinetics of Zhou et al (see Table 4.10). Concerning the kinetic constants, those shown in Table 4.4 are used. The straw composition is the same used by C. Yin et al. [239]. The operating conditions are the same as those used for modelling the combustion of coal particles, and are provided by Table 4.11. The size of the particles is also considered to be the same as that of coal particles is used in order to compare the characteristics of biomass with that of coal.

Table 4.11: operating conditions of pulverized biomass combustion.

Parameters	Units	Values
Biomass mass flow	kg/hr	1
Wall temperature	K	1523
Volume flow rate of biomass carrying air	m <sup>3</sup> /hr	2.38
Temperature of biomass carrying air	K	473
Volume flow rate of primary air	m <sup>3</sup> /hr	4.68
Temperature of primary air	K	523
Volume flow rate of secondary air	m <sup>3</sup> /hr	11.15
Temperature of secondary air	K	623

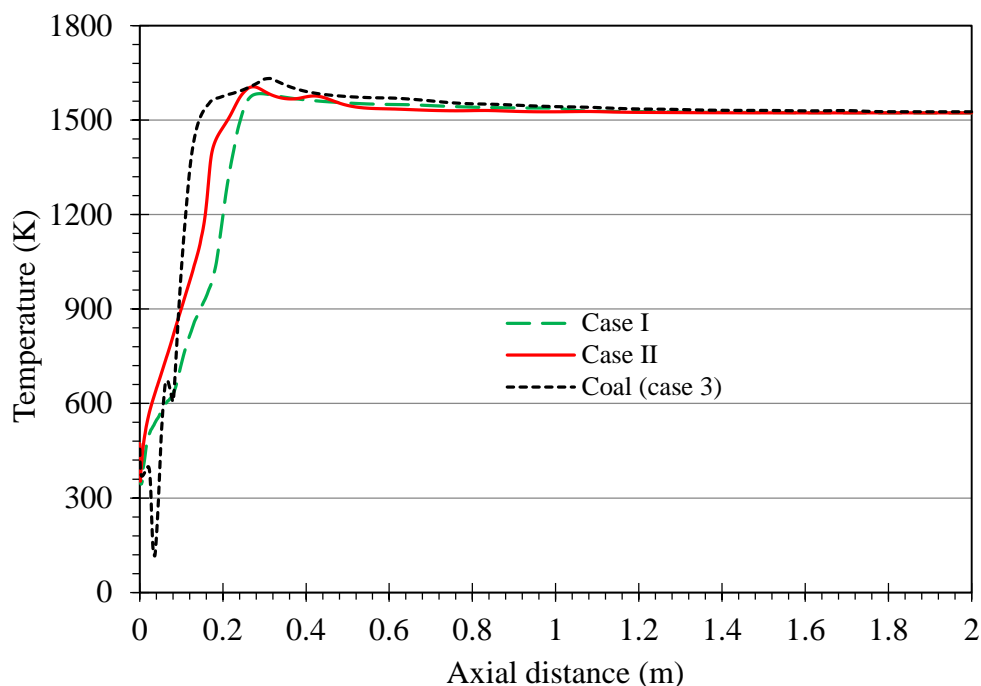


Figure 4.49: The variation of gas temperature along the centreline of the reactor.

The temperature variation in axial direction of the reactor along the centreline is shown in Figure 4.49. It can be seen that the two cases of straw give a temperature variation close to that of coal (case 3 in coal model). Even though, the high heating value of coal is higher than that of straw which should have resulted in more heat release during combustion, it is seen, when using the same operating conditions, that there is not a big difference between the maximum temperatures in all cases. Moreover, the temperature is almost the same when go further down towards the exit of the furnace. This may be attributed to the reason that not all the coal particles lose their mass as can be seen when referring to Figure 4.27 and Figure 4.28. The latter one shows that the particle with size of  $16 \mu\text{m}$  is the only particle that is completely burned out (% 100 burnout). The particles with bigger sizes ( $\geq 222 \mu\text{m}$ ) show a burn out less than 40 %, which means that less energy is released from them.

The distribution of gas temperature of the two cases is shown in Figure 4.50. Apart from the small differences between the two cases in the upstream region close to the burner, they show a similar temperature distribution.

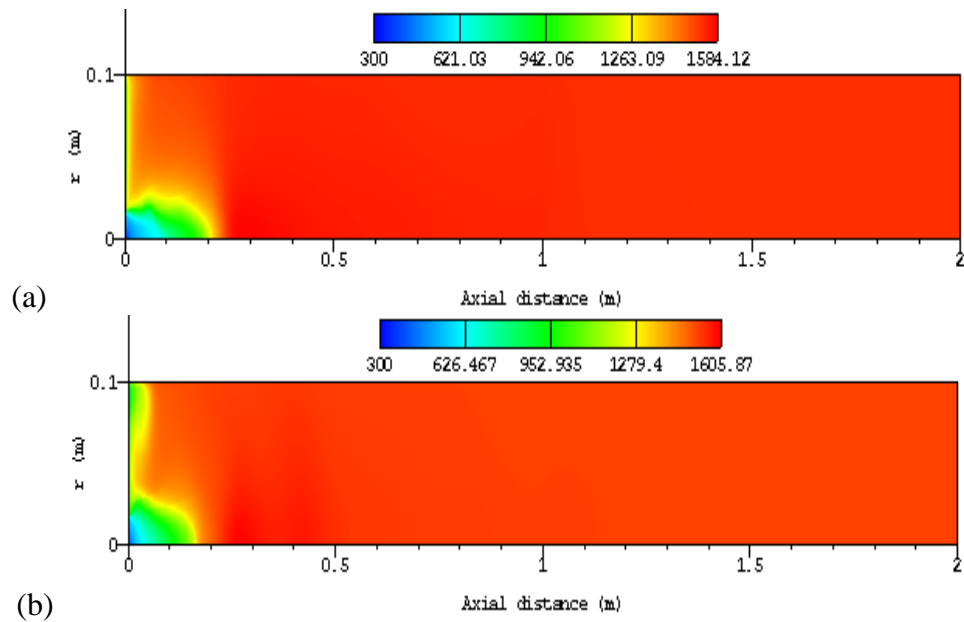


Figure 4.50: Gas temperature distribution of (a) case I and (b) case II.

Temperature profiles as a function of radial distance at different axial locations are shown in Figure 4.51. From Figure 4.51 (a), it can be seen that radial variation of temperature of both straw cases is close to that of coal case in the outer region far from the centre. On the other hand, only straw case II shows a radial variation close to that of coal case with a maximum difference of  $\sim 100$  K at radial distance ( $r = 0$ ). Straw case I shows a maximum difference of  $\sim 360$  K at ( $r = 0$ ) when compared with coal case.

It can be also seen that the difference in temperature between straw cases and coal case decreases when going downstream towards the exit of the furnace. For the axial location ( $x = 0.6$  m), shown in Figure 4.51 (b), it can be seen that the difference between the maximum temperature of coal case and that of both straw case is  $\sim 20$  K for case I and 34 K for case II at the radial distance ( $r = 0$ ). These differences are 5 K and 16.5 K in the middle of the furnace at axial location ( $x = 1$  m) as shown in Figure 4.51 (c). The radial variation of temperature is shown to be nearly the same (see Figure 4.51 (d)) and became identical at  $x = 1.8$  m with a difference of 4 K when compared with that of coal case as shown in Figure 4.51 (e).

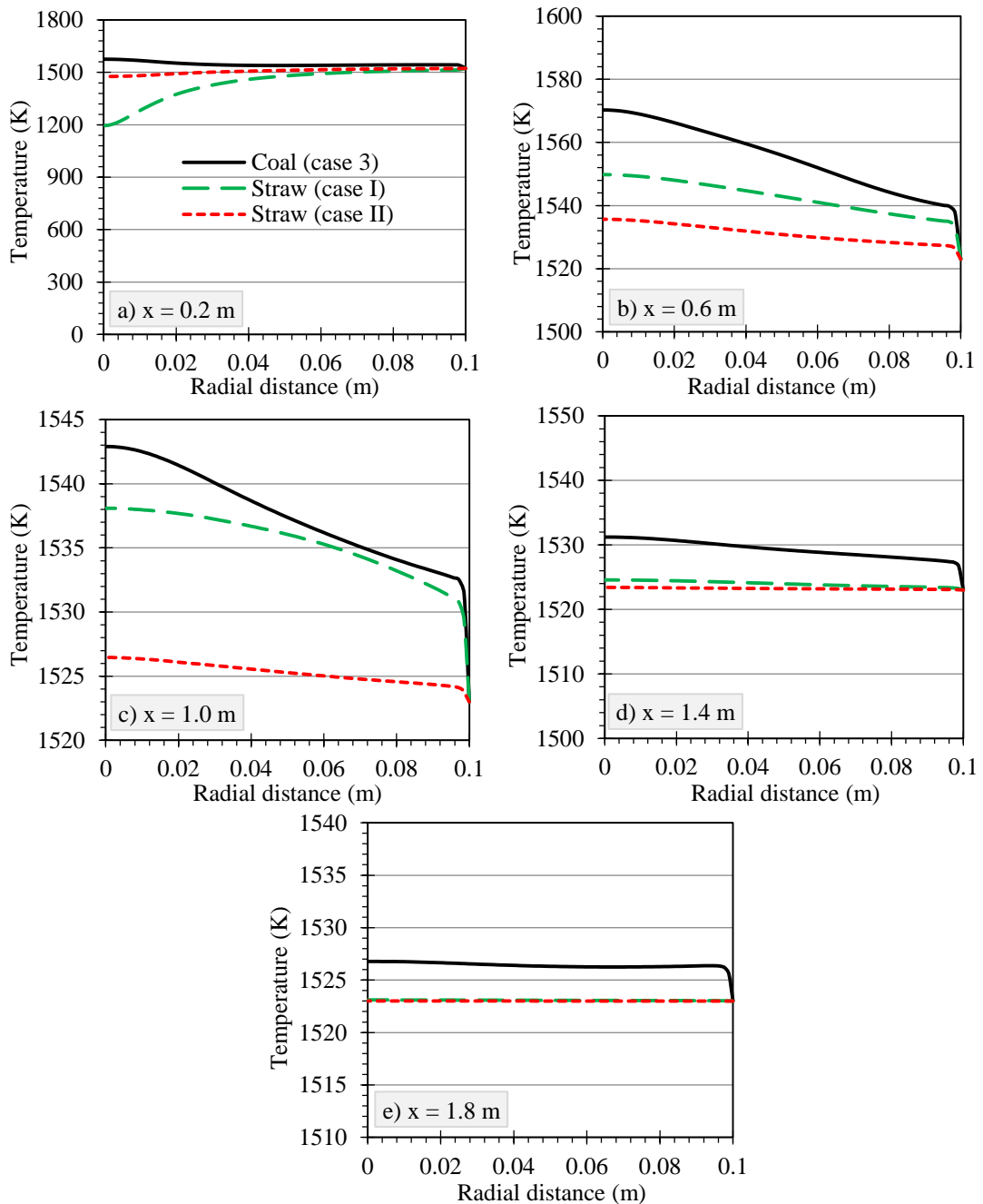


Figure 4.51: Radial temperature profiles at different axial locations.

The variation of volatiles concentration along the centreline of the furnace and the distribution of this concentration are depicted by Figure 4.52 and Figure 4.53, respectively. It is seen that the two cases show a similar trend. It is noted also that the release of volatiles in case II takes place faster than that in case I, but it reaches a maximum value of 0.016 that is less than that of the latter which is 0.0184 as can be seen from Figure 4.52. As it is evident from this figure and Figure 4.49, it can be seen that the release of volatiles and combustion occur in parallel and this is because of the overlap of the zones of the volatiles release and maximum temperature.

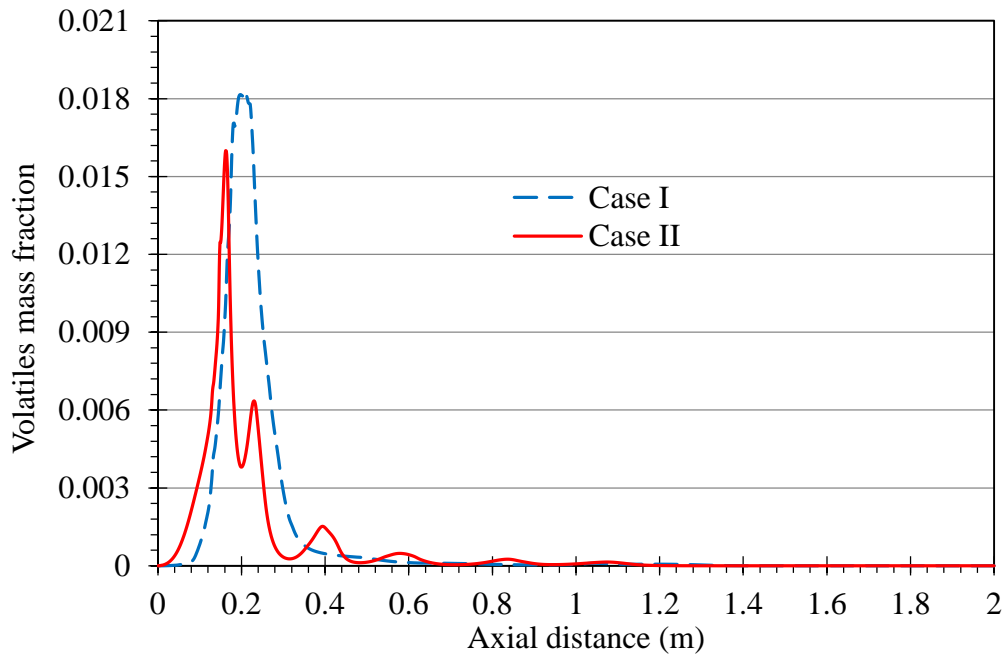


Figure 4.52: The variation of volatiles mass fraction along the centreline of the furnace.

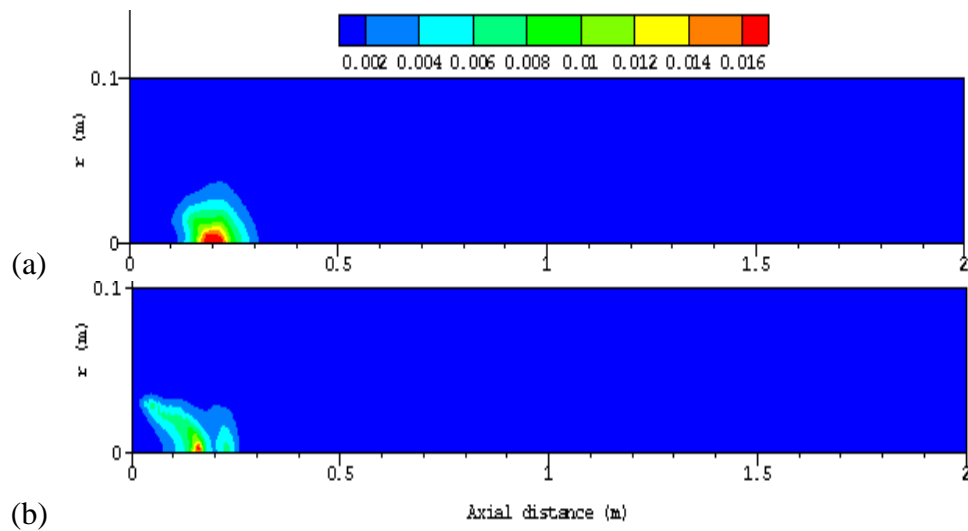


Figure 4.53: Volatiles mass fraction distribution: (a) case I and (b) case II.

Mass fractions along the centreline of the reactor are shown in Figure 4.54. It can be seen that the behaviour of the combustion is similar to that of coal discussed earlier. Compared to coal when referring to Figure 4.11 (case 3), it is seen that the mass fraction of oxygen is higher than that of coal at the exit of the reactor. Therefore, the occurrence of heterogeneous reactions (R4) and (R5) has a little influence on the combustion process as it is evidence from Figure 4.54. As it is seen from the figure, only very small fraction of CO and H<sub>2</sub> appear. For the former one, it can be attributed to that CO produced is immediately consumed according to the reaction (R6).

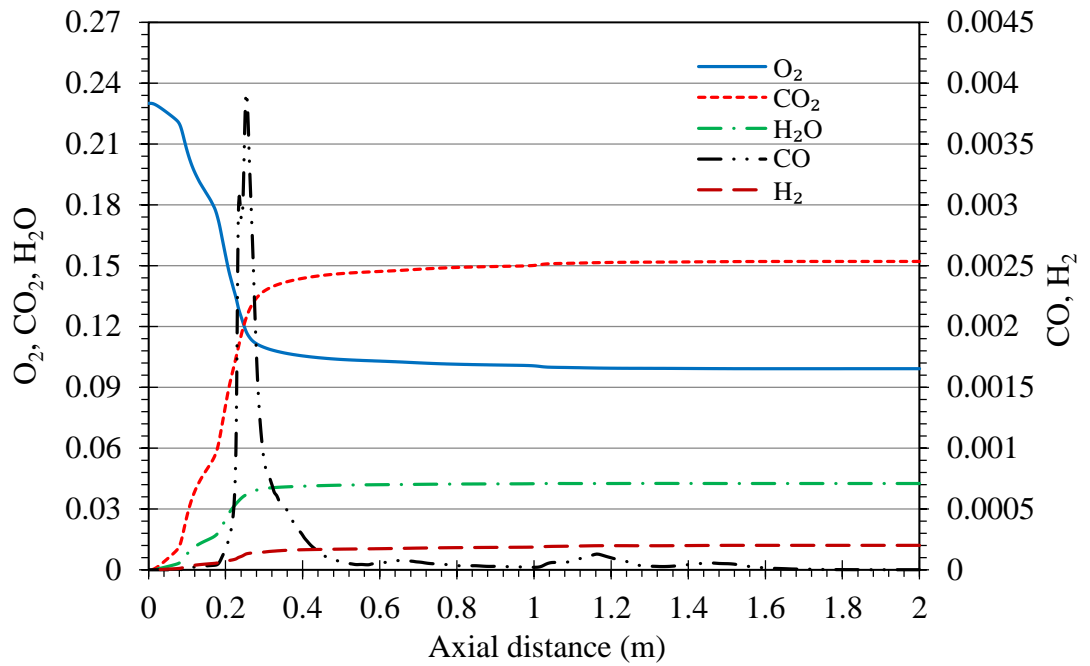


Figure 4.54: The variation of species mass fraction along the centreline of the reactor.

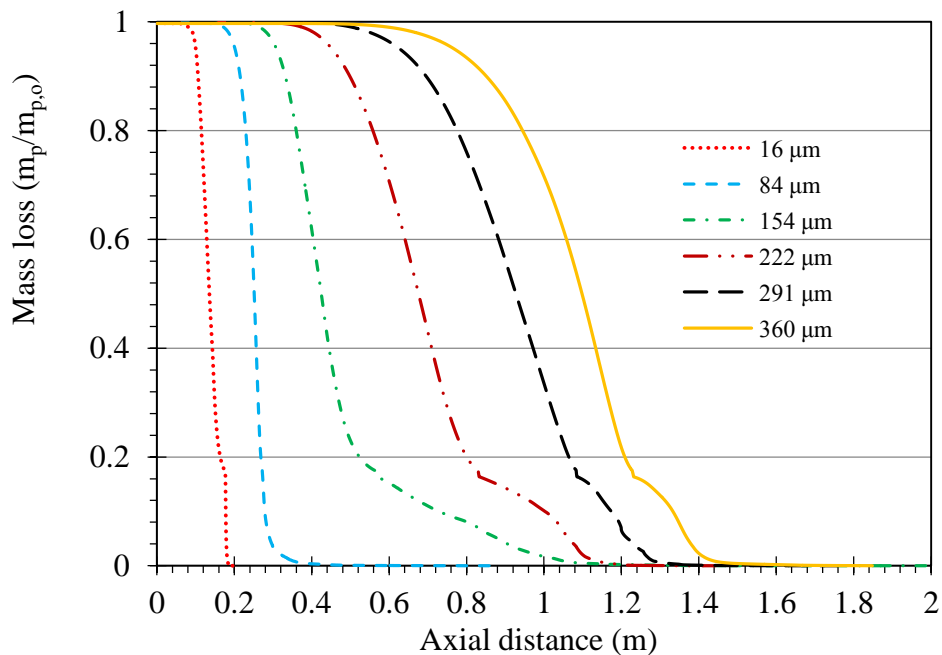


Figure 4.55: Mass depletion of particles with different sizes for case I.

The mass loss of straw particles and their burnout are illustrated by Figure 4.55 and Figure 4.56. On contrary to coal particles, it can be seen from the figures that the mass of all straw particles are depleted during their journey inside the reactor and before they reach the exit.



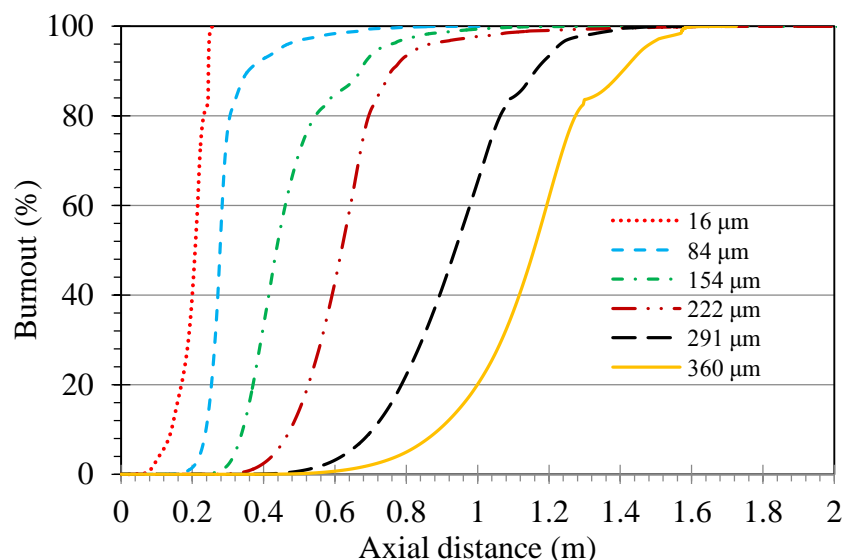


Figure 4.56: Burnout of straw particles with different sizes.

#### 4.10.2 NO<sub>x</sub> formation from straw burning

With regard to the formation of NO when burning biomass fuels, as mentioned earlier, it is of importance for NO<sub>x</sub> formation is the split of nitrogen in the solid fuel into volatiles and char. The fraction in the former one increases with increasing the oxygen content in the fuels with decreasing rank [240] and biomass can be included in such fuels. Moreover, compared with most coals, biomass such as straw and wood appears to release the nitrogen more readily as the temperature increases.

It is also of importance for NO<sub>x</sub> formation is the partitioning of volatile-N to intermediate species, which depends on the fuel type, devolatilization temperature and heating rate. For bituminous coals, the main species observed during the devolatilization at high heating rates is HCN [236] and this was the base for NO<sub>x</sub> modelling for coal, which has been discussed earlier. On the other hand, low rank coals and biomass tend to yield a significant amounts of NH<sub>3</sub> [241]. For biomass, it is believed that fuel-N can exist in amine form and therefore, NH<sub>3</sub> becomes the principle product of its conversion.

Based on the study by Liu and Gibbs [242] on woody-biomass as mentioned in FLUENT documents, due to the younger age of the fuel it has been suggested that the ratio of HCN to NH<sub>3</sub> is 1:9 which has been used in the current investigations of straw combustion. In the current study, the split of fuel-N is also assumed to be 70% for volatile-N and 30% for char-N based on the recent study [243]. Furthermore, the latter one decreases at high temperatures as shown in Figure 4.57, which shows the ratio of

the nitrogen content in the char and in the parent fuel as a function of pyrolysis temperature (on a DAF basis), and this makes this assumption acceptable. Based on the same study, is assumed to be converted to  $\text{NH}_3$  intermediate, which becomes  $\text{NO}$  after further reactions as pointed out earlier.

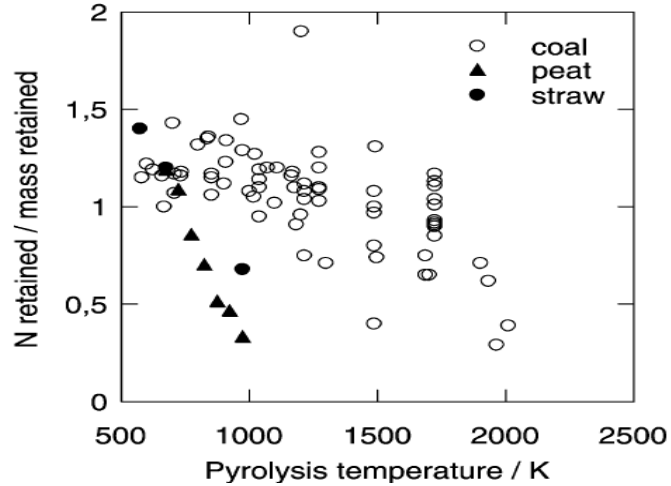


Figure 4.57: Nitrogen concentration in char versus pyrolysis temperature for selected fuels and various experimental methods [217].

The nitric oxide ( $\text{NO}$ ) profile as a function of the axial distance for the case of straw is shown in Figure 4.58. It can be seen that it qualitatively follows the same trend of that of coal. The values are higher for the case of coal than that of straw. The  $\text{NO}$  value was reduced by approximately 20% for case I and 26% for case II at the exit of the furnace. The results give an indication that switching to alternative fuels that would replace fossil fuels can be achieved and as a result produce low  $\text{NO}_x$  emissions.

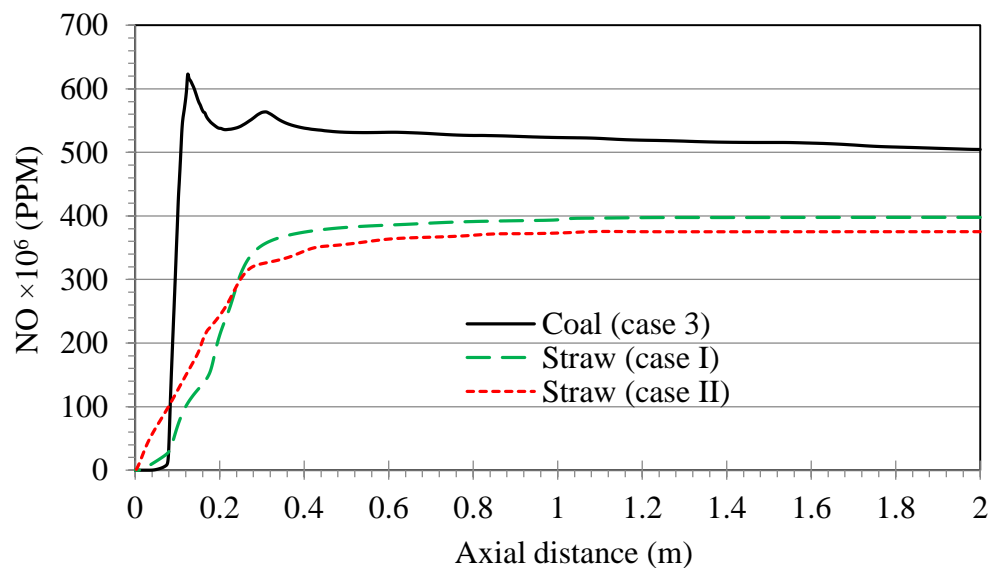


Figure 4.58: The variation of  $\text{NO}$  concentration of straw along the centreline of the furnace.

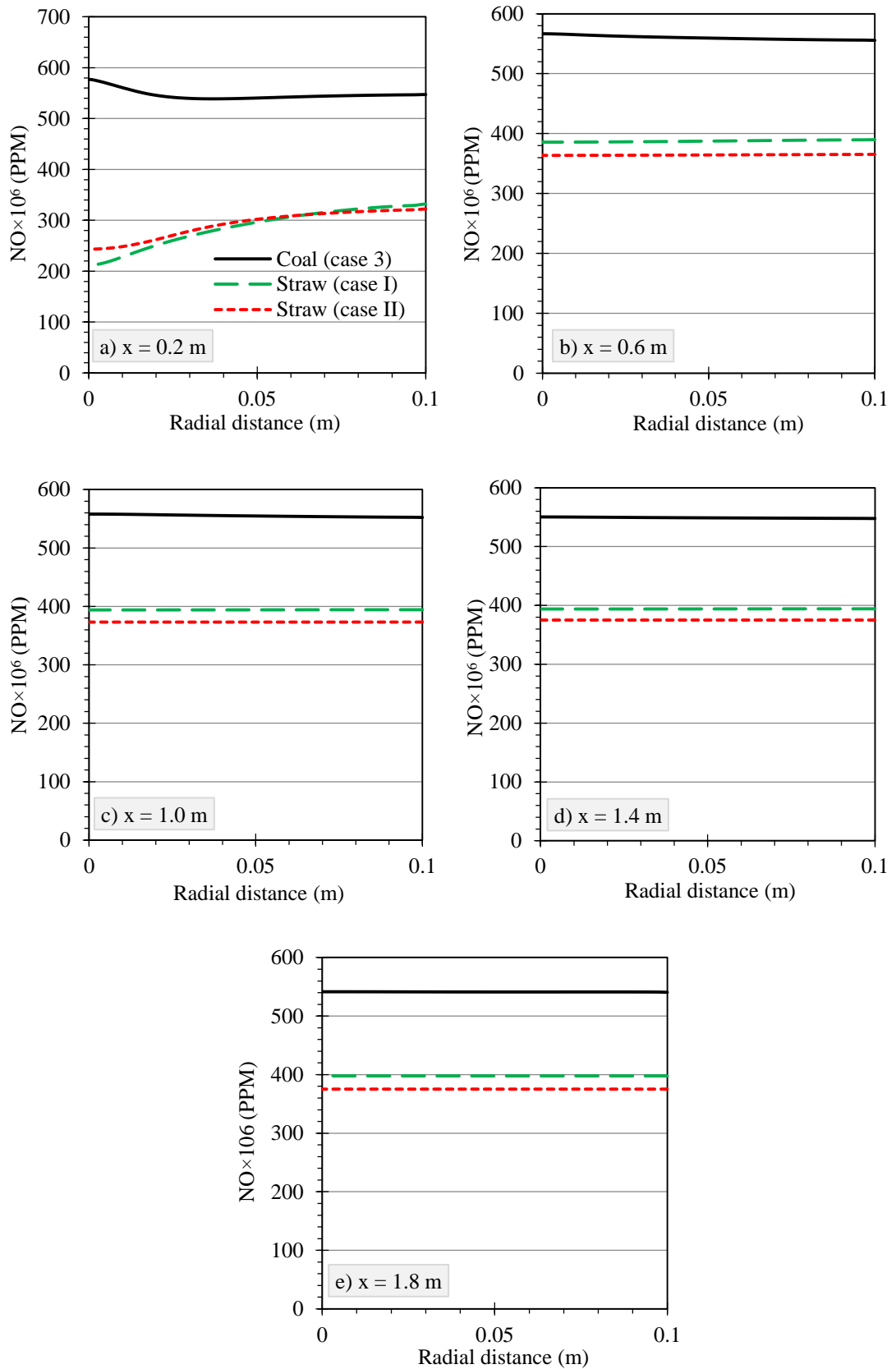


Figure 4.59: The radial profiles of NO mass fraction at various axial locations.

The radial profiles of NO are depicted by Figure 4.59. The figure shows that the two straw cases clearly exhibit lower NO concentration at all axial locations. At the axial location ( $x = 0.2$  m) as shown in Figure 4.59 (a), the variation of NO for straw case I and case II increases in the radial direction towards the outer region of the furnace away from the its centreline with lower values of the former one than those of the latter till the radial distance of  $\sim 0.05$  m, where they become nearly the same. The radial profile of NO follow the same trend as temperature profile (see Figure 4.51 (a)). The variation of NO at other axial locations is constant for all cases as can be seen in Figure 4.59 (b, c, d and e).

### 4.10.3 Co-firing of coal and biomass particles

Co-firing of coal and biomass in pulverized combustion offers the opportunities for biomass utilization. It is the fastest alternative that can use biomass for electric power generation and therefore saving the capital costs by using the existing pulverized coal combustion systems. Moreover, it reduces the levels of the undesirable emissions that affect the environment. In this study, the coal and straw particle are burned inside the furnace. The particle size distribution is assumed to be the same for coal and biomass particles. Several simulations were performed. The co-fired biomass fractions used on mass basis are 10, 20, 30 and 40%.

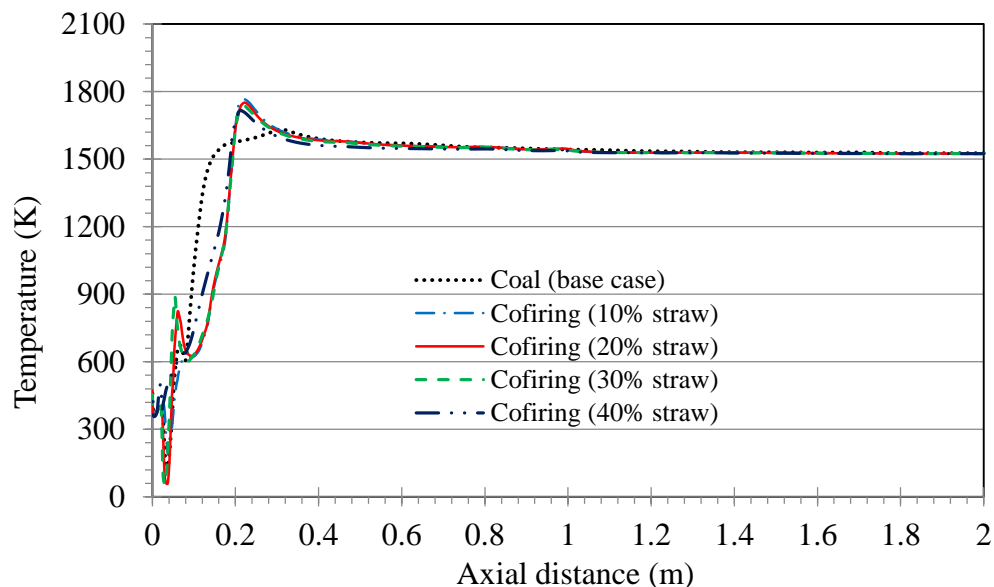


Figure 4.60: The variation of gas temperature along the centreline of the furnace for different co-firing cases.

The axial profile of the gas temperature along the centreline of the furnace is shown in Figure 4.60. As it is evident from the figure the temperature increases in the

combustion region. It reaches its maximum value which is about 1767 K for 10%, 1751 K for 20%, 1743K for 30% and 1718 K for 40% of co-firing straw. The temperature increased by 8, 6.7, 6.3 and 5%, respectively, when compared with coal (the base case). However, it can be seen that increasing the fraction of straw leads to decreasing the gas temperature.

The temperature distribution of the co-firing cases is shown in Figure 4.61. It can be seen that apart from the differences in the upstream region all the cases have the same temperature distribution in the rest of the furnace.

Figure 4.62 shows the mass weighted-average mass fraction of CO<sub>2</sub> at the exit of the furnace. It is shown that the concentration of CO<sub>2</sub> decreases with increasing the fraction of straw that is fired with coal.

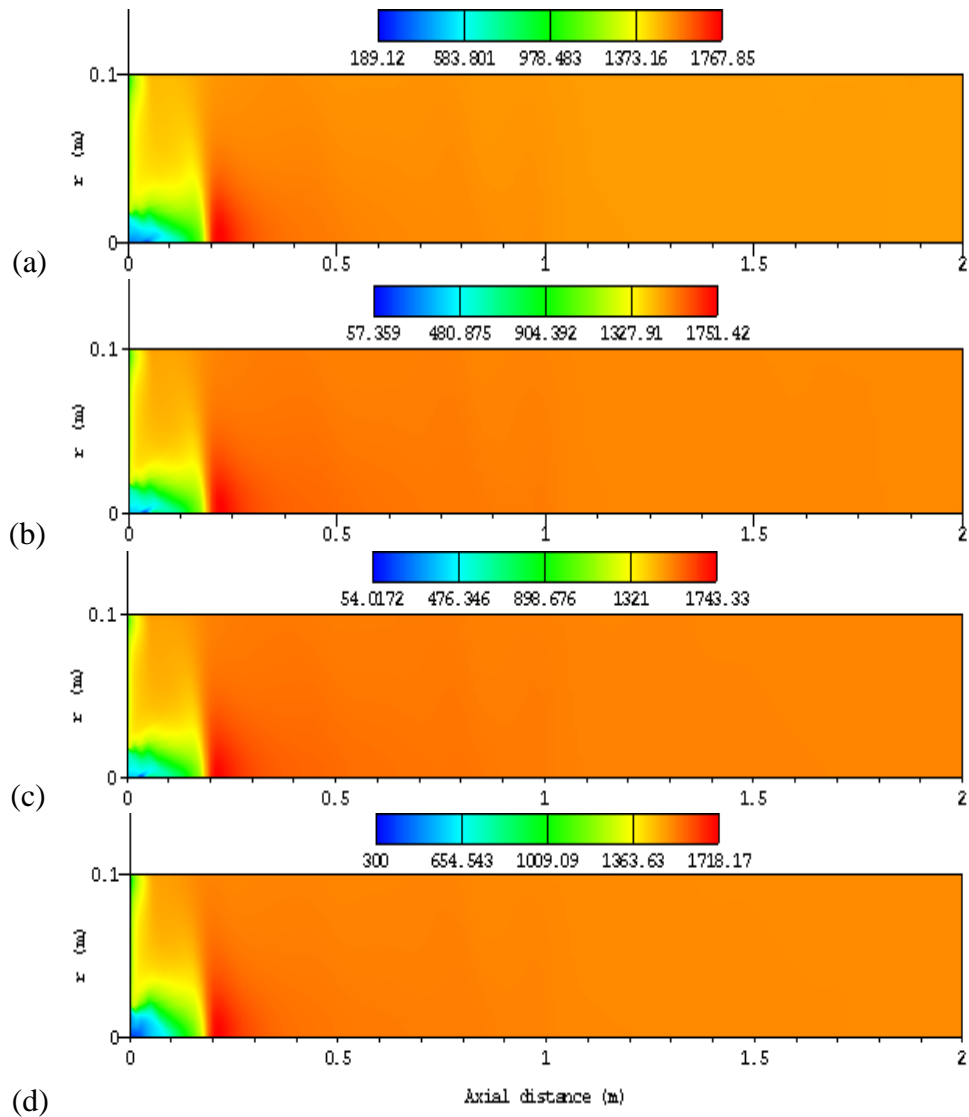


Figure 4.61: Distribution of gas temperature: 10% straw (a), 20% straw (b), 30% straw (c) and 40% straw.

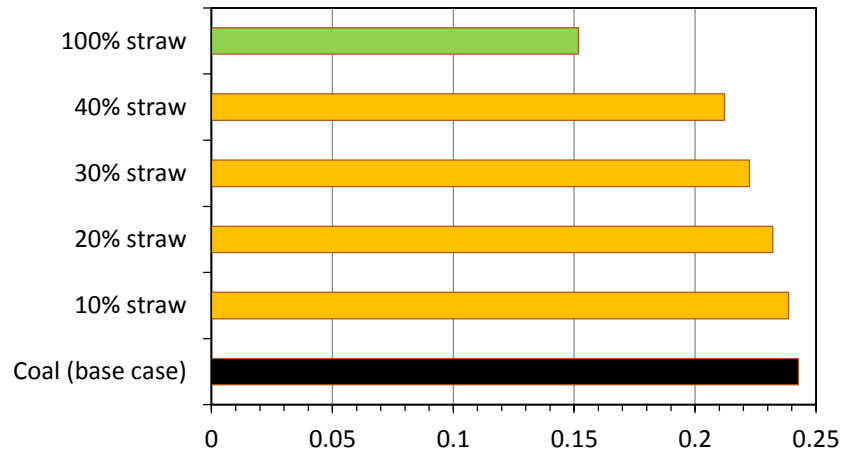


Figure 4.62: Mass weighted-average mass fraction of CO<sub>2</sub> at the exit of the furnace.

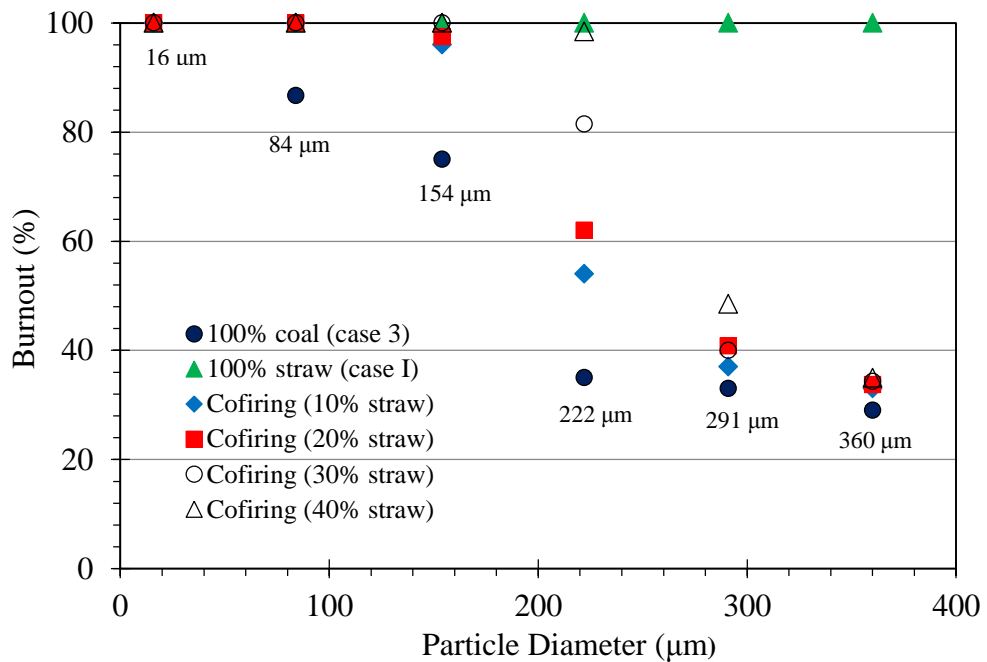


Figure 4.63: Particles burnout at the exit of the reactor.

Figure 4.63 shows the burnout of coal particles at the exit of the furnace for different cases. Regarding straw particles, the only particles burnout of case I is included in this figure for making a comparison. It can be seen that all straw particles are completely consumed as mentioned earlier. Concerning the case of coal (100% coal), the coal particle with the size of 16 μm is also completely burned inside the furnace before reaching the exit. Regarding the other particles, it can be seen that coal burnout remarkably decreases when the particle size increases. This can be the reason behind that the temperature of burning straw particles gives approximately a gas temperature distribution close to that of coal burning, since if the bigger coal particles had burned completely, they would have produced extremely higher temperature than the straw

particles do. When straw particles are burned with coal particles (co-firing cases), it is seen that the burnout of the coal particles is enhanced. It can be clearly seen that the burnout of the particles with sizes 84, 154 and 222  $\mu\text{m}$  is remarkably increased. On the other hand, the burnout of the other two particles does not show a great change except for the case of 40% straw, which show a reasonable increase in burnout in terms of the coal particle with the size of 291  $\mu\text{m}$ . The variation of coal particles burnout and mass loss for the co-firing cases is shown in Figure C. 1 in appendix (C).

## 4.11 Conclusion

To understand the combustion processes of burning solid fuels a numerical model for predicting the pulverized combustion of coal was formulated. It encompasses the stages, which are the devolatilization, the volatiles combustion and char oxidation and char gasification. The drying stage was excluded from the simulations as the coal particles were considered to be dry. In the devolatilization process, the volatiles are released and the heat is consumed, which causes the gas temperature to decrease. Both the combustion of volatiles and char oxidation make the temperature to increase rapidly and this provides the energy needed for char gasification. The influence of operating conditions on the combustion process and species concentrations is predicted using the model. The results show good agreement when compared with the available experimental data. They also show that the combustion inside the furnace was affected by the coal particles size. In comparison with the larger particles, it was shown that the volatiles from the smaller particles released rapidly and the temperature reached its maximum, followed by a decrease due to start of the endothermic reactions. Moreover, increasing the diameter of the coal particles reduces the coal burnout at the exit of the reactor.

Even though they took place, the gasification reactions (R4) and (R5) (the reduction reactions) have a little effect on the gas temperature for the base case which shows only a small decrease along the axial distance of the reactor after reaching its maximum value. On the other hand, when the wall temperature was increased it was shown that these reactions, specifically (R5), have a moderate effect on the variation of gas temperature along the centreline of the reactor. The carbon-steam reaction (R5) is the dominating in the reduction stage. This is clear when the wall temperature increased to 1800 K.

The influence of secondary air inlet rate was investigated and led to the conclusion that the gas temperature increases in the region where the combustion of volatiles and char takes place by decreasing the inlet velocity of the secondary air. Decreasing this velocity also led to enhancing the gasification reactions (R4) and (R5), which can be identified by the increase in the concentrations of CO and H<sub>2</sub> species in the downstream region of the furnace. This enhance of gasification reactions is reflected on the burnout process. It is concluded that the case with secondary inlet velocity of 11.5 m/s shows better burnout of the coal particles than the base case (15.5 m/s) does. The decrease in the inlet velocity of the secondary air also enhanced the burnout of the coal particle by making the particles to stay longer inside the furnace during their journey towards the exit of the furnace.

The model of NO<sub>x</sub> formation successfully predicts the NO<sub>x</sub> emissions in the furnace. Optimised parametric results are found for the chemical kinetics of NO<sub>x</sub> prediction. The NO concentration at the furnace exit was calculated and the results of run 3 gave the best combinations of parameters when compared with the experimental data.

The influence of wall temperature and secondary air inlet velocity on the formation of NO<sub>x</sub> was investigated as well. It was found that NO concentration is affected by both of them. Increasing wall temperature leads to increasing NO concentration. Regarding the effects of the secondary air rate, when compared with the base case (15.5 m/s), it was found that NO concentration increases whether the secondary air inlet velocity is increased or decreased. For the latter case (11.5 and 13.5 m/s), it was found that the slopes of the curves become more steeper in comparison with the base case and therefore, the concentration of NO decreases along the axial direction towards the exit of the furnace.

To compare the combustion of pulverised coal with other solid fuels, the model has been used to predict the combustion of pulverised biomass, which is represented by the combustion of pulverised straw. Within the context of combustion, the results obtained by using the same boundary conditions and particle size distribution of coal particles gives an indication that burning alternative fuels that can replace coal is applicable without affecting the performance of the furnace. It was found that the temperature distribution when burning straw particles is nearly the same as that obtained from burning coal. The saw particles with this size distribution are completely burned out inside the furnace when compared with the coal particles with the same size, which show that increasing the size of the particle results in reducing its burnout. It should be



bear in mind that milling the biomass particles to such a particle size distribution is not cost effective as mentioned earlier, therefore, instead of burning the straw particles alone they can be co-fired with coal particles to improve their burnout.

With regard to the formation of NO, when compared to coal combustion it was found that burning saw produces less NO with 20 and 26% for case I and Case II respectively.

It was found that the co-combustion of pulverized particles of coal and straw enhances the burnout of the coal particles and as a result the gas temperature inside the furnace increases. It was found that the fraction of 10% of fuel that was replaced by straw gave the highest temperature.

# 5 Multiphase modelling (Euler-Euler approach)

This chapter has been dedicated to developing a mathematical model based on the Euler-Euler approach. An attempt has been made to model the combustion of carbon particle inside a newly designed combustion chamber. In the combustion cases, which have been presented in the previous chapter, it was found that the Euler-Lagrange approach is better suited than the Euler-Euler approach for such cases (continuous flow of fuel). However, the latter one is more applicable for the following case because the carbon particles are located in a small cap inside the chamber (static combustion); i.e. there is no continuous flow of the fuel. The objective is to apply the Euler-Euler model to evaluate the influence of the particle size and the design of the chamber. Concerning the latter one, the effect of the chamber height on the combustion flame has been investigated.

## 5.1 Mathematical model

### 5.1.1 Conservation of mass and momentum

The descriptions of multiphase flow as interpenetrating continua incorporate the concept of phase volume fractions denoted by  $\alpha_i$ . Volume fractions represent the space occupied by each phase. Conservation equations of mass, momentum, energy and chemical species, are satisfied by each phase. The volume of phase, ( $i$ ), is defined by

$$V_i = \int_V \alpha_i dV \quad (5.1)$$

where

$$\sum_{i=1}^n \alpha_i = 1 \quad (5.2)$$

The effective density of phase ( $i$ ) is:

$$\hat{\rho}_i = \alpha_i \rho_i \quad (5.3)$$

The conservation of mass for a single phase is given by:

$$\frac{\partial \rho}{\partial t} + \nabla \cdot (\rho \vec{v}) = \Sigma(\text{external influences}) \quad (5.4)$$

where,  $\vec{v}$ , is the phase velocity. These external influences such as the rate of production of species in the phase by chemical reactions and the diffusion flux of the species. In the present case of multiphase modelling which includes a gaseous phase and granular solid phase, each phase would be modelled with its own conservation of mass equation.

For the gas phase is:

$$\frac{\partial(\alpha_g \rho_g)}{\partial t} + \nabla \cdot (\alpha_g \rho_g \vec{v}_g) = S_{gs} \quad (5.5)$$

For the solid phase is:

$$\frac{\partial(\alpha_s \rho_s)}{\partial t} + \nabla \cdot (\alpha_s \rho_s \vec{v}_s) = S_{sg} \quad (5.6)$$

where the subscript  $g$  is for the gaseous phase, the subscript  $s$  is for the solid phase and the source term,  $S_i$  is the specific rate of production of the mass of the phase,  $i$ , due to chemical reactions where

$$S_{gs} = -S_{sg} \quad (5.7)$$

For a general single phase case, the forces acting upon the control volume include body forces, pressure forces,  $\nabla p$ , gravitational forces,  $\rho \vec{g}$ , and the surface viscous forces,  $\nabla \cdot \bar{\tau}$ . Then the conversion of momentum equation becomes

$$\frac{\partial(\rho \vec{v})}{\partial t} + \nabla \cdot (\rho \vec{v} \vec{v}) = -\nabla p + \rho \vec{g} + \nabla \cdot \bar{\tau} \quad (5.8)$$

In the case of multiphase flow modelling an additional force that considers the interaction between the gas phase and the solid phase,  $K_{gs}(\vec{v}_g - \vec{v}_s)$  is required. Furthermore, in the case of reaction modelling the mass exchange between phases is considered in the form of source term.

The momentum equations for the gaseous phase and solid phase respectively as following:

$$\frac{\partial(\alpha_g \rho_g \vec{v}_g)}{\partial t} + \nabla \cdot (\alpha_g \rho_g \vec{v}_g \vec{v}_g) = -\alpha_g \nabla(p) + \nabla \cdot \alpha_g \bar{\tau}_g + \alpha_g \rho_g \vec{g} + K_{gs}(\vec{v}_g - \vec{v}_s) + S_{gs} \vec{v}_g \quad (5.9)$$

and

$$\frac{\partial(\alpha_s \rho_s \vec{v}_s)}{\partial(t)} + \nabla \cdot (\alpha_s \rho_s \vec{v}_s \vec{v}_s) = -\alpha_s \nabla p - \nabla p_s + \nabla \cdot \alpha_s \bar{\tau}_s + \alpha_s \rho_s \vec{g} + K_{gs}(\vec{v}_g - \vec{v}_s) + S_{gs} \vec{v}_s \quad (5.10)$$

The stress-strain tensors for the viscous forces are as following:

For the gaseous phase is

$$\bar{\tau}_g = \alpha_g \mu_g (\nabla \vec{v}_g + \nabla \vec{v}_g^T) - \frac{2}{3} \alpha_g \mu_g (\nabla \cdot \vec{v}_g) \bar{I}_g \quad (5.11)$$

and for the solid phase is

$$\bar{\tau}_s = \alpha_s \mu_s (\nabla \vec{v}_s + \nabla \vec{v}_s^T) - \alpha_s (\xi_s - \frac{2}{3} \mu_s) (\nabla \cdot \vec{v}_s) \bar{I}_s \quad (5.12)$$

where:  $\mu_g$  and  $\mu_s$  are the shear viscosity of the gaseous phase and solid phase respectively and  $\xi_s$  is the bulk viscosity of the solid phase and taken from works of Lun et al [190].  $K_{gs}$ , is the momentum exchange coefficient for fluid solid and calculated by using the Syamlal-O'Brien model [244] as following:

$$K_{gs} = \frac{3\alpha_s \alpha_g \rho_g}{4v_{r,s}^2 d_s} C_D \left( \frac{Re_s}{v_{r,s}} \right) |\vec{v}_s - \vec{v}_g| \quad (5.13)$$

$$Re_s = \frac{\rho_g d_s |\vec{v}_s - \vec{v}_g|}{\mu_g} \quad (5.14)$$

$$C_D = \left( 0.63 + \frac{4.8}{\sqrt{Re_s/v_{r,s}}} \right)^2 \quad (5.15)$$

$$v_{r,s} = 0.5 \left( A - 0.06 Re_s + \sqrt{(0.06 Re_s)^2 + 0.12 Re_s (2B - A) + A^2} \right) \quad (5.16)$$

where  $d_s$  is the diameter of the solid phase particles,  $C_D$  is the drag function which has a form derived by Dalla Valle [245],  $Re_s$  is the relative Reynolds number and  $v_{r,s}$  is the terminal velocity correlation for the solid phase [246]

with

$$A = \alpha_g^{4.14} \quad (5.17)$$

and

$$A = \alpha_g^{4.14} \quad \text{for } \alpha_g \leq 0.85 \quad (5.18)$$

and

$$B = \alpha_g^{2.65} \quad \text{for } \alpha_g > 0.85 \quad (5.19)$$

### 5.1.2 Conservation of energy

The fundamental physical principle is that the rate of change of energy must equal the sum of the rate of heat added and the work done on the fluid. Then, the conservation of energy is written in the forms of the enthalpy for each phase as follows:

$$\frac{\partial}{\partial t} (\alpha_g \rho_g h_g) + \nabla \cdot (\alpha_g \rho_g v_g h_g) = \nabla (\lambda_g \nabla T_g) + Q_{gs} + S_{gs} H_s \quad (5.20)$$

and

$$\frac{\partial}{\partial t} (\alpha_s \rho_s h_s) + \nabla \cdot (\alpha_s \rho_s v_s h_s) = \nabla (\lambda_s \nabla T_s) + Q_{sg} + S_{sg} H_s \quad (5.21)$$

where  $h_g$  and  $h_s$  are the enthalpies of gaseous phase and solid phase, respectively, and  $\lambda_g$  and  $\lambda_s$  are the thermal conductivities of both gaseous and solid phases respectively.  $Q_{gs}$  is the heat exchange between the phases and  $H_s$  represents the source term. It includes sources of enthalpy,  $h_i$  is the enthalpy for each species in the mixture and  $\lambda_i$  is the mixture thermal conductivity. The specific enthalpy,  $h_i$ , for the individual species in a mixture is defined as following:

$$h_i = \int_{T_0}^T c_{p,i} dT + \Delta h_{f,i} \quad (5.22)$$

where,  $c_{p,i}$ , is the specific heat, and  $\Delta h_{f,i}$  is the heat of formation.

$$Q_{gs} = -Q_{sg} = h_{gs}(T_g - T_s) \quad (5.23)$$

and the heat transfer coefficient  $h_{gs}$  which is related to the Nusselt number,  $Nu_s$  is given by

$$h_{gs} = \frac{6\lambda_g \alpha_s \alpha_g Nu_s}{d_s^2} \quad (5.24)$$

Nusselt number is typically calculated from one of the many correlations found in the literature. In this case, the one has been used is that proposed by Gunn [247].

$$Nu_s = (7 - 10\alpha_g + 5\alpha_g^2)[1 + 0.7Re^{0.2} Pr^{1/3}] + (1.33 - 2.4\alpha_g + 1.2\alpha_g)Re^{0.2} Pr^{1/3} \quad (5.25)$$

$$Pr = \frac{(c_p)_g \mu_g}{\lambda_g} \quad (5.26)$$

$$Re = \frac{\rho_g d_s |\vec{v}_s - \vec{v}_g|}{\mu_g} \quad (5.27)$$

## 5.2 Turbulence modelling

In this work, to model the gaseous phase, the  $k$ - $\epsilon$  model was used. Within the context of the  $k$ - $\epsilon$  models, Fluent [158] provides three methods for modelling turbulence in multiphase flows. In this case, the  $k$ - $\epsilon$  dispersed turbulence model is used to model the gaseous phase. This is because of the reason that the concentration of the secondary phase (solid phase) is dilute. Therefore, the interparticle collisions are neglected. The dominant process in the random motion of the solid phase is the influence of the turbulence of gas phase. Fluctuating quantities of the solid phase can therefore be given in terms of the mean characteristics of the gaseous phase and the ratio of the particle relaxation time and the eddy-particle interaction time.

The eddy viscosity model is used to calculate averaged fluctuating quantities. The Reynolds stress tensor for the gas phase is calculated by using the following equation:

$$\bar{\tau}_g = \alpha_g \mu_{t,g} (\nabla \vec{v}_g + \nabla \vec{U}_g^T) - \frac{2}{3} (\rho_g k_g + \rho_g \mu_{t,g} \nabla \cdot U) \bar{I}_g \quad (5.28)$$

$$\mu_{t,g} = \rho_g C_\mu \frac{k_g^2}{\epsilon_g} \quad (5.29)$$

$$\tau_{t,g} = \frac{3}{2} C_\mu \frac{k_g}{\epsilon_g \mu} \quad (5.30)$$

The transport equations for turbulent kinetic energy  $k$  and its dissipation rate  $\epsilon$  for the gaseous phase are as follows:

$$\frac{\partial(\alpha_g \rho_g k_g)}{\partial t} + \nabla \cdot (\alpha_g \rho_g \vec{U}_g k_g) = \nabla \cdot \left( \alpha_g \frac{\mu_{t,g}}{\sigma_k} \nabla k_g \right) + \alpha_g G_{k,g} - \alpha_g \rho_g \epsilon_g + \alpha_g \rho_g \Pi_{k,g} \quad (5.31)$$

$$\frac{\partial(\alpha_g \rho_g \epsilon_g)}{\partial t} + \nabla \cdot (\alpha_g \rho_g \vec{U}_g \epsilon_g) = \nabla \cdot \left( \alpha_g \frac{\mu_{t,g}}{\sigma_\epsilon} \nabla \epsilon_g \right) + \alpha_g \frac{\epsilon_g}{k_g} (C_{1\epsilon} G_{k,g} - C_{2\epsilon} \rho_g \epsilon_g) + \alpha_g \rho_g \Pi_{\epsilon_g} \quad (5.32)$$

where  $\vec{U}_g$  is the phase-weighted velocity,  $\mu_{t,g}$  is the turbulent viscosity,  $\tau_{t,g}$  is the characteristic time of the energetic turbulent eddies,  $\Pi_{k,g}$  and  $\Pi_{\epsilon_g}$  represent the influence of the dispersed phase (the solid phase on the gaseous phase) and  $G_{k,g}$  is the

production of turbulent kinetic energy. The model constants are taken from Launder and Spalding [153] to be as following:

$$C_{1\epsilon} = 144, C_{2\epsilon} = 1.92 \text{ and } C_{\mu} = 0.09$$

The turbulent Prandtl numbers for  $k$  and  $\epsilon$  are  $\sigma_k=1.0$  and  $\sigma_{\epsilon}=1.3$  respectively.

### 5.3 Overview of numerical methods

CFD software provides a user-defined function (UDF), with which the heterogeneous chemical reaction between the solid and gas phases was defined and incorporated. It is included in the appendix (D). For the boundary conditions, the velocity-inlet was selected for the inlet condition with air inlet velocity of 1 m/s. The pressure outlet was selected for the outlet of the chamber. The walls are stationary with no-slip condition. The method used for carrying out the simulations was the finite volume method. The simulations use unsteady-state solver. For the discretization of all conservation equations, volume fraction, mass fraction of chemical species, etc., a first-order upwind was used. The evaluation of gradients and derivatives was carried out by Green-Gauss cell based Gradient Evaluation method Table 5.1 summarize the parameters of the solver. The time step was set as  $1 \times 10^{-3}$  s.

Table 5.1: Solver parameters.

characteristic	Value
Pressure-based	Enable
Formulation	Implicit
Space	3-D
Velocity formulation	Absolute
Porous formulation	Superficial velocity
Discretization	First order upwind
Gradient option	Green-Gauss cell based
Pressure velocity coupling	Phase coupled simple

### 5.4 Geometry and boundary conditions

The geometry of a newly designed combustion chamber is shown in Figure 5.1 (a) which consists of a small cup located in the centre of the chamber. The computational domain is a cylinder with an internal diameter of 48 mm and length of 101 mm. The

dimensions of the cup are 20 mm in diameter and 10 mm in height. Solid carbon particles are placed in the cup and for the dispersion of the particles, the air is supplied through the three injection nozzles, each having a diameter of 3 mm, as shown in Figure 5.1 (b). The nozzle in the middle was made with an angle of  $30^\circ$  from the horizontal line for the sake of injecting the air into the centre of the cup. The geometry of the combustion chamber was created by using solid works which was then exported to the pre-processor GAMBIT to generate the mesh and specify the boundary conditions, as shown in Figure 5.1 (b, c).

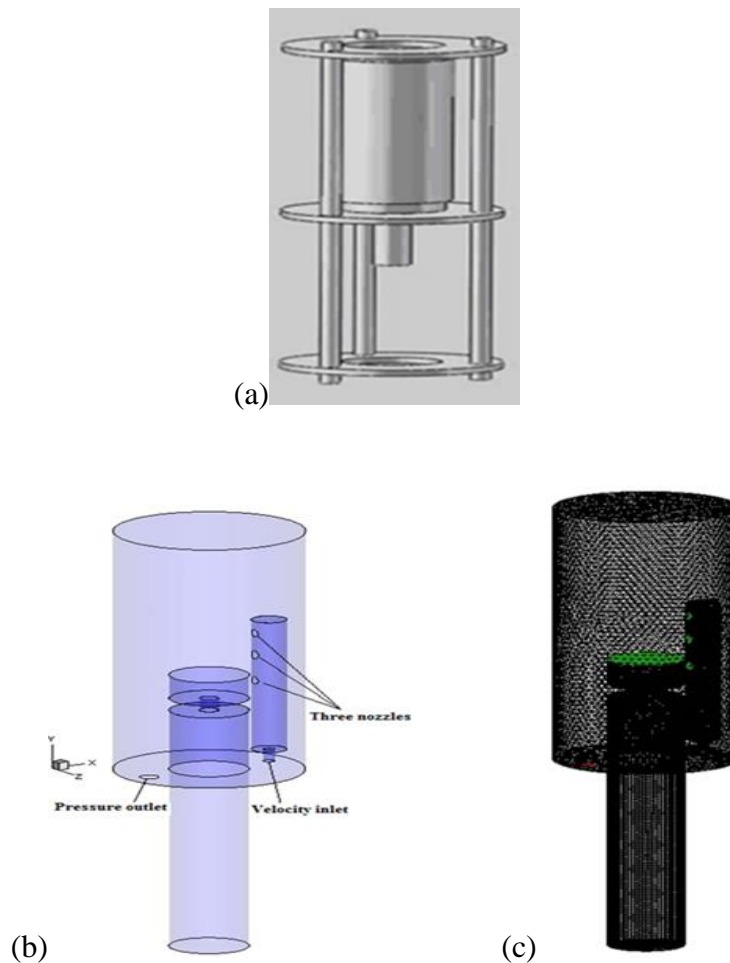


Figure 5.1: (a) Combustion chamber (Model 1) with holder frame, (b) computational domain and (c) grid of the domain.

For the boundary conditions, the velocity-inlet was selected with an air inlet velocity of 1 m/s. The pressure outlet (i.e. the zero gauge pressure) was selected at the outlet of the chamber as shown in Figure 5.1 (b) and the walls are stationary with no-slip condition. The combustion simulations are performed for particle sizes with different diameters (0.5mm, 1mm, 1.5mm, 2mm, 2.5mm and 3mm). The particle of 1mm diameter is assigned to the baseline case. The other particle diameters are also simulated for



comparison. The particles are assumed to be inelastic and mono-dispersed spheres. Thus, in each case, the solid phase is assumed to have a uniform particle size. The volume fraction of the solid phase is set to 0.6 for all cases, owing to the void that is always present between the particles. Each case has its own particle size, which means that six simulations are performed. An unsteady-state solver with a time-step of  $10^{-3}$  s is used. The combustion modelling is based on the two-phase Euler-Euler approach which takes into account the interactions of the gaseous and solid phases. The char combustion is considered according to the heterogeneous reaction (R1). The combustion rate of char is assumed to be limited by the chemical kinetics because the only reactive species that is included in the gas phase is  $O_2$ . Then, the reaction rate  $r_a$  ( $\text{kmol/m}^3\text{s}$ ) is defined as

$$r_a = k_a C_{c(s)} C_{o_2} \quad (5.33)$$

where  $C_{c(s)}$  and  $C_{o_2}$  ( $\text{kmol/m}^3$ ) are the concentrations of carbon and oxygen, respectively; and  $k_a$  is the reaction rate constant given by the Arrhenius type relation:

$$k_a = AT^\beta \exp\left(-\frac{E}{R_u T}\right) \quad (5.34)$$

The kinetic constants are provided in Table 4.4.

A user-defined function (UDF), with which the rate of the heterogeneous chemical reaction between the solid and gas phases is defined, is developed and coded in C++ language and incorporated in the solver. Some assumptions are made to simplify the combustion modelling: the composition of solid particles is a pure (100%) carbon. In reality, this is not the case and to some extent the existence of inherent moisture, sulphur, nitrogen, and other non-carbon components will affect the combustion characteristics. Moreover, the virtual mass effect is neglected because the density of the solid phase is greater than that of the gas phase. Since the particle size is small the lift force is not significant and as a result it has also been neglected. Therefore, the interaction between the phases is only due to the drag force.

## 5.5 Grid-independence study

Initially, a grid-refinement test is carried out in order to estimate the grid size and mesh quality required for the simulation. It is commonly known that more accurate solution can be obtained from numerical simulations with a higher number of computational

mesh cells. Therefore, a grid-refinement test is carried out for the coal particle size of (1 mm) by sequentially increasing the number of control volumes inside the chamber. The peak combustion temperature presented in Figure 5.2 against time (sec) shows that the variation in the results obtained by the two relatively higher resolution grids (551486 and 977899) is very moderate. And the results obtained by the grid cell size of 474748 lay between the results of the highest and lowest density grids. Thus, one of these relatively higher resolution grids will be suitable for the simulations, but in order to save the computational time the grid size of 474748 is used to perform all the numerical simulations.

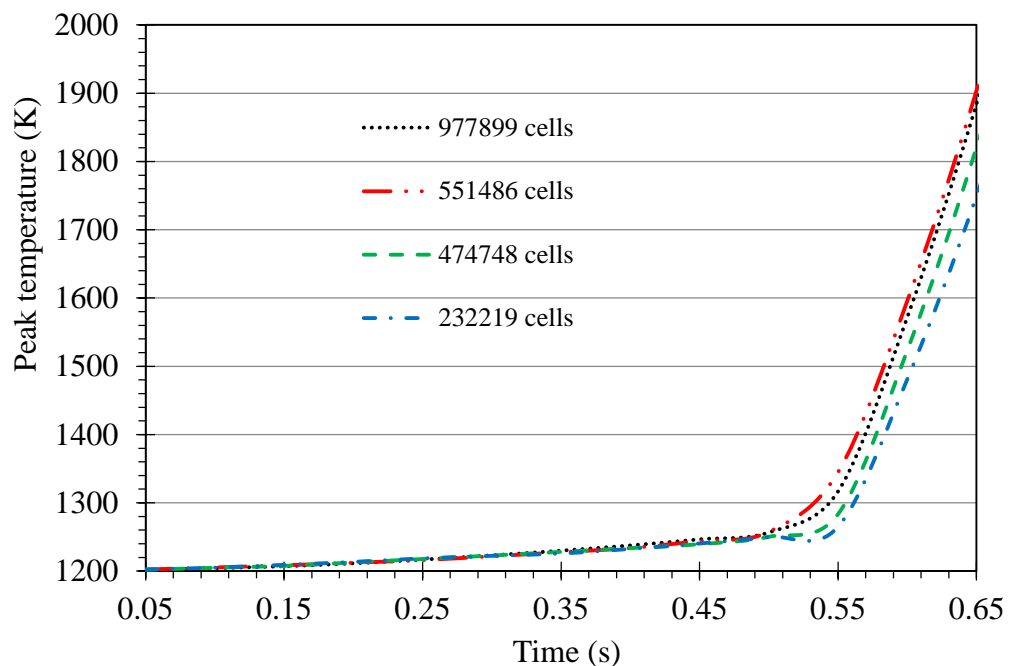


Figure 5.2: Maximum temperature inside the chamber for the particle size of 1 mm diameter for base case.

## 5.6 Results and discussion

### 5.6.1 Base case

For the case of a 1 mm particle diameter, the volume fraction at different simulation time-steps is shown in Figure 5.3. At the beginning the volume fraction was set to 0.6, and the results taken at the mid-plane of the combustion chamber show that the volume fraction of the solid phase progresses upward the chamber. It can also be seen that the carbon particles move upward where good mixing of the particles with the injected air through the nozzles was obtained.

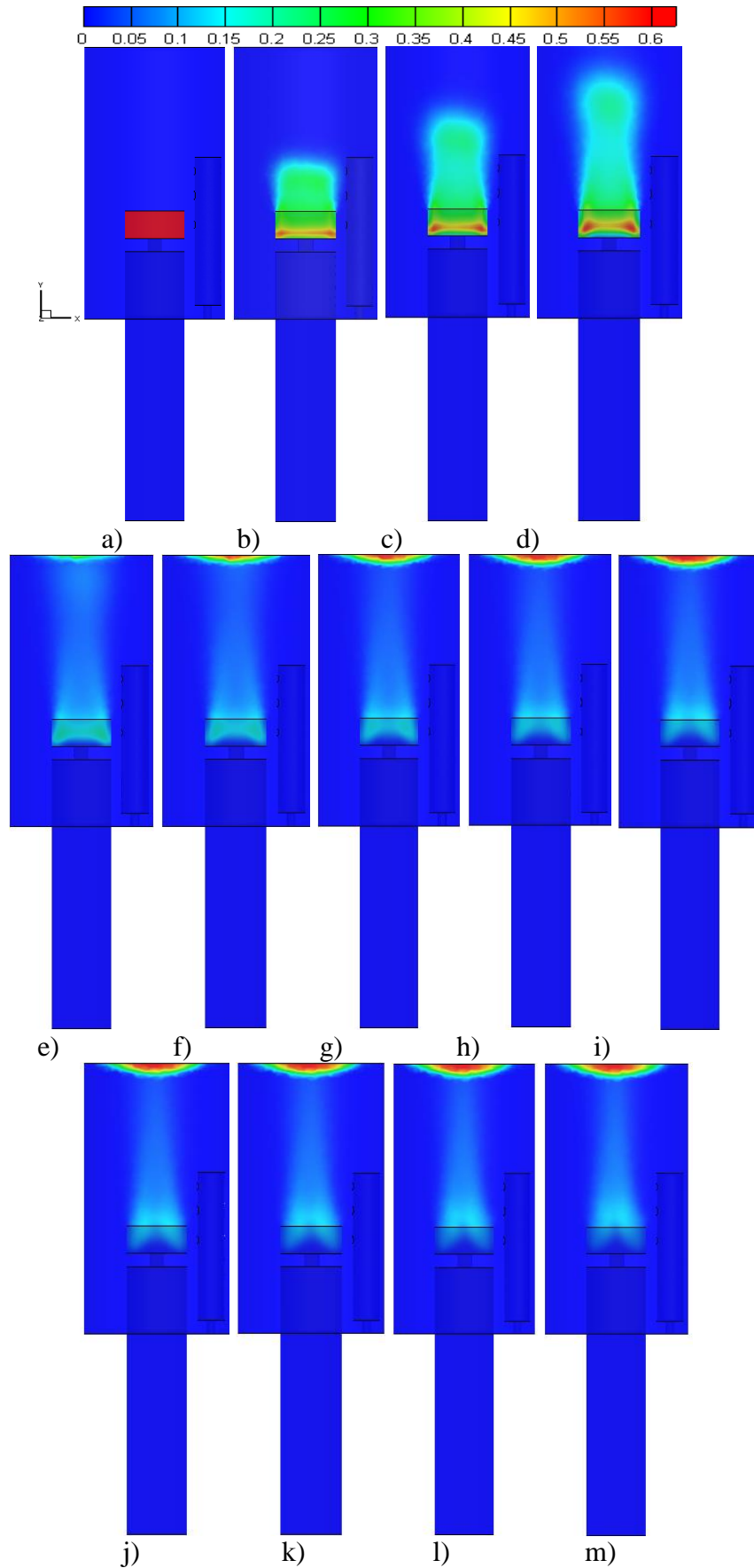


Figure 5.3: The variation of volume fraction of the solid phase at the middle plane for the base case (particle diameter of 1 mm) at different simulation times (s): (a) 0, (b) 0.05, (c) 0.1, (d) 0.15, (e) 0.2, (f) 0.25, (g) 0.30, (h) 0.35, (i) 0.40, (j) 0.45, (k) 0.50, (l) 0.55 and (m) 0.6.

Particularly, the results show that some particles are accumulated at the centre of the top wall of the chamber after 0.2 sec and this can be identified by referring to Figure 5.4, which illustrates the high temperature zone inside the chamber at the different time-steps.

From the temperature distribution at the middle plane shown in Figure 5.4, it is also clear that the combustion was sustained and the temperature of the gas phase rapidly propagates upward from the cup due to the release of heat during the process of combustion. Moreover, the temperature contour profiles further show that the location of the combustion zone moves to the top section of the chamber with time, and the waviness seen in the contours in the lower right region attributes to the air injection from the three nozzles. It is shown that the flame expands longitudinally in the chamber and after the time of 0.2 s it reaches the top wall of it and starts to expand laterally. The hot gas is reverted back towards the cup and expands laterally towards the side walls.

To visualize the propagation of the flame more clearly, some horizontal sections are taken at different locations of the chamber height. These locations are at  $y = 4, 6, 8$  and 10 cm. These slices display the temperature contours at different times as can be seen in Figure 5.5. The figure shows the progress of the gas temperature inside the chamber in two ways. It shows the variation of temperature contours as a function time in the vertical direction and as a function of chamber height in the horizontal direction.

It can be seen from Figure 5.5 that the flame is concentrated at the centre of the chamber and the temperature expands horizontally towards the side walls of the chamber as the time passes. At time 0.2 s, the flame reaches the top wall of the chamber (refer to Figure 5.4) then it starts to expand towards the side wall of the chamber. Therefore, it is seen that at the height location of 10 cm which is very close to the top wall that the flame expands towards the side walls at  $t = 0.3$  s. This is obvious at times of 0.4 and 0.5 s.

Temperature contours at the same height locations for the cases of the particle size with diameters of 0.5 mm and 1.5 mm are provided in appendix (E). It can be seen that there is not a big difference between the former one (see Figure E. 1) and the case of 1 mm particle size. On the other hand, the latter one (see Figure E. 2) shows a clear difference compared with the case of 1 mm particle size. The temperature distribution at horizontal sections at different locations of the height of the chamber for the other sizes' cases is shown in Figure E. 3 provided in the appendix (E) as well.

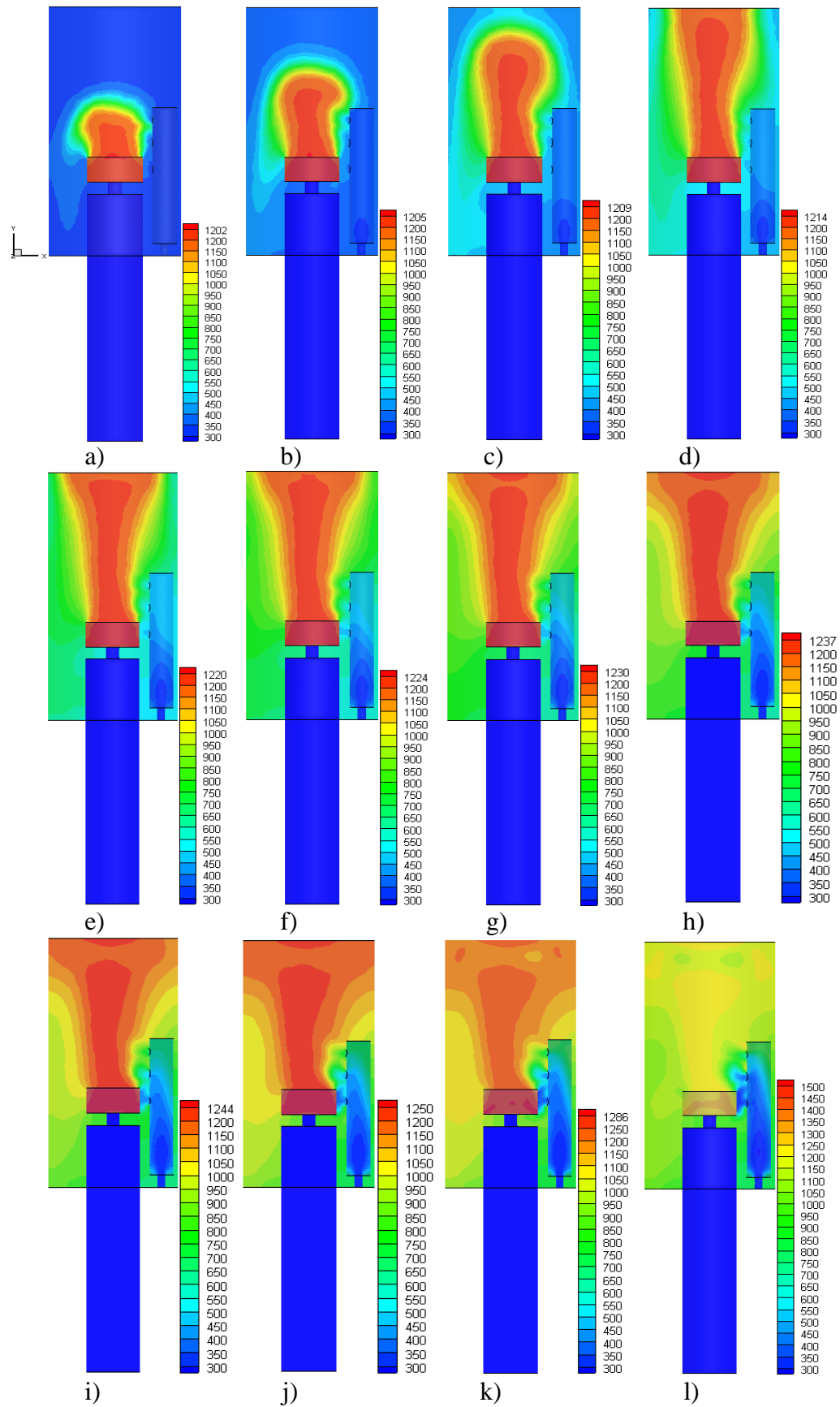


Figure 5.4: The variation of temperature at the middle plane for the base case (1 mm particle diameter) showing at time (s): (a) 0.05, (b) 0.1, (c) 0.15, (d) 0.2, (e) 0.25, (f) 0.3, (g) 0.35, (h) 0.4, (i) 0.45, (j) 0.5, (k) 0.55 and (l) 0.6.

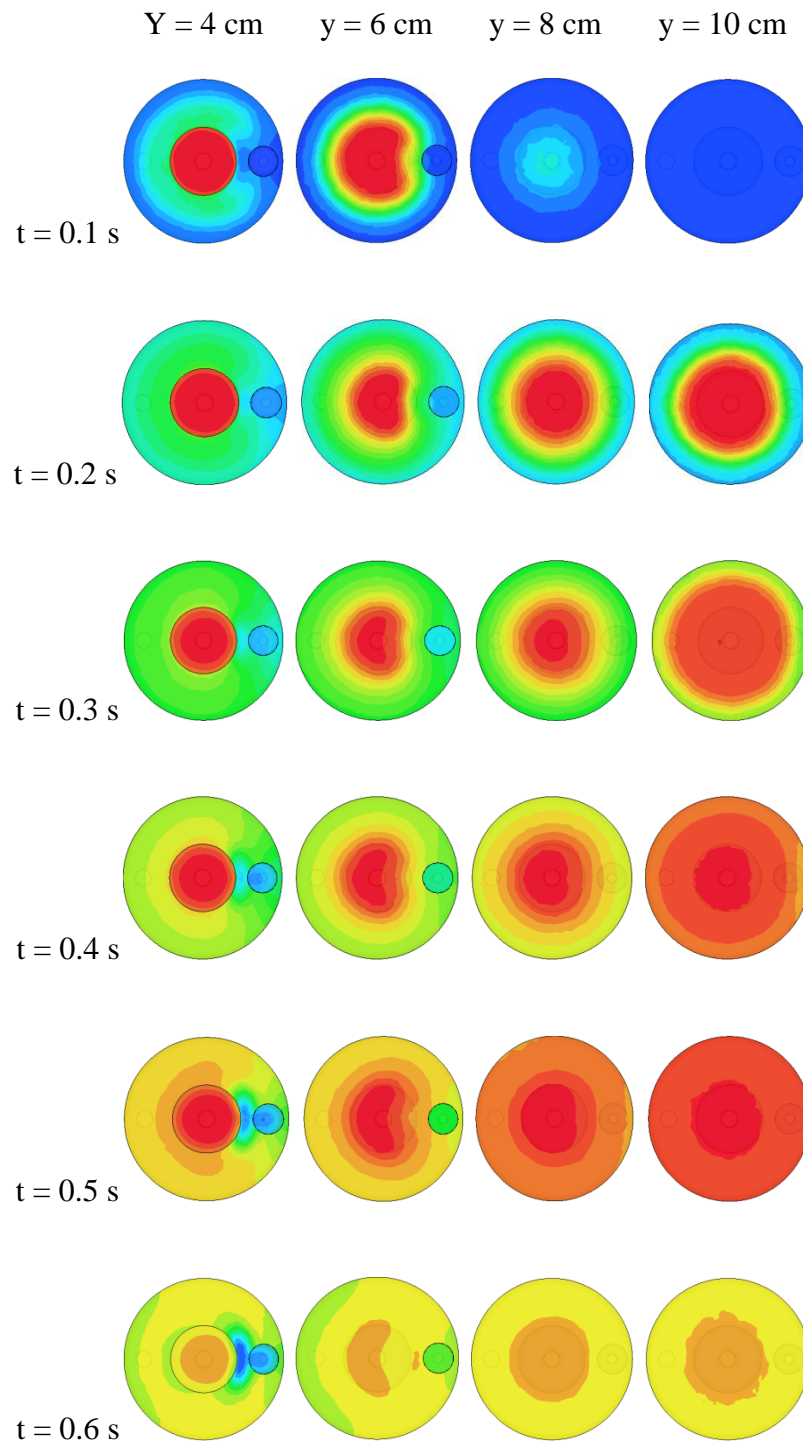


Figure 5.5: Temperature contours at different horizontal locations in  $y$  direction and at different times (s) for the base case (1 mm particle size).

The concentration of carbon dioxide ( $\text{CO}_2$ ) at the middle plane is depicted in Figure 5.6. It can be seen that the  $\text{CO}_2$  concentration is also progressing with the time. The concentration at the time of 0.25 sec also indicates the accumulation of the carbon particles at the centre of the top wall of the chamber as mentioned before.

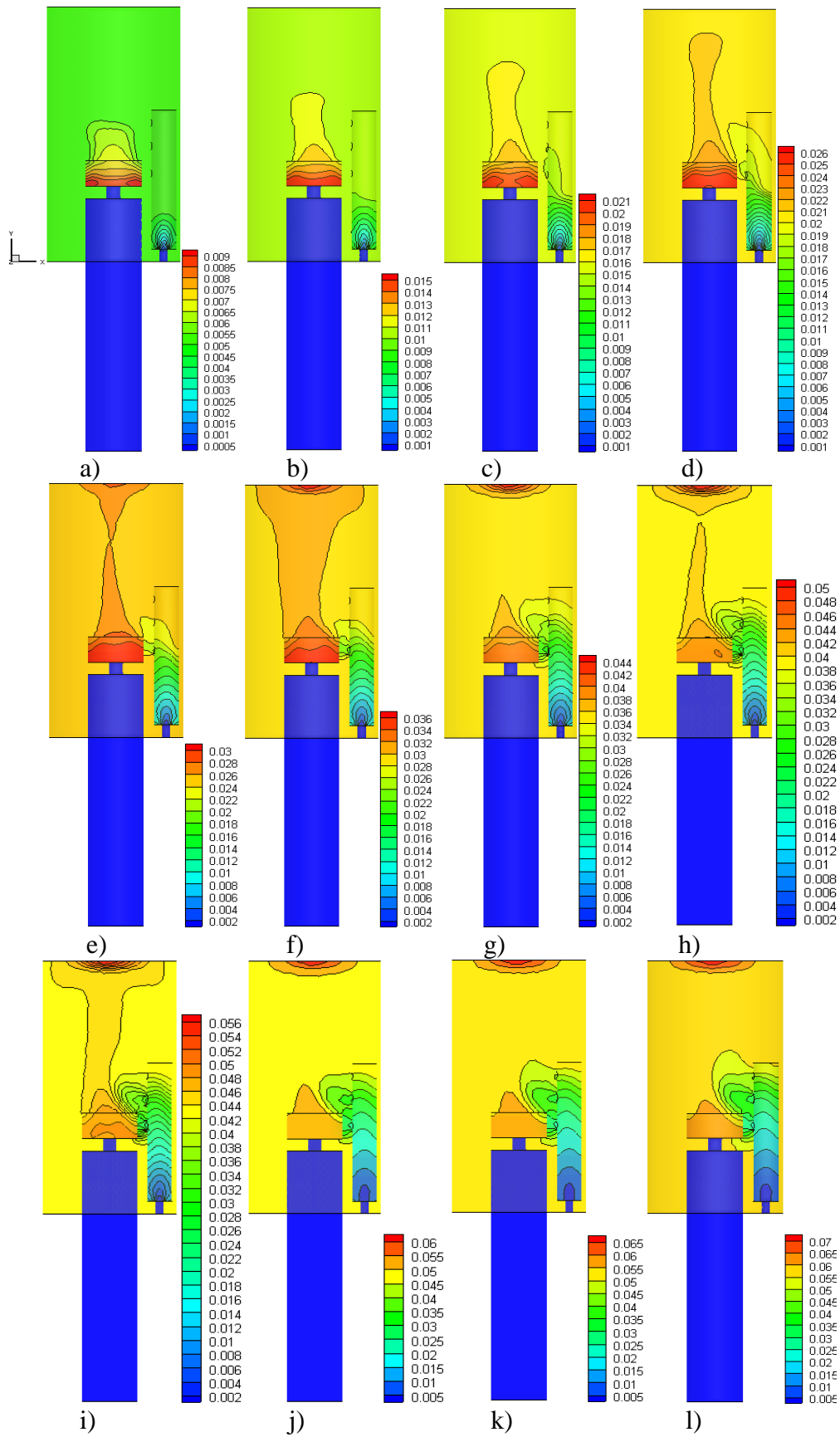


Figure 5.6: The mass fraction of  $\text{CO}_2$  at the middle plane at different time (s) for the base case (particle diameter of 1 mm): (a) 0.05, (b) 0.1, (c) 0.15, (d) 0.2, (e) 0.25, (f) 0.3, (g) 0.35, (h) 0.4, (i) 0.45, (j) 0.5 and (k) 0.55.

Figure 5.7 shows different temperatures' iso-surfaces at time 0.65 s for different cases with different particle diameters. From Figure 5.7 (a), it can be seen that for the case of particles' size of 0.5 mm that the flame is concentrated inside the cup. The height of the flame core is increased by increasing the particle size as shown for the cases of particles' size of 1, 1.5 and 2 mm. Then, it is reduced for the cases of particle sizes with a diameter of 2.5 and 3 mm. It is also seen that the highest temperature zones are at the air injection hole in the middle as seen in Figure 5.7 (e).

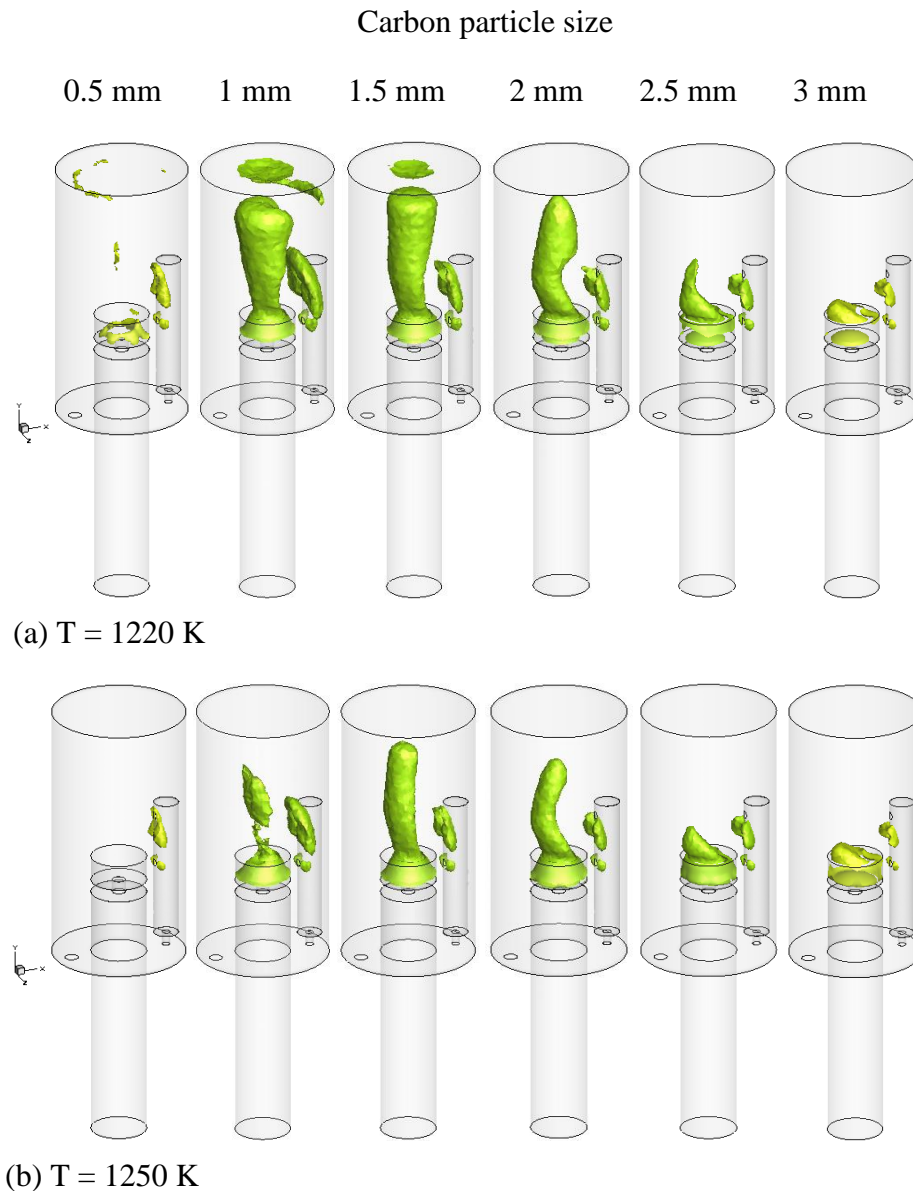


Figure 5.7: Iso-surfaces at time 0.65 s for the base case for different particle sizes: (a) 1220 K, (b) 1250 K, (c) 1280 K, (d) 1400 K and (e) 1550 K.



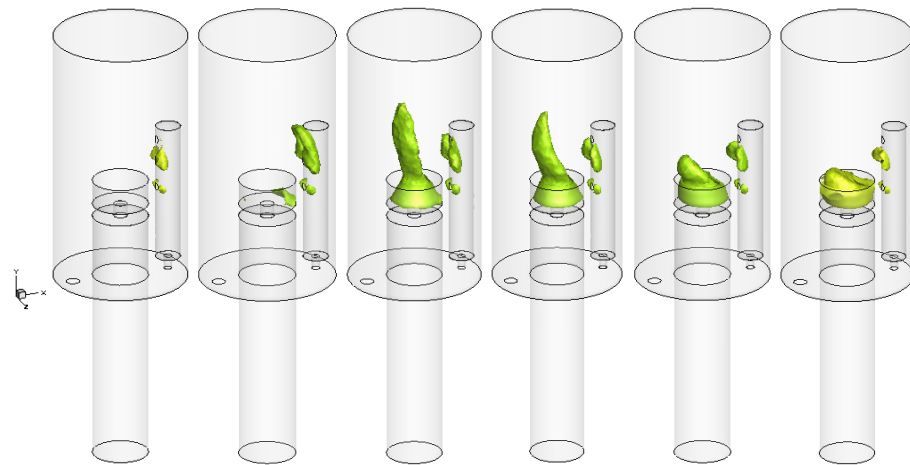
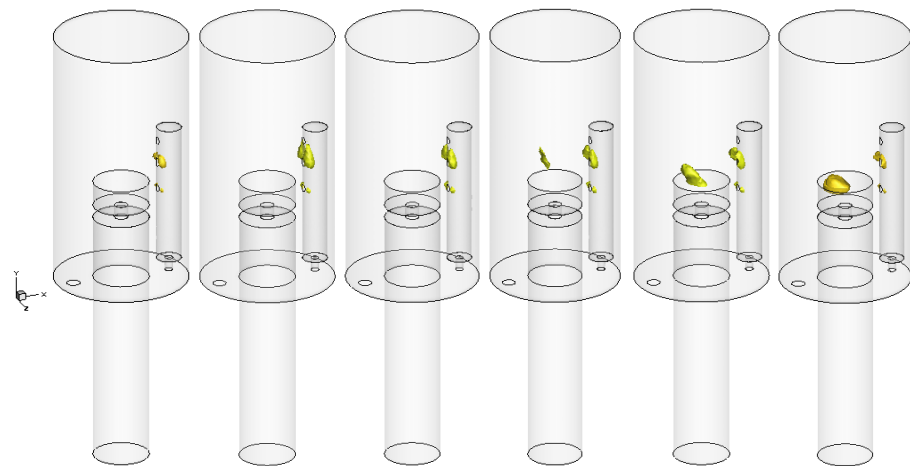
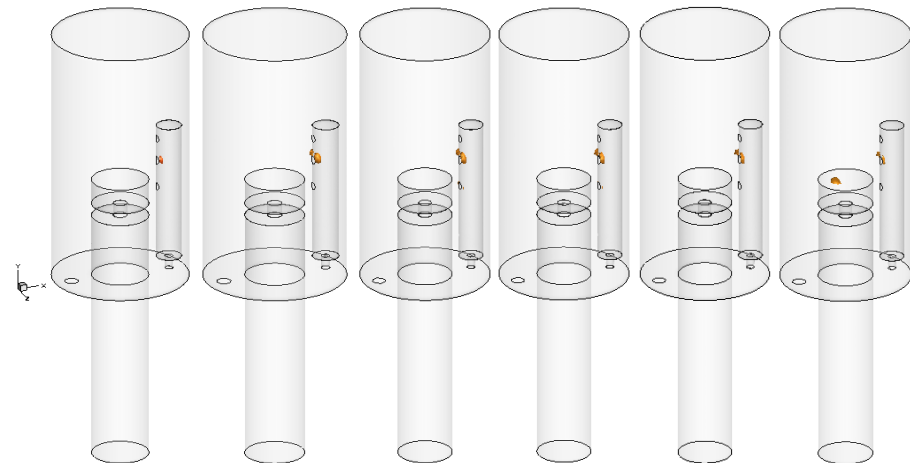
(c)  $T = 1280 \text{ K}$ (d)  $T = 1400 \text{ K}$ (e)  $T = 1550 \text{ K}$ 

Figure 5.7: Continued.

Figure 5.8 shows the variation of the peak temperature inside the chamber with time for cases with different particle diameters. At the beginning the temperature was 1200 K and when the combustion took place it increased with time. It is clear that the size of particle plays a crucial role in the combustion process as can be seen from this figure. It

It is obviously seen that as the particle size decreased, the peak temperature of the gas phase decreased till the time of 0.55 s. The bigger the particle size the higher the temperature is gained. It is shown that the higher temperature was obtained from the case of carbon particles with a diameter of 3 mm and the lower one was gained by burning carbon particles with a diameter of 0.5 mm. This seems to be counterintuitive as it is known that the smaller particles have a surface area to volume ratio larger than that of the larger particles and they should react more quickly as it has been presented in chapter 4. This may be attributed to the residence time of the carbon particles and the design of the burner. When the air is injected through the nozzles the particles are blown up out of the small cap and, therefore, the larger particles stay longer than the smaller ones inside the chamber. This may be due to the reason that the smaller particles follow the streamlines of the continuous phase. Whereas increasing the particle size leads to that the larger particles may deviate from the streamlines of the continuous phase. Consequently, this deviation may increase the slip velocity resulting in enhancing convective transports of heat and species concentrations.

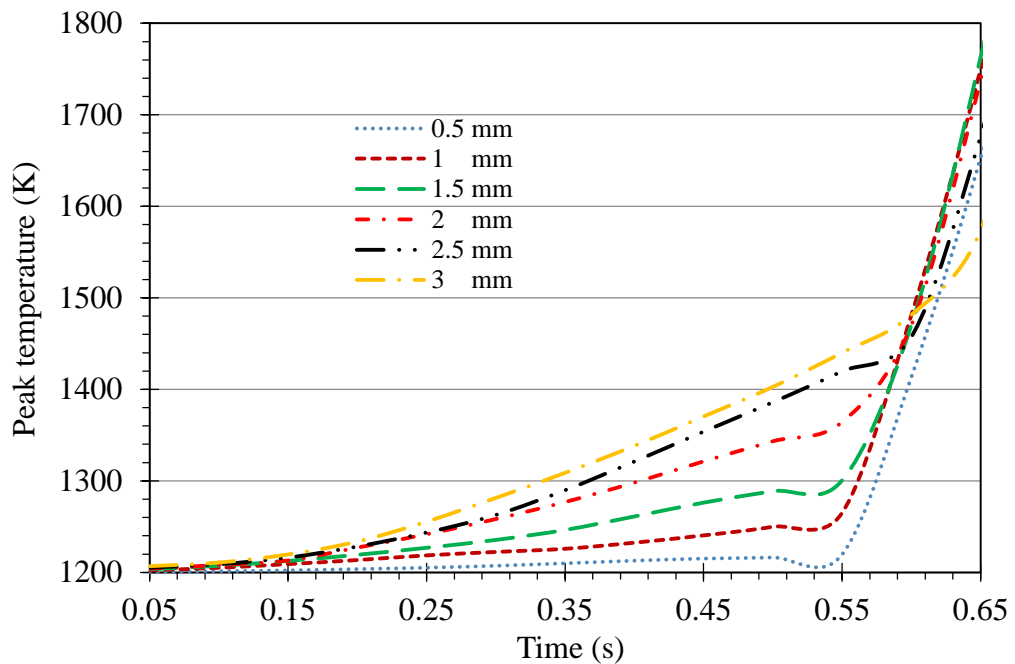


Figure 5.8: The peak temperature variation with time (s) for different particle sizes for the base case.

It is also shown that the peak temperature of the gas phase is getting close to each other for all the cases at time 0.6 sec, then the temperature of the smaller particles size increases when compared with that of the particles with bigger sizes. When referring to Figure 5.7 (e), one can extract the peak temperature is in the zone close to the middle air injection hole. The results after the time of 0.65 sec are excluded.

### 5.6.2 The influence of chamber height

The carbon particles in the base case were accumulated at the centre of the ceiling of the chamber (see Figure 5.3) due to the reason that there is not enough space for them to be dispersed inside the chamber. Therefore, the design of the chamber was modified by increasing the height of the chamber for the purpose of investigating its effect on the combustion inside the chamber. The height of the chamber was doubled in order to provide more space for the dispersion of the particles inside the chamber. Doing so will give the particles more space to mix well with the air inside the chamber and may prevent them from accumulating at the centre of the top wall of the chamber.

As can be seen in Figure 5.9, which illustrates the volume fraction of the solid phase at the middle plane for the case of particle size of 1 mm diameter, that most of the particles are burned before reaching the ceiling of the chamber when compared with the base case. This means that increasing the height of the chamber results in better mixing between the air and the carbon particles. It is also seen that some particles start to accumulate at top wall at time of 0.6 s which is clearly identified by the shape of the flame in Figure 5.10. This figure shows the temperature distribution at the middle plane and at different times. In comparison with the base case (see Figure 5.4), it is seen that the shape of the flame of this case is different. It can be seen the propagation of the flame occurs in a longitudinal direction till the time of 0.55 s when the horizontal expansion becomes clear.

Figure 5.11, which shows the temperature distribution at different horizontal planes, gives clear indications of the effects of increasing the height of the chamber in order to give more space for the carbon particle and, therefore, having good mixing with the injected air. When comparing it with Figure 5.5 (base case), one can notice the difference between them in the flame shape. It is seen that the temperature distribution is approximately the same at the time of 0.1 s except for the waviness in the flame shape which is clearer in the base case than the case of double height at the cross sections at heights  $y = 4$  and 6 cm. This can be attributed to the back reversion of the hot gas towards the cup. This can be confirmed from Figure 5.11 at times 0.5 s and up when the waviness becomes clear. At these times the flame moves close to the top wall and the hot gas is reverted and therefore the waviness in the flame shape increases. The mass fraction of  $\text{CO}_2$  at the middle plane is shown in Figure 5.12.

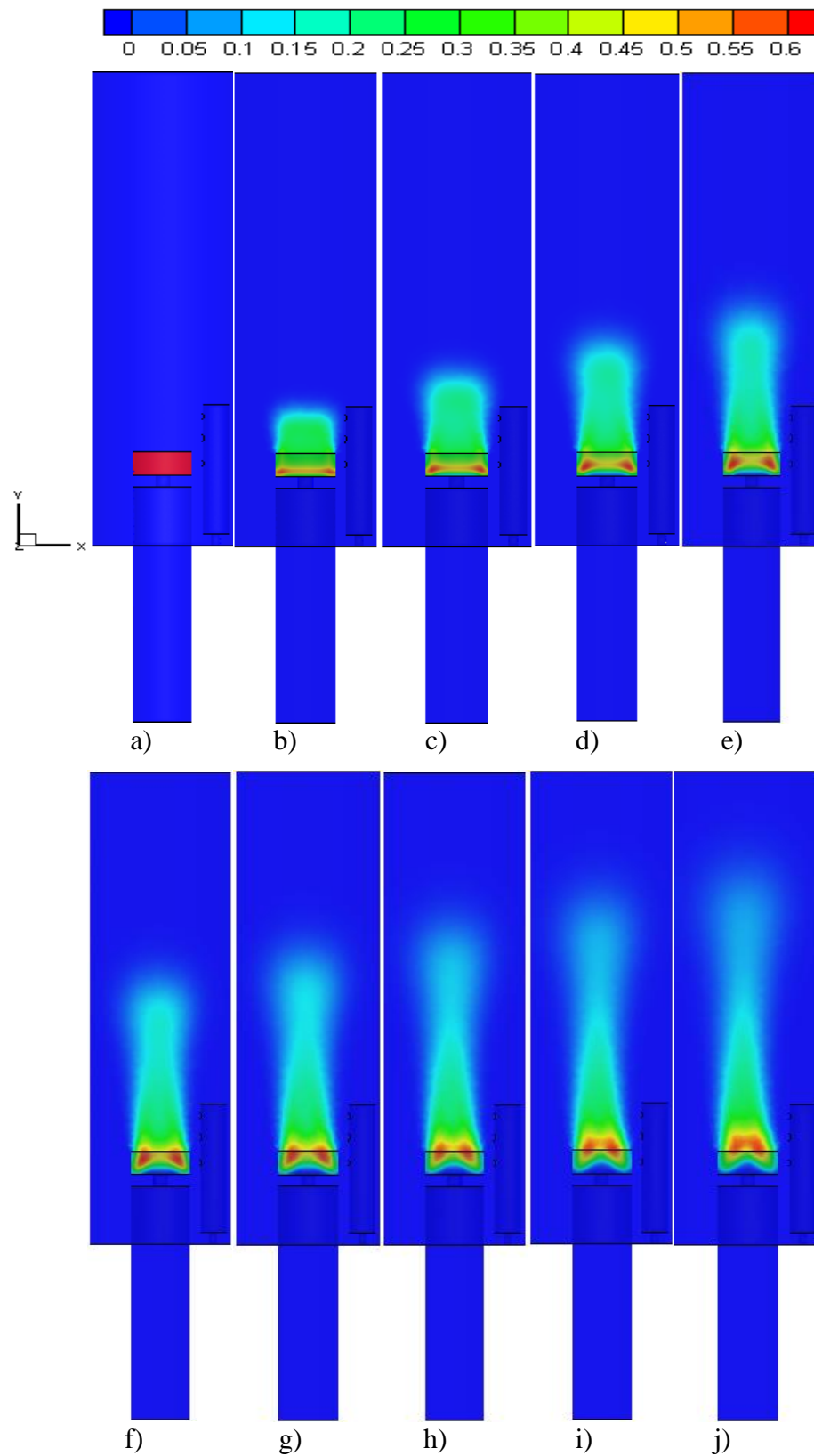


Figure 5.9: The variation of volume fraction of the solid phase at the middle plane showing at different times (s) for the doubled-height case (particle diameter of 1 mm): (a) 0, (b) 0.05, (c) 0.1, (d) 0.15, (e) 0.2, (f) 0.25, (g) 0.30, (h) 0.35, (i) 0.40, (j) 0.45, (k) 0.50, (l) 0.55, (m) 0.6 and (n) 0.65.

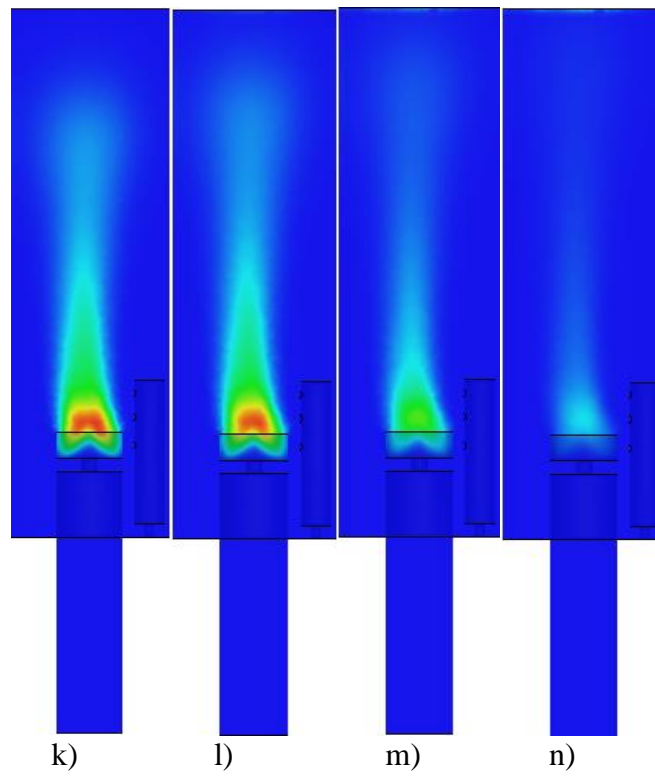


Figure 5.9: continued.

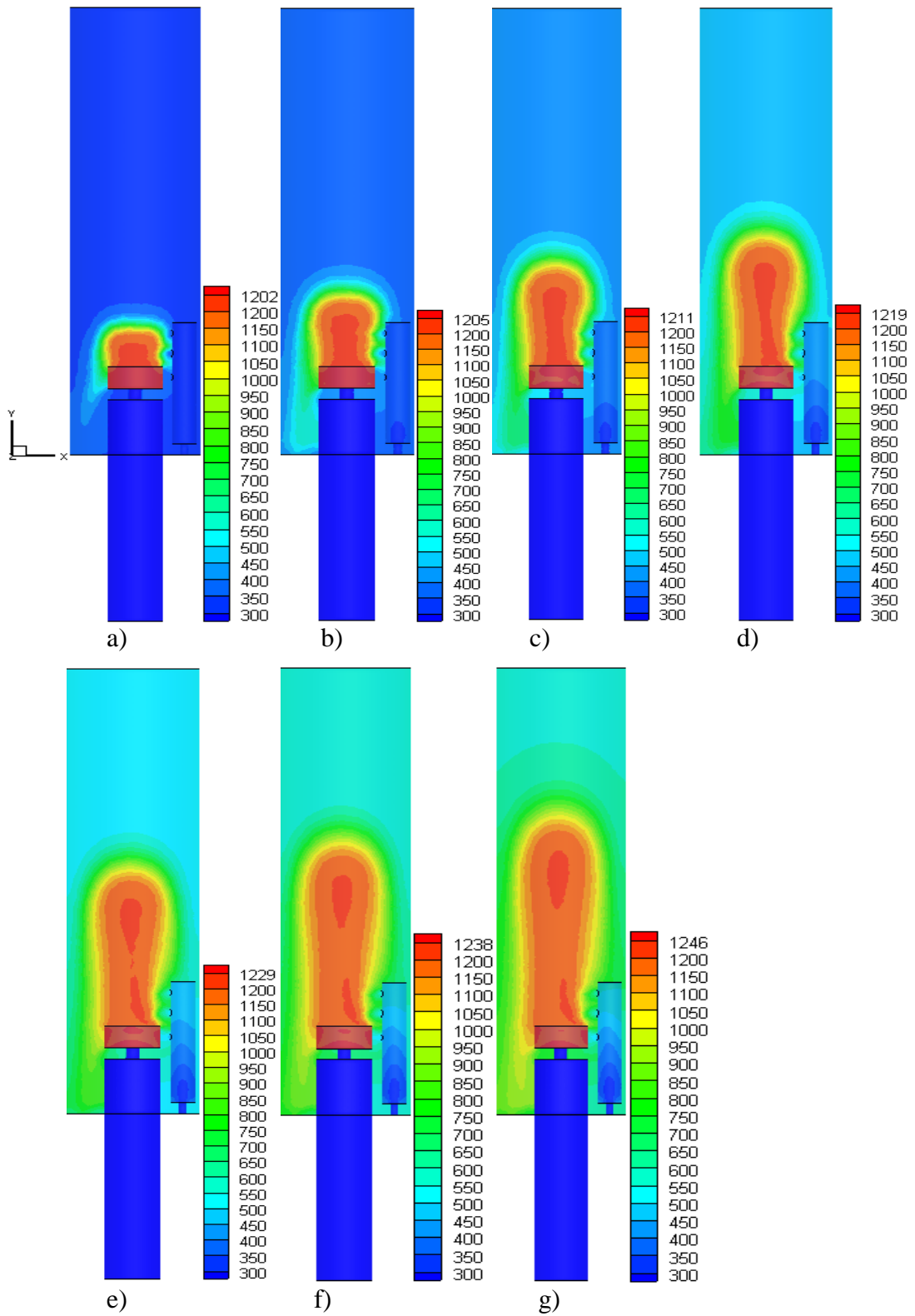


Figure 5.10: The distribution of temperature for the doubled-height case (1 mm particle diameter) showing at different times (s): (a) 0.05, (b) 0.1, (c) 0.15, (d) 0.2, (e) 0.25, (f) 0.3, (g) 0.35, (h) 0.4, (i) 0.45, (j) 0.5, (k) 0.55, (l) 0.6 and (m) 0.65.

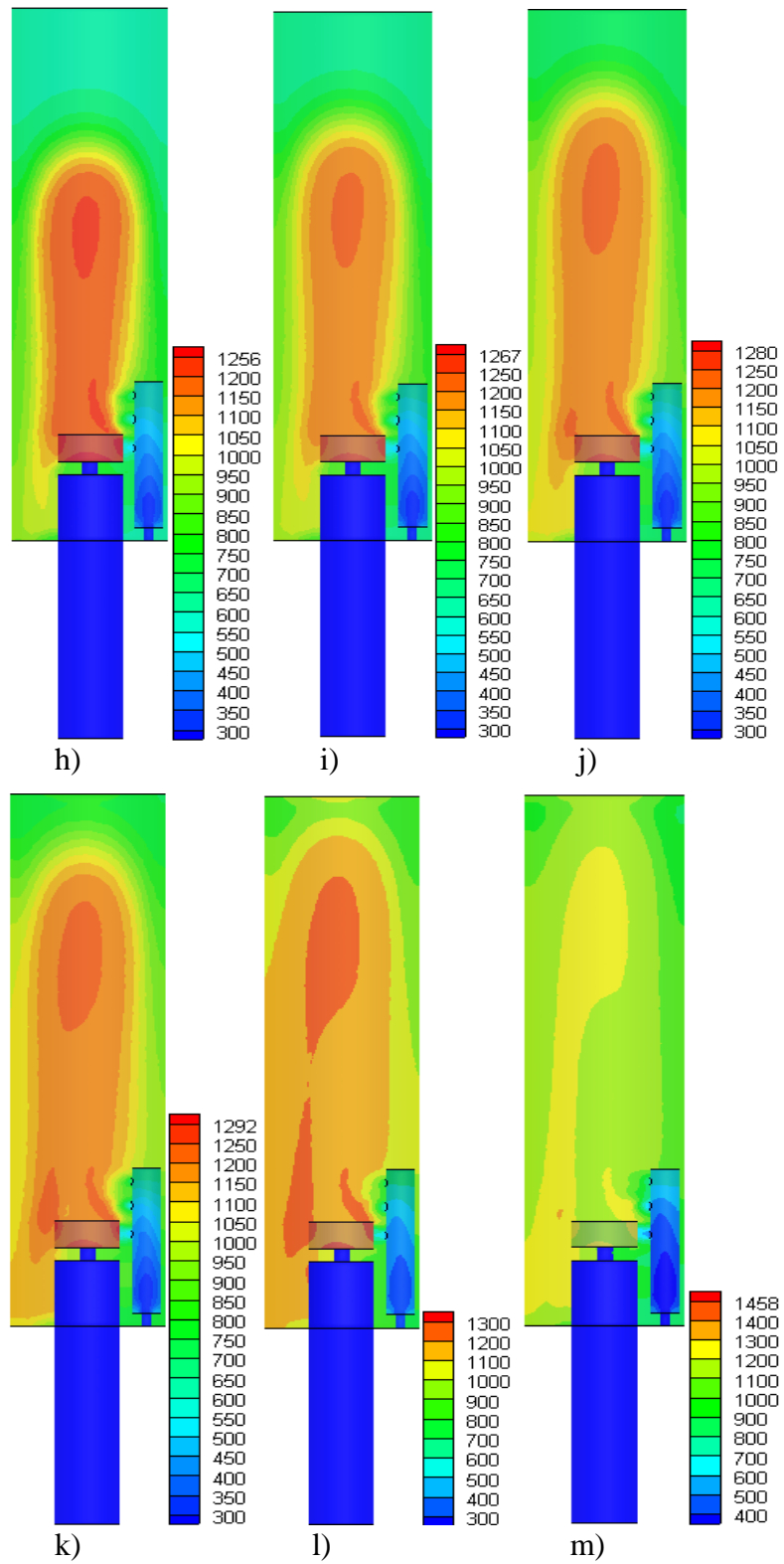


Figure 5.10: continued.

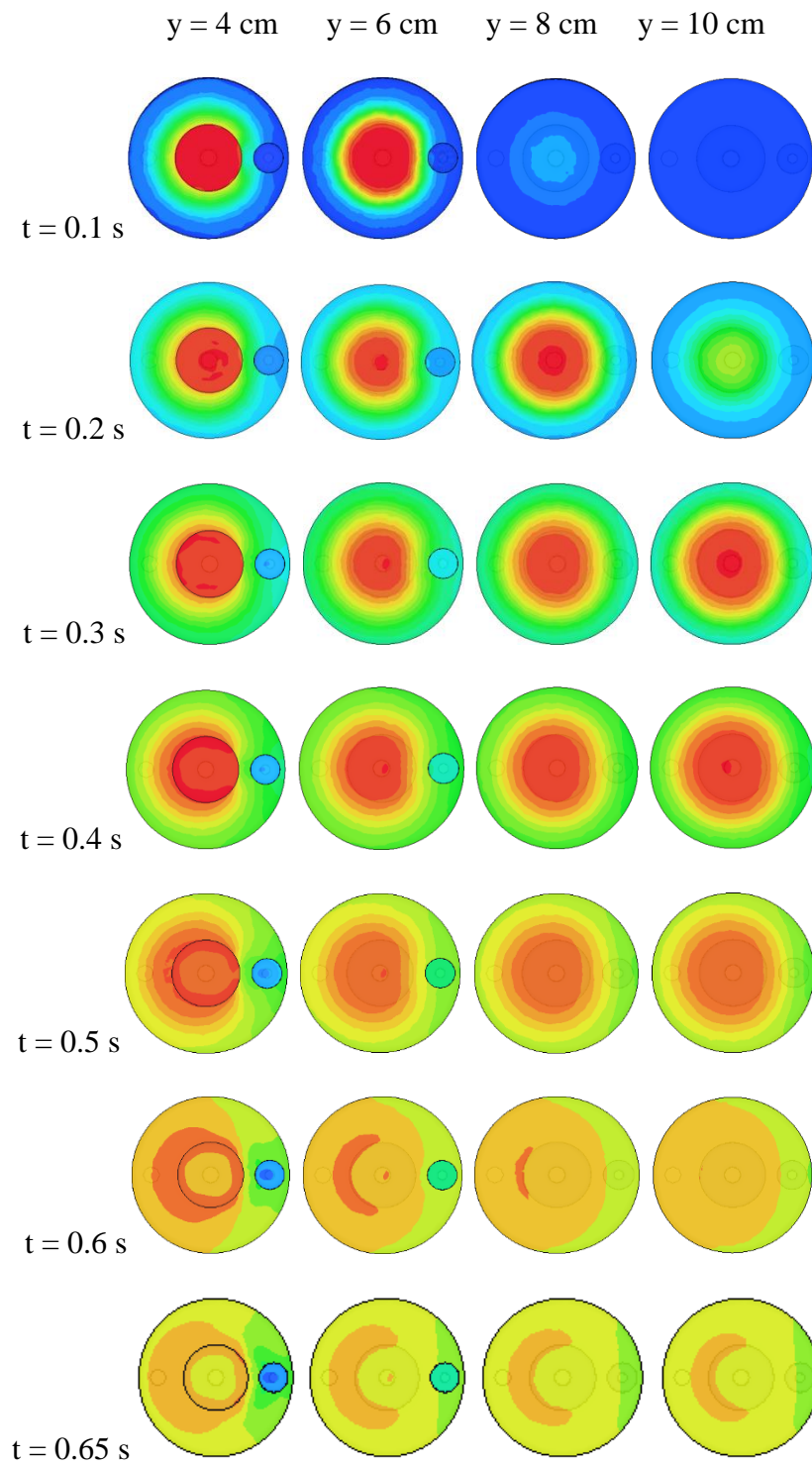


Figure 5.11: Temperature contours at different locations in y direction and different times (s) for the doubled-height case (particle diameter of 1 mm).



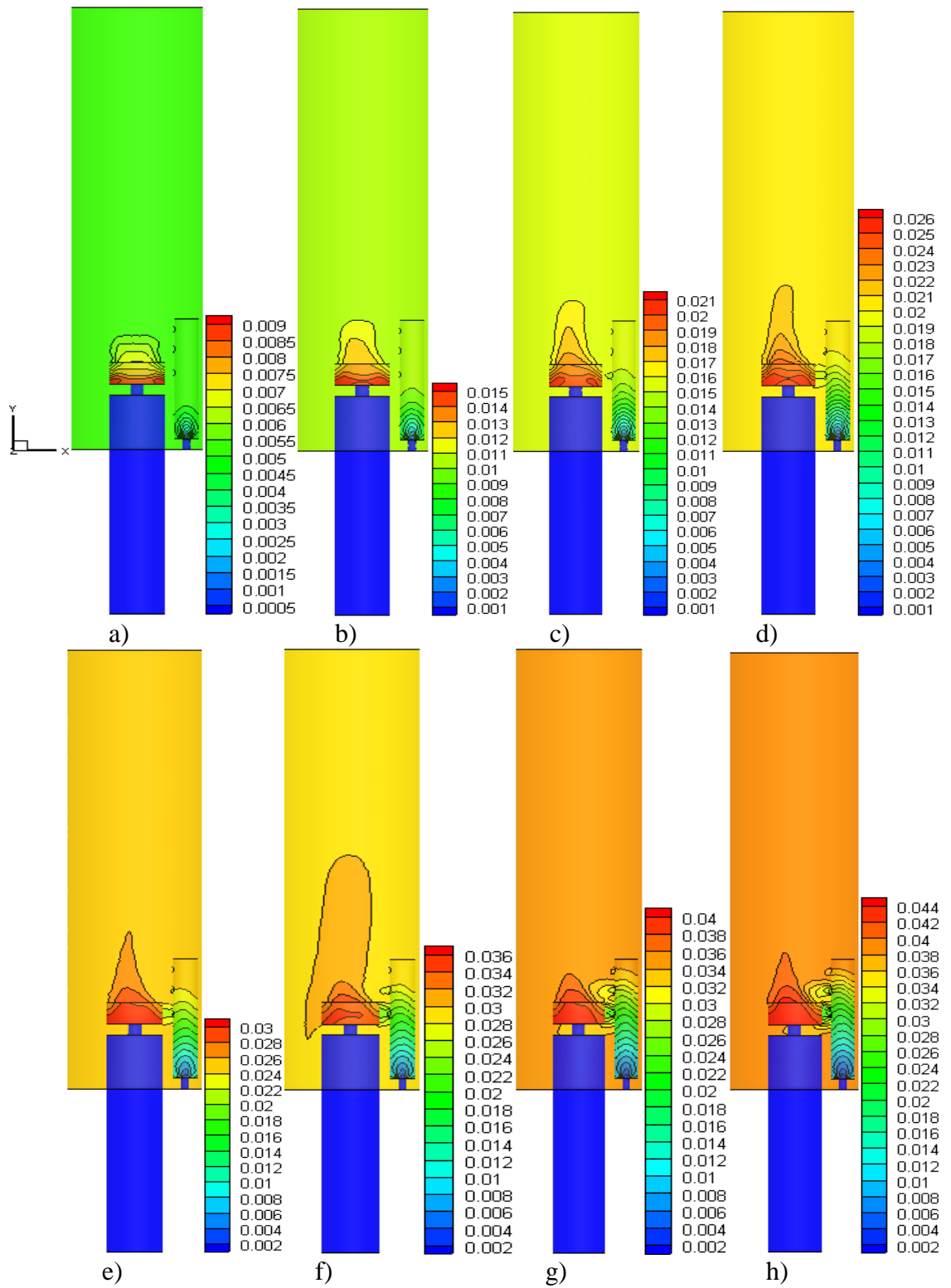


Figure 5.12: The mass fraction of CO<sub>2</sub> at different time (s) for the doubled-height case (particle diameter of 1 mm): (a) 0.05, (b) 0.1, (c) 0.15, (d) 0.2, (e) 0.25, (f) 0.3, (g) 0.35, (h) 0.4, (i) 0.45, (j) 0.5, (k) 0.55 and (l) 0.6.

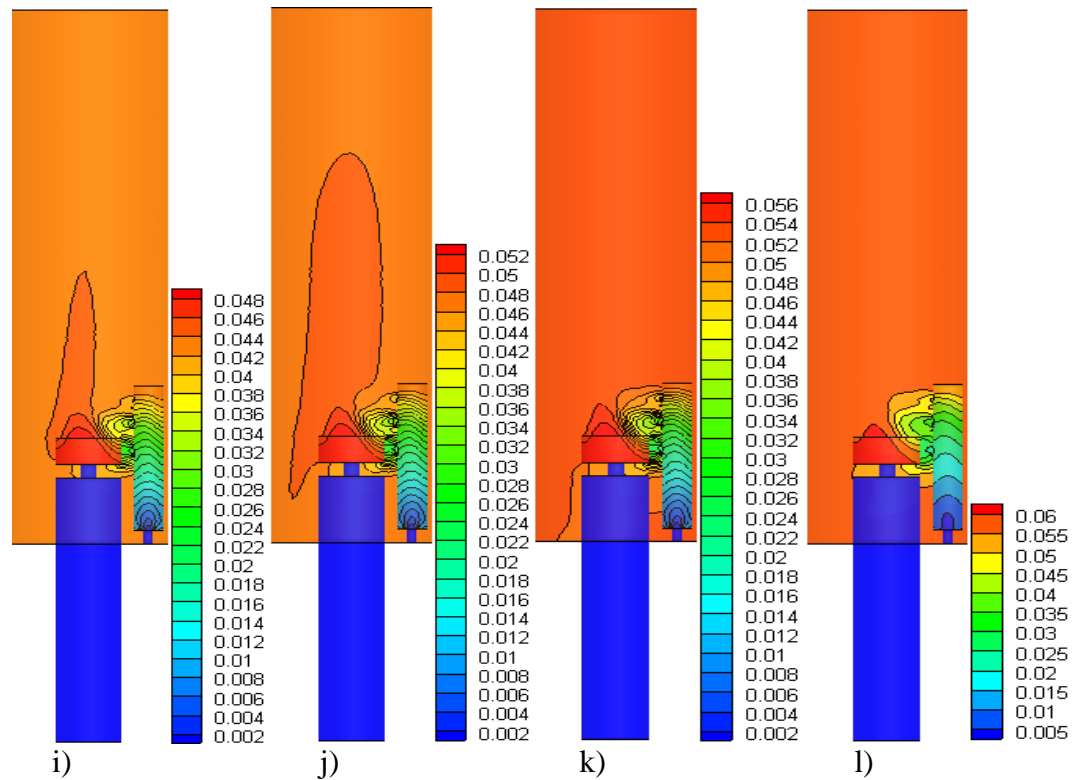


Figure 5.12: continued.

The variation of peak temperature inside the doubled-height chamber with time for different cases (different particle sizes) is depicted by Figure 5.13. The trend of variation is similar to that of the base case (see Figure 5.8). It is also seen that the larger particles produce high temperature than the smaller ones and this may due to the reason mentioned in §5.6.1.

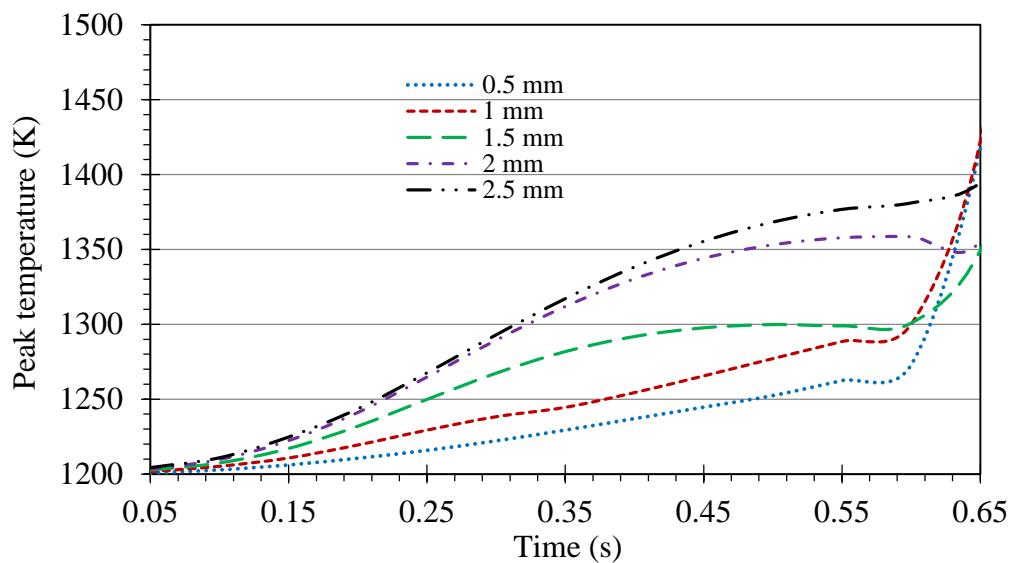


Figure 5.13: The peak temperature variation with time for different particle sizes for the doubled-height case.

The temperature iso-surfaces are shown in

Figure 5.14 at time 0.65 s. When comparing with base cases (refer to Figure 5.7), it can be seen that flame zone becomes bigger for the case of 0.5 mm particle size and the opposite is for the other cases.

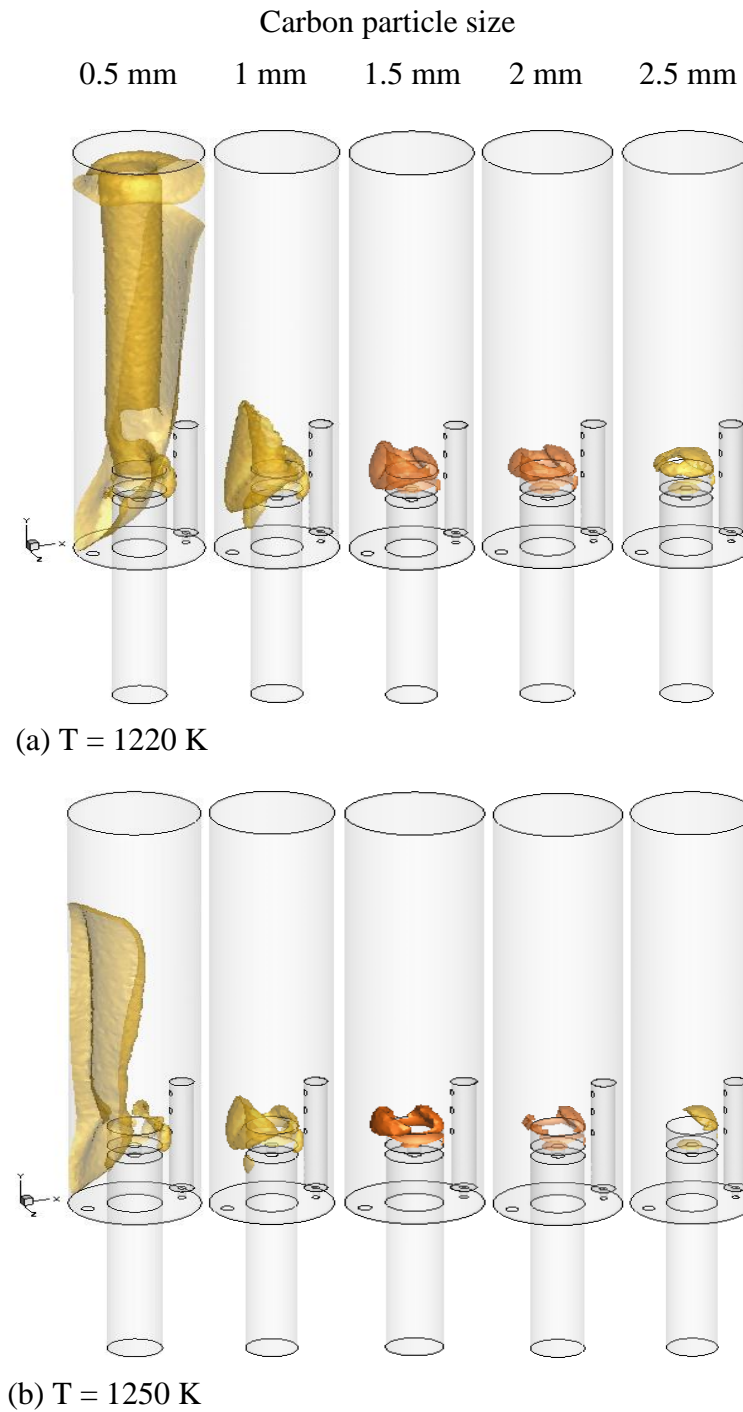
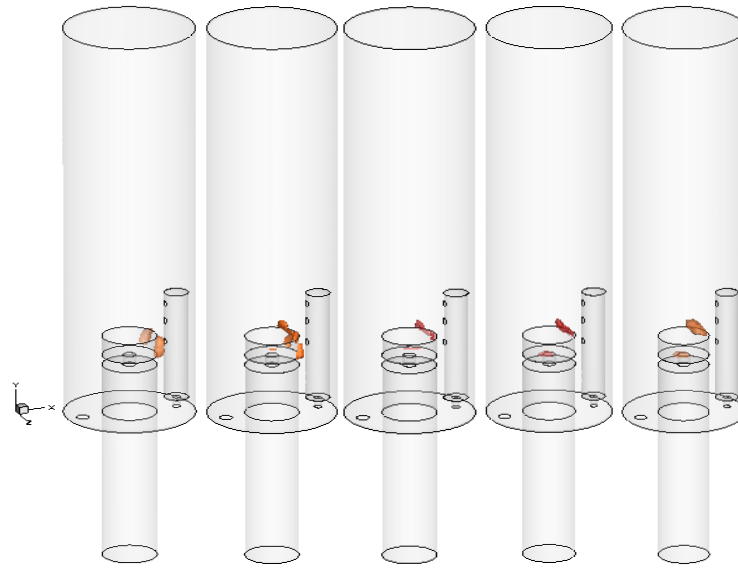


Figure 5.14: Iso-surfaces at time 0.65 s for different doubled-height cases with different

particle diameters: (a) 1220 K, (b) 1250 K, (c) 1280 K and (d) 1310 K.



(c)  $T = 1280$  K



(d)  $T = 1310$  K

Figure 5.14: Continued.

The comparison between the base cases and the double height cases in terms of the variation of peak temperature with time is shown in Figure 5.15. Up to approximately a time of 0.6s for most of the cases, it can be seen that the peak temperature inside the chamber for the double height chamber cases is higher than that of the base cases. Then, after this time the temperature of the base cases becomes higher. For the former

one, this can be attributed to the reason that more space is created when increasing the height of the chamber leads to the particles to have good mixing with the injected air and also to have a longer residence time, which supports the explanation of phenomenon (see §5.6.1) that the larger carbon particles produce high temperature than the smaller particles because their travel time is longer. Thus, when the chamber height is increased the particles of 0.5 mm travel longer inside the chamber than they do in the base case and as a result they produce higher temperature. The same trend is followed by the cases of the other particle sizes. Whereas, in the latter, it may be due to the reason that the hot gas reaches the ceiling of the chamber it quickly reverts back towards the cup in the base case in comparison with the doubled-height chamber case and, consequently, the particles are exposed to more heat in the base case than in the doubled-height case.

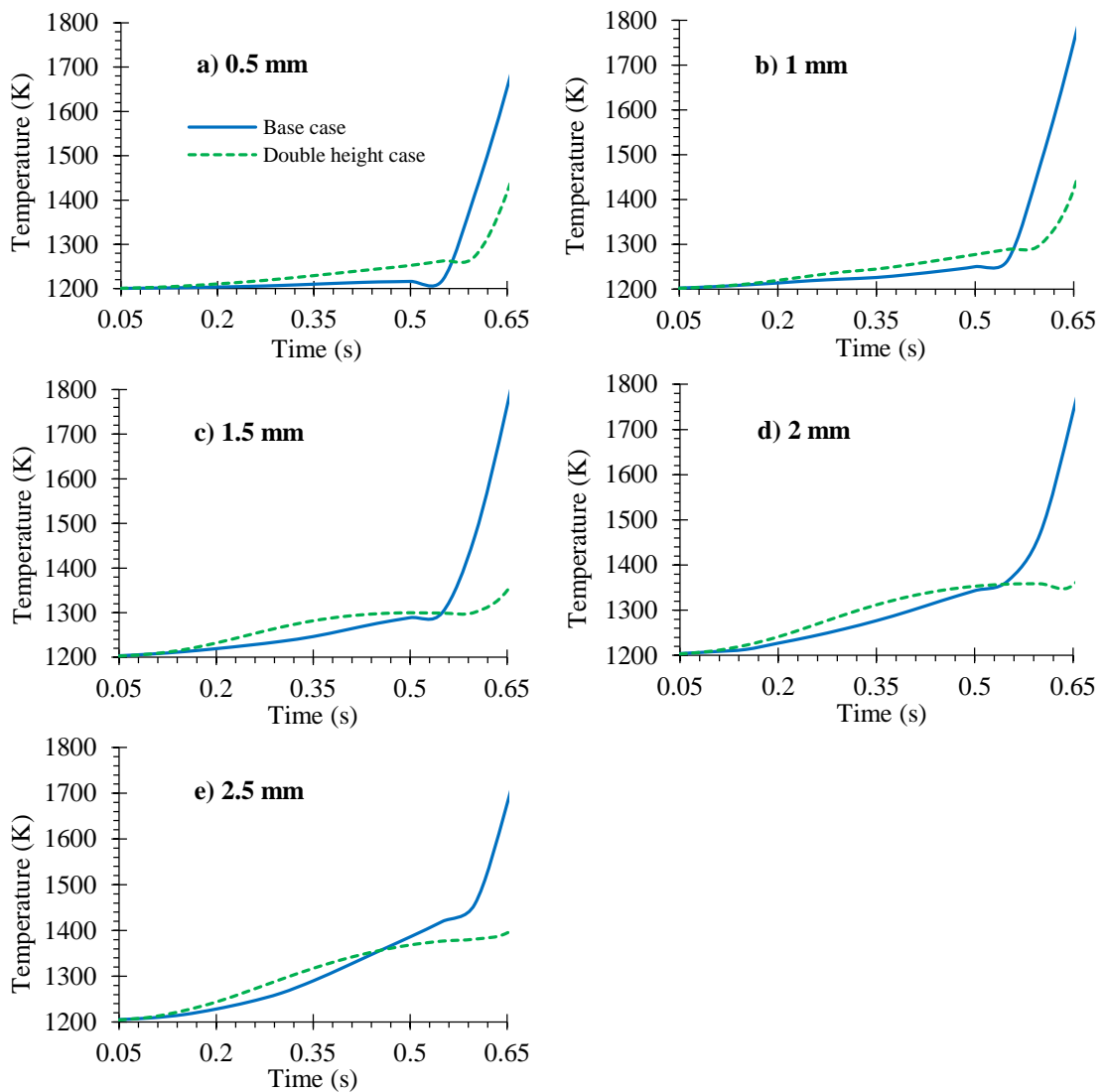


Figure 5.15: The peak temperature variation with time inside the chamber for both the base and doubled-height cases for different particle sizes: a) 0.5 mm, b) 1 mm, c) 1.5 mm, d) 2 mm and e) 2.5 mm.

## 5.7 Conclusion

Numerical simulations are an effective technology for optimizing the combustion devices. A three-dimensional modelling of the combustion of carbon particles in a small chamber has been developed. The Euler-Euler approach has been used for simulating the combustion of the particles. Simplification to the heterogeneous reaction was made and the rate of the reaction is defined in FLUENT 6.3.26 by incorporating a user-defined function (UDF). The carbon particles are assumed to be spherical and mono-sized. The results presented show that the combustion was sustained in the chamber as evidenced by the temperature distribution.

The effect of particle size was investigated and found that the temperature was affected by varying the size of the particles. Though the smaller particles have a surface/volume ratio larger than that of the larger particles and they should react more quickly, it was found that burning them produces lower temperature than burning the larger ones. This may be attributed to the reason that the smaller particles have a shorter residence time than the larger particles.

The influence of the design of the chamber on the combustion process was investigated. It was found by increasing the height of the chamber that the trend of the variation of the peak temperature with time inside the chamber is similar to that of the base case. On one hand, it was found within the period of time up to approximately 0.6 s for most of the cases that the peak temperature is higher in comparison with the base cases, which may be attributed to the better mixing between the carbon particles and the injected air as well as the longer residence time of the particles. On the other hand, after this time it was found that the peak temperature obtained from the base cases is higher, which may be due to the reason that the hot gas was reverted back towards the cup which helps to increase the temperature.

# 6 Final conclusions and recommendations for future research

The work presented in this thesis investigates different combustion scenarios using Computational Fluid Dynamics (CFD). The CFD simulations were carried out to model the combustion of methane, pulverized coal combustion, biomass coal combustion, the co-firing of coal and biomass and finally the combustion of carbon particles using the Euler-Euler approach. The findings of these simulations are summarized in § 6.1. Additionally, a number of useful recommendations for future study, summarized in § 6.2, have been made.

## 6.1 Conclusions

The combustion of different fuels was numerically investigated. The main results and conclusions of this thesis are presented below.

In chapter 3, the combustion of methane was investigated using four different simple reaction mechanisms. The results of the predicted temperature and species concentrations along both the axial and radial directions were compared with the experimental data [20] and computational results by Silva et al. [184] and Magel et al. [183]. In comparison with the experiment data, it was found that the trends of all cases are well reproduced. Despite some disagreement with the experimental data at some locations, good agreement is achieved in both quantitative and qualitative aspects. In terms of the results of the case in which a one-step reaction mechanism (M-III) and the case based on the five-step reaction mechanism (M-IV), it was found that both cases gives reasonable results when compared with the experimental data.

For the case based on the reaction mechanism (M-I) which consists of three reactions, it was observed that the results of all turbulence models show very good agreement with the experimental data in terms of temperature along the centreline in the half of the chamber close to the burner. In the direction towards the exit of the chamber the results obtained from standard  $k-\epsilon$  case are almost close to that obtained from RNG  $k-\epsilon$ . In the standard  $k-\epsilon$  case, it also observed that by modifying the turbulence model (the value of

turbulent Schmidt number ( $Sc$ ) is 0.85) the computational results were improved when comparing them with the ones of the base case (the default value of turbulent Schmidt number ( $Sc$ ) is 0.7). Even in the case in which the reaction mechanism (M-II), the modified turbulence standard  $k$ - $\epsilon$  model and the optimization of kinetic energy of reaction (r-2) also improved the results. To sum up, the numerical simulations indicate that the cases with the modified standard  $k$ - $\epsilon$  lead to generally best predictions.

In chapter 4, the pulverized combustion of both coal and biomass based on the Eulerian-Lagrangian approach was investigated. In the case of coal, the simulations were performed using two bituminous coals. The computational results of three cases with different char oxidation models, case 1 (diffusion model), case 2 (kinetics/diffusion model) and case 3 (multiple surface reaction model), were compared against the experimental data and showed very good agreement, but case 3 showed the best results. The heterogeneous reaction rates in case 3 were defined by incorporating a UDF in FLUENT.

The computational results of case 3 also show that the combustion inside the furnace was affected by the coal particles size. In comparison with the larger particles, it was shown that the volatiles from the smaller particles (e.g. 16 and 84  $\mu\text{m}$ ) are released rapidly and the temperature reached its maximum, followed by a decrease due to start of the endothermic reactions. Moreover, increasing the diameter of the coal particles reduces the coal burnout at the exit of the reactor. The burnout of the particle with a diameter of 16  $\mu\text{m}$  is 100%. Whereas, the burnout of the particles with diameters of 84, 154, 222, 291  $\mu\text{m}$  at the exit of the combustion domain is approximately 86, 75, 35, 33, 29 %, respectively.

The model of  $\text{NO}_x$  formation successfully predicts the  $\text{NO}_x$  emissions in the furnace for case 3. Optimised parametric results are found for the chemical kinetics of  $\text{NO}_x$  prediction. Different runs of simulation were performed and the  $\text{NO}$  concentration at the furnace exit was calculated and the results of run 3 gave the best combinations of parameters when compared with the experimental data.

The influence of wall temperature and the inlet secondary air velocity was investigated and found that increasing the former one enhances the gasification reactions specially the heterogeneous reaction (R5). Decreasing the latter one also enhances the gasification reactions, which is reflected on the burnout process. It can be concluded that the case with secondary inlet velocity of 11.5 m/s shows better burnout of the coal



particles than the base case (15.5 m/s) does. The decrease in the inlet velocity of the secondary air enhanced the burnout of the coal particle by making the particles to stay longer inside the furnace during their journey towards the exit of the furnace. The influence of the above mentioned parameters on the formation of NO was also observed. Increasing wall temperature increases NO concentration. Regarding the effects of the secondary air rate, when compared with the base case (15.5 m/s), it was found that NO concentration increases whether the secondary air inlet velocity is increased or decreased. For the latter case (11.5 and 13.5 m/s), it was found that the slopes of the curves become more steeper in comparison with the base case and therefore, the concentration of NO decreases along the axial direction towards the exit of the furnace.

The combustion of pulverized biomass, represented by straw, was investigated by assuming that the particle size distribution of straw particles is the same as that of coal particles. The same combustion model of pulverized coal (case 3) was applied and two simulations with different devolatilization kinetics were carried out. It was found that the temperature distribution when burning straw particles is nearly the same as that obtained from burning coal (case 3). This is attributed to that the straw particles are completely burned out when compared with the coal particles, which show that increasing the size of the particle results in reducing its burnout. In terms of NO<sub>x</sub> formation, it was also observed that burning saw particles produces less NO with 20 and 26% for case I and Case II respectively.

The cofiring of the coal and straw was investigated. The co-fired biomass fractions used on mass basis are 10, 20, 30 and 40%. It was found that the co-combustion of pulverized particles of coal and straw enhances the burnout of the coal particles and as a result the gas temperature inside the furnace increases. The temperature increased by 8, 6.7, 6.3 and 5%, respectively, when compared with coal (case 3). The burnout of the coal particles with sizes of 84, 154 and 222  $\mu\text{m}$  is remarkably increased. The burnout of the other two particles (291 and 360  $\mu\text{m}$ ) do not show a great change except for the case of 40% straw, which show a reasonable increase in burnout in terms of the coal particle with the size of 291  $\mu\text{m}$ .

In chapter 5, an attempt to investigate the heterogeneous combustion of carbon particles was made using the Euler-Euler approach. Simplification to the heterogeneous reaction was made and the rate of the reaction is defined in FLUENT 6.3.26 by incorporating a user-defined function (UDF). In this investigation, no comparison between the

predicted results and experimental data is possible. However, the present computational results show that the combustion was sustained in the chamber as evidenced by the temperature distribution. Therefore, this investigation can be considered as a basic step towards a more detailed study later. The effect of particle size was investigated and found that the temperature was affected by varying the size of the particles. The influence of the design of the chamber on the combustion process was investigated. By increasing the height of the chamber it was found within the period of time up to approximately 0.6 s for most of the cases (different particle sizes) that the peak temperature is higher in comparison with the base cases, which can be attributed to the better mixing between the carbon particles and the injected air. On the other hand, after this time it was found that the peak temperature obtained from the base cases is higher, which may be due to the reason that the hot gas was reverted back towards the cup which helps to increase the temperature.

## 6.2 Recommendations for future research

The field of combustion is complex and the investigations presented in the present research have been made as a step for better understanding the features of the combustion processes and provided an opportunity for further developments, which will lead to creating new insights into it. Therefore, a list of recommendations for further work to improve the models is summarized as following:

For the case of combustion of methane

- A further step is to consider modelling the turbulence with a better turbulent model such as large eddy simulation (LES) model, which can resolve the turbulence field better and give more detailed description of the eddy structure of the turbulent flames.
- Only the FR/ED model has been used for the turbulence-chemistry interaction. Thus, the computational results of the case of the five- step reaction mechanism (M-IV) are going to be evaluated by using the eddy-dissipation concept model (EDC).
- The intention for future work is to use the same modified standard  $k-\epsilon$  in modelling combustion cases other than the one presented in this work to see how it works.

For the case of pulverized combustion

- For simplicity in present work, the volatiles were treated as one species and its combustion in the gas phase was based on one reaction. Therefore, the species released during devolatilization process include many species that their reactions should be considered when modelling the gas phase to obtain more comprehensive results. In addition, the impact of ash on the combustion process as well as the combustion of tar should be investigated.
- Attention should be paid to the kinetics of the devolatilization process and biomass fuels other than straw should be investigated. In addition, further work could be done to investigate influence of the shape of the particles, which was assumed to be spherical in the present work.

For the case of Euler-Euler approach model

- Experimental work is required to compare the computational results with before any final conclusions about the validity of the model can be made and more attention to the boundary conditions should be paid.
- Extending the model to capture the combustion features of, for example coal particles, therefore, incorporating more reactions is required including the devolatilization process.

# References

- [1] A. A. Khan, W. D. Jung, P. J. Janssen, and H. Spliethoff, "Biomass combustion in fluidized bed boilers : Potentials, problems and remedies". *Fuel Processing Technology*. 2009, (90), 21-50.
- [2] M. M. Hoodwink, A. P. C. Fail, R. V. D. Broke, G. Bends, D. Gisele, and W. C. Turkenburg, "Exploration of the ranges of the global potential of biomass for energy". *Biomass and Bioenergy*. 2003, 119-133.
- [3] "BP reports: The Energy Roadmap - Setting the Direction for 21st Century Energy", <http://www.bp.com>.
- [4] World Energy Council, "World energy resources: Survey", 2013, <http://www.worldenergy.org/>.
- [5] H. S. Johnston, "Atmospheric ozone". *Annual Review of Physical Chemistry*. 1992, (43), 1-31.
- [6] R. D. Boardman, and L. D. Smoot, "Pollutant formation and control". In: L. D. Smoot(Editor). *Fundamentals of coal combustion for clean and efficient use*. Elsevier, Amsterdam, 1993, p433.
- [7] T. M. Lenton, and N. E. Vaughan, "The radiative forcing potential of different climate geoengineering options". *Atmospheric Chemistry and Physics Discussions*. 2009, (9), 2559-2608.
- [8] I. B. Fridleifsson, "Geothermal energy for the benefit of the people". *Renew. Sustain. Energy Rev*. 2001:5, 299-312.
- [9] European Renewable Energy Council (EREC), "Renewable energy scenario by 2040", Brussels, Belgium, 2006.
- [10] International Energy Agency, "World Energy Outlook", Paris, France, 2013.
- [11] European Renewable Energy Council (EREC), Brussels, Belgium, 2011.
- [12] D. L. Klass, "Biomass for renewable energy, fuels and chemicals". Academic Press, 1998.
- [13] V. K. Vera, S. Bram, F. Deleting, P. Lama, I. Vandendael, A. Hubin, and J. De Ruyck, "Agro-pellets for domestic heating boilers: Standard laboratory and real life performance". *Applied Energy*. 2011, 1-8.
- [14] J. Tissari, O. Sippula, J. Kouki, K. Vuorio, and J. Jokiniemi., "Fine particle and gas emissions from the combustion of agricultural fuels fired in a 20 kW burner". *Energy and Fuels*. 2008, (22), 2033-2044.
- [15] T. Nussbaumer, "Biomass combustion in Europe, overview on technologies and regulations. Report prepared for NYSERDA, April", 2008.
- [16] P. Pasu, "Biomass Gasification and Pysolysis: Practical Design and Theory". Elsevier Inc., 2010.
- [17] H. Lu, E. Ip, J. Scott, P. Foster, M. Vickers, and L. Baxter, "Effects of particle shape and size on devolatilization of biomass particle". *Fuel*. 2010, (89):5, 1156-1168.
- [18] H. K. Versteeg, and W. Malalasekera, "An introduction to computational fluid dynamics: the finite volume method". Pearson Education 2<sup>nd</sup> edition, 2007.
- [19] Y. Wang, and L. Yan, "CFD studies on biomass thermochemical conversion". *Int. J. Mol. Sci*. 2008, (9), 1108-1130.
- [20] D. Garréton, and O. Simonin, "First aerodynamics of steady state combustion chambers and furnaces workshop", EDF-DER, Chaton, 1994.
- [21] R. H Hurt, "Structure, properties and reactivity of solid fuels". In: 27<sup>th</sup> Symp. (Int.) on Combustion, The Combustion Institute, 1998, pp.2887-2904.
- [22] K. L. Smith, and L. D. Smoot, "Characteristics of commonly-used U.S. coals - towards a set of standard research coals". *Prog. Energy Combust. Sci*. 1990, (16), 1-53.

- [23] B. M. Jenkins, R. R. Bakker, and J. B. Wei, "On the properties of washed straw". *Biomass and Bioenergy*. 1996, (10):4, 177-200.
- [24] B. M. Jenkins, L. L. Baxter, T. R. Miles Jr, and T. R. Miles, "Combustion properties of biomass". *Fuel Processing Technology*. 1998, (54), 17-46.
- [25] D. W. Van Krevelen, "Coal: Typology - Chemistry - Physics - Constitution". Elsevier, Amsterdam, 3, 1993.
- [26] S. Van Loo, and J. Koppejan, "The handbook of biomass combustion and co-firing". Earthscan, London, 2008.
- [27] B. Miller, and D. Tillman, "Combustion engineering issues for solid fuel systems". Academic Press, 2008.
- [28] J. S. Tumuluru, S. Sokhansanj, C. T. Wright, R. D. Boardman, and N. A. Yancey, "A review on biomass classification and composition, co-firing issues and pretreatment methods". *Proceedings of the 2011 ASABE annual meeting*. 2011,
- [29] D. A. Bell, B. F. Towler, and M. Fan, "Coal gasification and its application". Elsevier Inc, 1<sup>st</sup> edition, 2011.
- [30] A. Williams, M. Pourkashanian, J. M. Jones, and N. Skorupska, "Combustion and gasification of coal". Taylor & Francis, New York, 2000.
- [31] Waterhouse, "GWC Coal Handbook". George Waterhouse Consultants, Ltd, Tallington, UK, 1994.
- [32] P. Averit, "Coal resources of the United States.", U.S. Geological Survey, 1975.
- [33] R. P. Hensel, "Coal: classification, chemistry and combustion, Coal-fired industrial boilers workshop". Raleigh, NC, USA, 1981.
- [34] American Society for Testing and Materials, "Annual book of ASTM standards 2006". Volume 5 part 6, Gaseous fuels; Coal and Coke.
- [35] European Parliament and the Council, "Directive 2001/77/EG", Brussels, 2001.
- [36] I. Campbell, "Biomass catalysts and liquid fuels". Lancaster: Technomic Publishing Co. Inc., 1983.
- [37] C. Hignan, and M. van der Burgt, "Gasification". Elsevier Inc., 2003.
- [38] O. Theander, "Cellulose, hemicellulose and extractives". In: R. P. Overend, T. A. Milne and L. K. Mudge (editors). *Fundamentals of biomass thermochemical conversion*. Elsevier, London, 1985,
- [39] P. Mckendry, "Energy from biomass (part1): overview of biomass". *Bioresources Technology*. 2002, (83), 37-46.
- [40] A. Demirbas, "Calculation of higher values of biomass fuels". *Fuel*. 1997, (76):5, 431-434.
- [41] D. Mohan, U. Charles, J. Pittman, and P. H. Steele, "Pyrolysis of wood / biomass for bio-oil: a critical review". *Energy and Fuels*. 2006, (20), 848-889.
- [42] S. V. Vassilev, D. Baxter, L. K. Andersen, and C. G. Vassileva, "An overview of the chemical composition of biomass". *Fuel*. 2010, (89):5, 913-933.
- [43] A. Demirbas, "Combustion characteristics of different biomass fuels". *Prog. Energy Combust. Sci.* 2003, (30), 219-230.
- [44] A. Demirbas, "Potential applications of renewable energy sources, biomass combustion problems in boiler power systems and combustion related environmental issues". *Prog. Energy Combust. Sci.* 2005, (31), 171-192.
- [45] R. H. Essenhigh, "Combustion and flame propagation in coal systems". In: 16<sup>th</sup> Symp. (Int.) on Combustion, The Combustion Institute, Pittsburgh, 1977,
- [46] H. Lu, and L. Baxter, "Biomass combustion characteristics and implications for renewable energy". In: P. Grammelis (editor). *Solid biofuels for energy: a lower greenhouse gas alternative*. Springer, 2011, pp.95-121.
- [47] M. J. Antal, and M. Gronli, "The art, science, and technology of charcoal production". *Ind. Eng. Chem. Res.* 2003, (42):8, 1619-1640.

- [48] W. Zhao, Z. Li, G. Zhao, F. Zhang, and Q. Zhu, "Effect of air preheating and fuel moisture on combustion characteristic of corn straw in a fixed bed". *Energy conversion and management*. 2008, (49), 3560-3565.
- [49] P. Quaak, H. Knoef, and H. Stassen, "Energy from biomass: a review of combustion and gasification technologies". The World Bank, U.S.A, 1999.
- [50] D. C. Dayton, B. M. Jenkins, S. Q. Turn, R. R. Bakker, R. B. Williams, D. Belle-Oudry, and L. M. Hill, "Release of inorganic constituents from leached biomass during thermal conversion". *Energy and Fuels*. 1999, (13), 860-870.
- [51] H. Lu, W. Robert, G. Peirce, B. Ripa, and L. Baxter, "Comprehensive study of biomass particle combustion". *Energy and Fuels*. 2008, (22), 2826-2839.
- [52] T. G. Bridgeman, L. I. Darvel, J. M. Jones, P. T. Williams, R. Fahmi, A. V. Bridgewater, T. Barraclough, I. Shield, N. Yates, S. C. Thain, and I. S. Donnison, "Influence of particle size on the analytical and chemical properties of two energy crops". *Fuel*. 2003, (86), 37-46.
- [53] L. Baxter, "Biomass-coal co-combustion: opportunity for affordable renewable energy". *Fuel*. 2005, (84), 1295-1302.
- [54] A. Bharadwaj, L. Baxter, and A. L. Robinson, "Effects of intraparticle heat and mass transfer on biomass devolatilization: Experimental results and model predictions". *Energy and Fuels*. 2004, (18), 1021-1031.
- [55] K. R. G. Hein, and J. M. Bemtgen, "EU clean coal technology: co-combustion of coal and biomass". *Fuel Processing Technology*. 1998, (54), 159-169.
- [56] K. Savolainen, "Co-firing of biomass in coal-fired utility boilers". *Applied Energy*. 2003, (74), 369-381.
- [57] M. C. Freeman, W. J. O'Dowd, T. D. Brown, R. A. Hargis Jr., R. A. James, S. I. Plasynski, G. F. Walbert, A. F. Lowe, and J. J. Battista Jr., "Pilot-scale air toxics R&D assessment of creosote-treated and PCP-treated wood cofiring for pulverized coal utility boiler applications". *Biomass and Bioenergy*. 2000, (19), 447-456.
- [58] L. S. Esteban, and J. E. Carrasco, "Evaluation of different strategies for pulverization of forest biomasses". *Powder Technology*. 2006, (166), 139-151.
- [59] N. Duffy, "Investigation of biomass combustion in grate furnaces using CFD". PhD thesis, National University of Ireland, Galway, 2007.
- [60] D. M. Kammen, and D. J. Lew, "Review of technologies for the production and use of charcoal", National Renewable Energy Laboratory, Golden, Colorado, USA, 2005.
- [61] C. Di Blasi, "Combustion and gasification rates of lignocellulosic chars". *Prog. Energy Combust. Sci.* 2009, (35):2, 121-140.
- [62] B. S. Brewster, L. Baxter, and L. D. Smoot, "Treatment of coal devolatilization in comprehensive combustion modeling". *Energy and Fuels*. 1988, (2), 362-370.
- [63] P. R. Solomon, T. H. Fletcher, and R. J. Pugmire, "Progress in coal pyrolysis". *Fuel*. 1993, (72):5, 587-597.
- [64] M. L. de Souza-Santos, "Comprehensive modelling and simulation of fluidized bed boilers and gasifiers". *Fuel*. 1989, (89), 1507-1521
- [65] J. Yu, J. A. Lucas, and T. F. Wall, "Formation of the structure of chars during devolatilization of pulverized coal and its thermoproperties: a review". *Prog. Energy Combust. Sci.* 2007, (33), 135-170.
- [66] R. C. Borah, P. Ghosh, and P. G. Rao, "A review on devolatilization of coal in fluidized bed". *International Journal Of Energy Research*. 2011, (35), 929-963.
- [67] Y. B. Yang, H. Yamauchi, J. Nasserzade, and J. Swithenbank, "Effects of fuel devolatilisation on the combustion of wood chips and incineration of simulated municipal solid wastes in a packed bed". *Fuel*. 2003, (82), 2205-2221.

- [68] T. Jurena, and J. Hajek, "Energy considerations in CFD modelling of biomass combustion in an experimental fixed-bed reactor". *Chem Eng Trans.* 2011, (25), 803-808.
- [69] K. L. Smith, "The structure and reaction processes of coal". Plenum Press, New York, USA, 1994.
- [70] J. D. Freihaut, M. F. Zabielski, and D. J. Seery, "A parametric investigation of tar release in coal devolatilization.". In: 19<sup>th</sup> Symp. (Int.) on Combustion, The Combustion Institute, 1982, pp.1159-1167.
- [71] P. R. Solomon, M. A. Serio, and E. M. Suuberg, "Coal pyrolysis: Experiments, kinetic rates and mechanisms". *Prog. Energy Combust. Sci.* 1992, (18), 133-220.
- [72] J. Yu, J. A. Lucas, and T. F. Wall, "Formation of the structure of chars during devolatilization of pulverized coal and its thermoproperties: a review". *Prog. Energy Combust. Sci.* 2007, (33), 135-170.
- [73] C. D. Sheng, and J. L. T. Azevedo, "Modeling biomass devolatilization using the chemical percolation devolatilization model for the main components". *Proceedings of the Combustion Institute.* 2003, 29: pp.407-414.
- [74] J. Werther, M. Saenger, E. U. Hartge, T. Ogada, and Z. Siagi, "Combustion of agricultural residues". *Prog. Energy Combust. Sci.* 2000, (26), 1-27.
- [75] R. Bassilakis, R.M. Carangelo, and M.A. Wójtowicz, "TG-FTIR analysis of biomass pyrolysis". *Fuel.* 2001, (80):12, 1765–1786.
- [76] J. M. Jones, M. Pourkashanian, A. Williams, and D. Hainsworth, "A comprehensive biomass combustion model". *Renewable Energy.* 2000, (19), 229-234.
- [77] J. J. Manyà, E. Velo, and L. Puigjaner, "Kinetics of biomass pyrolysis: a reformulated three-parallel-reactions model". *Ind. Eng. Chem. Res.* 2003, (42), 434-441.
- [78] P. T. Williams, and S. Besler, "The influence of temperature and heating rate on the slow pyrolysis of biomass". *Renewable Energy.* 1996, (7):3, 233–250.
- [79] G. M. Kimber, and M. D. Gary, "Rapid devolatilization of small coal particles". *Combust. Flame.* 1967, (11), 360-362.
- [80] H. Yeasmin, J. F. Mathews, and S. Ouyang, "Rapid devolatilization of Yallourn brown coal at high pressures and temperatures". *Fuel.* 1998, (78), 11-24.
- [81] A. S. Jamaluddin, J. S. Truelove, and T. F. Wall, "Devolatilization of bituminous coals at medium to high heating rates". *Combust. Flame.* 1986, (63), 329-337.
- [82] G. Maschio, C. Koufopoulos, and A. Lucchesi, "Pyrolysis, a promising route for biomass utilization". *Bioresource Technology.* 1992, (42):3, 219-231.
- [83] M. V. Gil, D. Casal, C. Pevida, J. J. Pis, and F. Rubiera, "Thermal behaviour and kinetics of coal/biomass blends during co-combustion". *Bioresource Technology.* 2010:101, 5601-5608.
- [84] Y. B. Yang, C. Ryu, A. Khor, N. E. Yates, V. N. Sharifi, and J. Swithenbank, "Effect of fuel properties on biomass combustion. Part II. Modelling approach--identification of the controlling factors". *Fuel.* 2005, (84), 2116-2130.
- [85] C. Ryu, Y. B. YANG, A. Khor, N. E. Yates, V. N. Sharifi, and J. Swithenbank, "Effect of fuel properties on biomass combustion: part I. experiments-fuel type, equivalence ratio and particle size". *Fuel.* 2006, (85), 1039-1046.
- [86] C. Di Blasi, "Kinetics and heat transfer control in the slow and flash pyrolysis of solids". *Ind. Eng. Chem. Res.* 1996, (35), 37-46.
- [87] Y. B. Yang, V. N. Sharifi, J. Swithenbank, L. Ma, L. I. Darvell, J. M. Jones, M. Pourkashanian, and A. Williams, "Combustion of a single particle of biomass". *Energy and Fuels.* 2008, (22), 306-316.
- [88] J. Blondeau, and H. Jeanmart, "Biomass pyrolysis in pulverized-fuel boilers: Derivation of apparent kinetic parameters for inclusion in CFD codes". *Proc. Combust. Inst.* 2011, 3: 2 pp.1787-1794.

- [89] S. Jiménez, P. Remacha, J. C. Ballesteros, A. Giménez, and J. Ballester, "Kinetics of devolatilization and oxidation of a pulverized biomass in an entrained flow reactor under realistic combustion conditions". *Combust. Flame*. 2008, (152), 588-603.
- [90] D. K. Shen, S. Gu, K. H. Luo, A. V. Bridgewater, and M. X. Fang, "Kinetic study on thermal decomposition of woods in oxidative environment". *Fuel*. 2009, (88), 1024-1030.
- [91] M. L. de Souza-Santos, "Solid fuels combustion and gasification: modeling, simulation, and equipment operation". Marcel Dekker, Inc., New York, 2004.
- [92] D. B. Anthony, and J. B. Howard, "Coal devolatilization and hydrogasification". *A.I.Ch.E. Journal*. 1976, (22), 625-656.
- [93] E. Biagini, F. Lippi, L. Petarca, and L. Tognotti, "Devolatilization rate of biomasses and coal-biomass blends: an experimental investigation". *Fuel*. 2002, (81), 1041-1051.
- [94] S. C. Saxena, "Devolatilization and combustion characteristics of coal particles". *Prog. Energy Combust. Sci.* 1990, (16):1, 55-94.
- [95] P.R. Solomon, M.A. Serio, and E.M. Suuberg, "Coal pyrolysis: Experiments, kinetic rates and mechanisms". *Prog. Energy Combust. Sci.* 1992, (18), 133-220.
- [96] C. Di Blasi, "Influences of physical properties on biomass devolatilization characteristics". *Fuel*. 1997, (76), 957-964.
- [97] C. Di Blasi, "Modeling chemical and physical processes of wood and biomass pyrolysis". *Prog. Energy Combust. Sci.* 2008, (34), 47-90.
- [98] S. Yaman, "Pyrolysis of biomass to produce fuels and chemical feedstocks". *Energy conversion and management*. 2004, (45), 651-671.
- [99] H. Kobayashi, J. B. Howard, and A. F. Sarofim, "Coal devolatilization at high temperatures". In: 16<sup>th</sup> Symp. (Int.) on Combustion, The Combustion Institute, Pittsburgh, 1977, 16: 1 pp.411-425.
- [100] W. C. Park, A. Atreya, and H. R. Baum, "Experimental and theoretical investigation of heat and mass transfer process during wood pyrolysis". *Combust. Flame*. 2010, (157), 481-494.
- [101] M. J. G. Alonso, A. G. Borrego, D. Alvarez, and R. Menéndez, "Pyrolysis behaviour of pulverized coals at different temperatures". *Fuel*. 1999, (78), 1501-1513.
- [102] A. Demirbas, "Biorefineries: current activities and future developments". *Energy conversion and management*. 2009, (50), 2782-2801.
- [103] C. Di Blasi, F. Buonanno, and C. Branca, "Reactivities of some biomass chars in air". *Carbon*. 1999, (37), 1227-1238.
- [104] O. Karlström, A. Brink, E. Biagini, M. hupa, and L. Tognotti, "Comparing reaction orders of anthracite chars with bituminous coal chars at high temperature oxidation conditions". *Proc. Combust. Ins.* 2013, 34: pp.2427-2434.
- [105] N. M. Laurendeau, "Heterogeneous kinetics of coal char gasification and combustion". *Prog. Energy Combust. Sci.* 1978, (4), 221-270.
- [106] R. H. Essenhigh, M. K. Misra, and D.W. Shaw, "Ignition of coal particles: A review". *Combust. Flame*. 1989, (77):1, 3-30.
- [107] R. K. Rathnam, L. K. Elliott, T. F. Wall, Y. Liu, and B. Moghtaderi, "Differences in reactivity of pulverised coal in air (O<sub>2</sub>/N<sub>2</sub>) and oxy-fuel (O<sub>2</sub>/CO<sub>2</sub>) conditions". *Fuel Processing Technology*. 2009, (90), 797-802.
- [108] R. H. Essenhigh, and A. M. Mescher, "Influence of pressure on the combustion rate of carbon". In: 26<sup>th</sup> Symp. (Int.) on Combustion, The Combustion Institute, Pittsburgh, 1999, pp.3085-3094.
- [109] P. L. Walker, F. Rusinko, and L. G. Austin, "Gas reactions of carbon". *Advances in Catalysis*. 1959, (11), 133-221.
- [110] A. Ismail H. Osman, "Numerical analysis of single-particle combustion of coal char", Singapore, 2011.



- [111] M. F. Mulcahy, and I. W. Smith, "Kinetics of combustion of pulverized fuel: a review of theory and experiment". *Reviews in Pure and Applied Chemistry*. 1969, (19):1, 81-108.
- [112] D. Gary, J. G. Cogoli, and R. H. Essenhigh, "Problems in pulverized coal and char combustion". *Advances in Chemistry*. 1974, (131), 72-91.
- [113] K. Yamamoto, "Biomass power generation by CFB boiler", NKK technical review, Japan, 2001.
- [114] I. Obernberger, "Reached development of biomass combustion technologies and future outlook". In: 17<sup>th</sup> European biomass conference, Hamburg, Germany, 2009,
- [115] H. Spliethoff, "Power generation from solid fuels". Springer Heidelberg Dordrecht, London, New York, 2010.
- [116] R. P. van der Lans, L. T. Pedersen, A. Jensen, P. Glarborg, and K. Dam-Johansen, "Modelling and experiments of straw combustion in grate furnace". *Biomass and Bioenergy*. 2000, (19):10, 199-208.
- [117] H. Makino, and H. Matsuda, "Improvement of pulverized coal combustion technology for power generation". *CRIEPI Review*. 2002, (46),
- [118] A. Gómez-Barea, and B. Leckner, "Modelling of biomass gasification in fluidized bed". *Prog. Energy Combust. Sci.* 2010, (36), 444-509.
- [119] D. Kunii, and O. Levenspiel, "Fluidization Engineering". Butterworth-Heinemann, 2<sup>nd</sup> edition, 1991.
- [120] R. H. Essenhigh, "Fundamentals of coal combustion". In: M. A. Elliott (editor). *Chemistry of coal utilization*. Wiley- Interscience, New York, pp.1153-1312.
- [121] L. D. Smoot, and D. T. Pratt, "Pulverized-coal combustion and gasification: theory and applications for continuous flow processes". Plenum Press, New York, 1979.
- [122] A. van der Drift, H. Boerrigter, B. Coda, M. K. Cieplik, and K. Hemmes, "Entrained flow gasification of biomass: ash behaviour, feeding issues and system analyses", ECN-C-04-039, 2004.
- [123] K. M. Bryden, and M. J. Hagge, "Modelling the combined impact of moisture and char shrinkage on the pyrolysis of a biomass particle". *Fuel*. 2003, (82), 1633-1644.
- [124] S. P. Shi, S. E. Zitney, M. Shahnam, M. Syamlal, and W. A. Rogers, "Modelling coal gasification with CFD and discrete phase method". *Journal of the Energy Institute*. 2006, (79):4, 217-221.
- [125] K. M. Bryden, K. W. Ragland, and C. J. Rutland, "Modelling thermally thick pyrolysis of wood". *Biomass and Bioenergy*. 2002, (22), 41-53.
- [126] D. M. Grant, R. J. Pugmire, T. H. Fletcher, and A. R. Kerstein, "Chemical model of coal devolatilization using percolation lattice statistics". *Energy and Fuels*. 1989, (3), 175-186.
- [127] M. M. Baum, and P. J. Street, "Predicting the combustion behavior of coal particles". *Combustion Science and Technologies*. 1971, (3):(5), 231-243.
- [128] S. Badzioch, and P. G. W. Hawksley, "Kinetics of thermal decomposition of pulverized coal particles". *Ind. Eng. Chem. Process Des. Dev.* 1970, (9):4, 521-530.
- [129] P. R. Solomon, D. G. Hamblen, R. M. Carangelo, M. A. Serio, and G. V. Deshpande, "General model of coal devolatilization". *Energy and Fuels*. 1988, (2):4, 405-422.
- [130] S. Niksa, and A. R. Kerstein, "FLASHCHAIN theory for rapid coal devolatilization kinetics. 1. Formulation". *Energy and fuels*. 1991, (5), 647-665.
- [131] B. Moghtaderi, "The state-of-the-art in pyrolysis modelling of lignocelluloseic solid fuels". *Fire and Materials*. 2006, (30):1, 1-34.
- [132] C. Di Blasi, "Modelling and simulation of combustion processes of charring and non-charring solid fuels". *Prog. Energy Combust. Sci.* 1993, (19), 71-104.

- [133] M. A. Field, "Rate of combustion of size-graded fractions of char from a low rank coal between 1200K-2000K". *Combust. Flame*. 1969, (13), 237-252.
- [134] A. Williams, M. Pourkashanian, and J.M. Jones, "The combustion of coal and some other solid fuels". In: 28<sup>th</sup> Symp. (Int.) on Combustion, The Combustion Institute, 2000, pp.2141-2162.
- [135] I. W. Smith, "The combustion rates of coal chars: a review". In: 19<sup>th</sup> Symp. (Int.) on Combustion, The Combustion Institute, 1982, pp.1045-1065.
- [136] J. Warantz, U. Maas, and R. W. Dibble, "Combustion: physical and chemical fundamentals, modeling and simulation, experiments, pollutant formation". Springer, Verlag Berlin Heidelberg, 3<sup>rd</sup> Edition, 2001.
- [137] R. W. Bilger, and R. E. Beck, "Turbulent diffusion flames". *Ann. Rev. Fluid Mech.* 1989:21, 101-135.
- [138] R. W. Bilger, "Future progress in turbulent combustion research". *Prog. Energy Combust. Sci.* 2000, (26), 367-380.
- [139] N. Peters, "Turbulent Combustion". Cambridge Press, 2000.
- [140] D. Veynante, and L. Vervisch, "Turbulent Combustion Modeling". *Prog. Energy Combust. Sci.* 2002, (28), 193-266.
- [141] J. Warnatz, U. Maas, and R. W. Dibble, "Combustion: Physical and Chemical Fundamentals, Modeling and Simulations, Experiments, Pollutant Formation". Springer-Verlag, Berlin Heidelberg, 3<sup>rd</sup> edition, 2001.
- [142] B. F. Magnussen, and B. H. Hjertageer, "On mathematical modelling of turbulent combustion with special emphasis on soot formation and combustion". In: 16<sup>th</sup> Symp. (Int.) on Combustion, The combustion Institute, 1976, pp.719-729.
- [143] B. F. Magnussen, "On the structure of turbulence and a generalized eddy-Dissipation concept for chemical reaction in turbulent flow", Nineteeth AIAA Meeting, St. Louis, 1981.
- [144] J. O. Hirschfelder, C. F. Curtiss, and R. B. Bird, "Molecular theory of gases and liquids". John Wiley & Sons, New York, 2<sup>nd</sup> edition, 1964.
- [145] K. K. Kuo, "Principles of Combustion". John Wiley & Sons, New York, 1986.
- [146] J. R. Howell, and R. O. Buckius, "Fundamentals of engineering thermodynamics". McGraw-Hill, Inc., 1992.
- [147] L. Vervisch, and T. Poinso, "Direct numerical simulation of non-premixed turbulent flames". *Ann. Rev. Fluid Mech.* 1998, (30), 655-691.
- [148] P. Moin, "Progress in large eddy simulation of turbulent flows". AIAA Technical report. 1997, 97-0749.
- [149] M. Lesieur, and O. Metais, "New trends in large-eddy simulations of turbulence". *Ann. Rev. Fluid Mech.* 1996, (28), 45-82.
- [150] T. J. Coakley, "Turbulence modeling methods for the compressible Navier-Stokes equations". In: 16<sup>th</sup> AIAA fluid and plasma dynamics conference, Danvers, MA, 1983,
- [151] S. Peng, L. Davidson, and S. Holmberg, "A modified low-reynolds number  $k-\omega$  model for recirculating flows". *Journal of Fluids Engineering*. 1997, (119):4, 867-875.
- [152] S. Zeierman, and M. Wolfshtein, "Turbulent time scale for turbulent flow calculations". *AIAA Journal*. 1986, (24):10, 1606-1610.
- [153] B. E. Launder, and D. B. Spalding, "Lectures in Mathematical Models of Turbulence". Academic Press, London, England, 1972.
- [154] D. C. Wilcox, "Turbulence Modeling for CFD". DCW Industries, Inc., La Canada, California, 1998.
- [155] V. Yakhot, and S. A. Orszag, "Renormalization Group Analysis of Turbulence: I. Basic Theory". *Journal of Scientific Computing*. 1986, (1):1, 1-51.

- [156] T. H. Shih, W. W. Liou, A. Shabbir, Z. Yang, and J. Zhu, "A new  $k-\epsilon$  eddy-viscosity model for high reynolds number turbulent flows - model development and validation". *Computers Fluids*. 1995, (24):3, 227-238.
- [157] J. O. Hinze, "Turbulence". McGraw-Hill Publishing Co., New York, 1975.
- [158] "FLUENT 6.3 User's Guide. Fluent Inc., Lebanon, NH, USA", 2006.
- [159] A. J. Corin, "Numerical solution of Navier-Stokes equations". *Mathematics of Computation*. 1968, (22), 745-762.
- [160] P. Cheng, "Two-dimensional radiating gas flow by a moment method". *AIAA Journal*. 1964, (2), 1662-1664.
- [161] R. Siegel, and J. R. Howell, "Thermal Radiation Heat Transfer". Hemisphere Publishing Corporation, Washington DC, 1992.
- [162] M. G. Carvalho, T. Farias, and P. Fontes, "Predicting radiative heat transfer in absorbing, emitting, and scattering media using the discrete transfer method". In: W. A. Fiveland et al. (editor). *Fundamentals of Radiation Heat Transfer*. Volume 160, ASME HTD, 1991, pp.17-26.
- [163] E. H. Chui, and G. D. Raithby, "Computation of radiant heat transfer on a non-orthogonal mesh using the finite-volume method". *Numerical Heat Transfer, Part B*. 1993, (23), 269-288.
- [164] G. D. Raithby, and E. H. Chui, "A finite volume method for predicting a radiant heat transfer in enclosures with participating media". *Journal of Heat Transfer*. 1990, (112), 415-423.
- [165] C. K. Westbrook, and F. L. Dryer, "Simplified reaction mechanisms for the oxidation of hydrocarbon fuels in flames". *Combustion Science and Technologies*. (27), 31-43.
- [166] W. P. Jones, and R. P. Lindstedt, "Global reaction schemes for hydrocarbon combustion". *Combust. Flame*. 1988, (73), 233-249.
- [167] D. G. Nicol, P. C. Malte, A. J. Hamaer, R. J. Roby, and R. C. Steele, "Development of a five-step globale methane oxidation-NO formation mechanism for lean premixed gas turbine combustion". *J. Eng. Gas Turbine Power*. 1999, (121), 272-280.
- [168] P. Glarborg, J. A. Miller, and R. J. Kee, "Kinetic modeling and sensitivity analysis of nitrogen oxide formation in well-stirred reactors". *Combust. Flame*. 1986, (65), 177-202.
- [169] J. A. Miller, and C.T. Bowman, "Mechanism and modeling of nitrogen chemistry in combustion". *Prog. Energy Combust. Sci*. 1989, (15), 287-338.
- [170] J. Warnatz, and Maas U, "Technische Verbrennung". Springer Verlag, New York, 1993.
- [171] M. Frenklach, H. Wang, C. T. Bowman, R. K. Hanson, G. P. Smith, D. M. Golden, Jr. W. C. Gardiner, and V. V. Lissianski, "GRI-Mech 2.11", 1995, [http://www.me.berkeley.edu/gri\\_mech](http://www.me.berkeley.edu/gri_mech).
- [172] G. P. Smith, D. M. Golden, M. Frenklach, N. W. Moriarty, B. Eiteneer, M. Goldenberg, C. T. Bowman, R. K. Hanson, S. Song, Jr. W. C. Gradiner, V. V. Lissianski, and Z. Qin, "GRI-Mech 3.0", 1999, [http://www.me.berkeley.edu/gri\\_mech](http://www.me.berkeley.edu/gri_mech).
- [173] A. Kazakov, and M. Frenklach, "Reduced reaction sets based on GRI-Mech 1.2", <http://www.me.berkeley.edu/drm/>.
- [174] E. L. Petersen, and R. K. Hanson, "Reduced kinetics mechanisms for ram accelerator combustion". *Journal of Propulsion and Power*. 1999, (15):4, 591-600.
- [175] P. Glarborg, N. I. Lilleheie, S. Bygstol, B. F. Magnussen, P. Kilpinen, and M. Hupa, "A reduced mechanism for nitrogen chemistry in methane combustion". In: 24<sup>th</sup> Symp. (Int.) on Combustion, The Combustion Institute, Pittsburgh, 1992, pp.889-898.

- [176] S. Yungster, and M. J. Rabinowitz, "Computation of shock-induced combustion using a detailed methane-air mechanism". *Journal of Propulsion and Power*. 1994, (10):5, 609-617.
- [177] S. C. Li, and F. A. Williams, "Reaction mechanisms for methane ignition". *Journal of Engineering for Gas Turbines and Power*. 2002, (124), 471-480.
- [178] N. Peters, and R. J. Kee, "The computation of stretched laminar methane air diffusion flames using a reduced four step mechanism". *Combust. Flame*. 1987, (68), 17-29.
- [179] S. C. Li, and F. A. Williams, "Reaction mechanisms for methane ignition". *Journal of Engineering for Gas Turbines and Power*. 2002, (124), 471-480.
- [180] J. E. Renner, "Numerical and experimental studies of the dynamics of diffusion flame sheets". PhD thesis, Northwestern, 2008.
- [181] J. Bibrzycki, and T. Poinso, "Reduced chemical kinetic mechanisms for methane combustion in O<sub>2</sub>/N<sub>2</sub> and O<sub>2</sub>/CO<sub>2</sub> atmospher". Working note ECCOMET WN/CFD/10/17, CERFACS. 2010,
- [182] H. C. Hottel, and A. F. Sarofim, "Radiative transfer". McGraw-Hill, New York, 1967.
- [183] H. C. Magel, U. Schnell, and K. R. G. Hein, "Simulation of detailed chemistry in a turbulent combustor flow". In: 26<sup>th</sup> Symp. (Int.) on Combustion, The Combustion Institute, 1996, pp.67-74.
- [184] C. V. Silva, F. H. R. França, and H. A. Vielmo, "Analysis of the turbulent, non-premixed combustion of natural gas in a cylindrical chamber with and without thermal radiation". *Combustion Sciences and Technologies*. 2007, (179), 1605-1630.
- [185] A. Brink, C. Mueller, P. Kilpinen, and M. Hupa, "Possibilities and limitations of the eddy break-up model". *Combust. Flame*. 2000, (123), 275-279.
- [186] R. S. Parikh, and R. Mahalingam, "Modeling and experimental studies on devolatilization yields from a bituminous coal". *Ind. Eng. Chem. Res.* 1987, (26), 2378-2384.
- [187] M. J. G. Alonso, A. G. Boreggo, D. Alvarez, and R. Menéndez, "Pyrolysis behaviour of pulverized coals at different temperatures". *Fuel*. 1999, (78), 1501-1513.
- [188] H. Zhou, A. D. Jensen, P. Glarborg, P. A. Jensen, and A. Kavaliauskas, "Numerical modeling of straw combustion in a fixed bed". *Fuel*. 2005, (84):4, 389-403.
- [189] Y. A. Levendis, K. Joshi, R. Khatami, and A. F. Sarofim, "Combustion behavior in air of single particles from three different coal ranks and from sugarcane bagasse". *Combust. Flame*. 2011, (158):3, 452-465.
- [190] C. K. K. Lun, S. B. Savage, D. J. Jeffrey, and N. Chepurniy, "Kinetic theories for granular flow: inelastic particles in couette flow and slightly inelastic particles in a general flow field". *J. Fluid Mech.* 1984, (140), 223-256.
- [191] C. F. M. Coimbra, J. L. T. Azevedo, and M. G. Carvalho, "3-D numerical model for predicting NO<sub>x</sub> emissions from an industrial pulverized coal combustor". *Fuel*. 1994, (73), 1128-1134.
- [192] N. Schaffel, M. Mancini, A. Szlek, and R. Weber, "Mathematical modeling of mild combustion of pulverized coal". *Combust. Flame*. 2009, (156), 1771-1784.
- [193] H. Stadler, D. Tobrin, M. Forster, and R. Kneer, "On the influence of the char gasification reactions on NO formation in flameless coal combustion". *Combust. Flame*. 2009, (156), 1755-1763.
- [194] D. F. Fletcher, B. S. Haynes, F. C. Christo, and S. D. Joseph, "A CFD based combustion model of an entrained flow biomass gasifier". *Applied Mathematical Modelling*. 2000, (24), 165-182.
- [195] A. Elfakhany, T. Klason, and X. S. Bai, "Modelling of pulverized wood combustion using a functional group model". *Combustion Theory and Modelling*. 2008, (12):5, 883-904.

- [196] A. M. Eaton, L. D. Smoot, S. C. Hill, and C. N. Eatough, "Components, formulations, solutions, evaluation and application of comprehensive combustion models". *Prog. Energy Combust. Sci.* 1999, (25), 387-436.
- [197] C. Crowe, S. Sommerfeld, and Y. Tsuji, "Multiphase flows with droplets and particles". CRC Press, 1998.
- [198] C. Crowe, "Multiphase flow handbook". Taylor & Francis Group, 2006.
- [199] S. A. Morsi, and A. J. Alexander, "An investigation of particle trajectories in two-phase flow systems". *J. Fluid Mech.* 1972, (55):2, 193-208.
- [200] J. Tomeczek, and H. Plauginok, "Specific heat capacity and enthalpy of coal pyrolysis at elevated temperatures". *Fuel.* 1996, (75), 1089-1093.
- [201] F. Boysan, W. H. Ayers, and J. Swithenbank, "A fundamental mathematical modeling approach to cyclone design". *Trans. IChemE.* 1982, (60), 222-230.
- [202] A. Bermúdez, J. L. Ferrín, A. Liñán, and L. Saavedra, "Mathematical modelling of pulverized coal furnaces". *Monografías de la Real Academia de Ciencias de Zaragoza.* 2010, (34), 27-50.
- [203] A. Williams, R. Backreedy, J. M. Jones, and M. Pourkashanian, "Combustion of pulverized coal and biomass". *Prog. Energy Combust. Sci.* 2001, (27), 587-610.
- [204] A. Silaen, and T. Wang, "Effect of turbulence and devolatilization models on coal gasification simulation in an entrained-flow gasifier". *International Journal of Heat and Mass Transfer.* 2010, (53), 2074-2091.
- [205] L. Ma, J. M. Jones, M. Pourkashanian, and A. Williams, "Modelling the combustion of pulverized biomass in an industrial combustion test furnace". *Fuel.* 2007, (86), 1959-1965.
- [206] A. Ajilkumar, and T. Sundararajan, "Numerical modeling of a steam-assisted tubular coal gasifier". *International Journal of Thermal Sciences.* 2009, (48), 308-321.
- [207] Y. Zhang, X. Wei, L. Zhou, and H. Sheng, "Simulation of coal combustion by turbulence-chemistry char combustion model and a full two-fluid model". *Fuel.* 2005, (84), 1798-1804.
- [208] M. Sami, K. Annamalai, and M. Wooldridge, "Co-firing of coal and biomass fuel blends". *Prog. Energy Combust. Sci.* 2001, (27), 171-214.
- [209] X. Chen, M. horio, and T. Kojima, "Numerical simulation of entrained flow coal gasifiers". Part , *Chemical Engineering Science.* 2000, (55), 3861-3874.
- [210] A. M. Mayers, "The rate of reduction of carbon dioxide by graphite". *Am. Chem. Soc. J.* 1934, (56), 70-76.
- [211] J. B. Howard, G. C. Williams, and D. H. Fine, "Fine. Kinetics of carbon monoxide oxidation in postflame gases". 14<sup>th</sup> Symp. (Int.) on Combustion. 1973, pp.975-986.
- [212] H. Robert, and P. E. Quig, "Clean power generation resulting from orimulsion utilization". In: 22<sup>nd</sup> International Technical Conference on Coal Utilization and Fuel Systems, 1997, pp.13-25.
- [213] C. T. Bowman, "Control of combustion-generated nitrogen oxide emissions: technology driven by regulations". *Proc. Combust. Inst.* 1993, 24: pp.859-878.
- [214] C. P. Fenimore, "Formation of nitric oxide in premixed hydrocarbon flames". *Proc. Combust. Inst.* 1971, 13: pp.373-380.
- [215] D. W. Pershing, and J. O. L. Wendt, "Pulverized coal combustion: The influence of flame temperature and coal composition on thermal and fuel NOx". *Proc. Comb. Inst.* 1977, 16: pp.389-436.
- [216] S. C. Hill, and L. D. Smoot, "Modelling of nitrogen oxides formation and destruction in combustion systems". *Prog. Energy Combust. Sci.* 2000, (26), 417-458.
- [217] P. Glarborg, A. D. Jensen, and J. E. Johnsson, "Fuel nitrogen conversion in solid fuel fired systems". *Prog. Energy Combust. Sci.* 2003, (29), 89-113.

- [218] P. J. Smith L. D. Smoot, "Coal combustion and gasification". Plenum, New York, 1985.
- [219] Y. B. Zeldovich, "The oxidation of nitrogen in combustion and explosions". *Acta Physicochem USSR*. 1946, (21), 577-628.
- [220] R. K. Hanson, and S. Salimian, "Survey of rate constants in H/N/O systems". In: W. C. Gardine (editor). *Combustion Chemistry*. 1984, pp.361-421.
- [221] A. A. Westenberg, "Kinetics of NO and CO in lean, premixed hydrocarbon-air flames". *Combustion Science and Technologies*. 1971, (9), 59-64.
- [222] W. Wang, S.D. Brown, C.J. Hindmarsh, and K.M. Thomas, "NO<sub>x</sub> release and reactivity of chars from a wide range of coals during combustion". *Fuel*. 1994, (73), 1381-1388.
- [223] C. Kim, and N. Lior, "A numerical analysis of NO<sub>x</sub> formation and control in radiatively/ conductively-stabilized pulverized coal combustors". *Chemical Engineering Journal*. 1998, (71), 221-231.
- [224] S. P. Visona, and B. R. Stanmore, "Modelling NO<sub>x</sub> release from a single coal particle; I. Formation of NO from volatile nitrogen". *Combust. Flame*. 1996, (105), 92-103.
- [225] M. Xu, J. L. T. Azevedo, and M. G. Carvalho, "Modelling of the combustion process and NO<sub>x</sub> emission in a utility boiler". *Fuel*. 2000, (79), 1611-1619.
- [226] F. C. Lockwood, and C. A. Romo-Millanes, "Mathematical modelling of fuel-NO emissions from PF burners". *J. Int. Energy*. 1992, (65), 144-152.
- [227] L. D. Smoot, and P. J. Smith, "NO<sub>x</sub> pollutant formation in a turbulent coal system". In: *Coal Combustion and Gasification*. Plenum, Plenum, NY, 1985, p373.
- [228] G. G. De Soete, "Overall reactions rates of NO and N<sub>2</sub> formation from fuel nitrogen". In: 15<sup>th</sup> Symp. (Int.) on Combustion, The Combustion Institute, Pittsburgh, 1975, pp.1093-1102.
- [229] J. M. Levy, L. K. Chen, A. F. Sarofim, and J. M. Beer, "NO/ Char reactions at pulverized coal flame conditions". In: 18<sup>th</sup> Symp. (Int.) on Combustion, The Combustion Institute, Pittsburgh, 1981, pp.111-120.
- [230] J. H. Pohl, and A.F. Sarofim, "Devolatilization and oxidation of coal nitrogen". In: 16<sup>th</sup> Symp. (Int.) on Combustion, The combustion Institute, Pittsburgh, 1977, pp.491-501.
- [231] N. Spitz, R. Saveliev, E. Korytni, M. Perelman, E. Bar-Ziv, and B. Chudnovsky, "Prediction of performance and pollutant emission from pulverized coal utility boilers". In: C. M. Lefebvre and N. Science (editors). *Electric Power: Generation, Transmission and Efficiency*. Nova Science, Lefebvre, 2007, pp.121-170.
- [232] J. D. Freihaut, M. F. Zabielsky, and D. J. Seery, "A parametric investigation of tar release in coal devolatilization". *Proc. Combust. Inst*. 1982, 19: pp.1159-1167.
- [233] Y. B. Yang, T. A. Naja, and B. M. Gibbs, " Optimisation of operating parameters for NO reduction by coal reburning in a 0.2 MWt furnace". *Journal of the Institute of Energy* 1997, (70), 9-17.
- [234] S. L. Chen, M. P. Heap, D. W. Pershing, and G. B. Martin, "Influence of coal composition on the fate of volatile and char nitrogen during combustion". *Proc. Combust. Inst*. 1982, 19: pp.1271-1280.
- [235] S. Niksa, and S. Cho, "Conversion of fuel-nitrogen in the primary zones of pulverized coal flames". *Energy and Fuels* 1996, (10), 463-473.
- [236] P. R. Solomon, D. G. Hamblen, R. M. Carangelo, and J. L. Krause, "Coal thermal decomposition in an entrained flow reactor". *Proc Combust Inst*. 1982, pp.1139-1149.
- [237] A. Arenillas, R. I. Backreedy, and J. M. Jones, "Modelling of NO formation in the combustion of coal blends". *Fuel*. 2002, (81):(5), 627-636.

- [238] Y. Zhang, L. Zhou, X. Wei, and H. Sheng, "Numerical simulation of NO<sub>x</sub> formation in coal combustion with inlet natural gas burning". *Chinese J. Chem. Eng.* 2005, (13), 318-323.
- [239] C. Yin, S. K. Kær, L. Rosendahl, and S. L. Hvid, "Co-firing straw with coal in a swirl-stabilized dual-feed burner: Modelling and experimental validation". *Bioresource Technology.* 2010, (101), 4169-4178.
- [240] R. Bassilakis, Y. Zhao, P. R. Solomon, and M. A. Serio, "Sulfur and nitrogen evolution in the argonne coals: experiment and modeling". *Energy and Fuels.* 1993, (7), 710-720.
- [241] M. J. Aho, J. P. Hämäläinen, and J. L. Tummavouri, "Importance of solid fuel properties to nitrogen oxide formation through HCN and NH<sub>3</sub> in small particle combustion". *Combust. Flame.* 1993, (95), 22-30.
- [242] H. Liu, and B. M. Gibbs, "Modeling of NO and N<sub>2</sub>O Emissions from Biomass-Fired Circulating Fluidized Bed Combustors". *Fuel.* 2002, (82), 271-280.
- [243] M. L. Holtmeyer, B. M. Kumfer, and R. L. Axelbaum, "Effects of biomass particle size during cofiring under air-fired and oxyfuel conditions". *Applied Energy.* 2012, (93), 606-613.
- [244] M. Syamlal, and T. J. O'Brien, "Computer simulation of bubbles in a fluidised bed". *AIChE Symp. Series.* 1989, (85), 22-31.
- [245] J. M. Dalla Valle, "Micromeritics". Pitman, London, 1948.
- [246] J. Garside, and M. R. Al-Dibouni, "Velocity-voidage relationships for fluidization and sedimentation". *I & EC Process Des. Dev.* 1977, (16), 206-214.
- [247] D. J. Gunn, "Transfer of heat or mass to particles in fixed and fluidized beds". *International Journal of Heat and Mass Transfer.* 1978, (21), 467-476.

# Appendix A

Coefficients of piecewise-polynomial function\* for temperature-dependent specific heat ( $c_p$ ) of species, which are taken from the material database given by Fluent Inc. (2005).

	$A_0$	$A_1$	$A_2$	$A_3$	$A_4$
CH <sub>4</sub>	403.5847 <sup>a</sup>	9.057335	-0.01442509	1.580519×10 <sup>-5</sup>	-6.343051×10 <sup>-9</sup>
	872.4671 <sup>b</sup>	5.305473	-0.002008295	3.516646×10 <sup>-7</sup>	-2.33391×10 <sup>-11</sup>
O <sub>2</sub>	834.8265	0.292958	-0.0001495637	3.413885×10 <sup>-7</sup>	-2.278358×10 <sup>-10</sup>
	960.7523	0.1594126	-3.270885×10 <sup>-5</sup>	4.612765×10 <sup>-9</sup>	-2.952832×10 <sup>-13</sup>
CO <sub>2</sub>	429.9289	1.874473	-0.001966485	1.29725×10 <sup>-6</sup>	-3.999956×10 <sup>-10</sup>
	841.3765	0.5932393	-0.0002415168	4.522728×10 <sup>-8</sup>	-3.15313×10 <sup>-12</sup>
CO	968.3898	0.4487877	-0.001152217	1.656882×10 <sup>-6</sup>	-7.34637×10 <sup>-10</sup>
	897.9305	0.4282316	-0.0001671392	3.023444×10 <sup>-8</sup>	-2.05137×10 <sup>-12</sup>
H <sub>2</sub> O	1563.077	1.603755	-0.002932784	3.216101×10 <sup>-6</sup>	-1.156829×10 <sup>-9</sup>
	1233.234	1.140523	-0.0004029141	5.542772×10 <sup>-8</sup>	-2.949824×10 <sup>-12</sup>
N <sub>2</sub>	979.043	0.4179639	-0.001176279	1.674394×10 <sup>-6</sup>	-7.256297×10 <sup>-10</sup>
	868.6229	0.4416295	-0.000168723	2.996788×10 <sup>-8</sup>	-2.004386×10 <sup>-12</sup>
NO	935.6001	0.3472092	-0.0009151535	1.445794×10 <sup>-6</sup>	-6.778306×10 <sup>-10</sup>
	899.2722	0.3516634	-0.0001389845	2.540701×10 <sup>-8</sup>	-1.738845×10 <sup>-12</sup>

\* Piecewise-polynomial function is defined as  $c_p(T) = A_0 + A_1T + A_2T^2 + A_3T^3 + A_4T^4$ ; <sup>a</sup> valid for temperature interval 300-1000 K; <sup>b</sup> valid for temperature interval 1000-5000 K



# Appendix B

FLUENT UDF for defining heterogeneous reaction rates:

```
#include "udf.h"
#define c1 5e-12
#define A1 0.002
#define E1 7.9e7
#define A2 0.052
#define E2 6.1e7
DEFINE_PR_RATE (user_rate, c, t, r, mw, pp, p, sf, dif_i, cat_i, rr)
{
/* Argument types
cell_t c
Thread *t
Reaction *r (reaction structure)
real *mw (species molecular weight)
real *pp (gas partial pressures)
Tracked_Particle *p (particle structure)
real *sf (current mass fractions of solid species in particle char mass)
int dif_i (index of diffusion controlled species)
int cat_i (index of catalyst species)
real *rr (rate of reaction kgmol/s) */
/* _____ */
/* Mass fractions */
real mhv_vol = C_YI(c,t,0);
real mO2 = C_YI(c,t,1);
real mCO2 = C_YI(c,t,2);
real mH2O = C_YI(c,t,3);
real mCO = C_YI(c,t,4);
real mH2 = C_YI(c,t,5);
real mN2 = C_YI(c,t,6);
/* _____ */
/* partial pressuers */
```

---

```

real pOp = 101325; /* Operating pressure (pa) */
real sum = (mhv_vol/20.672 + mO2/32 + mCO2/44 + mH2O/18 + mCO/28 + mH2/1 +
mN2/28);
real pO2 = mO2/32/sum*pOp;
real pCO2 = mCO2/44/sum*pOp;
real pCO = mCO/28/sum*pOp;
real pH2O = mH2O/18/sum*pOp;
/* _____ */
if (!strcmp(r->name, "reaction-3"))
/* C + O2 -> CO2 */
{
real Tg= C_T(c,t);
real Tp= P_T(p);
real ash_mass =
P_INIT_MASS (p)*(1.-DPM_CHAR_FRACTION (p)-
DPM_VOLATILE_FRACTION (p));
real one_minus_conv =
MAX (0.,(P_MASS(p)-ash_mass) / P_INIT_MASS(p)/ DPM_CHAR_FRACTION(p));
real Do = MAX(1.E-15, c1*pow(0.5*(Tp + Tg),0.75)/P_DIAM(p));
real R = A1*exp(-E1/UNIVERSAL_GAS_CONSTANT/Tp);
*rr=-P_DIAM (p)*P_DIAM (p)*M_PI*(Do*R)/(Do+R)*pO2*sf[0]*one_minus_conv;
}
/* _____ */
else if (!strcmp(r->name, "reaction-4"))
/* C + 0.5O2 -> CO */
{
real Tg= C_T(c,t);
real Tp= P_T(p);
real ash_mass =
P_INIT_MASS (p)*(1.-DPM_CHAR_FRACTION (p)-
DPM_VOLATILE_FRACTION (p));
real one_minus_conv =
MAX (0.,(P_MASS(p)-ash_mass) / P_INIT_MASS(p)/ DPM_CHAR_FRACTION(p));
real Do = MAX(1.E-15, c1*pow(0.5*(Tp + Tg),0.75)/P_DIAM(p));
real R = A2*exp(-E2/UNIVERSAL_GAS_CONSTANT/Tp);

```

---

```

*rr=-P_DIAM (p)*P_DIAM (p)*M_PI*(Do*R)/(Do+R)*pO2*sf[0]*one_minus_conv;
}
/* _____ */
else if (!strcmp(r->name, "reaction-5"))
{
/* C + CO2 -> 2CO */
/* k = 4.4*Tp*exp(-1.62x10^8/RTp) */
real ash_mass =
P_INIT_MASS (p)*(1.-DPM_CHAR_FRACTION (p)-
DPM_VOLATILE_FRACTION (p));
real one_minus_conv =
MAX (0.,(P_MASS(p) -ash_mass) / P_INIT_MASS(p)/
DPM_CHAR_FRACTION(p));
real rate = 4.4*P_T(p)*exp(-1.62e8/UNIVERSAL_GAS_CONSTANT/P_T(p));
*rr=-rate*P_DIAM (p)*P_DIAM (p)*M_PI*sf[0]*one_minus_conv;
}
/* _____ */
else if (!strcmp(r->name, "reaction-6"))
/* C + H2O -> CO + H2 */
/* K = 1.33*Tp*exp(-1.47x10^8/RTp) */
{
real ash_mass =
P_INIT_MASS (p)*(1.-DPM_CHAR_FRACTION (p)-
DPM_VOLATILE_FRACTION (p));
real one_minus_conv =
MAX (0., (P_MASS(p) -ash_mass) / P_INIT_MASS(p)/
DPM_CHAR_FRACTION(p));
real rate = 1.33*P_T(p)*exp(-1.47e8/UNIVERSAL_GAS_CONSTANT/P_T(p));
*rr=-rate*P_DIAM (p)*P_DIAM (p)*M_PI*sf[0]*one_minus_conv;
}
}
}

```

# Appendix C

Burnout of coal particles for the co-firing of coal and straw cases:

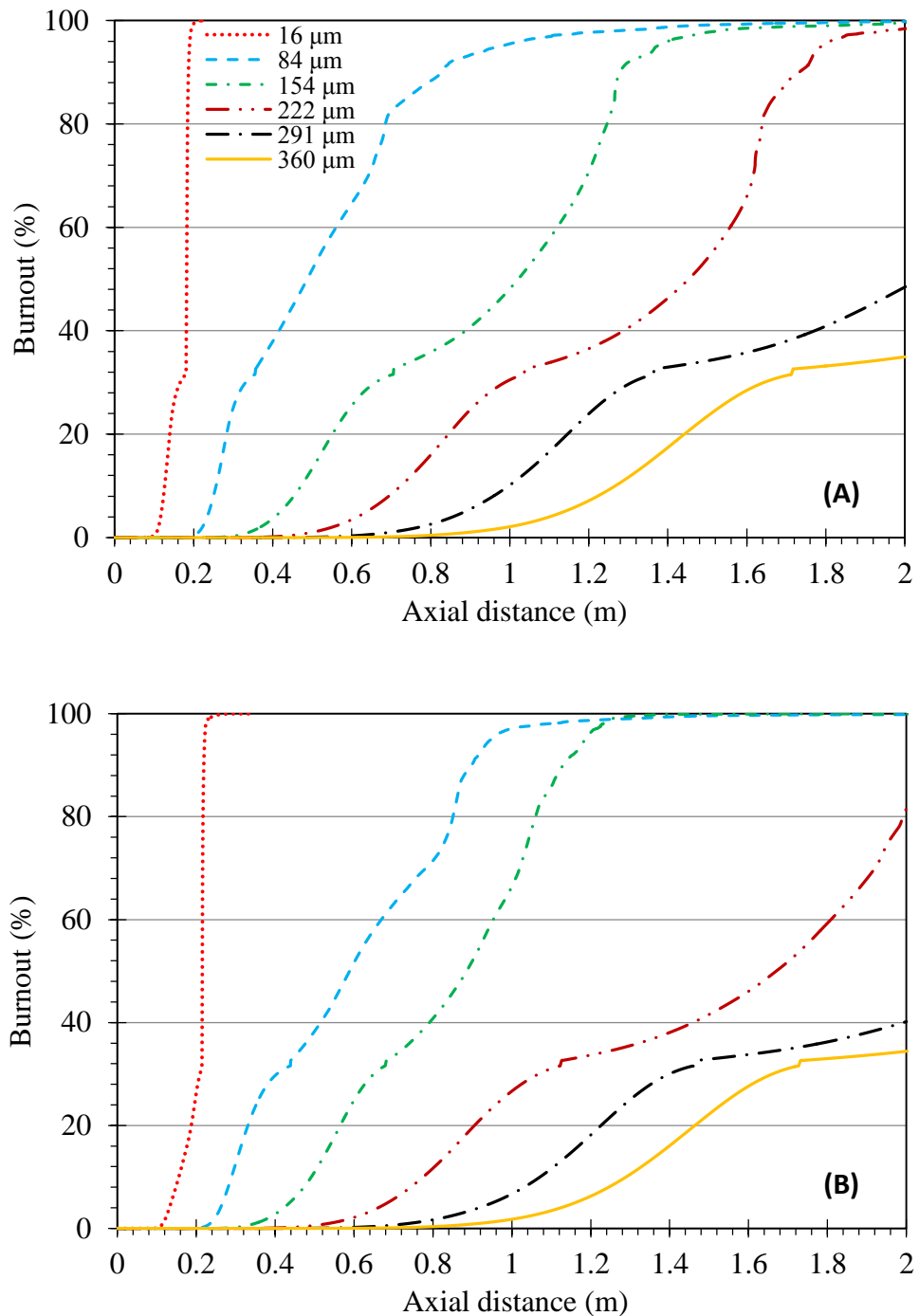


Figure C. 1: Burnout of coal particles with different sizes for co-firing of coal and straw at different shares on wt. basis: (A) 40% straw, (B) 30% straw, (C) 20% straw and (D) 10% straw.

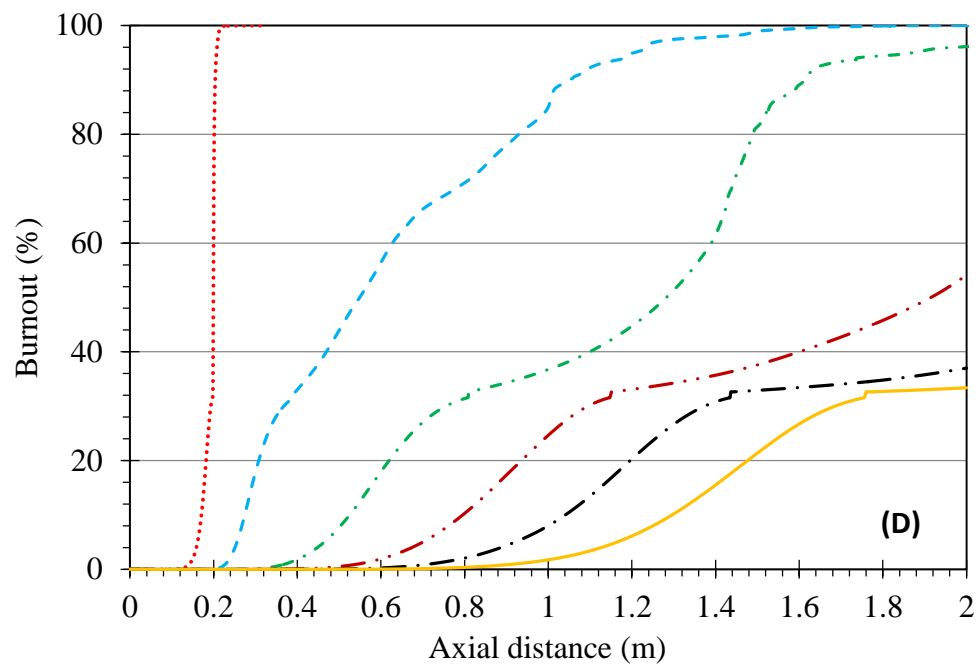
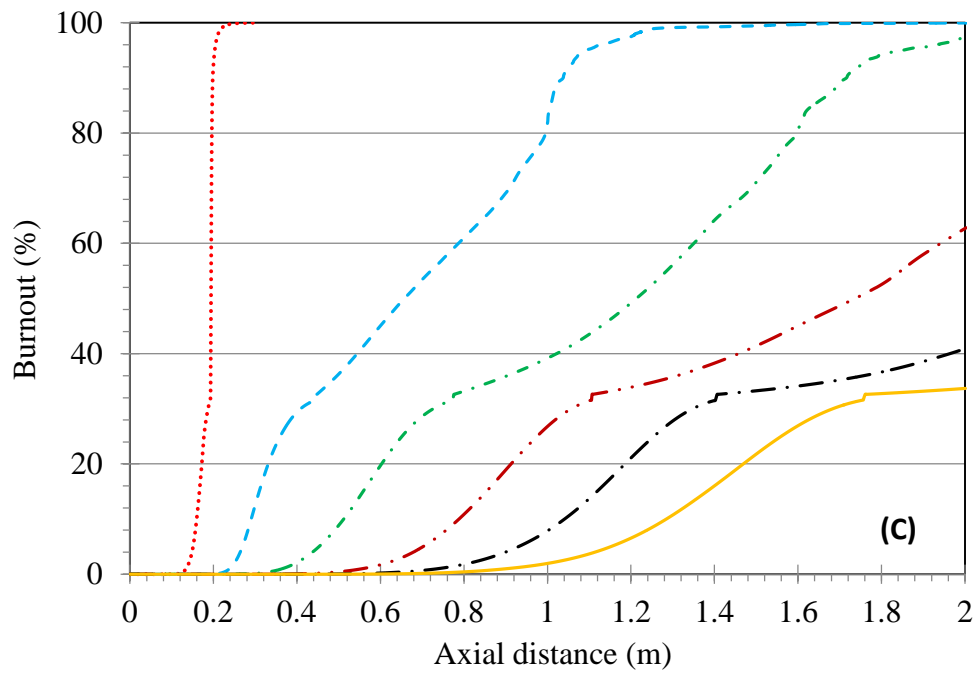


Figure C. 1: Continued.

# Appendix D

A UDF for defining the heterogeneous reaction (Euler-Euler model):

```
#include "udf.h"
static const real Arrhenius = 0.002;
static const real E_Activation = 79.e08;
#define SMALL_S 1.e-29
DEFINE_HET_RXN_RATE (arrh, c, t, hr, mw, yi, rr, rr_t)
{
    Thread **pt = THREAD_SUB_THREADS (t);
        Thread *tp = pt; /*Primary phase_gas*/
        Thread *ts = pt[1]; /*Secondary phase_solid carbon*/
        Domain **domain_reactant = hr->domain_reactant;
real *stoich_reactant = hr->stoich_reactant;
int *reactant = hr->reactant;
int i;
int sp_id;
int dindex;
Thread *t_reactant;
real ci;
real Tg=C_T(c,tp); /*Gas phase temperature*/
        real Tp=C_T(c,ts); /*Solid phase temperature*/
/* instead of compute rr directly, compute log (rr) and then
take exp */
*rr = 0;
for (i=0; i < hr->n_reactants; i++)
{
    sp_id = reactant[i]; /* species ID to access mw and yi */
    if (sp_id == -1) sp_id = 0; /* if phase does not have species,
mw, etc. will be stored at index 0 */
    dindex = DOMAIN_INDEX(domain_reactant[i]);
        /* domain index to access mw & yi */
    t_reactant = THREAD_SUB_THREAD (t,dindex);
```

---

```
/* get conc. */
ci = yi[dindex][sp_id]*C_R(c,t_reactant)/mw[dindex][sp_id];
ci = MAX(ci,SMALL_S);
*rr += stoich_reactant[i]*log (ci);
}
*rr += log (Arrhenius + SMALL_S) -
E_Activation/(UNIVERSAL_GAS_CONSTANT*Tg);
/* 1.e-40 < rr < 1.e40 */
*rr = MAX(*rr,-40);
*rr = MIN(*rr,40);
*rr = exp(*rr);
}
```

# Appendix E

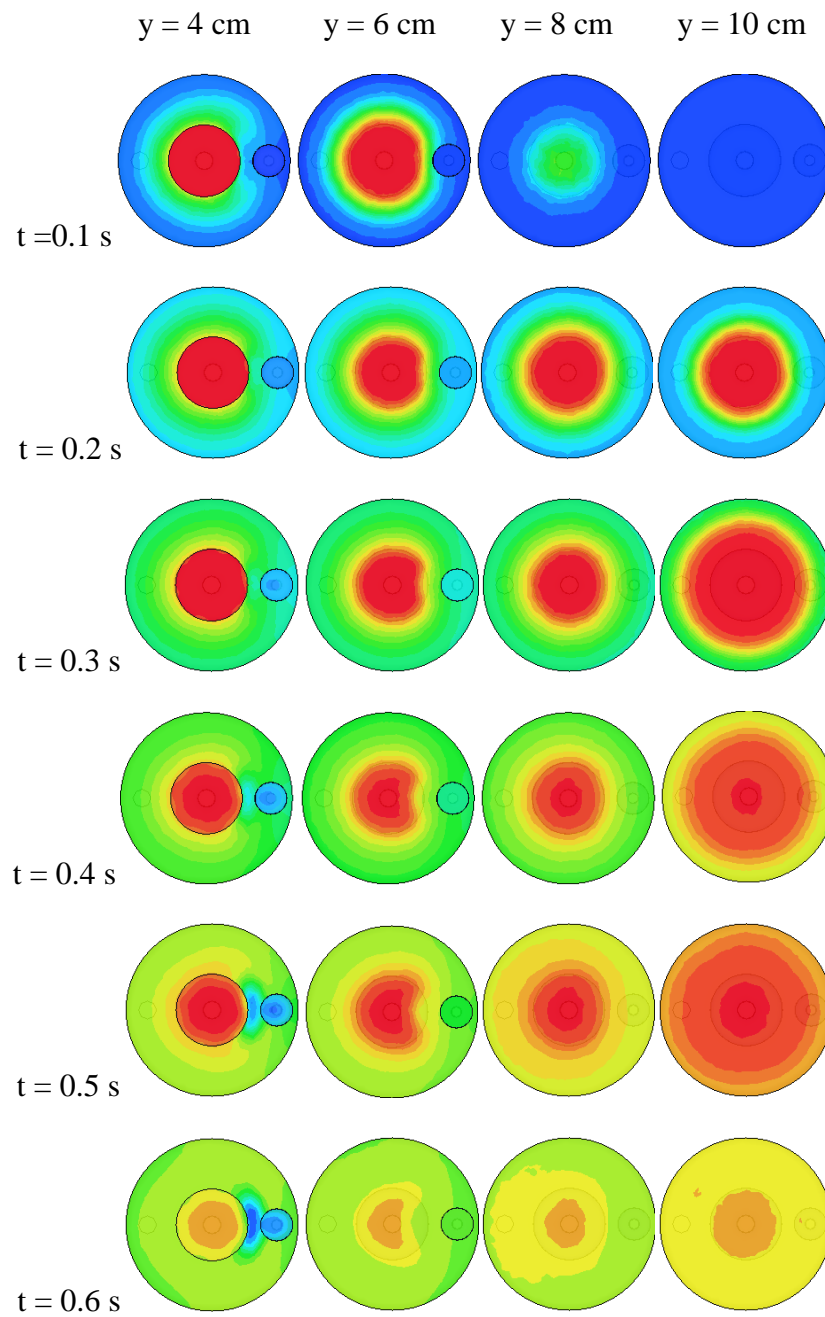


Figure E. 1: Contours of temperature at different locations in  $y$  direction showing at different times (s) for the base case (particle diameter of 0.5 mm).



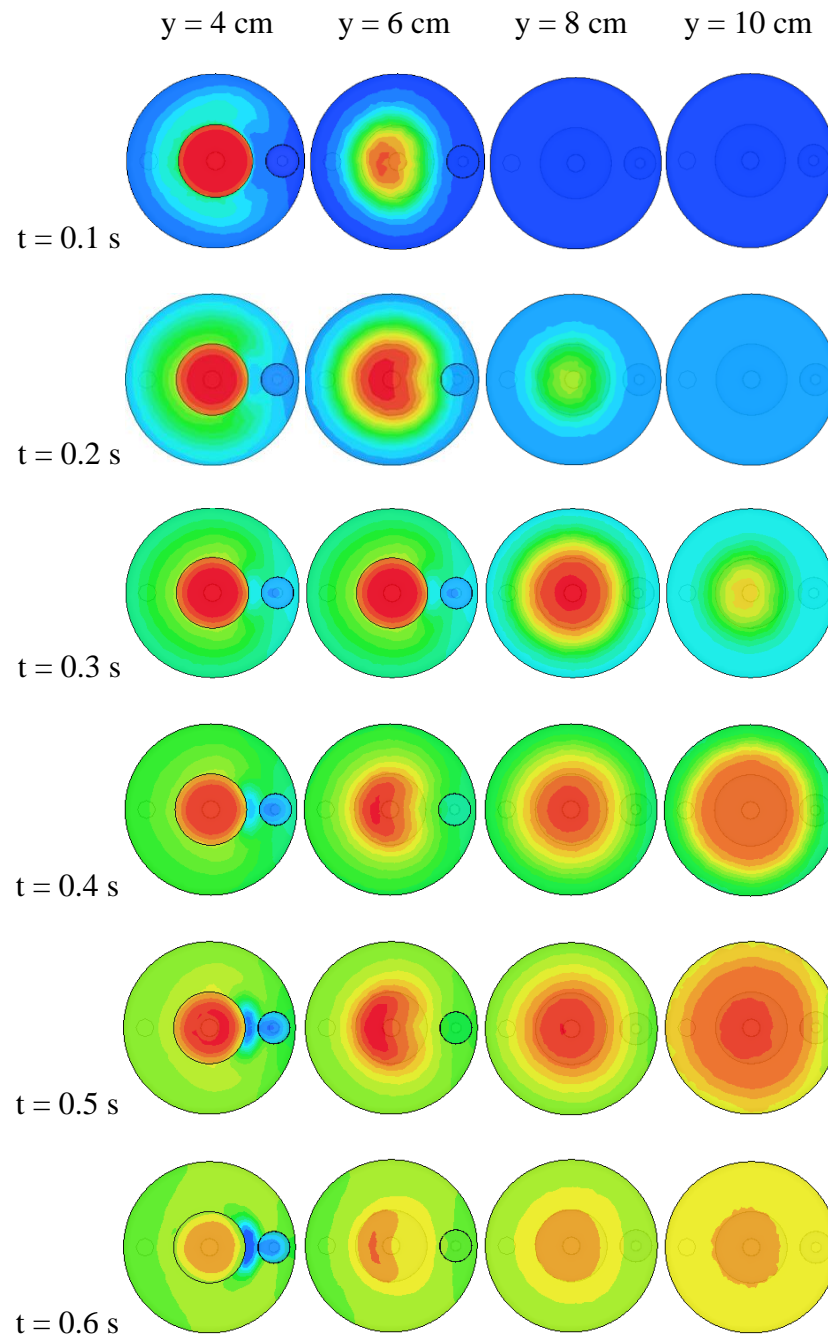
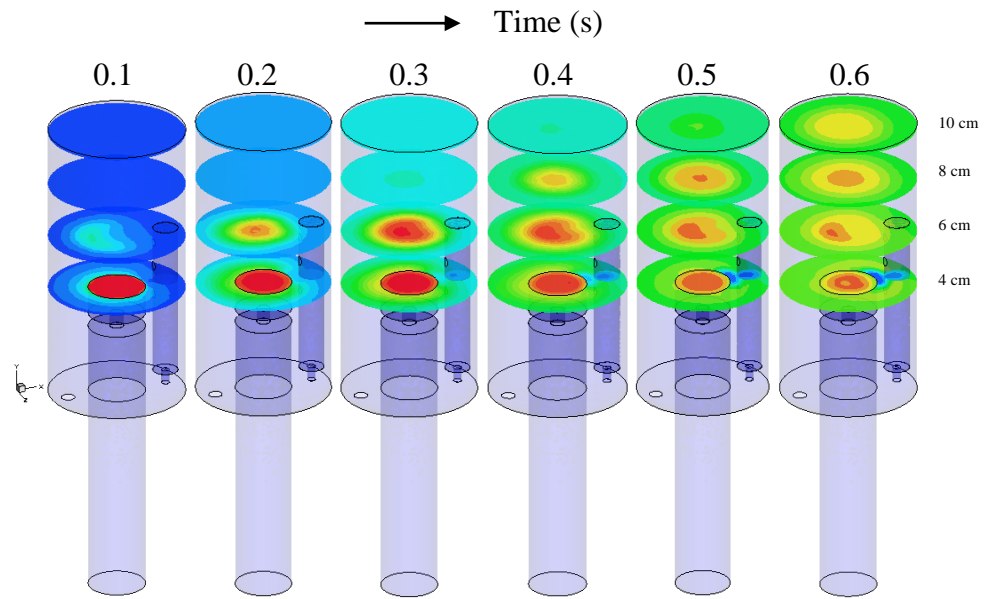
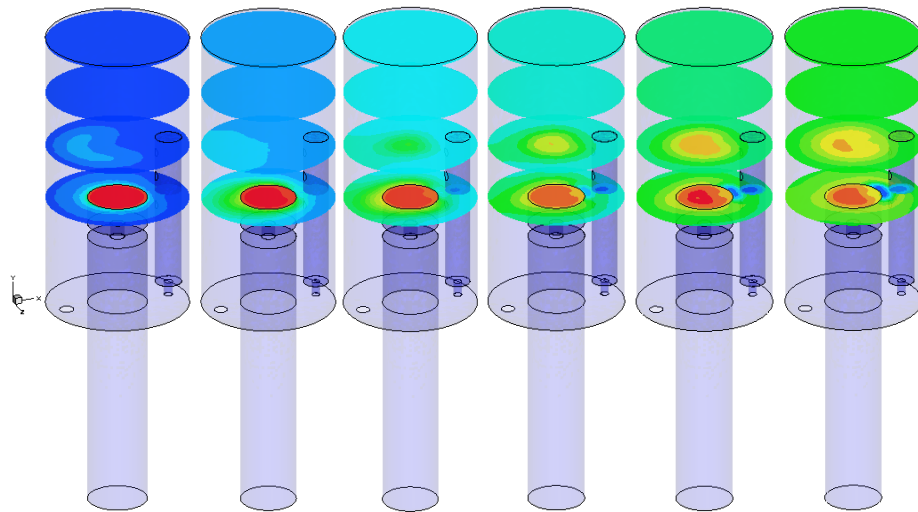


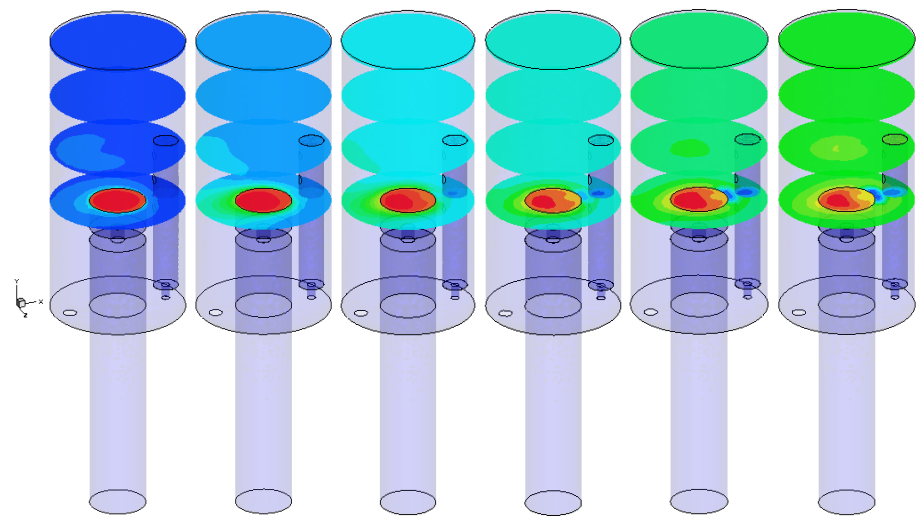
Figure E. 2: Temperature contours at different locations in  $y$  direction and different times (s) for the base case (particle diameter of 1.5 mm).



a) Case of 2 mm particle diameter.

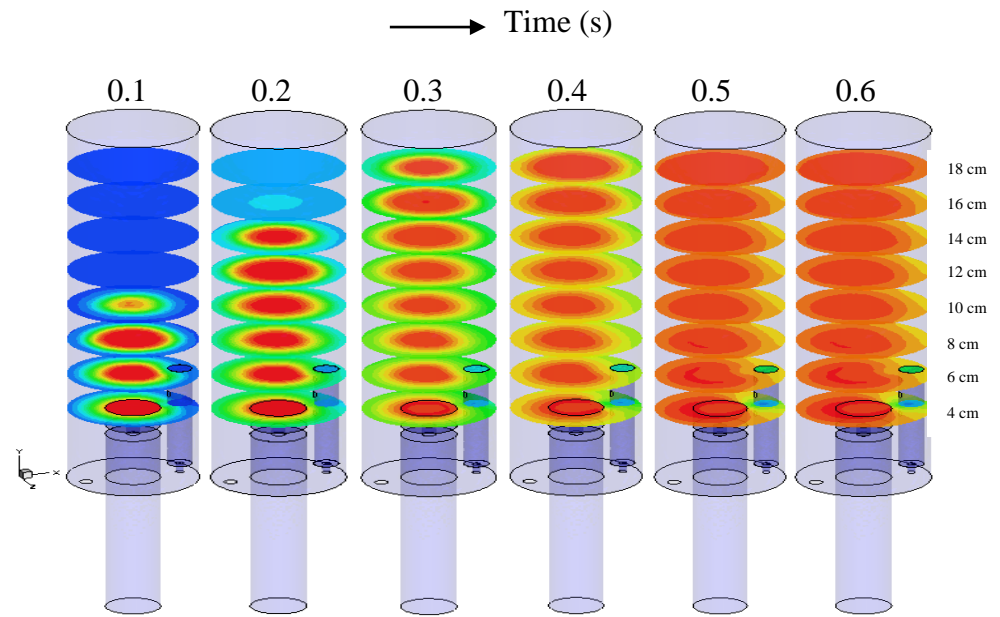


b) Case of 2.5 mm particle diameter.

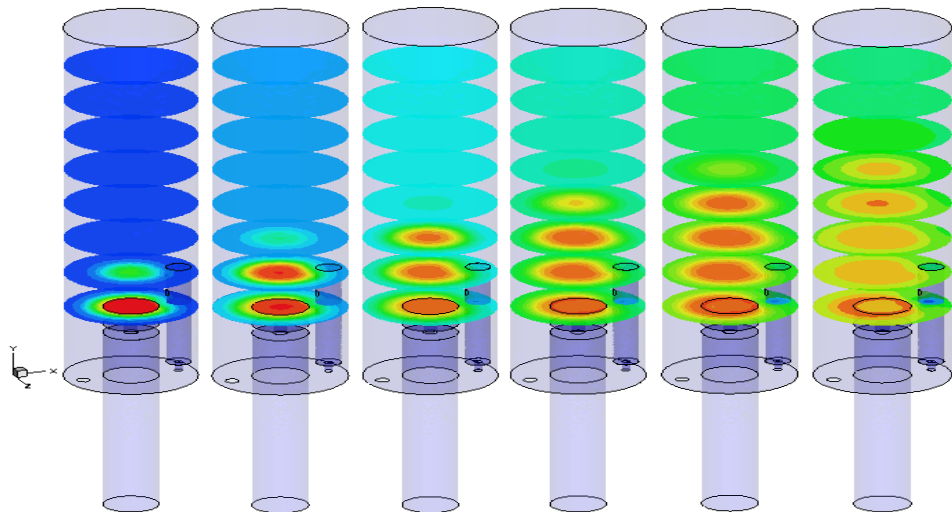


c) Case of 3 mm particle diameter.

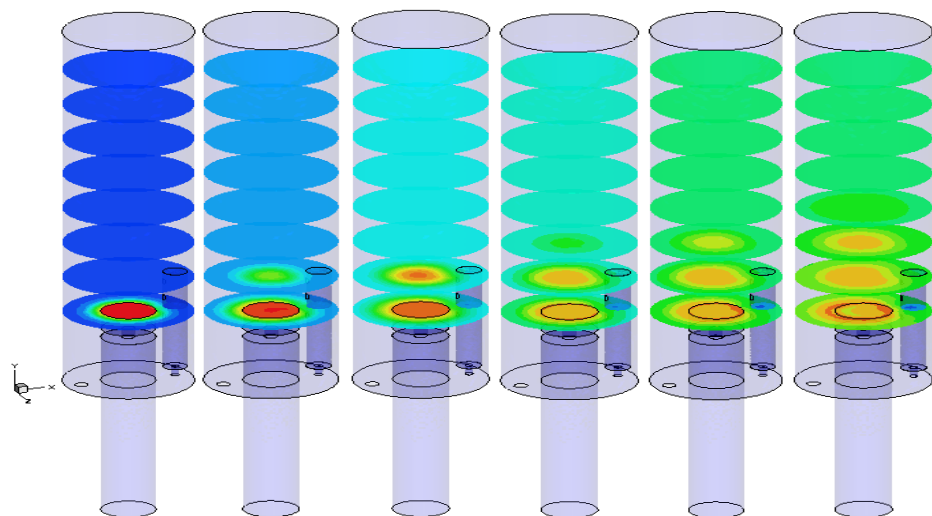
Figure E. 3: Temperature contours at different locations in y direction and different times (s) for the base case: a) 2 mm, b) 2.5 mm and c) 3 mm.



a) Case of 0.5 mm particle diameter.

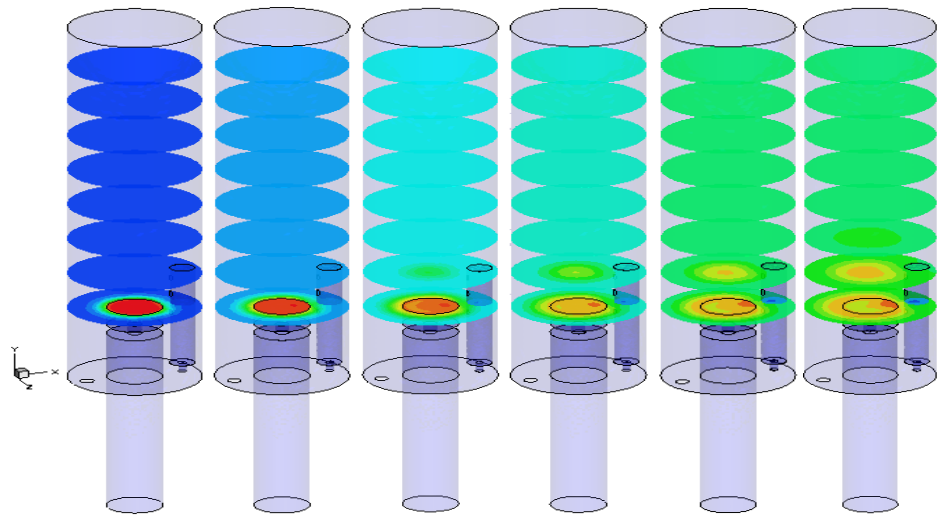


b) Case of 1.5 mm particle diameter.



c) Case of 2 mm particle diameter.

Figure E. 4: Temperature distribution for the doubled-height case at different times and different particle sizes: a) 0.5 mm, b) 1.5 mm, c) 2 mm and d) 2.5 mm



d) Case of 2.5 mm particle diameter.

Figure E. 4: Continued.

# Appendix F Publications and presentations

## Publications

1. Blaid Alganash, Manosh. C. Paul and Ian A. Watson: Numerical investigation of the heterogeneous combustion processes of solid fuels. *Fuel*, 141 (2015) 236-249.

## Conference Presentations

1. B. Alganash, M. C. Paul and I. A. Watson: Numerical study of heterogeneous combustion processes of solid fuels. In: 13<sup>th</sup> UK Heat Transfer Conference, London, UK, 2-3 Sep 2013.
2. B. Alganash, M. C. Paul and I. A. Watson: Investigation of heterogeneous combustion processes of biomass. In: 6<sup>th</sup> European Combustion Meeting, Lund, Sweden, 5-8 Jun 2013.
3. B. Alganash, M. C. Paul: Investigation of heterogeneous combustion processes of biomass. In 26<sup>th</sup> Scottish Fluid Mechanics Meeting on 29<sup>th</sup> May 2013 (Poster Presentation).
4. B. Alganash, M. C. Paul and I. A. Watson: Experimental and computational investigations of biomass mixing and combustion processes. In: 5<sup>th</sup> European Combustion Meeting, Cardiff University, 28<sup>th</sup> June -1<sup>st</sup> July 2011.
5. B. Alganash, M. C. Paul and I. A. Watson: Experimental and computational investigations of biomass and combustion processes. *Combustion Phenomena in Fire Science*, 2010.